Modelling of a laser-plasma injector for multi-stage acceleration

Patrick Lee

NNT : 2017SACLS180

Thèse de doctorat de l'Université Paris-Saclay préparée à l'Université Paris-Sud

Ecole doctorale n°572
École Doctorale Ondes et Matière
Spécialité de doctorat : Physique des plasmas

par

M. Patrick Lee

Modélisation d'un injecteur laser-plasma pour l'accélération multi-étages

Thèse présentée et soutenue à Orsay, le 11 juillet 2017.

Composition du Jury :

M.	Patrick Mora	Directeur de recherche au CNRS Ecole Polytechnique, Palaiseau	(Président)
M.	Alexander Thomas	Professeur associé University of Michigan, Ann Arbor	(Rapporteur)
M.	Luís O. Silva	Professeur des universités Instituto Superior Técnico, Lisboa	(Rapporteur)
M.	Jean-Luc Vay	Chargé de recherche LBNL, Berkeley	(Examinateur)
Mme.	Brigitte Cros	Directrice de recherche au CNRS LPGP, Orsay	(Directrice de thèse)

Nothing in life is to be feared, it is only to be understood. Now is the time to understand more, so that we may fear less.

Marie Curie

Acknowledgement

Admit it, you are reading this because you are looking for your name. Well, you have come to the right place.

Acknowledgement, the part of the thesis where I get to express my heartfelt thanks to everyone who was involved directly or indirectly in the present work. Without your guidance, your support and your encouragement, there is no way that this thesis can be written. Having you in my life, is already a privilege.

First of all, I would like to express my gratitude to my thesis advisor, Brigitte Cros, without your advice I would have been lost long time ago. Your guidance has helped me in all my research and writing of this thesis. What I learnt most from you is how to think like a scientist. Of course, a scientist has to be curious and ask the right question, but that is not all, one also requires the capability to convey research results to the public. From now on, my communication skills will only get better thanks to you, Brigitte.

I am grateful to Gilles Maynard for all insightful discussions that we have had. You are a wonderful mentor. You taught me how to keep the big picture in mind in whatever I am doing, which has helped me immensely in focusing on my work. Your advice in physics is always on point and gave me so many ideas to execute my research.

A very special gratitude goes out to Jean-Luc Vay for taking me under your wing. From you, I have learnt so much about the numerical challenges in laser wakefield acceleration (LWFA) simulations. A good listener, you always appreciate feedbacks, giving me the courage to voice my opinions. I would take this opportunity to thank you again for welcoming me to your group during my PhD study.

The aforementioned people are my three mentors. They have played a very important role in assuring the quality of my research work. I could not have imagined having better mentors.

At LPGP, I have had the pleasure of working alongside Thomas Audet (TA), Frédéric Desforges (FD) and without forgetting Bhooshan Paradkar (BP). TA and FD are both experimentalists, you were the ones who kept me grounded before I went on with my wild theoretical imagination. Although the time spent with BP was short, it was from you that I learnt how to perform my first LWFA simulation using the LUMAT clusters.

Talking about the LUMAT clusters, a very special gratitude goes out to Philippe Dos Santos, Michel Pascanu and Georges Raseev. You provided such tremendous technical support without which I wouldn't have acquired results to be included in this thesis.

As far as my programming skill is concerned, I could not thank Rémi Lehe and Henri Vincenti enough. Your careful review of my code on GitHub and feedbacks have made me a better developer. Your strong emphasis on code documentation has encouraged me to write comprehensive, elegant lines of code.

In the frame of the EuPRAXIA project, I have had the opportunity to interact with other scientists, from whom I have acquired some experience in working in an international project. Special thanks to Alban Mosnier, Arnaud Beck, Francesco Massimo, Li Xiangkun and Nghiem Phu Anh Phi for your fruitful discussions and contributions to this thesis.

From my experience, the atmosphere at LPGP is always a pleasant one. This could not have been possible without the positive energy of all members. Here I would like to first thank Tiberiu Minea for welcoming me to LPGP. Special mention to the administration staff Nicolas Dessaints, Thierry Devillers, Nathalie Rico-Perez, Bérénice Saidi and Sophie Granon for taking care of all paperwork so efficiently so that I could focus on my research. All post-docs, PhD students and interns, you have made the lab experience an unforgettable

one.

A special shout out to Martin Rudolph and TJ Petty. You took care of my sanity with your company and your uplifting mood during critical moments especially when writing this thesis. I have enjoyed every tea session that we have had in the lab and every silly stuff we have talked about at the table. I am so grateful to have known you guys.

To Daniel, Sandra and Jasmine, thank you for your dinner invitations. I have always had such lovely moments spending time with you.

I would like to take this opportunity to thank my running club, Paris FrontRunners for the intense training every Thursday that took my mind off my research, as a result I felt more alive and my spirit lifted high. Obviously, the trainings have also made me a better runner and for that I have to thank my running partners: Aymeric Sorin, Kaï Chu, Yvan Laurenti, René Lacroix, Jérôme Deraze etc.

Last but not least, I am grateful to my parents and my siblings, who have provided me through moral and emotional support. I am also grateful to my other family members and friends who have supported me along the way.

I couldn't believe that at some point in my life, I have to bid goodbye to some of you. From the bottom of my heart, I wish everyone with whom I have crossed paths all the best in your future endeavors.

For my parents.

Contents

List of Figures

Introduction

Conventional particle accelerators

The matter we know and that makes up all stars and galaxies only accounts for 5 % of the content of the universe. What about the other 95 %? This remaining 95 % is constituted of 27 % of dark matter and 68 % of dark energy that we know little about. Does the dark matter contain particles that move in the similar three dimensional space that we are familiar with, or does it also exist in higher dimensions? Can the dark matter be made up of vibrating strings? The 27 km-circumference Large Hadron Collider (LHC) in CERN (Fig. 1) is designed to help answer these questions.

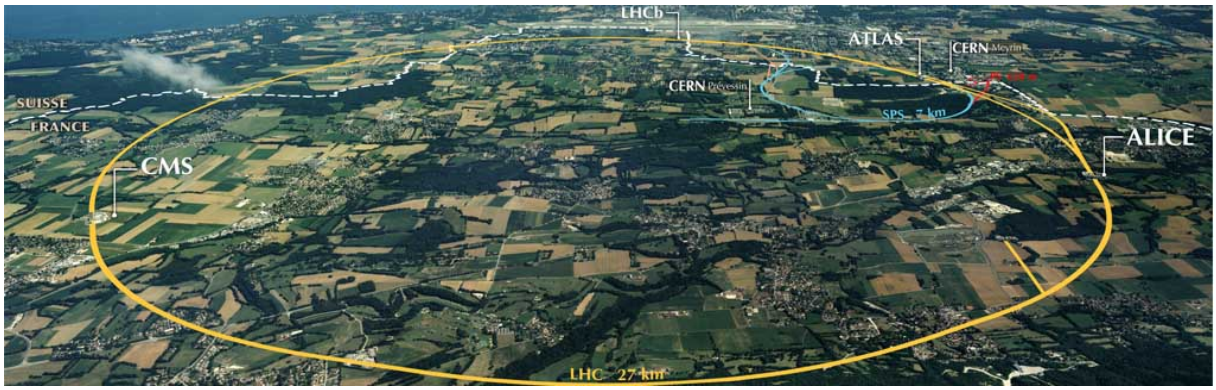

Figure 1: A bird's-eye view of CERN (Conseil européen pour la recherche nucléaire) that comprises of LHC (Large Hadron Collider) and SPS (Super Proton Synchrotron), and experiments such as LHCb (Large Hadron Collider beauty), ALICE (A Large Ion Collider Experiment), ATLAS (A Toroidal LHC ApparatuS) and CMS (Compact Muon Solenoid).

In this machine, particles are made to collide together at close to the speed of light, this collision creates more particles that physicists study to gain in-depth knowledge on how particles interact, and provides insights into the fundamental laws of nature. The discovery of the Higgs boson on the 4^{th} of July 2012 at LHC validated the Brout-Englert-Higgs mechanism in the Standard model, which explains how fundamental particles interact, governed by four fundamental forces. Particle accelerators are like a racetrack for particles, to accelerate these particles, two "track" configurations can be considered: the circular track and the linear track.

Circular racetracks like the LHC contain accelerating structures extending over certain sections in the ring, gradually accelerating particles to high energy when these particles pass through it. For instance, protons in the LHC make 11,000 laps every second for 20 minutes before they reach their collision energy ($7-8$ TeV) [1]. These particles are guided by magnets around the bends to keep them on course, but their energy is limited by the curves in the

accelerator. As a matter of fact, charged particles radiate energy when they are accelerated, more commonly known as the synchrotron radiation. In the case of electrons, the energy loss by synchrotron radiation is so high that they cannot be accelerated to reach the collision energy in a circular racetrack configuration. The energy loss of a charged particle, $\mathcal{E}_{part}$ due to synchrotron radiation is proportional to $\mathcal{E}_{part}^4/R_{machine}$ where $R_{machine}$ is the radius of the circular accelerator. To push the high-energy frontier, machines larger than the LHC need to be built. A study on a Future Circular Collider (FCC) is underway. This worldwide international project involves building an $80 - 100$ km circumference tunnel to accelerate protons to 100 TeV [2]. The cost review for this project is expected to be revealed in 2018 but it will obviously be more expensive than the LHC which has cost $8 billion to build, $1 billion/year to operate.

Linear accelerators do not face the same problem as circular accelerators. The only limitation to the particles' energy is the length of the track where they pass through accelerating structures to reach their desired energy. The longest linear accelerator (linac) is at SLAC (Stanford Linear Accelerator Center) which extends to 2.6 km, capable of delivering electron and positron beams with peak currents of approximately 20 kA that are focused down to below $30 \times 30\,\mu$m transverse spot size at 20 GeV using the rf (radiofrequency) cavities at FACET (Facility for Advanced Accelerator Experimental Tests) [3]. In theory, the accelerating gradients in conventional rf linear accelerators are currently limited to $\sim$ 100MV/m, partly due to the breakdown that occurs on the walls of the structure [4]. To accelerate particles to 10 TeV for instance, the linac length is required to be $\sim$ 100 km, which is at least as challenging as the 100 km circular racetrack.

The LHC has been instrumental in answering questions about the universe but in order to look deeper and further back toward the start of the universe, higher energy particles need to be created. If we rely on the same technology, particle accelerators will become prohibitively large and expensive. But we still want to continue answering these fundamental questions, therefore a change of technology is required. One option is to develop accelerating structure techniques to rapidly and effectively accelerate particles in linacs over a short distance. Or we can design and build stronger magnets that can bend ultra-high energy particles around the curves in circular accelerators. Research is ongoing in both areas. Our group focuses on the former, where we work on a novel accelerating structure that is plasma-based.

Other applications also benefit from accelerated particles. The betatron movement of the electron beam generates radiation in the X-ray region, with numerous applications in medicine, biology, material science etc.

Plasma-based accelerator: an alternative to the conventional accelerator

As the fourth state of matter, plasmas consist of electrons, ions and neutral atoms, usually at temperatures above 10^4 K. The sun and stars are plasmas, so are the earth's ionosphere, Van Allen belts, magnetosphere, etc. Indeed, plasmas make up much of the known matter in the universe. Their density and temperature span a huge range. Plasmas are also characterized by their dominating long-range electromagnetic interactions over their short range interatomic or intermolecular forces among a large number of particles. This gives rise to a collective behavior which depends not only on local perturbations but also on the state of the plasma in remote regions. There are three main parameters that characterize plasmas:

- thermal velocity, v_{th}: plasmas are in general high temperature entities, some of their

properties are connected with thermal effects,

- plasma frequency, ω_p: a simple unmagnetized plasma oscillates at a certain frequency when the charge distribution is locally perturbed from its equilibrium. This frequency has the expression $\omega_p \equiv \sqrt{(n_0 e^2/m_e\epsilon_0)}$, where n_0 is the ambient electron number density, e is the elementary charge, m_e is the electron mass and ϵ_0 is the vacuum permittivity,

- Debye length, λ_D : the distance a thermal particle travels during a plasma period. Its expression is $\lambda_D \equiv \sqrt{\epsilon k_B T_e/n_0 e^2}$, where k_B is the Boltzmann constant, T_e is the electron temperature.

Plasma-based accelerators rely on the electrostatic fields associated to plasma waves to accelerate electron beams. These plasma waves are driven by a force that perturbs locally the density of the plasma electrons and creates charge separation from ions. This force can be generated by several means, by the ponderomotive force of a single laser pulse [5], the mechanism is then known as the Laser WakeField Acceleration (LWFA); by the ponderomotive force due to the beating of two laser pulses, also known as the Plasma Beat Wave Acceleration (PBWA) [6, 7, 8]; or by the ponderomotive force using a self-modulated laser pulse, known as the Self-Modulated Laser WakeField Acceleration (SM-LWFA); or also by an electron beam (PWFA) [9]. This research work will focus on the single laser-driven plasma based accelerator (or LWFA).

The idea of using plasmas as a medium in an accelerator is of great interest because of their ability to sustain extremely large acceleration gradients, $E_0(\mathrm{V/m}) = cm_e\omega_p/e \approx 96\sqrt{n_0(\mathrm{cm}^{-3})}$, where c is the speed of light. This electric field is known as the cold non-relativistic wave breaking field [10] and it will be introduced in Chapter 1. Considering $n_0 = 10^{18}\,\mathrm{cm}^{-3}$, $E_0 \approx 96\,\mathrm{GV/m}$, which is nearly 1000 times higher than the accelerating gradients in conventional rf linacs. This implies that we can build particle accelerators that are cost-efficient and more compact.

Apart from the high accelerating gradients, the plasma wavelength or $\lambda_p(\mu\mathrm{m}) \approx 3.3 \times 10^{10}/\sqrt{n_0(cm^{-3})}$, e.g. $\lambda_p \approx 33\,\mu m$ for $n_0 = 10^{18}\,\mathrm{cm}^{-3}$, the electron bunch length will be less than half the plasma wavelength, which is two magnitudes shorter than those provided by photoinjectors. This opens up a whole lot of other applications that require short electron beams, e.g. in material science, the ultrashort duration of this electron bunch and radiation beam will provide time resolved measurements down to the motion of electrons on atomic scales. Coherent diffraction on single molecules will then become accessible, opening an entire new field of research [11].

Significant progress has been made over the last two decades on LWFA. The acceleration of electron beams in preformed plasma channels from capillary discharge waveguides up to 1 GeV has been demonstrated with 40 TW peak power laser pulses [12]. Subsequently, experiments have demonstrated $> 1\,\mathrm{GeV}$ electron beams in non-preformed plasmas with a 200 TW laser [13]. Using petawatt class lasers, electron beams were accelerated up to 2 GeV in a 7 cm-long gas cell [14]. Beams with energy tails up to 3 GeV were observed using a dual gas jet system of 1.4 cm [15]. The latest record in this race is the production of a 4.2 GeV electron beam using 16 J of laser energy in a preformed plasma channel waveguide produced by a 9 cm-long capillary discharge.

Although high beam energy is important for particle colliders, one must not neglect the control of the beam quality. In this context, much effort has been channeled in producing quasi-monoenergetic electron beams since the publication of [16, 17, 18]. Our group is

involved in the optimization of electron beams both experimentally and via plasma simulations. One of the goals of the group is to determine a set of laser plasma parameters that produce electron beam with narrow energy spread suitable for injection into a plasma accelerator, with high charge and low emittance. The specification of these properties depend on applications, but most applications require an energy spread of $< 10\,\%$, a charge of $\geq 10\,\mathrm{pC}$ and a transverse emittance of $\sim 0.1\,\mathrm{mm\,mrad}$.

Multi-stage laser-plasma accelerators

Acceleration of an electron beam in a single laser plasma accelerator stage is limited to a length determined by diffraction, depletion of the laser driver, or the dephasing of electrons (details are given in Chapter 1). For a 1 m-long preformed plasma fixed at $n_0 = 10^{17}\,\mathrm{cm}^{-3}$ providing laser guiding, an electron beam energy of 10 GeV can be delivered in theory. This energy is still insufficient for the particle collider application which requires particle energy of the order of TeV. Hence to reach this energy level, the proposed solution is a multi-stage accelerator. A proposed strategy consists of putting 100 LWFA modules in cascade. In this scheme, the electron beam is extracted from one module and injected into the subsequent module for further acceleration. Recently, Steinke et al. have succeeded in coupling two LWFA modules that are independently driven by two synchronized laser pulses [19]. This represents a milestone in the development of laser-driven, plasma-based accelerators for particle colliders, and for any other LWFA application that requires electron energies beyond the limits of single stages.

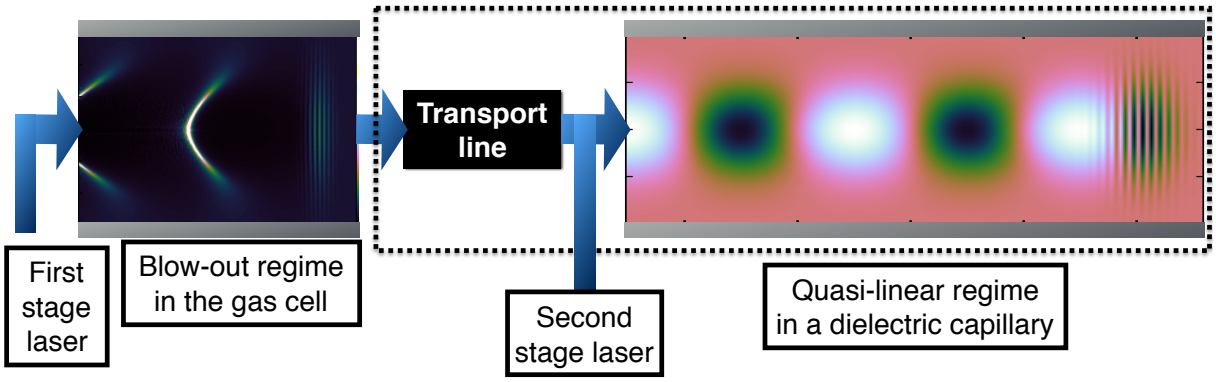

Figure 2: A schematic view of a two-stage laser plasma accelerator. The first stage is the injector stage where the electron beam is generated in a nonlinear regime in the gas cell. The electron beam is transported to the second stage, the accelerator stage via a transport line. In the second stage, the electron beam will be further accelerated in a quasi-linear regime in a dielectric capillary.

In Europe, there are several projects aiming at the demonstration of reliable multi-stage accelerators. The CILEX (Centre Interdisciplinaire Lumière Extrême) project which aims to develop an interdisciplinary research center using the Apollon-10P laser source is currently developed on the Plateau de Saclay by a consortium of French institutions. The Apollon-10P laser is expected to deliver two beams of 1 PW and 10 PW, ≥ 15 fs laser pulses, which will be used to test a two-stage LWFA [20] among other applications. Fig. 2 shows the configuration of a two-stage LWFA. The first stage laser creates a nonlinear plasma wave in a gas cell to generate an electron beam. This electron beam is then reshaped and transported

via a transport line to the second stage, where the second laser drives a quasi-linear plasma wave to avoid further generation of electron beam, in a dielectric capillary so that the laser pulse is guided. The second stage further accelerates the electron beam from the first stage to a higher energy.

The European project EuPRAXIA [21] is a 4-year project, started on the 1st November 2015 and aiming to deliver a conceptual design report for the worldwide first 5 GeV energy plasma-based accelerator that can provide industrial beam quality and user areas. It acts as the intermediate step between proof-of-principle experiments and ultra-compact accelerators for science, industry, medicine or the energy frontier.

Our group is one of the partners in both of these projects. We are actively involved in experimental and modeling work on the acceleration of electrons in the LWFA. The group conducts experiments at the UHI100 laser facility situated at CEA Saclay, France and at the Lund Laser Center (LLC), Sweden.

Particle-in-Cell (PIC) simulations, a tool for analysis and prediction

Three categories of plasma models can be used to describe laser-plasma interactions in the high-intensity (of the order of $\geq 10^{18}\,\mathrm{W/cm^2}$), short pulse($\leq 1\,\mathrm{ps}$) context, namely static, fluid or kinetic:

- ***Static model.*** The static approach treats the plasma as a passive medium created or altered as the laser pulse propagates through it. Through the modification of the electron density and the relativistic factor due to the laser pulse, the plasma has its dielectric constant modified. This will in turn influence the laser pulse propagation. This approach is well adapted to low density systems where the plasma period $\lambda_p = 2\pi/\omega_p$ is long relative to the interaction time. However, a static model can only be used for describing the laser propagation. The dynamics of the plasma particles is not included, so that this model cannot be used to determine the plasma wave properties.

- ***Fluid model.*** The fluid, or hydrodynamic modeling, is adapted to treat specific cases for which the velocity distribution function can be independently determined, with two limiting approximations. In the first one, the cold fluid approximation, the velocity distribution function is a delta function. That is all the particles of one species at one position have the same velocity, in amplitude and direction. This approximation has been used to describe the plasma wave in the quasi-linear regime of LWFA accelerator. It breaks down in the strongly non-linear regime, where there are many crossing of trajectories. Note also that in the case of an accelerator stage, the fluid model has to be combined to a kinetic one in order to describe the dynamics of the accelerated electrons. In this case one speaks of a hybrid model. The second type of approximation introduced in a fluid model is to use a Maxwellian velocity distribution function. This approximation is justified when particle-particle collisions play a dominant role. It is related to the study of the large-scale dynamic behavior of the plasma, for example under the influence of external electric and magnetic field, or heating by laser and/or particle beams. Timescales of interest are longer because they are governed by the ion motion, typically above picoseconds and up to several nanoseconds for laser-plasmas.

- ***Kinetic model.*** The kinetic model determines the particle distributions self-consistently. It is typically used in simulations of laser propagation, highly nonlinear plasma wave

generation where oscillation amplitudes are large, and some form of wave-particle interaction is present, i.e. trapping, wavebreaking. Particle-in-cell (PIC) is the mostly used numerical method to solve such model. It follows the evolution of the laser pulse on the short timescale associated with the laser period and simulates motion of charged particles, or plasma accordingly.

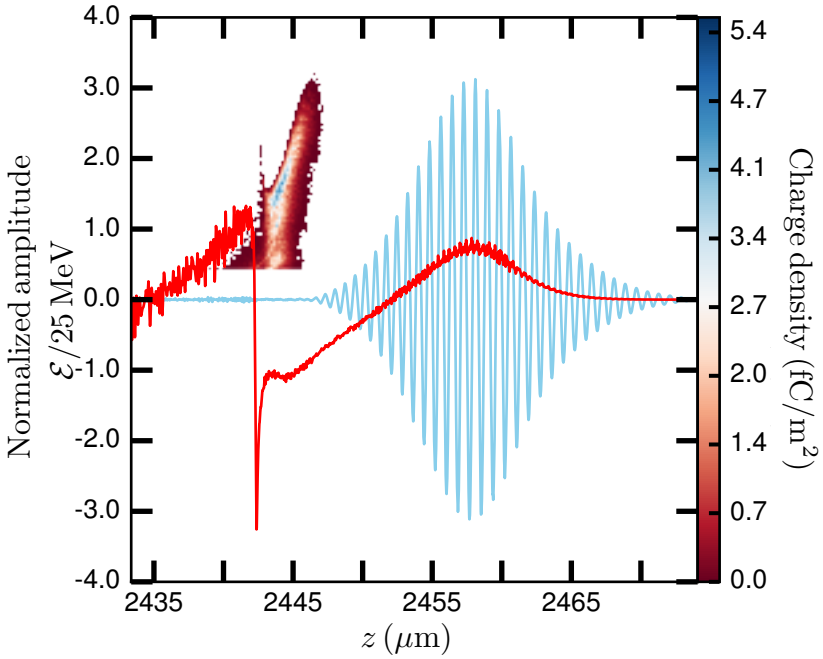

Figure 3: Typical PIC simulation snapshot shows the normalized laser field, $eE_y/m_ec\omega_0$ (in light blue), the normalized wakefield $eE_z/m_ec\mathbf{max}(\omega_p)$ (in red) and the energy, $\mathcal{E}/25$ of electrons (represented by a set of points) in a nonlinear regime. The color bar represents the charge density. The simulation is performed using Warp.

The physics of interest in LWFA concerns the plasma wave driven by the laser pulse, the transport of the laser pulse in the plasma and the dynamics of relativistic electrons that are trapped and/or accelerated by the plasma wave. The interaction of the electron beam with the wakefield often involves nonlinear effects which can only be taken into account by a kinetic model. This is the reason why the community working on the design and optimization of LWFA experiments has opted for this approach.

All simulations in this thesis were carried out using the PIC code Warp [22]. It is an open-source code, co-developed by the team led by Dr. Jean-Luc Vay in Lawrence Berkeley National Lab (LBNL). Warp is a three-dimensional time-dependent multiple-species PIC framework, with the addition of an accelerator lattice description. In the recent years, novel modules have been included in Warp to efficiently model LWFA experiments.

One example snapshot of a LWFA simulation using Warp illustrating a nonlinear plasma wave and beam loading effects is illustrated in Fig. 3. It shows the normalized laser field, $eE_y/m_ec\omega_0$ (in light blue), the normalized wakefield $eE_z/mc\mathbf{max}(\omega_p)$ (in red) and the energy, $\mathcal{E}$ of electrons (represented by a set of points). The color bar represents the charge density. From this figure, several important points have to be stressed. We observe that the accelerating field, can be as large or even larger than its wave breaking limit, indicating that the regime is highly nonlinear. Close to the $z-$axis position at which the density of accelerated electrons is maximum, we observe a 'small' bump in the longitudinal field curve.

This bump is due to beam loading effects, a process by which the field produced by the accelerated electrons significantly modifies the fields of the accelerating plasma wave. In fact, the density of the accelerated electrons become larger than the plasma density. This has a significant effect on the dispersion in energy. As will be shown in Chapter 5, when injection is performed through the ionization of a a gaseous medium with impurities, the relative contribution of the beam loading effect in the acceleration process can be clearly identified. As a final remark, the bunch of accelerated electrons is very close to the laser pulse. In some cases, corresponding to experimental situations, the relativistic electrons can interact with the tail of the laser pulse during a significant part of the acceleration process. The possible influence of this interaction should be carefully determined and will be discussed in Chapter 5.

The above discussion with Fig. 3 gives us a first illustration on the importance of the accuracy of the numerical scheme used in the numerical modeling. Due to the accumulation during the interaction process, even an a-priori small amount of error or numerical noise can have significant effect on the final properties of the electron bunch. That is why a lot of effort has been devoted in recent years in order to derive new numerical schemes, yielding better accuracy and lower noise. Most of these optimal schemes are implemented in Warp and have been used for our calculation. For a given numerical scheme, and in a cylindrical geometry, there are mainly three parameters, which value will control the numerical accuracy: widths of the numerical cell Δz, Δr in longitudinal and transverse directions and, to a lesser extend, the number of macro-particles per cell. Due to the fact that the time step is fixed by Δz (see Chapter 2) the computational time for a full calculation scales as $1/\left(\Delta z^2 \times \Delta r\right)$. A typical calculation on the optical injector performed in this thesis has required ~ 20000 CPU-Hours. Most of our calculations have been performed using $\Delta z = \lambda_0/30$ and $\Delta r = \lambda_0/4$, where λ_0 is the laser wavelength. From the scaling law it becomes obvious that parametric studies are not feasible with smaller Δz and Δr. Although we can get some guidelines from the accumulated expertise, the strong nonlinearity of our problem prevents us from getting an a-priori quantitative estimate of the accuracy of one calculation. This accuracy can only be derived by studying the convergence of the results with respect to numerical parameters. This convergence study can only be performed on an example of a given class of configuration, the results of which being then extrapolated to the whole class. An example of such study is given in Chapter 4. Globally we can assert that the aforementioned resolution used in our calculations, is sufficient to evaluate with a good accuracy first order properties of an accelerated electron beam such as the average energy and the energy spread but in the evaluation of the second-order beam properties, e.g the beam emittance, some uncertainties persist. A few calculations, with higher resolution, have been performed to determine second-order beam properties with a good accuracy for specific configurations.

The numerical grid size has already imposed an important number of CPU-hours required for a PIC simulation. In order to limit this amount, the simulation box size has to be reduced to its minimum. For that, open boundaries are crucial to ensure waves and disturbances originating with the model domain to leave the domain without affecting the interior solution in a way that is not physically realistic. For instance, in simulating a moderate power laser pulse propagating in a plasma longer than the Rayleigh length, the laser will start to diffract, some part of the wave will hit the transverse boundary. If no special treatment is done at this boundary, the wave will get reflected and impact the components that are still in the simulation box. One efficient implementation of open boundaries is Bérenger's Perfectly Matched Layer (PML) [23]. Study of its efficiency is done in the standard Yee scheme but not systematically at higher order. In Chapter 3, we demonstrate that the PML is

even more efficient in high-order finite-difference time-domain (FDTD) and pseudo-spectral time-domain (PSTD) electromagnetic (EM) solvers than in the standard Yee-solver.

From the previous paragraphs, we learn that the shortest scale in LWFA simulations is the laser wavelength, however the plasma response in Fig. 3 takes place at a scale length of 20 μm. Running a simulation of such resolution implies an over resolution of the plasma wave. The mixing of these very disparate length scales introduces a huge challenge to PIC simulations. In fact, a full three-dimensional (3D) PIC simulation for a 10 GeV stage, which sees the laser of $\lambda_0 = 0.8\,\mu$m propagating through a 30 cm plasma at $10^{17}\,\mathrm{cm}^{-3}$, requiring at least 1 Million time-steps is still out of reach.

Several reduced models that approximate some physics elements were proposed to efficiently describe plasma-based acceleration in an accessible computational time. These include the moving window method [24], quasistatic methods [25, 26, 27], the ponderomotive guiding center (PGC) method [28, 29] for modeling laser propagation. In some cases, these methods are combined, i.e. quasistatic field equations are combined with the PGC approximation in QuickPIC [26, 27] in LWFA modeling. Each of these methods allows for a significant speedup compared to full 3D PIC simulations because of approximations in the physical description of the system. They may be lacking in some important elements in physics, e.g. the quasistatic methods cannot accurately model self-injection, the PGC approximation cannot model full pump depletion distances for extremely high laser intensities, therefore the use of these models is very problem dependent. Another reduced method that takes into account the symmetry of the laser-plasma interaction in underdense plasmas in cylindrical coordinates (r, z) has been introduced in [30]. It is well adapted to LWFA simulations as long as the laser pulse is nearly axis-symmetrical. This method allows a 3D description of the laser plasma interaction at a computational cost that is equivalent to the one of a 2D PIC simulation. Since this method offers such advantages, we used it to perform most simulations for the analysis and optimization work presented in Chapter 5.

Another method to reduce the computational time of a PIC simulation is by running it in an optimal Lorentz-boosted frame (LBF) [31]. This approach exploits the properties of space and time dilation and contraction associated with the Lorentz transformation, without alteration to the fundamental equations of particle motion or electrodynamics. Due to the fact that the ratio of longest to shortest space and time scales of a system of two or more components crossing at relativistic velocities is not invariant under such a transformation, the number of computer operations (e.g. time-steps) becomes proportional to the ratio of the longest to shortest timescale of interest. In LWFA simulations, choosing a boosted frame moving at the group velocity of the laser will have the laser wavelength dilated, and the plasma length contracted, resulting in a reduction of time-steps because the crossing time between the laser and the plasma has become shorter. Being able to speed up simulations is not the end of the story, the simulated results have to be accurate. With this motivation in mind, the study of convergence of results obtained using the Lorentz-boosted frame technique is one of the research objectives of this thesis (see Chapter 4).

Objectives and Outline

This dissertation has two main objectives. Firstly, to carry out studies aiming to provide more accurate, more reliable and faster PIC simulations with PML and the Lorentz-boosted frame technique. Secondly, to analyze experimental results on the electron injector ELISA (ELectron Injector for compact Stage high energy Accelerator) [32] obtained at the Lund

Laser Center and at the UHI100 facility, and to prepare an optimized design for the laser-plasma injector in the frame of the CILEX and EuPRAXIA projects via simulations using realistic laser-plasma parameters. This thesis is organized as follows:

Chapter 1 details the basic physics of laser-plasma interaction relevant to wakefield acceleration and summarizes results which underlie current work.

Chapter 2 describes the state-of-the-art numerical tools and techniques used for LWFA simulations. It elaborates the PIC model and its features which construct the basis of the code framework Warp used in our studies.

Chapter 3 describes the Perfectly Matched Layer (PML) that is essential to efficiently treat the boundary of the simulation box. An efficiency analysis, using the coefficient of reflection as the figure of merit, on the PML in a high-order FDTD and a PSTD EM solvers is conducted. A theoretical model to quantify the coefficient of reflection is also given.

Chapter 4 studies and discusses the accuracy of simulation results using the Lorentz-boosted frame technique in the high laser intensity case where self-injection of electrons is susceptible to take place.

Chapter 5 first demonstrates the capability of Warp in producing reliable results using the azimuthal Fourier decomposition algorithm in cylindrical coordinates (r, z). In the second part, we report on PIC simulations performed with Warp to optimize the electron injector in order to obtain an electron beam that corresponds to the specifications defined in the CILEX project.

This three-and-a-half-year research work was performed in close collaboration between Laboratoire de la Physique des Gaz et Plasmas (LPGP) and Lawrence Berkeley National Lab (LBL). At LPGP, I worked closely with experimentalists, Brigitte Cros, Frédéric Desforges and Thomas Audet to analyze and understand experimental results obtained at the UHI100 facility and at the Lund Laser Center. I have had very fruitful and insightful discussions on the simulation results and also on the optimization work on the electron injector with Gilles Maynard. For a total period of one year, I was in LBL working with Jean-Luc Vay and Rémi Lehe on the efficiency of the PML and the accuracy of the Lorentz-boosted frame technique applied to LWFA simulations in the nonlinear regime.

Chapter 1

Physics of LWFA

Ever since Tajima and Dawson [5] published their article on laser plasma acceleration in 1979, suggesting the use of an intense electromagnetic pulse to create a wake of plasma oscillations to accelerate trapped electrons, there has been a lot of research work in this area. Theories have been established to describe the generation of the wakefield, the nonlinear effects due to the interaction between the laser pulse and the plasma, electron trapping and injection mechanisms and the acceleration limits of this concept. This chapter serves as an introduction to the state-of-the-art of LWFA and it covers all the physics concepts required to understand the body of work of the thesis. Since the quality of the accelerated electron beam appears recurrently, figures of merit used for its quantification such as the energy spread and the emittance are also included.

Contents

1.1 Qualitative picture

Well before lasers were invented, scientists have recognized that under certain restrictive conditions no net energy gain is possible for an electron when interacting with an electromagnetic field. These restrictive conditions constitute the Lawson-Woodward theorem [33, 34, 35], it assumes:

- the laser field is in vacuum, with no interfering walls or boundaries,
- the electron is highly relativistic ($\beta = v/c \to 1$) along the acceleration path,
- no static electric or magnetic fields are present,
- the region of interaction is infinite,

The introduction of a plasma in LWFA violates nearly all the Lawson-Woodward assumptions, thus electrons are susceptible to gain net energy by this means of acceleration.

LWFA relies on an underdense plasma to transfer the energy from a laser beam to a trailing bunch of electrons, either injected internally or externally. Its underlying physics is that the ponderomotive force of a laser pulse moving through the plasma pushes electrons ahead of the pulse and to the sides [36, 37, 38], creating a periodic trailing structure of rarefaction and concentration of electrons. This electronic density perturbation results in a Langmuir or plasma wave which is characterized by strong electric and magnetic fields, known as the wakefields. For example, a plasma density of $n_0 = 10^{18}\,\mathrm{cm}^{-3}$ yields an electric field of $E_z \approx 96\,\mathrm{GV/m}$.

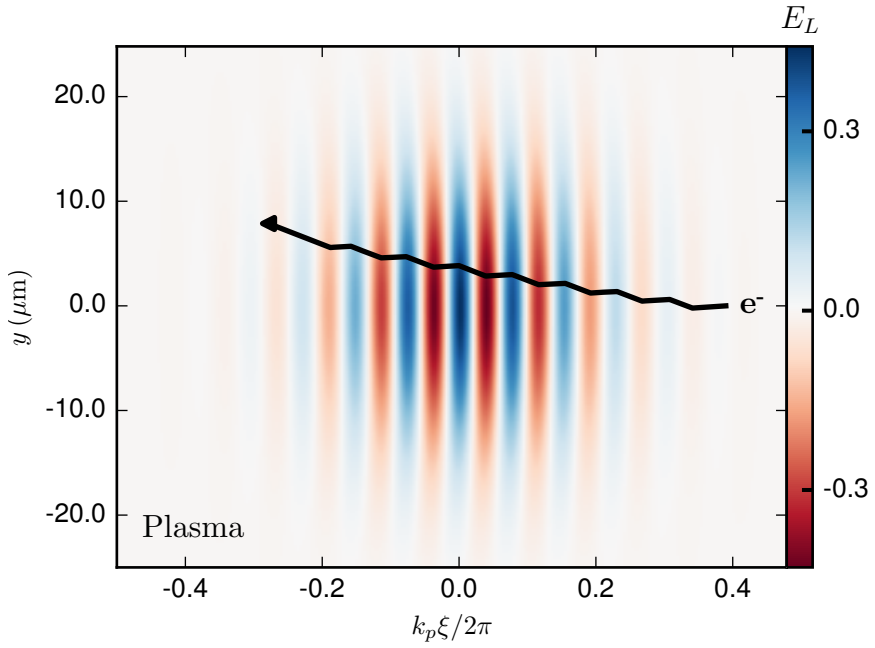

Figure 1.1: The trajectory of a single electron upon interacting with the laser field, E_L, polarized in the $y-$direction in a plasma. E_L is normalized to its maximum value and represented in the plane $(k_p\xi/2\pi, y)$. On the short time scale, the electron quivers while traversing the laser pulse; on the long time scale, the electron is removed from the axis due to the radiation or ponderomotive force.

In Fig. 1.1 is plotted the laser field, E_L (normalized to its maximum value) propagating in the $z-$direction, represented in the plane $(k_p\xi/2\pi, y)$, with $\xi = z - v_g t$, where v_g is the group velocity of the laser pulse, indicating that we are in the laser frame and k_p is the plasma wavenumber. An electron that is on the axis of a focused laser spot experiences a push away from the axis by the laser electric field and when the field reverses, it experiences a smaller push inward because the intensity is higher near the center. Over several cycles of the laser field, the electron migrates further outward. Interaction of this oscillation with the laser magnetic field also results in an axial force which pushes electrons ahead of the pulse (see Sec. 1.2 for quantitative derivation).

Electron motion can be separated into two time scales. On a short time scale, the electrons experience the oscillating electric and magnetic field of the laser pulse and acquire a momentum directly from it, known as the quiver momentum. On a long time scale, the average force associated with the laser pulse envelope, namely the ponderomotive force displaces the electrons while ions remain immobile.

The interaction between an intense laser pulse and a plasma is illustrated in Fig. 1.2. The figure shows the electronic density map represented in the coordinates $(k_p\xi/2\pi, x)$, with the laser that propagates from left to right. The movement of electrons upon interacting with the laser pulse creates a low electronic density region in the plasma at the rear of the laser pulse. Ions, being much heavier than electrons, are not significantly displaced in the time scale corresponding to the electron motion. The electric field induced by the electronic density perturbation causes the electron density to oscillate behind the laser pulse, creating a plasma wave that co-moves with the laser pulse, similar to the wake behind a speedboat. The laser pulse moves at a group velocity[1] $v_g \approx c$ with $v_g \approx c(1 - \omega_p^2/2\omega_0^2)$, ω_0 the laser frequency and c the speed of light. The plasma wave driven by the laser pulse will also move at $v_\phi \approx c$, with v_ϕ the phase velocity of the plasma wave, because the laser pulse travels near speed of light through the plasma [39, 5].

Let's consider a one-dimensional (1D) perturbation following the z-axis, such that all plasma electrons at equilibrium situated at $z = z_0$ are displaced by a distance $\xi(z_0, t)$ at instant t, the ions remain at rest and the electron thermal motion is neglected relative to motion induced by the perturbation. This displacement causes a rarefaction of electrons on the right hand side of $z = z_0 + \xi(z_0, t)$ at instant t, resulting in a charge separation. The charge separation induces an electric field E_z at $z_0+\xi$ that can be calculated using the Gauss theorem, giving

$$E_z S = \frac{n_0 e S \xi(z_0, t)}{\epsilon_0}, \tag{1.1}$$

where S is the area parallel to the transverse plane (x, y), n_0 is the ambient electron number density or plasma density, e is the elementary charge and ϵ_0 is the permittivity constant in vacuum. In the non-relativistic case, Newton's law states that $m_e \partial^2\xi/\partial t^2 = -eE_z$, where m_e is the electron mass. Upon substituting E_z of Eq. 1.1 into Newton's equation, we obtain a harmonic oscillator equation describing the Lagrangian displacement $\xi(z_0, t)$:

$$\frac{\partial^2 \xi}{\partial t^2} + \frac{n_0 e^2}{\epsilon_0 m_e}\xi = 0. \tag{1.2}$$

with a characteristic frequency of $\omega_p = \sqrt{n_0 e^2/\epsilon_0 m_e}$, more commonly known as Langmuir or electron plasma frequency.

[1]The laser group velocity is obtained by applying the definition $\mathrm{d}\omega_0/\mathrm{d}k_0$ on the dispersion relation $\omega_0^2 = k_0^2 c^2 + \omega_p^2$.

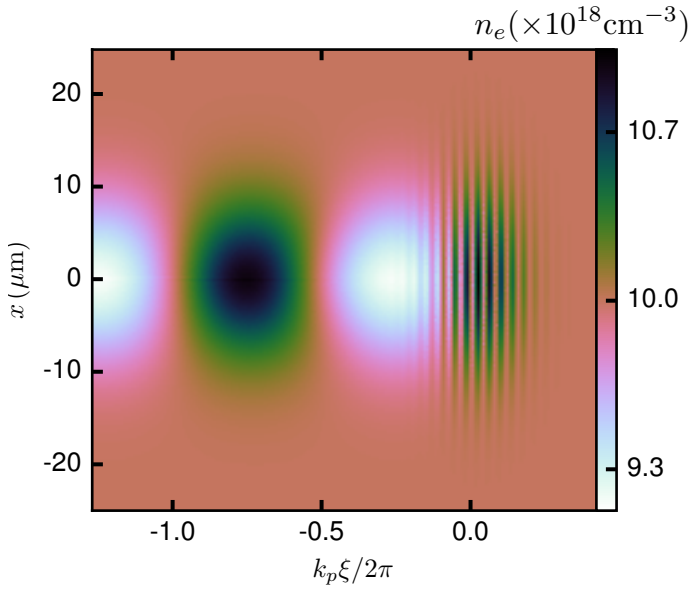

Figure 1.2: The interaction between an intense laser pulse (traveling from left to right) and a plasma creates an electronic density perturbation. The electronic density is represented in the plane $(x, k_p\xi/2\pi)$, a low electron density region in the plasma is created at the rear of the laser pulse (in bright tone), followed by a high electron density region (in darker tone), forming a periodic structure.

The plasma wave depends weakly on the shape of the pulse. The amplitude of the plasma wave is maximized for laser pulse length $c\tau_L \sim \lambda_p$, where τ_L is the laser pulse duration [40, 41, 5]. We refer $c\tau_L \sim \lambda_p$ as the resonant condition.

Fig. 1.3 shows the longitudinal and the radial electric fields E_z and E_r of the plasma wave represented in the plane $(k_p\xi/2\pi, x)$, with $\xi = z - ct$, in the frame following the laser pulse. This figure is useful to describe the force exerted on relativistic electrons. The transverse component of the force is $\boldsymbol{F}_\perp = -e(E_r - v_z B_\theta)\boldsymbol{e_r} = -eE_r\boldsymbol{e_r}$, this force is focusing in the first half-wavelength of the wakefield $(0 < k_p\xi < \pi)$ and defocusing in the second half-wavelength $(\pi < k_p\xi < 2\pi)$. By Panofsky-Wenzel theorem, the longitudinal component is expressed by $F_z = -eE_z$, so it is decelerating in the first quarter-wavelength $(0 < k_p\xi < \pi/2)$ and accelerating in the second quarter-wavelength $(\pi/2 < k_p\xi < \pi)$. Hence relativistic electrons placed in the second quarter-wavelength (indicated by the delimited zone) are both accelerated longitudinally and focused transversely. This allows confinement and acceleration of the electrons over long distances.

1.2 Ponderomotive force

As noted qualitatively in Sec. 1.1, the ponderomotive force results from the laser energy gradient. The laser field can be defined by the following wave vector:

$$\boldsymbol{A}(\boldsymbol{x}, t) = a_0 f(t - \frac{z}{v_g}) g(\boldsymbol{x}_\perp) cos\varphi, \tag{1.3}$$

where $\varphi = \omega_0 t - k_0 z$ is the phase of the wave, with ω_0 the laser frequency and k_0 the laser wavenumber; $g(\boldsymbol{x}_\perp)$ is a function with radial dependence; a_0 is the maximum amplitude of

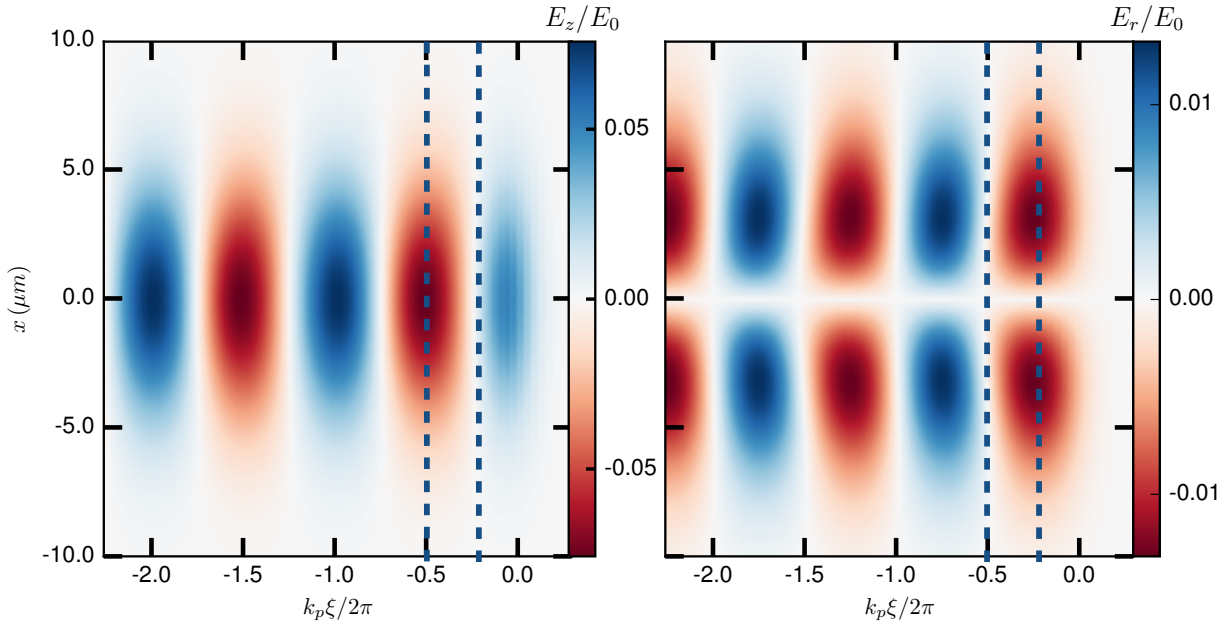

Figure 1.3: Longitudinal electric field E_z and radial electric field E_r colormaps represented in the plane $(k_p\xi/2\pi, x)$. The laser pulse propagates from left to right (not shown here), thus the first period of the generated wakefield is situated on the right of each plot. The dotted lines delimit the second quarter-wavelength which is both the focusing and accelerating phase.

the normalized vector potential. In terms of the peak intensity I_0, it is given by

$$a_0 = 0.85 \times 10^{-9} \lambda_0[\mu\text{m}] I_0^{\frac{1}{2}}[\text{W cm}^{-2}], \tag{1.4}$$

assuming linear polarization [4], where λ_0 is the laser wavelength in vacuum.

Since the laser field is transverse, the vector potential $\boldsymbol{A}$ is perpendicular to the direction of propagation z. $f(t)$ is a function considered to be slowly varying relative to the laser cycle, such that $df/dt < \omega_0 f$.

The starting point of this demonstration is the electron fluid momentum equation in the cold fluid limit, governed by the Lorentz equation

$$\frac{d\boldsymbol{p}}{dt} = -e\left(\boldsymbol{E} + \boldsymbol{v} \times \boldsymbol{B}\right), \tag{1.5}$$

where $\boldsymbol{E}$ are the electric field, $\boldsymbol{B}$ the magnetic field, $\boldsymbol{p} = \gamma m_e \boldsymbol{v}$, with $\boldsymbol{v}$ the velocity and $\gamma^2 = (1 + (\boldsymbol{p}/m_e c)^2)$, with $\boldsymbol{p}$ the momentum.

We use relations $\boldsymbol{E} = -\partial \boldsymbol{A}/\partial t$, $\boldsymbol{B} = \nabla \times \boldsymbol{A}$ from vectorial analysis. Introducing the normalization $\boldsymbol{a} = e\boldsymbol{A}/m_e c$. Eq. 1.5 becomes

$$\frac{\partial \boldsymbol{p}}{\partial t} + \frac{1}{\gamma m_e}\left(\boldsymbol{p} \cdot \nabla\right)\boldsymbol{p} = m_e c \frac{\partial \boldsymbol{a}}{\partial t} - \frac{c}{\gamma}\boldsymbol{p} \times \nabla \times \boldsymbol{a}, \tag{1.6}$$

Electrons interact with the radiation electric field in two separate ways. First, they quiver in response to the high frequency laser field. Second, they respond to the low frequency ponderomotive potential of the laser field, creating a nonlinear wake following the laser pulse. In this regard, we can separate the time scales of the electron motion into $\boldsymbol{p} = \boldsymbol{p^f} + \boldsymbol{p^s}$, with $\boldsymbol{p^f}$ the fast component, which scales as $1/\omega_0$ and is considered as first order, and $\boldsymbol{p^s}$ the slow component which scales as $1/\omega_p$ and is considered as second order. Note that $\omega_p \ll \omega_0$.

To the lowest order, the fast (transverse) component of the electron momentum follows the vector potential : $\boldsymbol{p^f} = m_e c\boldsymbol{a}$, which is the quiver momentum, as integrated from $\partial \boldsymbol{p^f}/\partial t = -e\boldsymbol{E}$. On the other hand, the slow or the second order component reads

$$\frac{\partial \boldsymbol{p^s}}{\partial t} + \frac{m_e c^2}{\gamma}\left(\boldsymbol{a}\cdot\nabla\right)\boldsymbol{a} = -\frac{m_e c^2}{\gamma}\boldsymbol{a}\times\nabla\times\boldsymbol{a}. \tag{1.7}$$

Using the identity $\boldsymbol{a}\times\nabla\times\boldsymbol{a} = \nabla|\boldsymbol{a}|^2/2 - \left(\boldsymbol{a}\cdot\nabla\right)\boldsymbol{a}$, we obtain

$$\boldsymbol{F_p} = \frac{\partial \boldsymbol{p^s}}{\partial t} = -\frac{m_e c^2}{2\gamma}\nabla|\boldsymbol{a}|^2, \tag{1.8}$$

where $\boldsymbol{F_p}$ is the ponderomotive force. This negative expression implies that the ponderomotive force tends to push electrons away from regions of locally higher intensity. As the electrons are being expelled by the center of the focused laser beam, they pick up a velocity equivalent to the quiver velocity in the process, $\boldsymbol{v^f} = \boldsymbol{p^f}/\gamma m_e$.

There are more rigorous derivations of the ponderomotive force with more sophisticated analyses in the literature, such as using covariant [42] or Lagrangian [43] formulations and they lead to the same expression.

1.3 Wakefield generation

From the previous section, we have seen that the ponderomotive force is derived from the envelop of the laser pulse, which is slowly varying in time. The nonlinear ponderomotive force is responsible for the generation of wakefield in plasmas. Over the years, several theories on the modeling of the wakefield have been established and these models are valid in certain regimes. Depending on the strength of the nonlinear ponderomotive force characterized by the normalized vector potential a^2, two regimes are identified [4]: the quasi-linear regime ($a^2 \ll 1$) and the nonlinear regime ($a^2 \geq 1$).

The quasi-linear regime can be described analytically in three dimensions using plasma fluid theory [44, 41, 40], which is valid provided that the perturbed density $\delta_n = (n_e - n_0) < n_0$, where n_e is the electronic density. Within the nonlinear regime, for a broad pulse ($k_p r_L \gg 1$), where r_L is the laser spot radius, the plasma fluid model given in [44, 41, 40] can be generalized and adapted to model the wakefield analytically in the 1D limit. However, for a radially bounded pulse in three dimensions ($k_p r_L \leq 1$), the wakefield must typically be modeled numerically, e.g. using particle-in-cell (PIC) code. This high intensity 3D regime has been referred to as the cavitation regime because it generates cavities where electrons are almost completely or completely evacuated. In the case where electrons are completely evacuated, it is referred to as the blowout or bubble regime. In addition to the wakefield generation, a fraction of plasma electrons can be self-trapped in the cavity and can be accelerated to high energies [17, 16, 18].

In this section, we will first establish the expressions that govern the propagation of waves in a cold plasma. Then, we will describe the generalized plasma fluid theory that is valid to model the quasi-linear regime and also the nonlinear regime in the 1D limit.

1.3.1 Nonlinear plasma waves and wave breaking limit in a cold plasma

The theory of wave motion of an electron plasma was pioneered by Akhiezer and Polovin [45] in 1956. They have investigated the oscillatory behavior of the plasma quite generally,

for arbitrary velocities. This section provides expressions of the accelerating field based on their work.

The starting equations are the Lorentz equation of motion for the electrons in a cold, unmagnetized plasma, plus the Maxwell's equations. The ions are treated as a homogeneous neutralizing background: $Zn_i = n_0$, with Z the atomic number and n_i the ion density. The plasma has a density that is lower than the critical density, defined as $n_c = \epsilon_0 m_e \omega_0^2 / e^2$ and written in an engineering formula: $n_c[\mathrm{cm}^{-3}] = 1.1 \times 10^{21} / \lambda_0[\mu m]^2$. In an underdense plasma ($n_0 \ll n_c$), the thermal motion is often neglected because the temperature remains small (few eV) compared to the typical oscillation energy (multi-keV) which the electrons acquire from the oscillation in the laser field.

$$\frac{\partial \boldsymbol{p}}{\partial t} + (\boldsymbol{v} \cdot \nabla)\, \boldsymbol{p} = -e\,(\boldsymbol{E} + \boldsymbol{v} \times \boldsymbol{B})\,, \tag{1.9}$$

$$\nabla \cdot \boldsymbol{E} = \frac{e\,(n_0 - n_e)}{\epsilon_0}, \tag{1.10}$$

$$\nabla \times \boldsymbol{E} = -\frac{\partial \boldsymbol{B}}{\partial t}, \tag{1.11}$$

$$\nabla \times \boldsymbol{B} = -\mu_0 e n_e \boldsymbol{v} + \frac{1}{c^2}\frac{\partial \boldsymbol{E}}{\partial t}, \tag{1.12}$$

$$\nabla \cdot \boldsymbol{B} = 0, \tag{1.13}$$

where we have directly inserted the expressions $\rho = e(n_0 - n_e)$ and $\boldsymbol{J} = -e n_e \boldsymbol{v}$.

The objective is to solve the wave equation, giving solutions of the form $f(\omega t - \boldsymbol{k} \cdot \boldsymbol{x})$ or $f(\tau)$, where $\tau = t - \hat{\boldsymbol{k}} \cdot \boldsymbol{x} / v_\phi$, and v_ϕ is the phase velocity of the plasma. Temporal and spatial derivatives can then be written as $\partial/\partial\tau = \partial/\partial t$, $\nabla\cdot = -\hat{\boldsymbol{k}}\partial/\partial v_\phi \tau \cdot$, $\nabla\times = -\hat{\boldsymbol{k}}\partial/\partial v_\phi \tau \times$, where $\hat{\boldsymbol{k}} = \boldsymbol{k}/k$ is the unit vector in the direction of propagation. With this new set of coordinates, the set of equations Eqs. 1.9-1.13 write

$$\frac{d\boldsymbol{p}}{d\tau}\left(1 - \frac{\hat{\boldsymbol{k}} \cdot \boldsymbol{v}}{v_\phi}\right) = -e\,(\boldsymbol{E} + \boldsymbol{v} \times \boldsymbol{B})\,, \tag{1.14}$$

$$-\hat{\boldsymbol{k}} \cdot \frac{d\boldsymbol{E}}{d\tau} = \frac{e v_\phi\,(n_0 - n_e)}{\epsilon_0}, \tag{1.15}$$

$$\boldsymbol{B} = \frac{1}{v_\phi}\hat{\boldsymbol{k}} \times \boldsymbol{E} + \boldsymbol{B}_0, \tag{1.16}$$

$$-\hat{\boldsymbol{k}} \times \frac{d\boldsymbol{B}}{d\tau} = -\mu_0 e v_\phi n_e \boldsymbol{v} + \frac{v_\phi}{c^2}\frac{d\boldsymbol{E}}{d\tau}, \tag{1.17}$$

$$\hat{\boldsymbol{k}} \cdot \frac{d\boldsymbol{B}}{d\tau} = 0. \tag{1.18}$$

Note that the partial derivatives are now replaced by total derivatives in the variable τ. The term $\boldsymbol{B}_0$ represents an external magnetic field, which is not considered in our case, therefore $\boldsymbol{B}_0 = 0$. From Eq. 1.16 and Eq. 1.18, it is shown that $\hat{\boldsymbol{k}} \cdot \boldsymbol{B} = \boldsymbol{E} \cdot \boldsymbol{B} = 0$ indicating that the $\boldsymbol{B}-$field is perpendicular to the wave vector and $\boldsymbol{E}-$field. For simplicity, we specify the wave vector $\boldsymbol{k}$ to be in the z-direction. Thus, we have $\hat{\boldsymbol{k}} = \boldsymbol{z}/z$, $\hat{\boldsymbol{k}} \cdot \boldsymbol{V} = V_z$ and $\hat{\boldsymbol{k}} \times \boldsymbol{V} = (-V_y, V_x, 0)$ where $\boldsymbol{V}$ represents any vector.

Taking the dot product of Eq. 1.17 with the direction vector $\hat{\boldsymbol{k}}$, we may eliminate $\boldsymbol{E}$ using Eq. 1.15. Defining $\boldsymbol{\beta} = \boldsymbol{v}/c$ we obtain an equation for the density:

$$n_e = \frac{\beta_p n_0}{\beta_p - \beta_z}, \tag{1.19}$$

where $\beta_p = v_\phi/c$. From this expression, we deduce the salient feature of a nonlinear plasma wave: in regions where the fluid velocity approaches the phase velocity, the electron density n_e becomes very large.

We obtain the transverse $\boldsymbol{B}-$field by taking the cross-product of the direction vector with Eq. 1.14, then using Eq. 1.11, therefore we arrive at an explicit equation for $\boldsymbol{B}$, namely:

$$\boldsymbol{B} = -\frac{1}{ev_\phi}\hat{\boldsymbol{k}} \times \frac{d\boldsymbol{p}}{d\tau}. \tag{1.20}$$

In a similar fashion, taking the cross product of the direction vector with Eq. 1.17 and making use of Eq. 1.16, we obtain an expression for $d\boldsymbol{B}/d\tau$ which reads

$$\frac{d\boldsymbol{B}}{d\tau} = \frac{\mu_0 e n_e v_\phi}{\beta_p^2 - 1}\hat{\boldsymbol{k}} \times \boldsymbol{v}. \tag{1.21}$$

$\boldsymbol{B}$ can now be eliminated by subtracting Eq. 1.21 from Eq. 1.20, leaving a transverse wave equation

$$\hat{\boldsymbol{k}} \times \frac{d^2\boldsymbol{p}}{d\tau^2} + \frac{\mu_0 e^2 n_e v_\phi^2}{\beta_p^2 - 1}\hat{\boldsymbol{k}} \times \boldsymbol{v} = 0. \tag{1.22}$$

Taking the transverse x and y components of Eq. 1.22 and making use of Eq. 1.19, together with the equations of plasma frequency, $\omega_p^2 = n_0 e^2/m_e\epsilon_0$, we obtain the coupled transverse wave equations:

$$\frac{d^2 p_x}{d\tau^2} + \frac{\omega_p^2\beta_p^2}{\beta_p^2 - 1}\frac{\beta_p\beta_x}{\beta_p - \beta_z} = 0, \tag{1.23}$$

$$\frac{d^2 p_y}{d\tau^2} + \frac{\omega_p^2\beta_p^2}{\beta_p^2 - 1}\frac{\beta_p\beta_y}{\beta_p - \beta_z} = 0. \tag{1.24}$$

Here $\boldsymbol{p}$ is normalized to $m_e c$.

The longitudinal component of the fluid motion can be derived by differentiating $\hat{\boldsymbol{k}}\cdot$(1.14), then $\boldsymbol{B}$ can be eliminated using Eq. 1.20. Similarly n_e can be eliminated using Eq. 1.19, this gives

$$\frac{d}{d\tau}\left[\left(\frac{\hat{\boldsymbol{k}}\cdot\boldsymbol{v}}{v_\phi} - 1\right)\hat{\boldsymbol{k}}\cdot\frac{d\boldsymbol{p}}{d\tau}\right] = \frac{e^2 v_\phi n_0}{\epsilon_0}\frac{\hat{\boldsymbol{k}}\cdot\boldsymbol{v}}{v_\phi - \hat{\boldsymbol{k}}\cdot\boldsymbol{v}} - \frac{1}{v_\phi}\frac{d}{d\tau}\left[\boldsymbol{v}\cdot\frac{d\boldsymbol{p}}{d\tau} - \left(\hat{\boldsymbol{k}}\cdot\boldsymbol{v}\right)\left(\hat{\boldsymbol{k}}\cdot\frac{d\boldsymbol{p}}{d\tau}\right)\right]. \tag{1.25}$$

In order to make this equation more tractable, we rewrite this equation considering z as the longitudinal component, thus giving

$$\frac{d}{d\tau}\left[\left(\beta_z - \beta_p\right)\frac{dp_z}{d\tau} + \beta_x\frac{dp_x}{d\tau} + \beta_y\frac{dp_y}{d\tau}\right] = \frac{\omega_p^2\beta_p^2\beta_z}{\beta_p - \beta_z}. \tag{1.26}$$

Eqs. 1.23, 1.24 and 1.26 are in agreement with the equation in [45]. They represent a closed set of equations for nonlinear plasma of arbitrary amplitude and fixed phase velocity, v_ϕ. Once $\boldsymbol{p}$ is solved, $\boldsymbol{E}$ and $\boldsymbol{B}$ (normalized to $m_e\omega_p c/e$ and $m_e\omega_p/e$ respectively) can be obtained.

- ***Transverse B-fields.*** We use Eq. 1.20 for the transverse $\boldsymbol{B}$-fields, thus giving

$$B_x = \frac{1}{\beta_p}\frac{dp_y}{d\omega_p\tau}, \tag{1.27}$$

$$B_y = -\frac{1}{\beta_p}\frac{dp_x}{d\omega_p\tau}. \tag{1.28}$$

- ***Transverse E-fields.*** With Faraday's law, we derive the transverse $\boldsymbol{E}$-fields, they write

$$E_x = \beta_p B_y = -\frac{dp_x}{d\omega_p\tau}, \tag{1.29}$$

$$E_y = -\beta_p B_x = -\frac{dp_y}{d\omega_p\tau}. \tag{1.30}$$

- ***Longitudinal B-field.*** With Gauss law, the longitudinal $\boldsymbol{B}$-field, B_z is obtained straightforwardly

$$B_z = 0. \tag{1.31}$$

- ***Longitudinal E-field.*** To derive the longitudinal $\boldsymbol{E}$-field, E_z, we take $\hat{\boldsymbol{k}}\cdot$(1.14), using the energy equation $d\gamma/dt = -\boldsymbol{v}\cdot\boldsymbol{E}$ to eliminate E_x and E_y from the resulting equation for $dp_z/d\tau$

$$E_z = -\frac{1}{\beta_p}\frac{d}{d(\omega_p\tau)}\left(\beta_p p_z - \left(1+p^2\right)^{\frac{1}{2}}\right). \tag{1.32}$$

A rather simple equation for the potential can be found by setting $E_z = \beta_p^{-1} d\phi/d\omega_p\tau$ in Eq. 1.32. We can proceed by integration, assuming that $\phi = p_z = 0$ and $\gamma = 1$ at $\tau = -\infty$ (the laser pulse has not encountered the plasma), thus ϕ is expressed as

$$\phi = \gamma - \beta_p p_z - 1. \tag{1.33}$$

The full set of fluid equations can in general not be solved analytically. Various limiting cases can be found in the original work of [45]. A thorough account of the types of solutions can be found in the review of Decoster (1978) [46]. Having the novel particle acceleration concepts in mind, Noble [47] has analyzed these cold plasma equations. In his work, the analysis that is of particular relevance to short pulse propagation is the study on pure longitudinal plasma oscillations. By setting $p_x = p_y = 0$, Eq. 1.26 simplifies to

$$\frac{d}{d\tau}\left[\left(\beta_z - \beta_p\right)\frac{dp_z}{d\tau}\right] = \frac{\omega_p^2\beta_p^2\beta_z}{\beta_p - \beta_z}. \tag{1.34}$$

Using the relation $p_z = \gamma\beta_z = \beta_z/\sqrt{1-\beta_z^2}$, the LHS of the above equation can be written as

$$\frac{d^2}{d\tau^2}\left[\gamma\left(1-\beta_p\beta_z\right)\right] = \frac{\omega_p^2\beta_p^2\beta_z}{\beta_p - \beta_z}. \tag{1.35}$$

Eq. 1.35 can be integrated once to give

$$\frac{1}{2}\left[\frac{d}{d\tau}\left[\gamma\left(1-\beta_p\beta_z\right)\right]\right]^2 = \beta_p^2\omega_p^2\left(\gamma_m - \gamma\right), \tag{1.36}$$

where $\gamma_m = (1-\beta_m^2)^{-1/2}$ and $\beta_m = (v_z/c)_{max}$: the maximum oscillation velocity of the wave. The waveform can thus be determined from the solution of :

$$\frac{d}{d\tau}\left[\gamma\left(1-\beta_p\beta_z\right)\right] = \pm\sqrt{2}\beta_p\omega_p\left(\gamma_m-\gamma\right)^{\frac{1}{2}}. \tag{1.37}$$

Once β_z is found, the density and E_z can be determined using Eq. 1.19 and Eq. 1.32 respectively, leading to

$$n_e(\tau) = \frac{\beta_p n_0}{\beta_p - \beta_z(\tau)}, \tag{1.38}$$

$$E_z(\tau) = \pm\sqrt{2}\left(\gamma_m-\gamma\right)^{\frac{1}{2}} \tag{1.39}$$

In finding the maximum electric field, Eq. 1.39 tells us that the fluid velocity γ_m cannot exceed the phase velocity $\gamma_\phi(\tau)$; otherwise, according to Dawson's one dimensional plasma model [48], the electron charge sheets may cross each other, and there will be fine-scale mixing of the various parts of the oscillation, leading to its destruction. In other words, the wave *breaks*. We can therefore define the relativistic wave breaking limit by taking $\beta_m = \beta_p$, or equivalently $\gamma_m = \gamma_\phi$. An extremum of the electric field occurs for $\gamma = 1$, corresponding to the point in the oscillation where the electrons are momentarily stationary, therefore Eq. 1.39 becomes

$$E_{max} = \frac{m_e c\omega_p}{e}\sqrt{2}\left(\gamma_p-1\right)^{1/2}. \tag{1.40}$$

The non relativistic phase velocities can be obtained straightforwardly considering $\gamma_p - 1 \approx \beta_p^2/2$, thus

$$E_{max} = E_0 = \frac{m_e\omega_p v_\phi}{e}, \tag{1.41}$$

which is also known as the 'cold wave-breaking limit', a term coined by Dawson and Oberman [49]. In their derivation, they used a more physically motivated Lagrangian sheet model. In this picture, wavebreaking can be thought of as the crossing of neighboring charge sheets, accompanied by a density singularity.

1.3.2 Plasma waves driven by a laser pulse

In the previous section, we have only described the behavior of nonlinear waves in a cold plasma. In this section, we include a laser pulse as the driver of plasma waves. The following theory is valid for both the linear regime and the nonlinear regime in the 1D limit.

The laser propagation is described by the transverse wave equations as given by Eqs. 1.23-1.24, which are coupled with the longitudinal wave equation Eq. 1.26 through nonlinear terms.

Relativistic effects become important for electron quiver momenta $p_y/m_e c \sim 1$. For intensities beyond $10^{18}\,\mathrm{W/cm^2}$ or $p_y/m_e c \gg 1$, a fully nonlinear model, valid for arbitrary plasma densities is needed. Several studies focused on this aspect, among the pioneers, Sprangle et al. [50] formulated a fully nonlinear ODE for the wake potential in the limit $v_g = c$. Similar 1D formulations are presented in [51, 52, 53]. The generalization to arbitrary transformation velocity, i.e. v_g or v_ϕ instead of c, was the focus of the work presented in [54, 55, 56, 57]. The main properties of the strong relativistic regime will be outlined in the following. The solution of equations describing this regime is generally found with the help of numerical simulation.

The starting equations are the Lorentz equation Eq. 1.9 and the Maxwell's equations Eqs. 1.10-1.13.

To get a better understanding of the physical effects, the 1D case is described here. The geometry is chosen so that the laser wave propagates along the z-axis: $E_L = (0, E_y, 0)$, $B_L = (B_x, 0, 0)$. We can solve for the transverse momentum p_y by expressing these in terms of the vector potential A_y.

It is often convenient to introduce the scalar and vector potentials in solving Maxwell equations, expressing the $\boldsymbol{E}-$ and $\boldsymbol{B}-$fields using the relationships $\boldsymbol{E} = -\partial \boldsymbol{A}/\partial t - \boldsymbol{\nabla} \cdot \phi$ and $\boldsymbol{B} = \boldsymbol{\nabla} \times \boldsymbol{A}$, and adapting them to our geometry, gives the following equations

$$E_y = -\frac{\partial A_y}{\partial t}, \tag{1.42}$$

$$B_x = -\frac{\partial A_y}{\partial z}. \tag{1.43}$$

Substituting the above equations Eqs. 1.42-1.43 in Eq. 1.9 gives

$$\frac{dp_y}{dt} = e\frac{dA_y}{dt}. \tag{1.44}$$

If there is no initial drift in the y-direction, then $p_y = eA_y$.

Likewise the longitudinal component of Eq. 1.9 gives us:

$$\frac{dp_z}{dt} = -e\left(-\frac{\partial \phi}{\partial z} + v_y \frac{\partial A_y}{\partial z}\right) \tag{1.45}$$

Using the identity of Eq. 1.44 and normalizing p_x to $m_e c$, ϕ to $m_e c^2/e$ and A_y to $m_e c/e$, we obtain

$$\frac{d\gamma\beta_z}{dt} = c\frac{\partial \phi}{\partial z} - \frac{c}{2\gamma}\frac{\partial a^2}{\partial z}, \tag{1.46}$$

where $\beta_z = v_z/c$.

The relativistic factor $\gamma = (1 - \boldsymbol{\beta}^2)^{-1/2}$ can be separated into longitudinal and transverse components, thus:

$$\gamma = \gamma_\perp \gamma_\parallel = \sqrt{\frac{1 + a^2}{1 - \beta_z^2}}. \tag{1.47}$$

As in most problems involving fluids, we can write down a continuity equation for the mass or in this case, the charge density

$$\frac{\partial n_e}{\partial t} + \boldsymbol{\nabla} \cdot (n_e \boldsymbol{v}) = 0,$$

rendering it to 1D, the equation writes

$$\frac{\partial n_e}{\partial t} + c\frac{\partial}{\partial z}(n_e \beta_z) = 0. \tag{1.48}$$

In the same manner, we introduce the potentials into Ampere's law, Eq. 1.12 and then make use of the Coulomb gauge $\boldsymbol{\nabla} \cdot \boldsymbol{A} = 0$ to obtain an equation for the electromagnetic modes. After some algebra, we obtain

$$\frac{1}{c^2}\frac{\partial^2 \boldsymbol{A}}{\partial t^2} - \boldsymbol{\nabla^2 A} = -\mu_0 e n_e \boldsymbol{v} - \frac{1}{c^2}\frac{\partial}{\partial t}\boldsymbol{\nabla} \cdot \phi \tag{1.49}$$

In general, the scalar potential $\boldsymbol{\nabla} \cdot \partial\phi/\partial c^2 t$ is negligible with respect to the transverse current, $\mu_0 e n_e \boldsymbol{v}$. In 1D, it vanishes exactly. Therefore Eq 1.49 written in 1D is

$$\frac{1}{c^2}\frac{\partial^2 A_y}{\partial t^2} - \nabla^2 A_y = -\mu_0 e n_e v_y. \tag{1.50}$$

The choice of the Coulomb gauge implies that $A_x = 0$, which we implicitly assume while deriving Eq. 1.46. Normalizing as before, with $v_y = eA_y/m_e\gamma = ac/\gamma$ and $n = n_e/n_0$, Eq.1.49 can be re-written as:

$$\frac{\partial^2 a}{\partial t^2} - c^2\nabla^2 a = -\omega_p^2 \frac{na}{\gamma}. \tag{1.51}$$

Eqs. 1.46-1.51 together with the Poisson's equation written in normalized units

$$\frac{\partial^2 \phi}{\partial z^2} = k_p^2 \left(n - 1\right), \tag{1.52}$$

constitute a closed set for the coupled electromagnetic and plasma waves.

To further our analysis, we use the quasistatic (QSA) [50] approximation with the following transformations: $\tau = t$; $\xi = z - v_g t$. Our partial derivatives then become : $\partial/\partial z = \partial/\partial\xi$, $\partial/\partial t = \partial/\partial\tau - v_g\partial/\partial\xi$.

The QSA assumes that the characteristic time for the laser pulse to evolve is sufficiently short ($\partial/\partial\tau = 0$) compared with the electron transit time through the laser pulse. The laser wavelength (frequency) is much smaller (greater) than all other characteristic lengths (times) in the system, i.e. $\omega_p \ll \omega_0$ and $w(z) \gg c/\omega_0$ where $w(z)$ is the laser spot radius with respect to the position z. The laser spot radius evolves according to $w(z) = w_0(1+z^2/Z_R^2)^{1/2}$, where w_0 is the minimum spot radius in the focal plane located at $z = 0$, also known as the laser waist and $Z_R = k_0 w_0^2/2$ is the Rayleigh length. The evolution timescale τ of the pulse envelope is typically the Rayleigh diffraction time, t_R:

$$t_R = \frac{2Z_R}{c} = \frac{k_0 w_0^2}{c} \gg \tau_L, \tag{1.53}$$

where τ_L is the laser pulse duration. This inequality allows us to neglect $\partial/\partial\tau$ relative to $\partial/\partial\xi \sim ik_0$, given that the vector potential has the form $a = a(\xi, r, \tau)\exp\left(ik_0\xi\right)$ in the co-moving frame. The quasistatic approximation is only valid for plasma electrons with sufficiently low energy. It fails for electrons which have been accelerated to high energy and traveling with the laser pulse.

Applying the new transformation coordinates, Eq. 1.46 becomes

$$\begin{aligned}\frac{d}{dt}\left(\gamma u\right) &= \left(\frac{\partial}{\partial\tau} - v_g\frac{\partial}{\partial\xi} + cu\frac{\partial}{\partial\xi}\right)\gamma\beta_z, \\ &= c\frac{\partial\phi}{\partial\xi} - \frac{c}{2\gamma}\frac{\partial a^2}{\partial\xi}.\end{aligned} \tag{1.54}$$

Using the identity in Eq. 1.47 to substitute $\partial a^2/\partial\xi$ and letting $\beta_g = v_g/c$, Eq. 1.54 writes

$$\frac{1}{c}\frac{\partial}{\partial\tau}\left(\gamma u\right) = \frac{\partial}{\partial\xi}\left[\phi - \gamma\left(1 - \beta_g\beta_z\right)\right]. \tag{1.55}$$

Likewise, the continuity equation in these new coordinates becomes

$$\frac{1}{c}\frac{\partial n}{\partial\tau} = \frac{\partial}{\partial\xi}\left[n\left(\beta_g - \beta_z\right)\right]. \tag{1.56}$$

We proceed by applying this QSA to fluid equations; this consists of setting $\partial/\partial\tau = 0$ in Eq. 1.56 and in Eq. 1.55 and integrating to yield the following conservation relations

$$n = \frac{\beta_g}{\beta_g - \beta_z}, \tag{1.57}$$

requiring that $n(\xi = +\infty) = 1$, and

$$\phi - \gamma\left(1 - \beta_g\beta_z\right) + 1 = 0, \tag{1.58}$$

considering that $\phi = \beta_z = 0$ in the absence of a plasma wave (when $\beta_z = 0$ at $\xi \to \infty$).

With these manipulations, we observe that the set of PDE for the fluid variables β_z, n and ϕ have been reduced to one ODE for ϕ. The algebraic expressions Eq. 1.47, Eq. 1.57 and Eq. 1.58 are useful to relate β_z, n, ϕ and the normalized vector potential a. As in the QSA, the laser is considered as being fixed on the fluid timescale τ, all the wakefield quantities can be determined independently of the laser evolution. We can therefore express the fluid quantities entirely in terms of the normalized vector potential a.

From Eq. 1.58, we can solve for β_z in terms of a and ϕ, giving

$$\beta_z = \frac{\beta_g - \psi}{1 - \beta_g\psi}, \tag{1.59}$$

where

$$\psi = \left(1 - \frac{1 + a^2}{\gamma_g^2\left(1 + \phi\right)^2}\right)^{\frac{1}{2}}. \tag{1.60}$$

Using Eq. 1.59 to eliminate β_z from Eq. 1.57, we find the density:

$$n = \gamma_g^2\beta_g\left(\frac{1}{\psi} - \beta_g\right). \tag{1.61}$$

Then we substitute Eq. 1.61 into Poisson's equation Eq 1.52 in the co-moving coordinates, we obtain the nonlinear ODE for the wake potential in the QSA:

$$\frac{\partial^2\phi}{\partial\xi^2} = k_p^2\gamma_g^2\left\{\beta_g\left(1 - \frac{1 + a^2}{\gamma_g^2\left(1 + \phi\right)^2}\right)^{-\frac{1}{2}} - 1\right\}. \tag{1.62}$$

This expression can be integrated numerically for a given pulse amplitude $a(\xi)$ at a given time τ. Once solved for $\phi(\xi)$, we can immediately obtain β_z and n from Eq. 1.59 and Eq. 1.61.

Here we notice that there are similarities between solutions derived using QSA and nonlinear plasma wave solutions of Akhiezer and Polovin [45] given in Section 1.3.1. Comparing Eq. 1.33 with Eq. 1.58, and Eq. 1.38 with Eq. 1.57, we realize that if we let $\beta_p \to \beta_g$ and $\tau = -\xi$, these two expressions are identical. This symmetry can be explained by the fact that the plane wave ansatz explicitly excludes spatial derivatives ($\partial/\partial\xi = 0$), resulting in all variables being a function of the retarded time variable $\tau = t - z/v_\phi$ only, while the QSA excludes times derivatives ($\partial/\partial\tau = 0$) in the wake following the pulse. These two pictures are equivalent, suggesting that the transverse laser pulse can be introduced into the longitudinal equation Eq. 1.35 as a slowly varying envelope $p_\perp = a(\tau)$ without violating the initial plane wave ansatz.

In some sense, these nonlinear features for wakefield generation by short pulse derived using QSA are already included in the original works by Akhiezer and Polovin [45], and in the subsequent analysis by Noble [47]. One advantage of the QSA version is that it is more readily accessible in terms of physics. Generalization to include a laser pulse in two and three dimensions are featured in [58, 59].

1.3.3 Regimes of plasma wave excitation

Regimes in LWFA are controlled by the laser pulse strength. Three regimes can be identified: the quasi-linear regime, the nonlinear regime and the blowout regime.

Quasi-linear regime

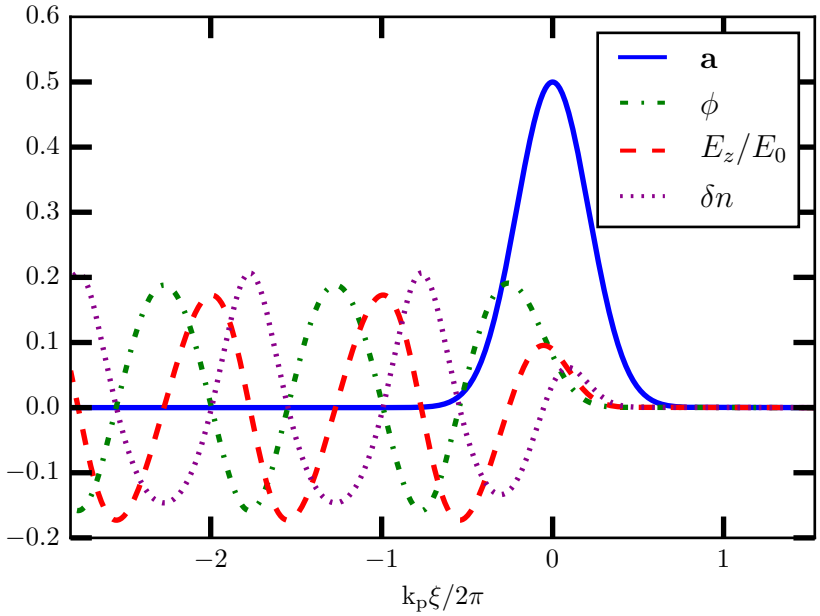

Figure 1.4: Normalized envelope of the laser vector potential ϕ, the associated wakefield, E_z/E_0 and perturbed density δn as a function of the normalized phase for $a_0 = 0.5$, $\tau_L = 16.99\,\mathrm{fs}$.

The numerical solution of Eq. 1.62 with these parameters give us an immediate insight to the nature of these generated plasma waves. Once solved for ϕ, E_z/E_0 and n can be deduced from $E_z = -\nabla\phi$ and from the Poisson's equation Eq. 1.52 respectively. In the linear regime ($a^2 \ll 1$), we consider a laser vector potential $a = a_0 \exp(-\xi^2/c^2\tau_L^2)$. The linear response of the plasma wave using the plasma fluid theory is illustrated for a maximum amplitude of the normalized vector potential $a_0 = 0.5$ and a laser pulse duration of $\tau_L = 16.99\,\mathrm{fs}$ in Fig. 1.4. This figure shows the classical linear Langmuir wave with normalized electric field, E_z/E_0 and the normalized perturbed density $\delta n = (n_e - n_0)/n_0$, which is 90° out of phase.

This regime provides regular plasma wave and symmetric regions of acceleration-deceleration and focusing-defocusing as shown in Fig. 1.3, and it ensures no self-injected electrons into the wakefields since the accelerating gradient does not attain the cold wave-breaking limit, $E_z \ll E_0$. Consider the Gaussian laser pulse with the aforementioned parameters: $a_0 = 0.5$, $\tau_L = 16.99\,\mathrm{fs}$, the required plasma density evaluated with the resonant condition $\omega_p\tau_L \sim 2$ gives $n_0 = 4.35 \times 10^{18}\,\mathrm{cm}^{-3}$. The amplitude of the accelerating field of the plasma wave is approximately $E_z/E_0 \approx 0.76(a_0^2/2\gamma_\perp)$ for a resonant Gaussian laser pulse [60], where $\gamma_\perp = (1 + a_0^2/2)$. In the considered configuration in Fig. 1.4, $E_z \approx 20$ GV/m $< E_0$.

The quasi-linear ($a_0^2 \sim 1$) regime offers attractive features for the design of an accelerator. Its main drawback is that the Gaussian laser pulse will diffract after a distance of propagation on the order of Rayleigh length, Z_R. Since the energy gain is evaluated with $\mathcal{E} = -eE_zL_{acc}$, where L_{acc} is the acceleration length, to ensure that electrons gain the maximum energy possible, the acceleration length should be the electron dephasing length, L_d defined as the

length for electrons in the accelerating phase of the wakefield to outrun it and slip into the decelerating phase (see Sec. 1.5 for more details). Generally, $Z_R < L_d$, therefore some sort of laser guiding e.g. plasma channel (parabolic transverse plasma density transition) is necessary.

Nonlinear regime

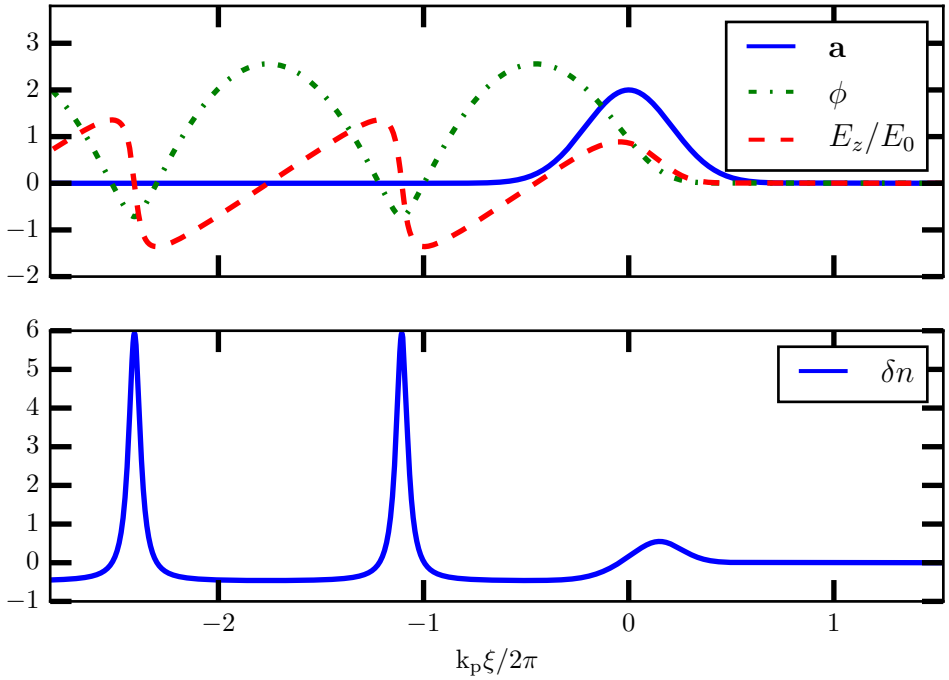

Figure 1.5: Upper panel: Wake potential, ϕ by solving the ODE in Eq. 1.62. The laser parameters are $a_0 = 2.0$, $\tau_L = 16.99$fs. E_z/E_0 shows a sawtooth behavior with a stronger pump. Bottom panel: The normalized perturbed density δn shows a cavitation of electrons in the region following the laser pulse and then a high electronic density peak.

The generated plasma waves evaluated in the nonlinear regime ($a^2 \geq 1$) using the 1D nonlinear plasma fluid theory are shown Fig. 1.5. Here we consider $a_0 = 2$. In Fig. 1.5, we observe a sawtooth electric field and spiked density perturbation, accompanied by a lengthening of the oscillation period by a factor $\leq \gamma_g$ compared to the unperturbed plasma period due to the enhanced inertia of electrons as their velocity becomes relativistic. With $E_z > E_0$, this suggests that electron self-trapping is susceptible to occur. However this is not a strict rule, the wakefield amplitude measured in several experiments [61] appears to be in the range $E_z/E_0 \approx 10 - 30\%$, well below the cold wave breaking-limit, suggesting that additional laser plasma instabilities such as the coupling of Raman backscatter (RBS) and Raman sidescatter (RSS) [62] may play a role in lowering the effective amplitude for electron self-trapping.

This regime is particularly interesting for both the design of an injector and an accelerator. In fact, it is the simplest scheme for an electron injector as self-injection is based on the crossing of electron charge sheets. In ionization-induced injection scheme, the required value of a_0 is determined by the intensity necessary to ionize heavier atoms added to the light background gas. For nitrogen atoms, an a_0 of ~ 2 is required for K-shell ionization, hence the interaction occurs in the nonlinear regime. Injection techniques will be developed further

in Sec. 1.4. Since this thesis is about the optimization of the electron beam properties in an electron injector using ionization injection scheme via PIC simulations, we will essentially be working in the nonlinear regime.

Blowout regime

So far, most analytical theories used in describing the nonlinear plasma waves and wakefield excitation have either been restricted to linear fluid theory [39] or the 1D nonlinear fluid theory [45, 10]. These one dimensional models give a good description of the plasma waves, however most LWFA experiments generating self-injected electrons [16, 63, 17] take place in the blowout regime. Neither fluid nor one-dimensional (axial) theory applies in this regime because in addition to wave steepening and period lengthening, the radial structure of the plasma wave can exhibit nonlinearities. One such effect is that the wave front of the plasma wave can be curved and the greater the distance behind the laser driver, the more severe the curvature becomes, resulting in a nonlinear plasma wavelength that is greater on axis than off axis. Moreover, the laser intensity can be sufficiently high so as to expel all plasma electrons away from the vicinity of the axis [64, 65, 66], leaving a cavity behind the laser pulse instead of a periodic plasma wave as observed in the linear regime. These plasma waves are complicated because their fields are electromagnetic, relativistic mass are important and trajectory crossing occurs.

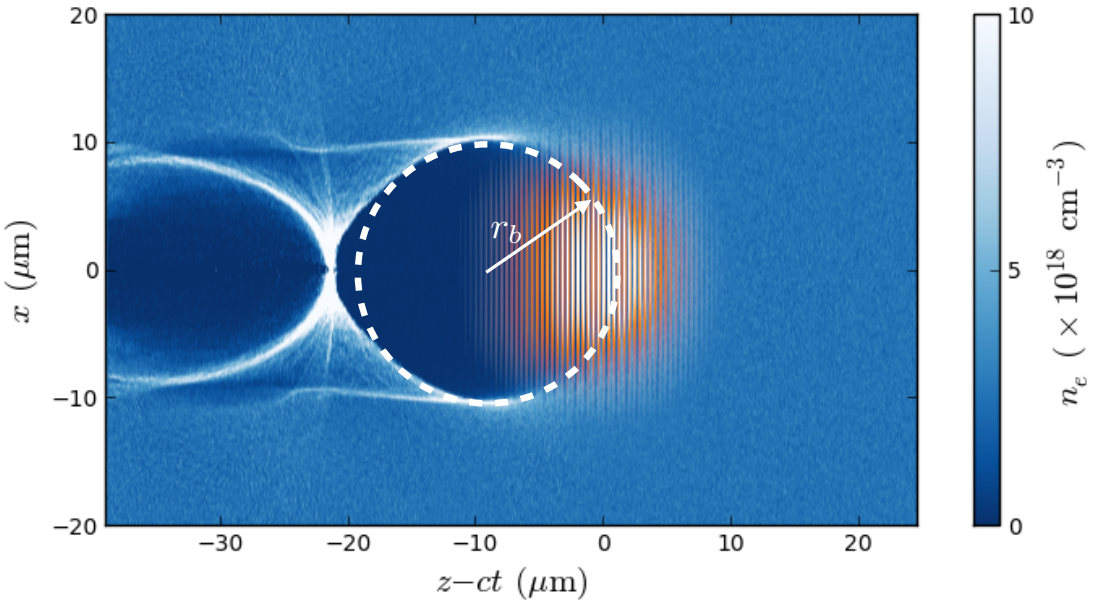

Figure 1.6: Electron density map represented in the $(z - ct, x)$ plane. The red and yellow laser pulse is superposed onto the electron density map. A white dashed circle with a blowout radius r_b highlights the shape of the blown out region. Courtesy of R. Lehe [67].

The study of LWFA using a 3D PIC simulations was first investigated by Pukhov et al. [68]. He used the term "bubble" regime instead of the blowout regime because of the spherical shape of the cavity driven by the laser. Subsequently, a phenomenological theory in this regime was proposed [69]. Lu et al. have proposed phenomenological [70] and nonlinear [66] theories for relativistic plasma wakefields in this regime. In order to get some insights on electron dynamics in this nonlinear regime, the plasma wave can be described entirely in

terms of the cavity radius, $r_b(\xi)$. The maximum blowout radius r_m is determined from force balance and the equation of motion can then be used to determine the shape of the cavity behind the laser. An illustration of the blowout electron density map is shown in Fig. 1.6.

In this regime, the two forces that need to be balanced are the space-charge force of electrons and the ponderomotive force of the laser. For a given laser power P_L and plasma density n_e, there is a matched spot radius that provides spherical density boundary. The estimate of the matched spot radius is given by $k_p r_m \approx 2\sqrt{a_0}$ where the factor of 2 is deduced from full PIC simulation [66]. In the case of unmatched spot radius, if the spot radius is much larger than this matched radius, the maximum amplitude of the normalized vector potential a_0 will be too small to cause blowout initially. Conversely, if the laser is focused to a spot radius smaller than the matched radius, the normalized vector potential blows out all electrons at the laser edge and little ponderomotive force is felt by the electrons, consequently, they move very little, resulting in a very wide sheath. Furthermore, the laser will diffract because its spot radius is too small to be guided.

This regime is equally considered in the design of an accelerator because the focusing forces for electrons inside the cavity are linear and uniform for all phases as $\boldsymbol{F}_\perp = -m_e\omega_p^2 r/2$ [66], and the accelerating field is independent of the transverse position with respect to the cavity axis.

In [70], some scaling laws have been established according to the phenomenological theory in the current regime. The laser depletes (pump depletion length) after a distance

$$L_{pd} \approx \frac{\omega_p^2}{\omega_0^2} c\tau_L, \tag{1.63}$$

and the distance that the trapped electrons travel before they outrun the wave (dephasing length) is

$$L_d = \frac{2}{3}\frac{\omega_0^2}{\omega_p^2} r_b. \tag{1.64}$$

To calculate the energy gain, we consider $\mathcal{E} = qE_{z,avg}L_{acc}$, where $E_{z,avg}$ is the average accelerating field of the beam loaded plasma wave, L_{acc} is the acceleration length. The desired acceleration length is the dephasing length, so we impose $L_{pd} > L_d$. The bubble is roughly spherical and consider that the electrons are either self-injected or externally injected at the rear, the electrons then travel a relative distance r_b before they dephase. The peak accelerating field is $E_{z,max} = \sqrt{a_0}E_0$, with $E_0 = m_e c\omega_p/e$. Since the wakefield is roughly linear, the average accelerating field becomes $E_{z,avg} \approx \sqrt{a_0}E_0/2$. The approximate equation for the energy gain can therefore be written as:

$$\mathcal{E} \approx \frac{2}{3} m_e c^2 \left(\frac{\omega_0}{\omega_p}\right)^2 a_0. \tag{1.65}$$

1.4 Electron Trapping and Injection

In a laser-wakefield accelerator, only electrons located in the accelerating and focusing phase of the wakefield propagating at a relativistic velocity along the axis of propagation, z will be accelerated. A resting electron would slip back with respect to the propagating wakefield, experience a succession of accelerating and decelerating wakefields and end up without any net energy gain. It is clear that to obtain accelerated electrons, the first step is to inject electrons in the wakefield. The injection process consists of placing a fraction of electrons

that have already a sufficient initial velocity in the accelerating and focusing region of the wakefield, so that they remain trapped in it. The study of electron trapping can be carried out using a one-dimensional Hamiltonian model.

1.4.1 One-dimensional Hamiltonian model

With the one-dimensional Hamiltonian model, together with QSA, we derive analytically the trajectories of electrons in a laser field and plasma waves. In Sec. 1.3.2, we have obtained Eq. 1.62 which represents the plasma wakefield. We assume a laser vector potential, polarized in the $y-$direction, given by

$$\boldsymbol{a} = \hat{a}(\xi)\cos\varphi\,\boldsymbol{e_y}, \tag{1.66}$$

where $\hat{a}$ represents the longitudinal shape of the pulse and $\varphi = \omega_0 t - k_0 z$ We assume a Gaussian shape for $\hat{a}$ so that $\hat{a}(\xi) = a_0 \exp(-\xi^2/c^2\tau_L^2)$.

The Hamiltonian for an electron interacting with a laser and plasma wave [71] writes

$$H = \gamma - \phi(z - v_g t) = \sqrt{1 + \tilde{p}_\perp^2 + \tilde{p}_z^2} - \phi(z - v_g t), \tag{1.67}$$

where $\tilde{p}_\perp = p_\perp/m_e c$, $\tilde{p}_z = p_z/m_e c$. The Hamiltonian depends on $\xi = z - v_g t$, we change the variables using a canonical transformation $(z, \tilde{p}_z) \rightarrow (\xi, \tilde{p}_z)$. We use a second type generating function $F_2(\xi, \tilde{p}_z) = \tilde{p}_z \xi$, thus satisfying $z = \partial F_2/\partial \tilde{p}_z$ and $\partial F_2/\partial \xi = \tilde{p}_z$. the new Hamiltonian, denoted by H' reads

$$\begin{aligned} H' &= H - \frac{\tilde{p}_z v_\phi}{c}, \\ &= \sqrt{1 + \tilde{p}_\perp^2 + \tilde{p}_z^2} - \phi(\xi) - \tilde{p}_z \beta_p. \end{aligned} \tag{1.68}$$

In 1D, the transverse canonical momentum is conserved such that $\dot{\tilde{p}}_\perp = -\partial H/\partial r_\perp = 0$, therefore the perpendicular component gives $\tilde{p}_\perp(\xi) - a_\perp(\xi) = \tilde{p}_0$, where u_0 is a constant of motion representing the initial perpendicular momentum of the electron; $\tilde{p}_0 = 0$ if electron has just been ejected from an atom via multiphoton ionization. In the case of an electron initially at rest in front of the laser pulse, $\xi_i = +\infty$, $\tilde{p}_\perp(\xi) = a(\xi)$, the index i denotes initial.

Eq. 1.68 does not contain time explicitly, that is $dH'/dt = 0 \Rightarrow H' = constant$, so the energy is conserved along an electron trajectory. As a result, for an electron with an initial energy H_0, one can solve for its longitudinal momentum and the expression writes

$$\tilde{p}_z = \beta_p^2 \left(H_0' + \phi\left(\xi\right)\right) + \gamma_p \sqrt{\gamma_p^2 \left(H_0' + \phi\left(\xi\right)\right)^2 - \gamma_\perp}. \tag{1.69}$$

This equation describes the electron trajectory in $(\xi, \tilde{p}_z)$ phase space once $a(\xi)$ and $\phi(\xi)$ are known.

From Fig. 1.7, three types of trajectories can be distinguished depending on the electron initial position and momentum. The first one are electrons situated initially at rest in the front of the laser pulse, i.e. $\xi_i = +\infty$ and $\tilde{p}_z(\xi_i) = \tilde{p}_\perp(\xi_i) = 0$, the Hamiltonian, $H_0' = 1$. The trajectory of such electrons are referred to as the fluid orbit and contribute to the formation of the plasma wakefield (shown in red in Fig. 1.7). They are not trapped and oscillate in the plasma wakefield with low energies.

The second trajectory is defined by electrons initially located at a minimum potential $\phi(\xi_{min}) = \phi_{min} < 0$ and moving along z with $\tilde{p}_z(\xi_{min}) = \gamma_p \beta_p$. This special trajectory is denominated the separatrix, it separates the trapped and the untrapped orbits (drawn

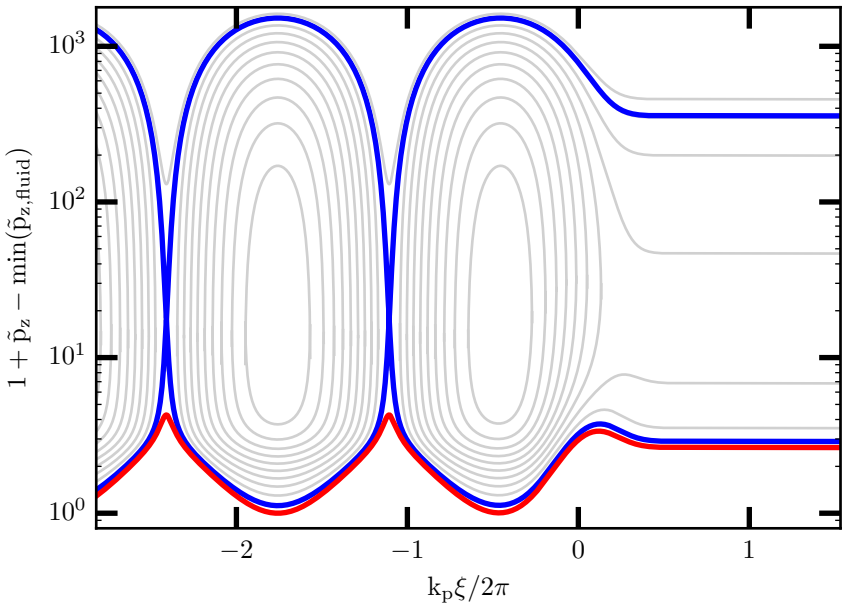

Figure 1.7: A picture of the phase space. The $y-$axis is plotted in log-scale and to avoid any negative values, $1+\tilde{p}_z-\min(\tilde{p}_{z,fluid})$ is plotted, where $u_{z,fluid}$ is the fluid orbit. The red line represents the trajectory of electrons that contribute to the plasma wakefield formation, $\tilde{p}_z = 0$, the blue line represents the separatrix, which separates the trapping and non-trapping orbits, $\tilde{p}_z = \gamma_p\beta_p$. The gray lines represent the trajectory of trapped electrons. The parameters are $a_0 = 2$, $n_e/n_c = 0.44\%$, $\lambda = 0.8\,\mu$m and $\tau_L = 16.99\,$fs.

in blue). Conservation of canonical momentum gives $\tilde{p}_z(\xi_{min}) = a(\xi_{min})$, leading to the Hamiltonian H_{sep}

$$H_{sep} = \frac{\sqrt{1+a^2(\xi_{min})}}{\gamma_p} - \phi_{min}. \tag{1.70}$$

The third trajectory refers to electrons that are found in the trapped orbits (drawn in light gray). Trapped orbits are obtained when the Hamiltonian satisfies $H_{trapped} \leq H_{sep}$. Consider a trapped electron behind the laser pulse at phase $\xi_{trapped}$ and moving along z at $\tilde{p}_z(\xi_{trapped}) = \gamma_p\beta_p$. At this point in phase space, the plasma wave potential is such that $\phi(\xi_{trapped}) = \phi_{trapped} \geq \phi_{min}$. Following Eq. 1.68, the Hamiltonian for a trapped electron can be written as

$$\begin{aligned} H_{trapped} &= \sqrt{1+\gamma_p^2\beta_p^2} - \phi_{trapped} - \gamma_p\beta_p^2, \\ &= \frac{1}{\gamma_p} - \phi_{trapped}. \end{aligned} \tag{1.71}$$

Since $\phi_{trapped} \leq \phi_{min}$, the necessary and sufficient condition for trapping is therefore $H_{trapped} \leq H_{sep}$.

1.4.2 Injection mechanisms

Self-injection

In the previous section (Sec. 1.4.1), we have described the basic trajectories. Our interest lies on the one of trapped electrons. They are considered to be initially located in the front of the laser pulse and possess an initial longitudinal momentum greater than the initial

momentum of the separatrix, i.e. $\tilde{p}_z(+\infty) > \tilde{p}_{z,sep}(+\infty)$. According to Eq. 1.69, this is simply $\tilde{p}_{z,sep}(+\infty) = \beta_p\gamma_p^2 H_{sep} - \gamma_p\sqrt{\gamma_p^2 H_{sep}^2 - 1}$, therefore electrons with initial energy $\mathcal{E} > \mathcal{E}_{trapped}$ will be trapped and accelerated in the wakefield, for

$$\mathcal{E}_{sep} = \mathcal{E}_{trapped} = mc^2(\sqrt{1 + \{\tilde{p}_{z,sep}\,(+\infty)\}^2} - 1), \tag{1.72}$$

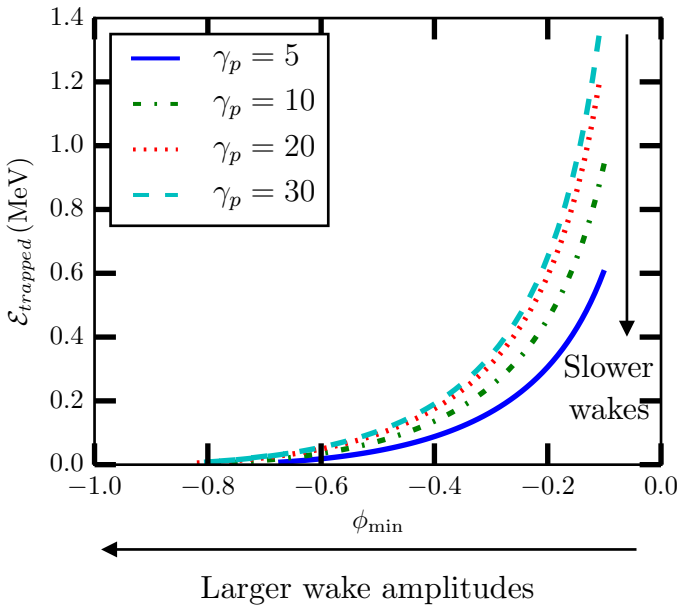

Figure 1.8: Energy thresholds for trapping with respect to ϕ_{min} which represents the amplitude of the wake for different phase velocities of the plasma, γ_p.

Fig. 1.8 shows the variation of the energy threshold as a function of the minimum plasma wave amplitude ϕ_{min} of which it is achieved for different values of the plasma wave Lorentz factor γ_p. It is clear that the trapping is easier when the wake amplitudes are large and slow. Interestingly, we also observe that when $\phi_{min} \to -1$, $\mathcal{E}_{trapped} \to 0$, implying that electrons that are initially at rest, located at this high-amplitude of wake, get injected into the plasma wave. In fact, this is correlated to the fact that the longitudinal electric field reaches the relativistic cold wave-breaking limit, E_{max} (defined earlier in Sec 1.3.1). More complicated three-dimensional models for self-injection were developed to fully capture the physics and can be found in [69, 72, 73, 74, 75].

In three-dimensional models, wave breaking happens for ultrarelativistic intense laser pulses shorter than λ_p. These laser pulses are intense enough to break the plasma wave just after the first plasma wave period. From 3D PIC simulations, it has been observed that injected electrons are in general located at one laser waist from the axis ($r \sim w_0$), where w_0 is the laser waist in vacuum. These electrons circulate around the laser pulse and the bubble, and attain a velocity larger than the wake-phase velocity when reaching the axis at the rear of the bubble [74, 73, 76]; this injection mechanism is called transverse self-injection. Conversely, electrons that are close to the axis feel a weak radial ponderomotive force, therefore they are weakly deviated when crossing the laser pulse and remain in the region of largest accelerating field E_z. These electrons are likely to catch up with the plasma wave and be injected [75]. This injection mechanism is called longitudinal self-injection.

These two injection mechanisms have advantages and drawbacks. The transverse self-injection is well suited for applications that require a high charge ($\geq$ 100pC) but can cope

with little stability, and produce electron bunches with large energy spread (10%) and a poor emittance. In contrast, longitudinal self-injection is ideal for applications in which low emittance is essential but low bunch charges are expected.

Ionization-induced injection

We have seen in the previous section that wave breaking contributes to the injection of electrons in the plasma wave. Another injection scheme proposed in [77, 78, 13], requires the use of gas medium composed of low Z gas usually hydrogen or helium and a trace of high atomic number (Z) atoms usually oxygen, nitrogen, or argon. Instead of relying on wave breaking, this injection scheme uses the laser field to control the injection process into the wakefield, achieved by ionizing deeply bound electrons from a the high-Z gas at a proper phase inside the laser-driven wakefield, such that they reside above the wake separatrix and, therefore, are trapped and accelerated. This additional degree of freedom allows the trapping of electrons at lower plasma densities, using lower laser intensities as compared to the self-injection scheme.

This scheme relies on the ionization conditions of heavy atoms in the laser fields. We thus start by recalling ionization of atoms in the laser field before describing the trapping conditions for the electrons created inside the laser pulse.

Tunneling photo-ionization. The required laser intensity to ionize K-shell is approximately two orders of magnitude stronger than the intensity matching the binding strength of the electron to the atom ($I_a \approx 3.51 \times 10^{16}\,\mathrm{W\,cm^{-2}}$); the associated laser field will therefore distort the Coulomb field felt by the electron.

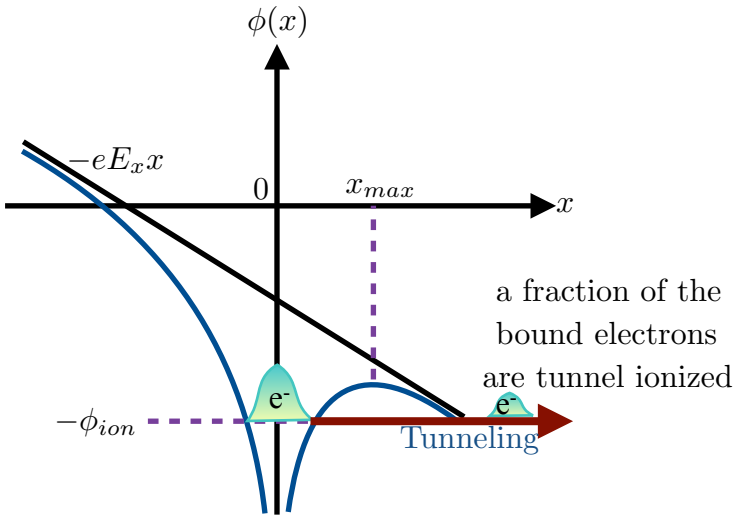

Figure 1.9: Schematic picture of tunneling by a strong external electric field, E_x. The resulting potential ϕ as a function of the distance x is plotted, electrons situated at $x = 0$ are the bound electrons and electrons which are found at $x \gg x_{max}$ are electrons that have undergone the tunneling-ionization process.

We use a classical picture of this phenomenon [79], in which the Coulomb potential is modified by a stationary homogeneous electric field. The resulting potential $\phi(x)$ can be expressed as:

$$\phi(x) = -\frac{Ze^2}{x} - eE_x x, \tag{1.73}$$

where x is the distance.

In Fig. 1.9 is illustrated a schematic picture of tunneling photo-ionization where the resulting potential ϕ as a function the distance x is plotted, electrons situated at $x = 0$ are the bound electrons and electrons which are found at $x \gg x_{max}$ are electrons that have undergone the tunneling-ionization process. We see that the Coulomb barrier has been suppressed by a strong external electric field, E_x for $x > 0$. For $x \gg x_{max}$, the modified Coulomb barrier is lower than the electron binding energy, so that the electron may tunnel through this barrier with some finite probability [80] with an initial energy $\mathcal{E}$, given by

$$w(\mathcal{E}) \sim \exp\left\{-\frac{2}{3}\left[\frac{\lambda_0}{\lambda_{\rm C}}a^3\gamma_{\rm K}^3\frac{E_k}{|E_L(\tau)|}+\frac{\gamma_{\rm K}^3\mathcal{E}}{\hbar\omega}\right]\right\}, \tag{1.74}$$

where $E_L(\tau)$ is the laser field, $E_k = m_e c^2 k_0/e$, $\gamma_{\rm K} = (U_i/2U_p)^{1/2} = (\alpha_f/a)(U_i/U_{\rm H})^{1/2}$ is the Keldysh parameter, with $U_{\rm H} = 13.6\,\text{eV}$ the ionization potential of hydrogen, U_I is the ionization potential, $U_p = m_e c^2 a^2/4$ is the laser ponderomotive potential, $\alpha_f = e^2/\hbar c \approx 1/137$ is the fine structure constant, and $\lambda_{\rm C} = h/m_e c = 2.4263 \times 10^{-10}$cm is the Compton wavelength. In the high-field limit, $\gamma_{\rm K} < 1$, tunneling ionization is dominant.

In Eq. 1.74, we have omitted the initial momentum along the laser propagation direction because it is negligible with respect to the one along the laser polarization direction. In explicit PIC modeling, the implementation of a tunnel photo-ionization module is based on the direct current (DC) ionization rate model because the sub-wavelength scale of the laser is well-resolved and the simulation time-step is much smaller than the laser period [81], i.e. $\Delta t \ll T_0$, where Δt is the simulation time-step and $T_0 = \lambda_0/c$ is the laser period. Within each simulation time-step, the laser field can be approximated as a DC field.

Eq. 1.74 indicates that a large number of electrons will be ionized at the peak of the laser electric field. Since the transverse canonical momentum will be conserved, $\boldsymbol{p}_\perp = e\boldsymbol{A}_\perp$, electrons ionized at the peak of the laser field have zero transverse momentum upon exiting the laser, allowing them to be trapped in the longitudinal field of the plasma wave. On the other hand, electrons ionized off-peak of the laser electric field exit the laser with a residual transverse momentum, thus contributing to the increase of transverse emittance.

In Fig. 1.10(a) is plotted the modulus of the laser potential $\boldsymbol{a}$, as defined by Eq. 1.66 and the ionization probability $\mathrm{P_{ioniz}} = 1 - \exp(-cdf[w(\mathcal{E})]T_0)$, where *cdf* stands for cumulative distribution function and $T_0 = \lambda_0/c$ the laser period. We consider a gas medium composed of hydrogen atoms and a small fraction ($< 10\%$) of nitrogen atoms. The leading edge of the laser pulse with an intensity typically below $10^{16}\,\mathrm{W\,cm^{-2}}$, is intense enough to fully ionize hydrogen atoms and the outer five electrons of nitrogen. These electrons then contribute to the formation of the plasma wave. The large difference of the ionization potential (IP) between the $5^{\rm th}$ (L-shell) electron (IP 98 eV) and the two K-shell electrons (IP 552 and 667eV) of nitrogen atom is the key point to this scheme. Ionization from the K-shell occurs at higher intensities typically for $\mathrm{I} > 10^{18}\mathrm{Wcm^{-2}}$, so these electrons are born at rest in regions of strong fields, often at the laser peak intensity. These newly ionized electrons slip backwards relative to the laser pulse and the wakefield. If they gain enough energy from the longitudinal electric field, E_z to move at the phase velocity of the wakefield, they are trapped and will gain additional energy from the wakefield as they move forward.

Fig. 1.10(b) shows the ionization probability, $\mathrm{P_{ioniz}}$ plotted with respect to the maximum amplitude of the normalized vector potential a_0 for two K-shell electrons of nitrogen. A lower a_0 is required to start the ionization process $\mathrm{N^{5+}} \rightarrow \mathrm{N^{6+}}$ as compared to the ionization process $\mathrm{N^{6+}} \rightarrow \mathrm{N^{7+}}$. For the rest of this thesis, we call the 6^{th} electron the electron created from the ionization process $\mathrm{N^{5+}} \rightarrow \mathrm{N^{6+}}$ and the 7^{th} electron from $\mathrm{N^{6+}} \rightarrow \mathrm{N^{7+}}$.

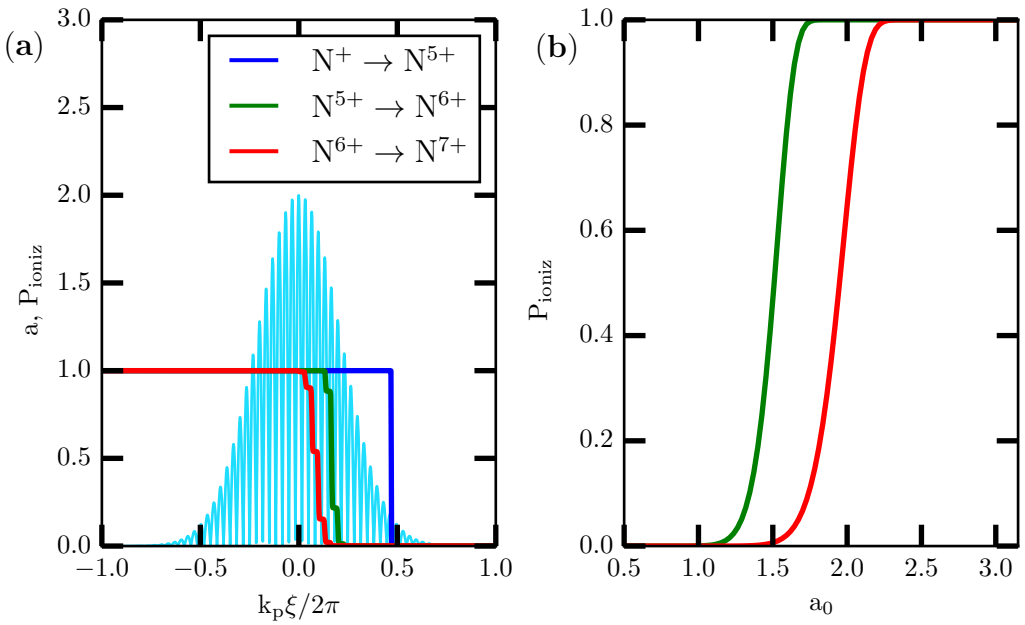

Figure 1.10: (a) Ionization probability P_{ioniz} of a nitrogen atom as a function of normalized position: the first five electrons, from N^+ to N^{5+}, appear at the front of the laser pulse, while electrons from $N^{5+} \rightarrow N^{6+}$ and $N^{6+} \rightarrow N^{7+}$ appear at the peak of the laser envelope. The normalized laser vector potential a follows the Gaussian distribution. Here $a_0 = 2$, $\tau_L = 16.99\,\text{fs}$, $\lambda_0 = 0.8\,\mu\text{m}$. (b) Ionization probability, P_{ioniz} of the ionization processes $N^{5+} \rightarrow N^{6+}$ (in green) and $N^{6+} \rightarrow N^{7+}$ (in red)as a function of the peak value of laser envelope a_0.

Trapping conditions. We now determine the condition under which the 6^{th} and the 7^{th} electrons will be trapped. For simplicity, since we are considering a small concentration of high-Z gas, we will neglect the modification of the wakefield due to ionization process of nitrogen atoms, therefore Eq. 1.62 is still valid [82].

An electron will be trapped provided $H \leq H_{sep}$. An electron ionized at a wake phase ξ_i witnesses the corresponding laser amplitude $a(\xi_i)$. Since ionization occurs mostly at the peak of the laser field in linear polarization, $a(\xi_i) \approx 0$, therefore in the case of an ionized electron born at rest, conservation of canonical momentum reads $\tilde{p}_\perp(\xi) = a(\xi) - a(\xi_i) \approx a(\xi)$. The initial Hamiltonian of such electrons can be found from Eq. 1.68 as

$$H_i = 1 - \phi_i, \tag{1.75}$$

the trajectory of the electron can be computed using Eq. 1.69. This trajectory is shown in gray in Fig. 1.11(a). The conditions for trapping can be summarized in two key points:

- the intensity at position ξ_i should be large enough for ionizing a given electron level, i.e. $a(\xi_i) > a_{thres}$;
- the electron should be born on a trapped orbit, i.e. $H_i < H_{sep}$.

In practice, electron trapping in this scheme requires a moderately high intensity laser pulse (typically $a > 1$) and a large amplitude plasma wave obtained with laser pulse length $c\tau_L \sim \lambda_p$.

Fig. 1.11(a) shows a phase space picture of the fluid orbit (in red), the separatrix (in blue) and the typical trajectory of trapped ionized electrons in the first period of the wakefield (in gray). This illustrates the local injection volume, defined as the volume in phase

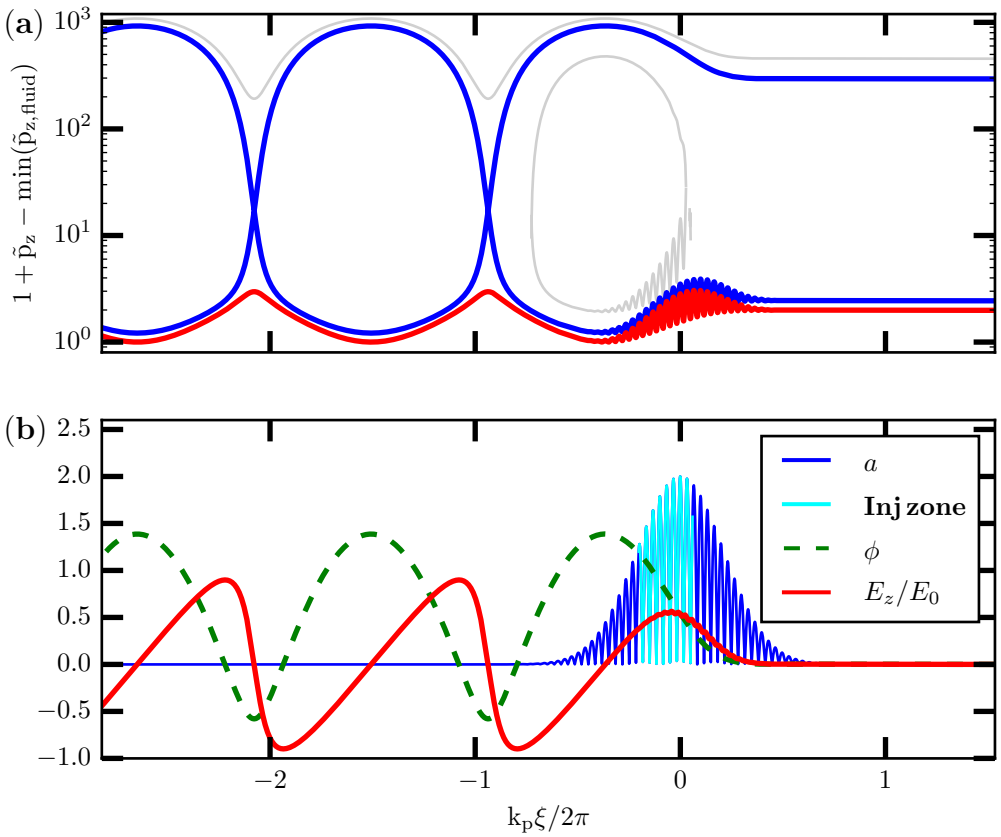

Figure 1.11: (a) A phase space picture showing the fluid orbit (in red), the separatrix (in blue) and the typical trajectory of trapped ionized electrons in the first period of the wakefield (in gray). (b) Laser pulse with normalized vector potential a drives the wakefield, E_z and gives rise to the wake potential, ϕ. An electron ionized in the region colored in cyan will be injected and trapped in the wakefield. The parameters are $a_0 = 2$, $n_e/n_c = 0.44\%$, $\lambda_0 = 0.8\,\mu$m and $\tau_L = 16.99\,$fs.

space, delimited by the separatrix where electrons satisfy trapping conditions at a given time; whereas the global injection volume is the local injection volume integrated over time. The number of injected and accelerated electrons and the energy spread of the bunch are determined over the global injection volume in phase space. Large global injection volume leads to bunches with large injected charge and large energy spread; small global injection volume might overcome the energy spread at the detriment of the injected charge.

Fig. 1.11(b) shows a laser pulse with normalized vector potential $\boldsymbol{a}$ driving a plasma wave, the potential of the plasma wave, ϕ and the wakefield E_z/E_0. An electron 'born' in the local injection zone (in cyan) satisfies trapping conditions and therefore is susceptible to be trapped in the wakefield. The local injection zone is governed by the wakefield amplitude and the ionization threshold. Experiments have demonstrated the concept of ionization injection using nitrogen and argon [77, 78]. Results obtained show broad energy distributions due to the fact that ionization injection occurs all along the propagation. In fact, ionization injection occurs as long as the laser intensity exceeds the threshold intensity assuming that the amplitude of the plasma wave is large. This is the major drawback of this injection mechanism.

As pointed out in [82], there is a linear correlation between the energy spread and the mixed gas length provided that trapping conditions are satisfied throughout the interaction

length, implying that the beam quality can be improved by reducing the gas length. Several experimental studies implement a mixed gas length reduced to a few mm in structured targets [83, 84, 85, 15, 14]; yet the generated electrons straight out of the injector still have a large energy spread, signifying that the mixed gas length is still longer than optimum and efficiency of coupling to the accelerating stage can be improved. In this respect, much efforts were directed to tailoring the gas-density profile [86, 87] and to using moderate power pulses [88] to limit the injection volume, showing promising results.

Density gradient based injection

Another method of controlling the injection process is by tailoring the plasma density, which gives us control over the plasma wave phase velocity, v_ϕ. We have seen previously that the lower the phase velocity, the lower the trapping threshold, as illustrated in Fig. 1.8. Therefore, injection can be triggered in a local manner by inducing a local decrease in the phase velocity. For example, this can be achieved by sending the laser pulse through a downward density ramp, which causes the wakefield to slow down. Note that $v_\phi \neq v_g$. Density gradient based injection schemes can be characterized by the density scale length $L_s = n_0/|dn_0/dz|$ and the plasma skin depth $k_p^{-1} = v_g/\omega_p$, where $v_g \approx c$ is the laser group velocity. Two categories can be identified:

- smooth density down ramp ($L_s \gg k_p^{-1}$) [89];
- sharp downward density transition ($L_s < k_p^{-1}$)[90].

Injection in smooth density down ramp. This injection scheme takes place when wave breaking occurs, where the electric field is equivalent to E_{max} as in Eq. 1.40. In the one-dimensional case, wave breaking can either completely destroy the regular structure of the wave, or it can develop gently, with only a small portion of the wave involved in the break. The latter serves the purpose of injecting a portion of the electrons into the accelerating phase in the wake behind the laser pulse. One way to make this happen is to introduce a plasma with inhomogeneous density. The plasma wave wavenumber depends on time t through the relationship $\partial k_p/\partial t = -\partial\omega_p/\partial z$. The resulting growth over time of the wavenumber results in the break of a small portion of the wave even when the initial wave amplitude is below the wavebreaking threshold, possibly resulting in the injection of electrons into the wakefield.

The Hamiltonian model described in Sec 1.4.1 no longer holds in a density transition because the wakefield potential also depends on z, as $\phi(z, \xi)$. To provide some physical intuition of the process, a simple fluid model is developed here. Consider the weakly relativistic case ($a^2 \ll 1$) and a smooth density gradient $k_p L_s \gg 1$. The plasma equation in the QSA limit reads

$$\left[\frac{\partial^2}{\partial\xi^2} + k_p(z)^2\right]\phi = \frac{k_p(z)^2}{2}\left\langle a^2\right\rangle, \tag{1.76}$$

where $\langle a^2\rangle$ is the $\xi-$averaged peak intensity of the laser pulse. Using a Green's function, Eq. 1.76 can be integrated and the solution behind the laser pulse has the form

$$\phi(\xi) = \phi_0(z)\sin\left[k_p(z)(z - v_g t)\right], \tag{1.77}$$

where the wakefield amplitude is $\phi_0(z) = -(\sqrt{\pi}/4)a_0(z)^2 k_p(z) c\tau_L \exp[-(k_p(z)c\tau_L/2)^2]$ and its phase is $\varphi = k_p(z)(z - v_g t)$, so that one can compute the local oscillation frequency and

wavevector:

$$\omega = -\frac{\partial \varphi}{\partial t} = k_p(z) v_g = \omega_p(z), \tag{1.78}$$

$$k = \frac{\partial \varphi}{\partial z} = k_p(z) + \frac{\partial k_p(z)}{\partial z}(z - v_g t). \tag{1.79}$$

In a downward density gradient where $\partial k_p/\partial z < 0$ and $z - v_g t < 0$ behind the laser pulse, the wavevector increases with time while the plasma frequency does not depend on time, i.e. $\omega = \omega_p(z)$. As a result of this time-varying wavevector, the phase velocity $v_\phi(z,t) = \omega_p(z)/k(z,t)$ becomes

$$v_\phi(z,t) = v_g \Big/ \left(1 + \frac{z - v_g t}{k_p(z)} \frac{dk_p(z)}{dz}\right). \tag{1.80}$$

Consequently the phase velocity decreases as the wavevector increases, creating a favorable condition for the injection to occur behind the laser pulse as the wakefield becomes slow enough to trap plasma background electrons.

Several experiments have been conducted to study electron trapping in wakefields with a gentle density downramp gradient [91, 92, 93, 94]. Outcomes of these experiments have all shown more stable beams with an energy spread in the range of 10%.

Injection in sharp downward density transition. The smooth density downramp has shown promising results but in the quest of reducing the energy spread, Suk [90] has introduced a sharp, localized density gradient. Due to the sharp transition in the density, this injection method is more commonly known as shock-front injection.

In this scheme, a single short laser pulse is sent through an underdense plasma with a sharp downward density transition with $k_p L_s < 1$; two distinct regions are distinguished: (I) a dense upstream region, (II) a less dense downstream region, as shown in Fig. 1.12(a), where the density $n_0/max(n_0)$ is shown with respect to the laser propagation axis z. A sharp, localized density transition of length $L_s = 0.6/k_p$ is shown in the region in blue. Fig. 1.12(b) shows the laser in red-orange and the wakefield cavity is delimited by thick black lines in regions (I) and (II).

The mechanism of injection [95] can be explained as follows:

1. As shown in Fig. 1.12(b)(I), when the laser propagates in the high density region (I), it drives a cavity or a nonlinear plasma wave of wavelength $\lambda_{p,\mathrm{I}}$. Here, the amplitude of the plasma wave is assumed to be below the threshold for self-injection, therefore no electron is injected in the cavity.

2. Upon entering the region of lower density (II), electrons remain at the same distance behind the laser pulse due to the sharpness of the transition.

3. In the low density region (II), the driven plasma wave has a wavelength $\lambda_{p,\mathrm{II}} > \lambda_{p,\mathrm{I}}$, the cavity expands and electrons created at a previous position in z are now located in the accelerating phase, where some of them are trapped and accelerated, as shown in Fig. 1.12(b)(II).

In the shock-front injection scheme, plasma electron trapping occurs in the first rarefied cavity, due to localized nonlaminar motion near the sharp density transition, and at plasma wave amplitudes well below conventional wavebreaking.

Several research groups have performed experiments by creating a shock in the gas flow [96, 95], or by using another laser pulse to create a density perturbation [92]. The resulting

beam energy has shown some tuning abilities by controlling the injection location [95, 97]. Furthermore, the trend observed in these experiments show that the lower the energy spread, the lower the charge, implying that the reduction of energy spread comes at the expense of charge.

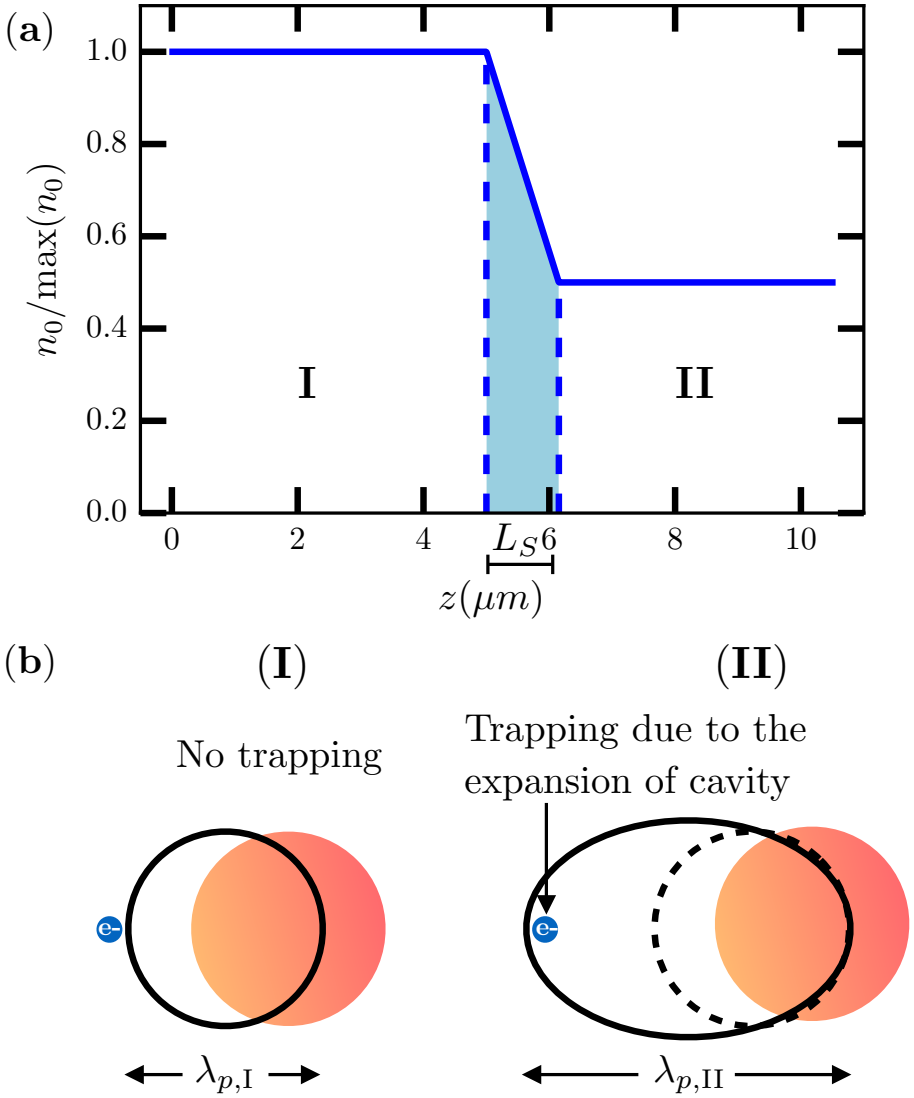

Figure 1.12: Principle of injection with a sharp downward density transition. Labels I and II indicate regions of high and low density. (a) Normalized longitudinal density profile, $n_0/\max(n_0)$. $L_s k_p = 0.6$. Adapted from [87]. (b) Laser in red-orange and the wakefield delimited by black circle. In region I, a plasma cavity is formed but no trapping is observed. Once the laser enters region II, the plasma cavity expands, electrons from the initial wave are trapped in the accelerating phase of the cavity.

Optical injection

Another way to inject electrons into wakefield structure is by using optical injection techniques. These techniques trigger the injection in a precise local manner using several laser pulses: the first pulse generates the wakefield (pump pulse), and the second one triggers injection of electrons in wakefield (injection pulse).

Optical injection was first proposed in [98]. In this scheme, injection is triggered by an injection pulse coming perpendicularly to the pump pulse. When the injection pulse collides with the wakefield, the transverse ponderomotive force of the pulse provides some electrons with the necessary momentum to cross the wakefield separatrix and be trapped in the wakefield structure.

Another scheme using three pulses was proposed in [54]. This scheme is known as the colliding pulse optical injection scheme. In this scheme, an intense pump pulse generating a large wakefield (20 GV/m), and two counterpropagating injection pulses are used. The pump pulse generates a fast ($v_{p0} \approx c$) wakefield while the injection pulses collide at some distance behind the pump and generate a slow ponderomotive beat wave with a phase velocity $v_{pb} \approx \Delta\omega/2k_0$. As a result, the beatwave due to the overlapping between the injection pulses injects electrons into the fast wakefield structure (generated by the pump pulse) for acceleration to high energies. This technique allows for the use of lower injection pulse intensities, i.e. 2 orders of magnitude less intensity than required in [98] and offers a detailed control of the injection process, i.e. the injection phase can be controlled via the position of the forward injection pulse, the beat phase velocity via $\Delta\omega$, the injection energy via the pulse amplitudes and the number of trapped electrons via the backward pulse duration.

Further simplification on the colliding pulse optical injection scheme by keeping the collinear geometry but only using two pulses has been done in [63, 99, 100, 101]. In order to inject low energy electrons directly into the wakefield structure, Davoine et al.[102] has introduced the use of two counterpropagating laser pulses, with a very low-energy second pulse so that the longitudinal electron motion remains frozen and electrons can enter into the propagating plasma wave, at a position allowing their injection. The above mentioned injection schemes produce energy dispersions of the order of $5 - 10\%$, however in the regime of parameters that were hitherto tested, the injected and accelerated electron beam has a charge (a few tens of pC) [63].

Another technique uses the pulse collision to trigger a transient and fast deformation of the bubble (as seen in ***Injection in sharp downward density transition***) to control transverse injection [103]. This technique, known as the optical transverse injection has been studied using PIC simulations. Results from simulations show that it can generate electron beam that meets the requirements of low emittance (~ 0.17 mm.mrad), relatively high charge ($\sim 50 - 100$ pC) while retaining the low energy dispersion (2%) associated with colliding-pulse schemes.

Although self-injection scheme generates electron bunch with high charge but it lacks shot-to-shot stability [75] and it requires a high laser strength a_0 to enable trapping of electrons in wakefield. Gradient-based injection scheme does not require a high a_0 for injection and offers a narrow energy spread in the case of shock-front injection, but it reduces the charge and requires high technical skills to tailor a precise density gradient. Optical injection techniques offer a precise control on the injection of electrons in the plasma wave, however in practice they are difficult to be implemented experimentally because the laser pulses have to be synchronized. Ionization-induced injection scheme generates electron bunch with high charge (higher charge than self-injection scheme in the same conditions) and requires only a moderate laser pulse, however continuous injection might occur as long as a_0 is greater than the injection threshold, a control on a_0 is therefore necessary. Our group has chosen to study in details the ionization injection scheme because of the easy experimental implementation and the given additional control parameter which is the concentration of the low Z gas, and works on optimizing the generated electron beam properties in experiments and via PIC

simulations (refer to Chapter 5).

Mixed techniques

In recent years, novel injection schemes have been proposed by making use of the best features from various injection schemes. Some of them are presented in the following paragraphs.

One can obtain an electron beam with optimum characteristics by having control on its formation. This has been one of the core research topics in our group. By selecting the focal spot position in vacuum along a density tailored profile, the position where ionization injection occurs can be controlled [104]. In fact, the position of the laser focal plane causes self-focusing of the laser pulse while propagating in the plasma, which in turn modifies the laser vector potential along the propagation axis.

Work on combining both density tailoring and ionization injection schemes was also carried out. Golovin et al. [105] have demonstrated an independent control of laser-wakefield acceleration and injection in two overlapped composite gas jets: the first gas jet containing only N_2 acts as the injector; the second gas jet containing only H_2 acts as the accelerator. In addition, Vargas et al. [106] have used a stereolithography based 3D printer to produce two-stage gas targets for LWFA experiments on the HERCULES laser system at the University of Michigan. With these configurations, electron trapping was confined to the injector and the trapped electrons were then accelerated to high energy in the accelerator, resulting in tunable electron beams with reduced energy spread. In the same line of thought, our work on the tailoring of the density profile in the accelerating phase [107] shows that the electron bunch energy can also be tuned while having its energy spread preserved. In both articles, the energy spread remains in the range of 10% at FWHM (Full Width at Half Maximum), a great improvement as compared to the ionization injection scheme alone.

Another mixed technique that combines ionization injection and a sharp downward density transition [87] has generated more stable shot-to-shot electron beams than those obtained in a shock front injection. Compared to ionization injection, this technique ensures electron trapping in a small region, leading to the injection of electron beams with rather low energy spread, the charge is of the order of 30 pC, more than as obtained using only the sharp density transition.

1.5 Acceleration limits

Several mechanisms can limit the energy gain in a LWFA, namely laser diffraction, electron dephasing, pump depletion and laser-plasma instabilities. Other effects such as beam loading can affect the beam charge and the beam quality. Therefore, one has to work around these limits to produce a high current, high energy and high quality electron beam.

1.5.1 Laser diffraction

In vacuum a laser pulse undergoes Rayleigh diffraction, therefore some form of guiding is necessary; otherwise the laser-plasma interaction distance will be limited to Z_R before it gets diffracted. Various methods of optical guiding, including relying on the self-focusing [108] of the laser pulse, using preformed plasma density channels [109, 110, 111, 112, 113, 114, 17, 115] or dielectric capillaries [116, 117, 118, 119]. For this thesis, we will only focus on the diffraction and the self-focusing of the laser pulse.

Geometric optics picture of self-focusing and diffraction

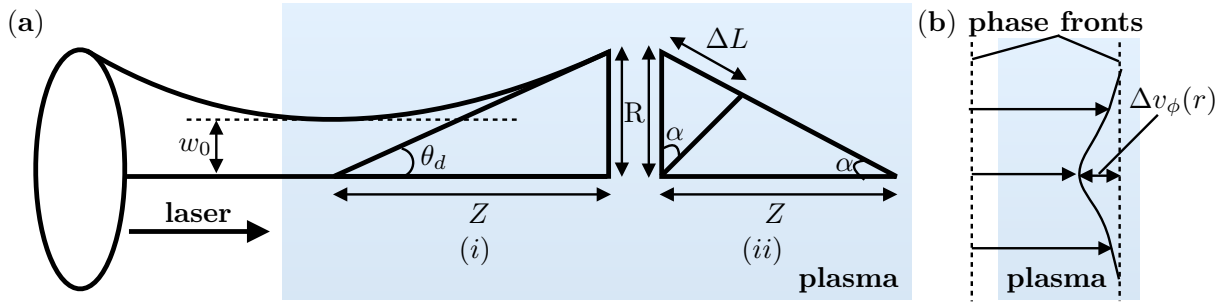

Figure 1.13: (a) Geometrical view of (i): the diffraction; (ii): the self-focusing of the Gaussian laser beam. (b) Phase front bending due to refraction. Adapted from [120].

The geometrical schematic picture in Fig. 1.13(a) introduces key parameters governing nonlinearity effects that take place while the laser propagates in a plasma. It shows the Gaussian envelope as a function of the direction of propagation of a laser pulse with radial profile $a(r) = a_0 \exp(-r^2/2w_0^2)$ focused to a laser waist w_0 (determined in vacuum) inside a region of uniform, underdense plasma. In the absence of nonlinear effects the beam will diffract, as shown in Fig. 1.13(a)(i) with a divergence angle [121]

$$\theta_d = \frac{dR}{dZ} = \frac{w_0}{Z_R} = \frac{2}{k_0 w_0}. \tag{1.81}$$

At high intensities, the dispersion relation of the laser electromagnetic wave is altered due to the effective relativistic mass increase of electrons in the plasma, therefore

$$\omega_0^2 = c^2 k_0^2 + \frac{\omega_p^2}{\gamma_0}, \tag{1.82}$$

where ω_p^2/γ_0 is the effective plasma frequency. The corresponding refractive index writes

$$\eta(r) \equiv \frac{ck_0}{\omega_0} = \sqrt{\frac{\omega_0^2 - \frac{\omega_p^2}{\gamma_0}}{\omega_0^2}} = \sqrt{1 - \frac{\omega_p^2}{\omega_0^2 \left(1 + \frac{a(r)^2}{2}\right)^{1/2}}}. \tag{1.83}$$

From Eq. 1.83, we observe that $\eta(r)$ is peaked on axis, i.e. $d\eta/dr < 0$, which represents a positive or focusing lens in optic terminology, in contrast with the divergent refractive index where $d\eta/dr > 0$.

We can further evaluate the condition where diffraction is compensated by self-focusing. Considering $a^2 \ll 1$, we first approximate the phase velocity of the wave fronts passing through the medium using Eq. 1.83, that yields

$$\frac{v_\phi(r)}{c} = \frac{1}{\eta} \approx 1 + \frac{\omega_p^2}{2\omega_0^2}\left(1 - \frac{a^2(r)}{4}\right), \tag{1.84}$$

Fig. 1.13(b) shows the phase fronts being bent due to refraction. The phase fronts of the beam profile travels more slowly at the center than at the edge, the velocity difference, $\Delta v_\phi(r)$ is given by

$$\frac{\Delta v_\phi(r)}{c} = \frac{\omega_p^2}{8\omega_0^2} a_0^2 \exp\left(\frac{-r^2}{w_0^2}\right). \tag{1.85}$$

The curvature of the phase front bends the rays proportional to their relative path difference and the maximum path difference is given by

$$\Delta L = |\Delta v_\phi|_{max} t = \left|\frac{\Delta v_\phi}{c}\right|_{max} Z = \alpha R, \tag{1.86}$$

where Δv_ϕ is maximum on axis $r = 0$, α and R are geometrical quantities shown in Fig. 1.13. This implies that the maximum focusing angle is

$$\alpha^2 = \frac{\omega_p^2}{8\omega_0^2 a_0^2}. \tag{1.87}$$

Laser diffraction will therefore be canceled by self-focusing effects if $\alpha^2 \geq \theta_d^2$, yielding

$$a_0^2 \left(\frac{\omega_p w_0}{c}\right)^2 \geq 32. \tag{1.88}$$

This relationship can be re-written as a function of laser power since $P_L \approx 21.5(w_0 a_0/\lambda_0)^2$ where a linearly polarized laser field with a Gaussian radial profile is assumed. The condition for laser self-focusing is $P_L \geq P_C$, where $P_C = 16.2\omega_0^2/\omega_p^2$ [GW] [122] is the critical power for relativistic self-focusing. Other approaches solving the nonlinear Schrödinger equation leads to the same results [40, 123, 124].

1.5.2 Laser pump depletion

The laser depletes its energy into the plasma wave over a distance where the energy deposited in the wake equals the laser pulse energy. The aforementioned distance is known as the pump depletion length L_{pd} and it can be estimated by equating the laser pulse energy to the energy left behind in the wakefield, $E_L^2 c\tau_L \approx E_{z,max}^2 L_{pd}$, where E_L is the laser field [125, 126], $E_{z,max} = \max(E_z)$ the maximum electric field amplitude of the plasma wave behind the laser pulse.

We evaluate the order of magnitude of the laser depletion length using the plasma fluid theory. Consider a square laser pulse profile ($a_0 = constant$ for $0 < \xi \leq \lambda_p/2$ and $a_0 = 0$ elsewhere), with optimal length for plasma wave excitation ($c\tau_L \approx \lambda_p/2$). The driven wakefield $E_{z,max}$ is written in terms of a_0: $E_{z,max}/E_0 = (a_0/2)^2/(1 + a_0^2/2)$ [127, 128]. where E_0 is the cold wave breaking limit, as recalled here $E_0 = m_e c\omega_p/e$. In the quasi-linear regime ($a_0^2 \ll 1$), $E_{z,max}/E_0$ can be approximated as $a_0^2/2$, therefore

$$\begin{aligned} L_{pd} &= \frac{E_L^2 c\tau_L}{E_{z,max}^2} \\ &= \frac{(\omega_0 m_e c a_0/e)^2(\lambda_p/2)}{(\omega_p m_e c/e)^2(a_0^4/4)} \\ &= 2\frac{\lambda_p^3}{a_0^2\lambda_0^2}. \end{aligned} \tag{1.89}$$

Similarly, considering the previous square laser pulse profile, we evaluate the dephasing length in the nonlinear regime ($a_0^2 \geq 1$). Here, the optimal length for plasma wave excitation is $c\tau_L \approx \lambda_{Np}/2$, where λ_{Np} is the nonlinear plasma wavelength [52, 50, 51, 4] and it writes

$$\lambda_{Np} = \lambda_p \begin{cases} 1 + \frac{3}{16}\left(\frac{E_{z,max}}{E_0}\right)^2 & \text{if} \quad \frac{E_{z,max}}{E_0} \ll 1, \\ \frac{2}{\pi}\left(\frac{E_{z,max}}{E_0} + \frac{E_0}{E_{z,max}}\right) & \text{if} \quad \frac{E_{z,max}}{E_0} \gg 1. \end{cases} \tag{1.90}$$

Performing the same calculation as before, we obtain $L_{pd} = (\sqrt{2}/\pi)(\lambda_p^3/\lambda_0^2)a_0$ in the nonlinear regime.

The above results are obtained assuming constant laser amplitude, plasma density and wakefield throughout the propagation. An evolving plasma wave amplitude and 3D effects alter these results. For example, [129] showed that the effects of laser diffraction can lead to a more restrictive trapping condition for linear plasma waves. Since the laser pump depletion is dependent on the pulse profile, hence the depletion length is generally written as $L_{pd} \propto (\lambda_p^3/\lambda_0^2)a_0^{-2}$ for $a_0^2 \ll 1$ and $L_{pd} \propto (\lambda_p^3/\lambda_0^2)a_0$ for $a_0^2 \geq 1$.

Analytic solutions are unavailable for multidimensional nonlinear regime or for realistic pulse profiles, in these cases we turn to numerical simulations to obtain the plasma response and particle behavior. Such simulations are described in Chapter 5. Although simulations and scaling laws from previous experiments help us choose appropriate laser plasma parameters to obtain beam of certain properties in experiments and to interpret data from experiments, the linear and 1D nonlinear theories still provide useful guides to establish operating regime. Once pump depletion occurs, staging with a fresh pump pulse is necessary.

1.5.3 Electron dephasing

Since the plasma wave travels at the group velocity of the laser $v_g < c$, electrons in the accelerating phase of the wakefield will eventually outrun it and slip into the decelerating phase over a length referred to as the electron dephasing length, L_d [5, 130, 131, 39]. This effect limits the energy gain to the dephasing length.

To evaluate the exact dephasing length requires to know the exact acceleration dynamics. Here we assume that the acceleration dynamics is constant throughout the propagation, we can then develop a lower limit by considering the propagation distance L_d it takes a hypothetical test particle to travel across the accelerating and focusing phase. The slippage is defined by the difference in velocity times the time taken, yielding:

$$\Delta v \frac{L_d}{c} = \frac{\lambda_p}{4}, \tag{1.91}$$

where Δv is the velocity difference between the particle and the wave.

For a particle moving close to c, and the laser traveling at group velocity v_g, $\Delta v = (c - v_g)$, Eq. 1.91 becomes

$$\begin{aligned} c\left[1 - \left(1 - \frac{\omega_p^2}{2\omega_0^2}\right)\right]\frac{L_d}{c} &= \frac{\lambda_p}{4} \\ L_d &= \frac{\lambda_p^3}{2\lambda_0^2}. \end{aligned} \tag{1.92}$$

Notice that for $a_0 \approx 1-2$, the electron dephasing and the pump depletion lengths are nearly equal. This statement assumes that particles are already injected when the laser starts propagating in the plasma and at an energy of several rest mass, i.e. velocity$\approx c$.

The limitation due to dephasing could in principle be overcome by staging the laser-plasma accelerator, such that when the electron bunch outruns the plasma wave, it is re-injected into a new plasma wave at the appropriate phase.

1.5.4 Influence of laser diffraction, pump depletion and electron dephasing on an injector

The acceleration limits have to be taken into account in the design and optimization of present and future LWFA experiments. For example, the production of multi-GeV electron bunches in cm-scale plasmas [132, 133, 15] depends strongly on the properties of the laser-driven plasma wave, more specifically, the plasma-wave velocity which determines the dephasing length, and, hence the maximum energy gain for electrons. In the production of high quality electron bunches with low energy spread and low emittance, one can rely on the phase space rotation when high energy electrons are decelerated once they attain the dephasing length [134].

One of the objectives of our group is to optimize the laser-plasma injector in order to produce a high quality electron beam with narrow energy spread, high charge and low emittance in multi-stage laser-plasma acceleration schemes as described in the frame of the CILEX project [20]. For that, we can first use the acceleration limits based on linear, 1D nonlinear theories and scaling laws of previous experiments or from the phenomenological theory [70] to guide us in choosing laser-plasma parameters, then proceed with PIC simulations to validate the chosen parameters.

Here we'll apply these scaling laws to determine the adapted configuration for an injector that generates an electron beam with energy range between $50 - 200\,\mathrm{MeV}$. We consider the laser parameters of our collaborators at the Lund Laser Center (LLC). This facility delivers a 35 TW Gaussian-shaped laser pulse with $\sim 800\,\mathrm{mJ}$ at the focal plane, an optimized waist of $w_0 = 16\,\mu\mathrm{m}$, a pulse length of $c\tau_L = 10.2\,\mu\mathrm{m}$, a wavelength of $\lambda_0 = 0.8\,\mu\mathrm{m}$. With these parameters, $Z_R \sim 1\,\mathrm{mm}$. We first evaluate the optimum laser-plasma parameters necessary for the trapping of electrons in wakefield using ionization injection scheme. Recall that the two conditions for electron trapping are the normalized vector potential and the plasma wave amplitude:

- an a_0 of 2 to create 6^{th} and 7^{th} nitrogen electrons (see Fig. 1.10),
- a large amplitude plasma wave creates a favorable condition for the trapping of electrons. This is obtained using $k_p w_0 = 2\sqrt{a_0}$, thus the optimum plasma density can be deduced, $n_0 = 8.8 \times 10^{17}\,\mathrm{cm}^{-3}$.

Based on these parameters, we calculate the pump depletion and electron dephasing lengths, giving $L_{pd} \sim L_d \approx 2.2\,\mathrm{cm}$. Once again, the length above is valid only for electrons already injected and at energy of several rest masses (hence velocity $\approx c$). This simple analysis suggests that acceleration of electrons over the longest possible distance, i.e. the dephasing length, requires guiding of the drive pulse beyond Z_R (as $Z_R < L_d$) for our laser parameters.

The maximum energy an electron can gain from the wakefield can be estimated using $\mathcal{E} = eE_{z,avg}L_d$ if the drive pulse is guided. Using 1D nonlinear regime theory, we solve Eq. 1.62 numerically and deduce the average electric field amplitude of the plasma wave, $E_{z,avg}/E_0 \approx 0.6$, with $E_0 = m_e c\omega_p/e$. Assuming that $E_{z,avg}$ stays constant throughout the laser propagation in the plasma, then $\mathcal{E} = 1.2\,\mathrm{GeV}$. However, in the design study of the injector as described in the CILEX project, the specification in terms of electron beam energy is in the range of $50 - 200\,\mathrm{MeV}$, therefore an acceleration length of $\approx 3.6\,\mathrm{mm}$ is sufficient to obtain 200 MeV. The guiding of the drive pulse through laser self-focusing, though hardly controllable, is usually sufficient to attain the required acceleration length because $a_0^2(\omega_p w_0/c)^2 \approx 32$. The analysis here fulfilled the energy requirement for the electron

bunch of the injector, however the energy spread and the emittance are yet to be determined with PIC simulations. Simulations of this sort are included in Chapter 5.

1.5.5 Beam loading

A trapped electron bunch with a relativistically large mass can exert a space charge force and displace plasma electrons which are of relativistically lighter mass and generate its own wakefield. The plasma wave generated by the bunch can significantly modify the fields of the accelerating plasma wave and eventually place severe limitations on the beam current that can be accelerated, and the efficiency of the plasma-based accelerator. This process is known as beam loading [130, 135].

It is insightful to compare the amount of charge that can be loaded in linear and nonlinear plasma waves. Consider a linear plasma wave with an effective area of $\approx c^2/\omega_p^2$, which is required for high efficiency and good beam quality [130], we have

$$\frac{Q_l E_l}{4\pi\epsilon_0 m_e c^2/r_e} = \frac{1}{8\pi}\left(\frac{n_l}{n_0}\right)^2\left(1-\frac{E_l^2}{E_0^2}\right), \tag{1.93}$$

where the subscript l represents quantities in the linear regime, Q_l is the charge, $r_e = e^2/(4\pi\epsilon_0 m_e c^2)$ is the classical electron radius, n_l/n_0 is the normalized density perturbation and in the linear regime $n_l/n_0 \ll 1$. In the nonlinear regime [135], the expression for the charge writes

$$\frac{Q_{Nl} E_{Nl}}{4\pi\epsilon_0 m_e c^2/r_e} = \frac{1}{4^3}\left(k_p r_b\right)^4, \tag{1.94}$$

where the subscript Nl refers to quantities in the nonlinear regime. In the blowout regime, the total accelerating force scales with the fourth power of the blowout radius r_b, i.e a radius $k_p r_b \sim 5$ leads to a total force ~ 1000 times larger than in the linear regime. Written as an engineering formula, Eq. 1.94 reads

$$\frac{Q_{Nl}}{1\mathrm{nC}}\frac{eE_{Nl}}{m_e c\omega_p} \approx 0.047\sqrt{\frac{10^{16}\,\mathrm{cm}^{-3}}{n_p}}\left(k_p r_b\right)^4. \tag{1.95}$$

Although beam loading has limits severely on the energy that trapped relativistic electrons might gain, it has proven to be beneficial to prohibit the injection process in the ionization injection scheme and to reduce the energy spread of the electron beam [107]. More details will be given in Chapter 5.

1.6 Properties of an accelerated electron bunch

Convenient figures of merit for designating the quality of a beam are related to energy spread and emittance.

For a number of potential applications of laser wakefield accelerators, narrow energy spread and low emittance electron bunch are required. For instance, in the hope of building compact high-energy colliders with LWFA [136, 60], the key requirements are electron bunch with low energy spread and high brightness, which in turn requires low emittance [137]. Radiation therapy, more particularly in Very High-Energy Electron Therapy (VHEET) which requires an electron bunch of energy in the range between 50 and 250MeV for treatment of deep-seated tumors ($>$ 10cm) [138, 139], favors narrow energy spread and low emittance

in order to deliver the dose only to a small targeted tumor area [140]. Finally, the quality requirement is even more critical for a prospective LWFA-based free-electron laser (FEL) [141]. The FEL mechanism requires both a small transverse size so as to preserve the high intensity of the bunch and a low divergence for coherence purposes, these two requirements can be again summed up to a low emittance ($< \pi$ mm mrad) [142]. These quantities are defined in the following sections.

1.6.1 Energy spread

There are several ways to define the energy spread. The most commonly used definitions are the root-mean-square (rms) and the full-width at half-maximum (FWHM) if the distribution of the electron bunch can be fitted with the Gaussian distribution.

The rms energy spread, $\Delta\mathcal{E}_{\text{rms}}$ is given by the following expression

$$\Delta\mathcal{E}_{\text{rms}} = \sqrt{\langle(\Delta\mathcal{E} - \langle\Delta\mathcal{E}\rangle)^2\rangle}, \tag{1.96}$$

where $\langle\rangle$ defines the average value of the particle distribution.

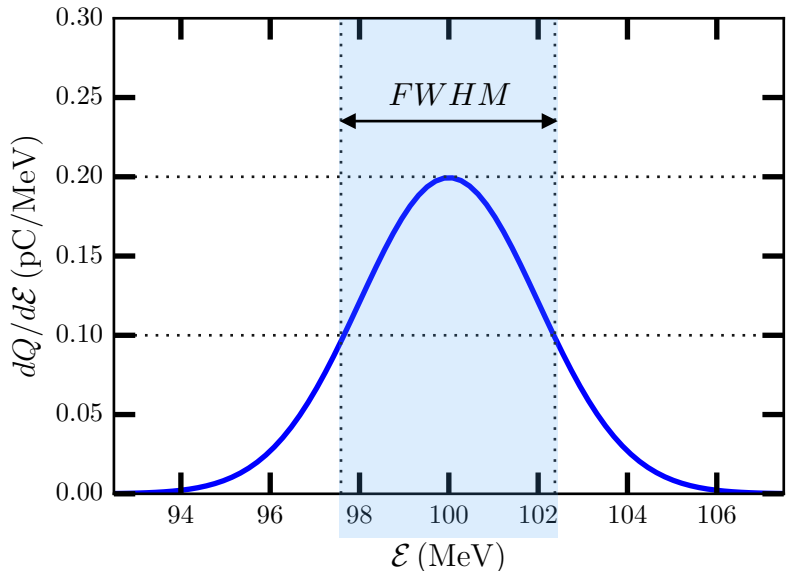

Figure 1.14: Energy spectrum curve $dQ/d\mathcal{E}$ vs. $\mathcal{E}$. This energy spectrum follows a Gaussian distribution function of a mean energy $\langle\mathcal{E}\rangle = 100$ MeV and a standard deviation $\boldsymbol{\sigma} = 2$ MeV. The delimited width in light blue area is the energy spread at full-width at half-maximum (FWHM).

The energy spread at full-width at half-maximum (FWHM) is formally defined by the width of the energy spectrum curve measured between those points on the $y-$axis which are half the maximum amplitude. Fig. 1.14 shows the energy spectrum curve of an electron bunch that follows a Gaussian distribution function. The delimited width in the light blue region indicates the energy spread at FWHM, $\Delta\mathcal{E}_{\text{FWHM}}$. This particular electron bunch shows an energy peaked at $\mathcal{E}_{peak} = 100$ MeV and an energy spread of $\Delta\mathcal{E}_{\text{FWHM}}/\mathcal{E}_{peak} = 4.5\%$. In terms of rms energy spread, we have $\Delta\mathcal{E}_{rms}/\mathcal{E}_{peak} = 3.3\%$. For the rest of the thesis, $\Delta\mathcal{E}_{\text{FWHM}}/\mathcal{E}_{peak}$ will simply be noted as $\Delta\mathcal{E}/\mathcal{E}$.

Energy spread degradation

There are several sources of degradation of the energy spread in the electron injector. The following is not an exhaustive list.

- ***Degradation due to large injection volume***. In ionization injection mechanism, as long as the laser intensity is high enough to produce the 6^{th} and 7^{th} electrons and the wake amplitude large enough for trapping, electrons will be continuously injected into the wakefields. In this case, the global injection volume is large. These electrons might not all be injected at the same phase in the wakefields. The difference in the accelerating force experienced by the front and the back of the bunch will tend to increase the bunch energy spread.
- ***Degradation due to betatron oscillation***. Electron bunch that undergoes strong transverse focusing forces $F_\perp = -m_e c^2 K^2 r$ in plasma waves exhibit betatron oscillation [143] where K is the focusing constant. Individual electrons oscillate with a frequency $\omega_\beta = \omega_p/\sqrt{2\gamma}$ (known as the betatron frequency) and it is dependent on the electron energy. This oscillation results in synchrotron radiation that causes energy loss, since electrons do not all oscillate at the same frequency, some might lose more energy than others, as a result the energy spread degrades.

1.6.2 Emittance

The beam emittance provides a quantitative basis for describing the quality of the beam, its measure is equivalent to the product of the beam width and divergence, where the divergence relates to the velocity spread [144, 145]. By convention, the transverse beam emittance ε is usually represented by an ellipse that contains the whole particle distribution in trace space $(\boldsymbol{x}_\perp, \boldsymbol{x}'_\perp)$, where $\boldsymbol{x}'_\perp = \boldsymbol{p}_\perp/\boldsymbol{p}_\parallel$, such that the trace space area $A = \pi\varepsilon$. In the following, we consider only $x-$direction, all formulas apply equivalently to quantities in $y-$direction.

Since the ellipse equation is written as:

$$\gamma_x^2 + 2\alpha_x x' + \beta_x x'^2 = \varepsilon_x, \tag{1.97}$$

where x and x' are the particle coordinates in the phase space and the coefficients $\alpha_x(z)$, $\beta_x(z)$, $\gamma_x(z)$ are called Twiss parameters, generally related by the geometrical condition:

$$\beta_x\gamma_x - \alpha_x^2 = 1. \tag{1.98}$$

In simulations, we use a statistical approach to evaluate the beam emittance. The definition that we employ is the r.m.s normalized emittance, $\epsilon_{n,rms}$ for which the transverse momentum $p_x = p_z x' = m_e c\beta\gamma x'$ is used instead of the divergence, the equation is written as:

$$\begin{aligned}
\epsilon_{xn,rms} &= \frac{1}{m_e c}\sqrt{\sigma_x^2\sigma_{p_x}^2 - \sigma_{xp_x}^2} \\
&= \frac{1}{m_e c}\sqrt{\langle\widetilde{x}^2\rangle\,\langle\widetilde{p}_x^2\rangle - \langle\widetilde{x}\widetilde{p}_x\rangle^2} \\
&= \sqrt{\langle\widetilde{x}^2\rangle\,\langle\beta^2\gamma^2\widetilde{x}'^2\rangle - \langle\beta^2\gamma^2\widetilde{x}\widetilde{x}'\rangle^2}
\end{aligned} \tag{1.99}$$

Here $\widetilde{x} = x - \langle x\rangle$. The term $\sigma_{xp_x}^2$ reflects a correlation between x and p_x which occurs, for instance when the beam is converging or diverging.

The reason for introducing a normalized emittance is that the divergences of the particles $x' = p_x/p_z$ are reduced during acceleration as p_z increases. Thus, acceleration reduces the "un-normalized emittance", but does not affect the normalized emittance. Assuming a small energy spread within the beam, the normalized and "un-normalized emittances" can be approximated by $\varepsilon_{n,rms} \approx \langle \beta\gamma \rangle \varepsilon_{rms}$. This approximation, which is often used in conventional accelerators, may be strongly misleading when adopted for describing beams with significant energy spread, like those presently produced by LWFA. In [146], the author gave a detailed explanation on the relationship between normalized and "un-normalized emittance".

Emittance degradation

The transverse emittance of electron bunches generated and trapped in laser-wakefield accelerators using ionization injection is given directly by the laser vector potential at ionization [147]. Further emittance growth in the plasma can be due to several factors.

- ***Degradation by finite energy spread***. In Sec. 1.6.1, we mentioned that synchrotron radiation results in growth of energy spread, this in turn will degrade the emittance. As individual electrons rotate around the origin of the (x, p_x) phase space with the betatron frequency, this suggests that low-energy electrons will rotate faster than high-energy electrons in phase space. This difference in frequencies results in an increased emittance at a later time via a phenomenon known as decoherence [148].

- ***Degradation by nonlinear focusing forces***. Nonlinear focusing forces in the transverse directions can degrade emittance. For instance, nonlinear force due to focusing fields of a linear laser plasma waves affect electrons traveling very far from the axis (refer to Fig. 1.3). Note that this does not happen in the blowout regime because the focusing forces are always linear in r and independent of ξ as long as the electrons remain inside the ion cavity. As a consequence, electrons experience different focusing fields depending on their transverse positions, altering their distribution in the phase space, thus degrading the emittance of the electron bunch.

- ***Degradation by direct interaction with the laser pulse***. Direct Laser Acceleration (DLA) where electrons gain energy due to the laser transverse electric field has been demonstrated to be an additional acceleration mechanism [149]. In this configuration, the betatron oscillations of the electrons in the plane of the laser polarization lead to an energy transfer from the laser transverse electric field to the transverse momentum of the electrons [150]. Though DLA brings additional gain to the electron bunch energy, it also increases transverse momentum of the electrons. As a result, this increase in the transverse momentum jeopardizes the emittance of the electron bunch.

Chapter 2

Particle-In-Cell (PIC) Code

We have presented in the previous chapter the main physical processes occurring in LWFA. We have also analyzed these processes through an analytical approach, which can only provide information of qualitative nature. Accurate quantitative analysis or prediction of an experiment can only be obtained via numerical modeling. Due to the complexity of the considered physics, LWFA simulations might require a large amount of computing resources, thus limiting the number of parametric studies. Optimization in both the physical model and numerical solvers has thus become necessary.

In this chapter, we will first introduce the full kinetic approach for LWFA modeling. The following section is devoted to the numerical implementation of this physical model through the Particle In Cell (PIC) method. Then, we address the issue on the reduction of the numerical noise due to the projection on a finite size grid in the standard PIC model through high-order and pseudo-spectral solvers. Finally, we introduce the specific technique of azimuthal Fourier decomposition in a cylindrical geometry that is used for the modeling of the laser-plasma injector.

Contents

2.1 Governing equations

The interaction between a high intensity laser pulse with a plasma has three aspects: the propagation of the laser pulse, the evolution of the charge and current densities induced by the interaction between the laser pulse and the plasma, and the generation of an electromagnetic field by these charge and current densities. In the strong nonlinear regime encountered in the laser-plasma injector, the amplitude of the plasma wakefield can be as large as the laser electric field. The ionization rate of the outer-shell bound electrons, through tunnel ionization, reaches the fs^{-1} rate at laser intensity of about $10^{14}\,\mathrm{W\,cm^{-2}}$, whereas the considered range of maximum laser intensity in LWFA is above $10^{18}\,\mathrm{W\,cm^{-2}}$. The plasma is therefore highly ionized, hence the polarization effect of bound electrons can be safely neglected. Moreover, the loss of laser energy through ionization is also negligible, therefore charge and current densities are only produced by free electrons and ions. The governing equations of our physical system will therefore describe the relations between the electromagnetic fields and the dynamics of free charges (electrons and ions).

2.1.1 Description of the electromagnetic fields

The evolution of the total electromagnetic fields are derived from none other than the Maxwell's equations, as recalled here:

$$\frac{\partial \boldsymbol{B}(\boldsymbol{x},t)}{\partial t} = -\nabla \times \boldsymbol{E}(\boldsymbol{x},t), \tag{2.1}$$

$$\frac{\partial \boldsymbol{E}(\boldsymbol{x},t)}{\partial t} = c^2 \nabla \times \boldsymbol{B}(\boldsymbol{x},t) - \frac{1}{\epsilon_0}\boldsymbol{J}\left(\boldsymbol{x},t\right), \tag{2.2}$$

$$\nabla \cdot \boldsymbol{B}(\boldsymbol{x},t) = 0, \tag{2.3}$$

$$\nabla \cdot \boldsymbol{E}(\boldsymbol{x},t) = \frac{\rho(\boldsymbol{x},t)}{\epsilon_0}, \tag{2.4}$$

where $\boldsymbol{E}$, $\boldsymbol{B}$ are the electric and magnetic fields and ρ, $\boldsymbol{J}$ the local statistical average of the charge and current densities, which can be expressed in terms of the sum over the single-particle distribution of all species:

$$\rho(\boldsymbol{x},t) = \sum_s q_s \int f_s(\boldsymbol{x},\boldsymbol{p},t) d\boldsymbol{p}, \tag{2.5}$$

$$\boldsymbol{J}(\boldsymbol{x},t) = \sum_s q_s \int \boldsymbol{v} f_s(\boldsymbol{x},\boldsymbol{p},t) d\boldsymbol{p}, \tag{2.6}$$

where f_s is the single-particle distribution function of the species s with charge q_s. The velocity $\boldsymbol{v}$ is calculated from the momentum $\boldsymbol{p}$ through $\boldsymbol{v} = \boldsymbol{p}/\gamma_s$, with γ_s the Lorentz factor $\gamma_s = \sqrt{1 + (\boldsymbol{p}/(m_s c))^2}$. In describing the particle dynamics in the injector, the Lorentz factor of the accelerated electrons can be much larger than 1, implying that relativistic effects have to be fully taken into account. Ions, on the other hand, are non-relativistic due to their large mass.

The Maxwell's equations can also be written in an alternative, but equivalent way by introducing the vector and scalar potentials $\boldsymbol{A}$ and ϕ:

$$\boldsymbol{E}(\boldsymbol{x},t) = -\frac{\partial \boldsymbol{A}\left(\boldsymbol{x},t\right)}{\partial t} - \boldsymbol{\nabla} \cdot \phi, \tag{2.7}$$

$$\boldsymbol{B}(\boldsymbol{x},t) = \boldsymbol{\nabla} \times \boldsymbol{A}. \tag{2.8}$$

Combined with the Lorenz gauge $\boldsymbol{\nabla A} + \partial\phi/\partial c^2 t = 0$, the Maxwell's equations yield the standard wave equations for the two potentials:

$$\left(\nabla^2 - \frac{1}{c^2}\frac{\partial^2}{\partial t^2}\right)\boldsymbol{A}\left(\boldsymbol{x},t\right) = -\mu_0 \boldsymbol{J}\left(\boldsymbol{x},t\right), \tag{2.9}$$

$$\left(\nabla^2 - \frac{1}{c^2}\frac{\partial^2}{\partial t^2}\right)\phi\left(\boldsymbol{x},t\right) = -\frac{\rho\left(\boldsymbol{x},t\right)}{\epsilon_0}. \tag{2.10}$$

Although the wave and the Maxwell's equations are physically equivalent, their numerical implementation can be quite different. Furthermore some approximations can be more easily introduced in the wave equations.

The choice of the physical framework is made based on the ratio between some characteristic times (lengths): the laser period $T_L = 2\pi/\omega_0$ (laser wavelength $\lambda_0 = cT_L$), the laser duration τ_L (laser length $l_0 = c\tau_L$), the plasma period $T_p = 2\pi/\omega_p$ (plasma wavelength $\lambda_p = cT_p$) and the characteristic time τ_x related to the change in the laser amplitude during its propagation, defined by $\tau_x = Z_R/c$, Z_R being the Rayleigh length. For the regimes currently explored in the injector, the maximum electron number density is around $10^{19}\,\mathrm{cm}^{-3}$, which is 1000 times smaller than the critical density at $\lambda_0 = 0.8\,\mu$m. Hence, the laser propagates in an underdense plasma and we have $\epsilon_1 = T_L/T_P \ll 1$. To maintain the quasi-resonant condition so that the laser pulse creates a large amplitude of accelerating field, the laser duration should be slightly less than the plasma period: $\tau_L \simeq T_p$, so that $\epsilon_2 = T_L/\tau_L \ll 1$. Using the relation $Z_R = \pi w_L^2/\lambda_L$, one obtains $\varepsilon_3 = \tau_L/\tau_x \simeq T_p/\tau_x \ll 1$. Several approximations, based on $\epsilon_{1,2,3}$ can now be introduced.

With $\epsilon_1 \ll 1$ and $\tau_L \simeq T_p$, one can distinguish two non-overlapping frequency domains: a high frequency domain for the laser angular frequency ω_0 and a low frequency domain for the plasma frequency ω_p. Since $\epsilon_2 \ll 1$, the spectral width of the high frequency field is relatively small: $\delta\omega_{HF}/\omega_L \ll 1$. Taking all these into consideration, one can describe more efficiently the evolution of the laser amplitude by putting aside the high frequency variation of its phase, and using the Slowly Varying Envelope Approximation (SVEA). Under the SVEA approximation, the laser propagation is determined by solving the wave equations as given in Eq. 2.9 for the envelope described by its vector potential. The $\boldsymbol{J}$-term in this equation is determined by calculating the velocity of electrons acted upon by the laser field only. Moreover, as $w_0/\lambda_0 \gg 1$, the paraxial approximation can be combined with the SVEA to simplify the resolution of the wave equation.

The previous paragraph concerns the laser propagation, here we focus on the interaction between the laser and the plasma. The laser ponderomotive force creates charge separation in the plasma, which in turn induces low frequency electromagnetic fields, as derived in the preceding chapter. The evolution of these fields are then determined by solving the Maxwell's equations.

The main advantage of this technique is that the characteristic time for the evolution of the fields is much larger than the laser period, allowing for a large time-step, leading to a large speedup in numerical simulations. This method has been implemented in several numerical codes, such as Inf&rno [28] and Wake [25]. It is well adapted when considering the quasi-linear regime in the low density plasma of a LWFA acceleration stage. When compared with the simulation results produced using Wake [25], we observed that the wave propagation is still well reproduced in most of the considered situations for the laser-plasma injector. Some problems however arise when considering higher plasma densities ($\simeq 10^{19}\,\mathrm{cm}^{-3}$), which have been experimentally investigated at the UHI100 laser facility. At such high densities, non-linear effects such as self-focusing and self-steepening are severe, increasing the values of $\epsilon_{2,3}$

and reducing the validity of the SVEA and the paraxial approximation. For instance, in the case of ionization-injection scheme, the injection process, which can be very fast, generates harmonics of the laser frequency, and the injected electrons can interact continuously with the laser field over large distances. The modeling of such cases by the previous proposed technique (separation of the low and high frequency terms in the electron dynamics) is no longer possible. For these reasons, we have chosen to solve the Maxwell's equations directly to model the laser-plasma injector. In Chapter 4, we will introduce a numerical technique that allows increase, by a large factor, of the numerical time-step, yielding a numerical efficiency comparable to the envelope method, even in the highly nonlinear regime of an injector stage.

2.1.2 Description of the particle dynamics

As shown by Eqs. 2.5-2.6, the single-particle distribution functions $f_s(\boldsymbol{x}, \boldsymbol{p}, t)$ are the basic quantities necessary to determine the source terms of the Maxwell's equations. The characteristics of the accelerated beam is also determined by a single-particle distribution function $f_e(\boldsymbol{x}, \boldsymbol{p}, t)$. When considering the highly nonlinear processes occurring during laser-plasma interaction in the injector, a full kinetic approach is mandatory in order to describe in details the properties of the injected and accelerated electrons. The basic equations are then either the Boltzmann or the Vlasov equations depending on the importance of close collisions. We describe the interaction process in the injector in a domain of a length of the order of a few λ_p. The parameter that defines the importance of collision is thus $\Gamma = (\nu_c/\omega_p)^{-2/3}$, ν_c being the mean electron-ion collision frequency for momentum transfer, Γ is also known as the plasma coupling parameter. As ν_c scales as $n_e/T_e^{3/2}$, where n_e is the electron density and T_e the electron temperature, the domain of strongly correlated plasmas ($\Gamma \geq 1$), is only reached at very high densities, close to the solid one, and at low temperature of a few eV. The operating regime in LWFA is low in density and high in average energies, therefore $\Gamma \ll 1$, consequently collisions are negligible in the interaction process.

An important property of kinetic plasmas ($\Gamma \ll 1$) is that the characteristic length of collective effect is much larger than the average distance between two plasma particles, that is $N_D = n_e \lambda_D^3 \gg 1$, with $\lambda_D = v_{th}/\omega_p$, where N_D is the Debye number, λ_D is the Debye length and v_{th} the average thermal velocity of the electrons. At relativistic velocities, in particular for a perturbation propagating at $c \gg v_{th}$, we obtain $\lambda_D = c/\omega_p = \lambda_p$ yielding $n_e \lambda_p^3 \gg 1$. Note that for $\lambda_0 = 0.8\,\mu$m and at $n_e = 10^{18}\,\mathrm{cm}^{-3}$, which is less than the lowest considered density in the injector, $n_e \lambda_0^3$ is still $\gg 1$. More generally, using λ_D as the characteristic length to represent the variation of the electromagnetic fields inside the plasma of a laser-plasma injector, we can assert that

$$N_D = n_e \lambda_D^3 \gg 1. \tag{2.11}$$

This inequality plays a central role in the numerical scheme described in the following section.

From the previous paragraphs, we have shown that binary collisions are negligible, the Vlasov equation becomes naturally the adapted equation to determine particle distribution functions of free electrons and ions during the interaction of a high intensity laser pulse with the plasma in the injector. The Vlasov equation also should take into account the relativistic effects for electrons and the generation of new particles through tunnel-ionization when considering injection through ionization, represented by the source term G_s. The

Vlasov equation for the function $f_s(\boldsymbol{x}, \boldsymbol{p}, t)$ can be written as

$$\frac{\partial f_s(\boldsymbol{x}, \boldsymbol{p}, t)}{\partial t} + \boldsymbol{v} \cdot \nabla_{\boldsymbol{x}} f_s(\boldsymbol{x}, \boldsymbol{p}, t) + F_s(\boldsymbol{x}, \boldsymbol{p}, t) \cdot \nabla_{\boldsymbol{p}} f_s = G_s(\boldsymbol{x}, \boldsymbol{p}, t), \tag{2.12}$$

where

$$\boldsymbol{v} = \frac{\boldsymbol{p}}{m_s \gamma_s}, \tag{2.13}$$

$$\gamma_s = \sqrt{1 + \left(\frac{\boldsymbol{p}}{m_s c}\right)^2} \tag{2.14}$$

$$F_s(\boldsymbol{x}, \boldsymbol{p}, t) = q_s \left[\boldsymbol{E}(\boldsymbol{x}, t) + \boldsymbol{v} \times \boldsymbol{B}(\boldsymbol{x}, t)\right] \tag{2.15}$$

In Eq. 2.12, the source term G_s is related to tunnel ionization, for which the generated electron is at rest in the reference frame of the parent ion.

From the above equations, it is clear that due to their much lower mass, electrons play the dominant role in the dynamics of the charged particles. Then comes the question of completely neglecting the ion motions, that is to use the so-called Jellium model in which the ion contribution is only introduced through a uniform neutralizing background. However, in the case of the injector, even a small density modification close to the laser propagation axis can induce a non-negligible effect on the characteristics of the accelerated electron beam, which might have a very small transfer size. That is why the dynamics of the ions have also been included in our calculations. In fact, due to their slow motion, the dynamics of the ions introduce only a small additional cost in the numerical modeling.

2.2 Introduction to the PIC method

The numerical implementation of the Maxwell-Vlasov equation solve the following problem: Starting at a given time $t^{(n)}$ at which the state of the physical system is known at specific times $t^{(n')}$ where $t^{(n')} \leq t^{(n)}$, we calculate the new values of the physical parameters at time $t^{(n+1)} = t^{(n)} + \Delta t$, with Δt the time-step, which in the PIC simulation has a constant value.

The greatest strength of the PIC method is that the calculation can be separated into two distinct independent steps:

1. solve the Maxwell's equations for the fields, for known source terms;
2. solve the Vlasov equation in order to derive the evolution of the source terms, for known values of the electromagnetic fields.

In the following sections, we will first describe these two steps independently, then we will show how they are combined in the full PIC calculation.

2.2.1 Numerical implementation of the Maxwell's equations

Within the physical model described in the previous section, all numerical methods introduce a numerical grid in position in order to solve the Maxwell's curl equations given by Eqs. 2.1-2.2. This numerical grid is used either to perform a projection of specific functions within spectral methods, as will be detailed in Chapter 3, or in the more standard finite-difference (Yee) or non-standard finite-difference (NSFD) methods, as will be described in

the present chapter. Here we consider Cartesian coordinates, the cylindrical coordinates will be considered later in Sec. 2.5 and the laser is propagating along the z axis.

The numerical grid is uniform with a cell width of Δx, Δy, Δz. The interaction process is described over a length of L_z of a few λ_p, whereas its duration is given by L_{plasma}/c, where L_{plasma} is the plasma length in the injector. For the laser-plasma injector, $\lambda_p < 50\,\mu$m, whereas L_{plasma} can reach several mm. In order to reduce the spatial domain to be computed, the technique of a moving window is used. This technique consists of a fixed-size simulation box of a few λ_p in length, co-moving at the speed of light like the laser pulse to only describe the interaction process. This is done by adding continuously new cells in the front of the box and destroying the same amount at the back. Note however that within the box, the Maxwell's equations are still solved in the laboratory frame.

The Maxwell's equations are solved on the numerical grid using the Finite-Difference Time-Dependent (FDTD) method, with a second-order accurate explicit solver. This second-order accuracy is obtained by centering the differentiation both in time and in space, implying that both the fields and the charge and current densities are evaluated at specific times, and positions. For the time integration, the leap-frog scheme, shown in Fig. 2.1 is used. In this scheme, the values of the physical parameters are calculated at time $t + \Delta t$, knowing the values of their time derivative at time $t + \Delta t/2$:

$$F\left(\boldsymbol{x}, t + \Delta t\right) = F\left(\boldsymbol{x}, t\right) + \Delta t \left(\frac{\partial F\left(\boldsymbol{x}, \tau\right)}{\partial \tau}\right)_{\tau = t + \Delta t/2}. \tag{2.16}$$

By combining Eq. 2.16 with Eqs. 2.1-2.2, we deduce that the current density and the magnetic field should be calculated at $\Delta t/2$ away from the electric field. Furthermore, from the continuity equation

$$\frac{\partial \rho\left(\boldsymbol{x}, t\right)}{\partial t} = -\boldsymbol{\nabla} \boldsymbol{J}\left(\boldsymbol{x}, t\right), \tag{2.17}$$

it is deduced that the charge density should be evaluated at the same time as the electric field. The global time ordering of the fields and densities is then the one represented in Fig. 2.1. The leap-frog scheme is commonly used since it is fast as compared to other higher-order integration methods (e.g. Runge-Kutta), it is sufficiently accurate for plasma modeling and it allows the separation of the Maxwell's and Vlasov equations.

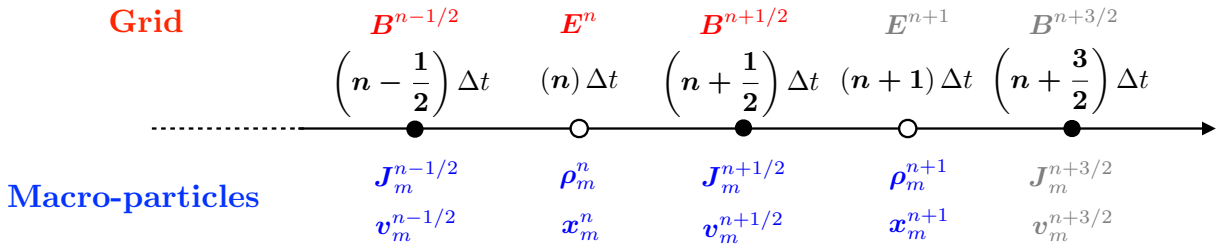

Figure 2.1: Temporal layout of field and macro-particle quantities used in the FDTD treatment of the Maxwell's equations. The known values at the current time-step are colored in red and blue, unknown values are colored in gray. The objective in one time-step calculation is to determine the unknown values from the known ones. Adapted from [67].

In order to get a second-order accuracy for the spatial derivatives in the Maxwell's equation, the fields have to be evaluated at specific positions. These positions are given by the Yee lattice [151], which provides centered spatial derivative, with second-order accuracy. We show this lattice in Fig. 2.2 as an illustration for the TM (transverse magnetic) mode,

$\boldsymbol{k}\cdot\boldsymbol{B}=0$, with $z-$ axis the propagation axis. In this mode only E_z, E_x and B_y components in Cartesian coordinates have non-zero values. Similar approach can be applied in the TE (transverse electric) mode or the TEM (transverse electric and magnetic) mode.

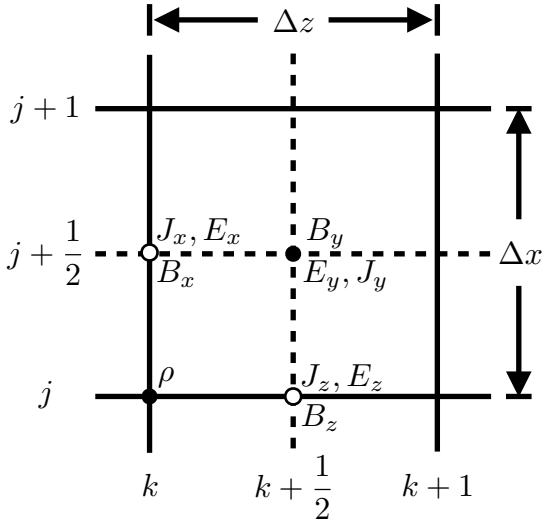

Figure 2.2: Spatial layout of field quantities $\boldsymbol{E}$ and $\boldsymbol{B}$ on the two-dimensional grid, together with the source terms $\boldsymbol{J}$ and ρ.

In the following, we describe the numerical implementation of the explicit forward integration scheme [152, 153, 154] of the Maxwell's equations with the time and spatial layout of Figs. 2.1-2.2 for the TM mode. Let us first introduce some notations to make the writing more tractable. The time derivatives become (for any $\boldsymbol{E}-$ and $\boldsymbol{B}-$fields):

$$(D_t\boldsymbol{E})^{n+1/2}\equiv\frac{\boldsymbol{E}^{n+1}-\boldsymbol{E}^{n}}{\Delta t}, \tag{2.18}$$

$$(D_t\boldsymbol{B})^{n}\equiv\frac{\boldsymbol{B}^{n+1/2}-\boldsymbol{B}^{n-1/2}}{\Delta t}. \tag{2.19}$$

As for the spatial derivatives accurate to the second-order, we have (for any fields and source terms $\boldsymbol{F}$):

$$(D_x\boldsymbol{F})_{j',k'}\equiv\frac{\boldsymbol{F}_{j'+1/2,k'}-\boldsymbol{F}_{j'-1/2,k'}}{\Delta x}, \tag{2.20}$$

$$(D_y\boldsymbol{F})_{j',k'}\equiv\frac{\boldsymbol{F}_{j',k'+1/2}-\boldsymbol{F}_{j',k'-1/2}}{\Delta y}, \tag{2.21}$$

where j' and k' are related to the position in x and z respectively and can be integers or half-integers.

With these notations, the different Maxwell's equations Eqs. 2.1 and 2.2 in the TM mode are written as follows

$$(D_tE_x)^{n+1/2}_{j+1/2,k}=-c^2(D_zB_y+\mu_0J_x)^{n+1/2}_{j+1/2,k}, \tag{2.22}$$

$$(D_tE_z)^{n+1/2}_{j,k+1/2}=c^2(D_xB_y-\mu_0J_z)^{n+1/2}_{j,k+1/2}, \tag{2.23}$$

$$(D_tB_y)^{n+1/2}_{j+1/2,k+1/2}=(D_zE_x-D_xE_z)^{n+1/2}_{j+1/2,k+1/2}. \tag{2.24}$$

Taking Eq. 2.22 as an example, once E_x^n, $B_y^{n+1/2}$ and $J_x^{n+1/2}$ are known, E_x^{n+1} can be determined. Writing the expansion of this equation explicitly leads to

$$E_{x_{j+1/2,k}}^{n+1} = -c^2 \Delta t \left(\frac{B_{y_{j+1/2,k+1/2}}^{n+1/2} - B_{y_{j+1/2,k-1/2}}^{n+1/2}}{\Delta z} + \mu_0 J_{x_{j+1/2,k}}^{n+1/2} \right) + E_{x_{j+1/2,k}}^{n}. \tag{2.25}$$

The update of fields $\boldsymbol{E}$ and $\boldsymbol{B}$ alternates, beginning with $\boldsymbol{E}$, then $\boldsymbol{B}$, as shown in Fig. 2.1.

2.2.2 Numerical implementation of the Vlasov equation

Knowing the electromagnetic fields in the plasma, the dynamics of the free plasma electrons and ions is given by the equations Eqs. 2.12-2.15. Since the electromagnetic fields are evaluated only at specific positions on the numerical grid, it is tempting to evaluate the single-particle distribution function $f_s(\boldsymbol{x}, \boldsymbol{p}, t)$ on the same position grid. This implies that the velocities are also calculated on the numerical grid to cover the full 6 dimensions of the phase space. In fact, this approach is known as the Vlasov calculations and it has been implemented in [155, 156]. These Vlasov simulations are proven to be almost noise-free, however they are very time consuming, even one-dimensional problems require the use of parallel computers. The reason why these simulations are computationally heavy is depicted in Fig. 2.3(a). It shows a phase space (x, p_x). The shaded area represents the region occupied by plasma particles, where the associated two-dimensional distribution function $f(x, p_x)$ is non-zero whereas the unshaded area is void of particles.

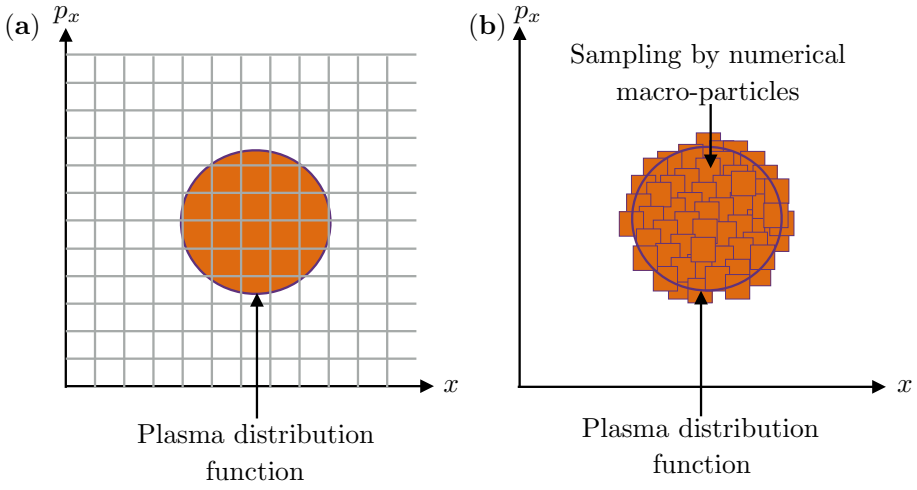

Figure 2.3: Kinetic plasma simulations: (a) Vlasov method, using an Eulerian grid in the phase space; (b) PIC method, sampling by numerical particles to mark the distribution function.

In the Vlasov method, one has to process these empty regions and maintain them as parts of the numerical arrays, leading to a waste of computational time and computer memory. This problem has been partially solved using sophisticated numerical methods, such as the used of an adaptive phase-space grid [156]. Nevertheless, as the efficiency of the Vlasov method reduces exponentially with the number of dimensions, presently only 1D and 2D Vlasov simulations have been proposed. To perform a calculation in a 3D position space, which is mandatory for the modeling of the injector in LWFA, a more computationally effective method has to be used.

Looking at the Vlasov equation Eq. 2.12, for a fixed value of the electromagnetic fields, it is identical to the Louiville's equation of charged particles moving in an external electromagnetic field excluding the source term. However, in order to make the connection with the Maxwell's equations in which the values of the charge and current densities are required on the numerical grid, the point-like particles have to be replaced by the so called macro-particles, which should have a size larger or equal to the dimension of the grid cells. This is the basic feature of the Particle In Cell (PIC) method [153, 157]. Therefore, in a PIC calculation, the single-particle distribution functions of the charged particles are written as

$$f_s\left(\boldsymbol{x},\boldsymbol{p},t\right)=\sum_{m=1}^{N_s(t)} w_{s,m} S\left[\boldsymbol{x}-\boldsymbol{x}_m(t)\right]\delta\left[\boldsymbol{p}-\boldsymbol{p}_m(t)\right]. \tag{2.26}$$

In this equation, $S(\boldsymbol{x}-\boldsymbol{x}_m)$ is the shape factor or the support function centered at the position of the macro-particle, $w_{s,m}$ is the weight of the macro-particles, and $N_s(t)$ is the total number of macro-particles in the considered interaction domain. In order to simplify the calculation, the shape factor is a fixed function, which is identical for all macro-particles of all species and is normalized through the relation

$$\int S(\boldsymbol{x}-\boldsymbol{x}_m)d\boldsymbol{x}=1. \tag{2.27}$$

In Eq. 2.26, the $\delta\left[\boldsymbol{p}-\boldsymbol{p}_m(t)\right]$ term ensures that there is no deformation of $S(\boldsymbol{x}-\boldsymbol{x}_m)$ during the propagation. The weighting factor $w_{s,m}$ can depend on the species and also on the spatial position at which the macro-particle is created. In particular, it is through $w_{s,m}$ that the longitudinal and transverse density profile of the plasma can be taken into account.

The introduction of Eq. 2.26 in the Vlasov equation Eq. 2.12 yields

$$\begin{aligned}
&\left\{\frac{dN_s}{dt}w_{s,N_s}S\left[\boldsymbol{x}-\boldsymbol{x}_{N_s}(t)\right]\delta\left[\boldsymbol{p}-\boldsymbol{p}_{N_s}(t)\right]-G_s\left(\boldsymbol{x},\boldsymbol{p},t\right)\right\}\ldots\\
&\ldots+\left\{\sum_{m=1}^{N_s(t)} w_{s,m}\left(\boldsymbol{v}-\dot{\boldsymbol{x}}_m\right)\boldsymbol{\nabla}_{\boldsymbol{x}}S\left[\boldsymbol{x}-\boldsymbol{x}_m(t)\right]\delta\left[\boldsymbol{p}-\boldsymbol{p}_m(t)\right]\right\}\ldots\\
&\ldots+\left\{\sum_{m=1}^{N_s(t)} w_{s,m}\left(F_s\left(\boldsymbol{x},\boldsymbol{p},t\right)-\dot{\boldsymbol{p}}_m\right)S\left[\boldsymbol{x}-\boldsymbol{x}_m(t)\right]\boldsymbol{\nabla}_{\boldsymbol{p}}\delta\left[\boldsymbol{p}-\boldsymbol{p}_m(t)\right]\right\}=0.
\end{aligned} \tag{2.28}$$

In Eq. 2.28, the first bracket indicates that the variation of the number of macro-particles is given by the source term, G_s. For tunnel-ionization, which is the only source term considered here, the electron is generated at zero velocity in the reference of the parent ion. Besides, the total charge is conserved during the ionization process:

$$\sum_s q_s S_s\left(\boldsymbol{x},\boldsymbol{p},t\right)=0 \tag{2.29}$$

Therefore, a parent macro-particle with a weight w, corresponding to the ion with a charge q, that goes through a tunnel-ionization process will be destroyed and a new pair of electron-ion macro-particle will be created, both the new macro-particles will have the same weight and the ion will have a charge of $q+1$.

In the second bracket of Eq. 2.28, the presence of the $\delta\left[\boldsymbol{p}-\boldsymbol{p}_m(t)\right]$ yields

$$\frac{d}{dt}\boldsymbol{x}_m=\boldsymbol{v}_m=\frac{\boldsymbol{p}_m}{m_s\gamma_{s,m}} \tag{2.30}$$

Considering now the last bracket of Eq. 2.28, due to the fact the force F_s depends on the position and the shape factor has a finite size, the expression $F_s(\boldsymbol{x}, \boldsymbol{p}, t) - d\boldsymbol{p}_m/dt$ cannot cancel exactly. An optimized value of $d\boldsymbol{p}_m/dt$ is obtained by integration over space, yielding

$$d\boldsymbol{p}_m/dt = \bar{\boldsymbol{F}}_s \tag{2.31}$$

$$\bar{\boldsymbol{F}}_s = \bar{\boldsymbol{E}}(\boldsymbol{x}_m) + \boldsymbol{v}_m \times \bar{\boldsymbol{B}}(\boldsymbol{x}_m), \tag{2.32}$$

$$\bar{\boldsymbol{E}}(\boldsymbol{x}_m) = \int d\boldsymbol{x}\, S(\boldsymbol{x} - \boldsymbol{x}_m)\boldsymbol{E}(\boldsymbol{x}), \tag{2.33}$$

$$\bar{\boldsymbol{B}}(\boldsymbol{x}_m) = \int d\boldsymbol{x}\, S(\boldsymbol{x} - \boldsymbol{x}_m)\boldsymbol{B}(\boldsymbol{x}). \tag{2.34}$$

In order to reduce the error introduced by the difference between $\boldsymbol{F}_s$ and $\bar{\boldsymbol{F}}_s$ the size in each direction of the shape factor should be much less than that of the characteristic length for field variation along this direction. In addition, because the single-particle distribution represents a statistical average over the particle trajectories, the size of the shape function should also be large compared to the average distance between two plasma particles. These two conditions are in fact compatible in our case of a kinetic plasma, thanks to the condition established by Eq. 2.11 given in the previous section.

In order to be consistent with the numerical treatment of the Maxwell's equations, the trajectory of the macro-particles are determined by solving the two equations of motion as given by Eq. 2.30 in the second-order time-centered leap-frog scheme:

$$\boldsymbol{x}_m(t + \Delta t) = \boldsymbol{x}_m(t) + \left(\frac{\boldsymbol{p}_m}{m_s \gamma_{s,m}}\right)(t + \Delta t/2)\,\Delta t \tag{2.35}$$

$$\boldsymbol{p}_m(t + \Delta t) = \boldsymbol{p}_m(t) + \bar{\boldsymbol{F}}_s(t + \Delta t/2)\,\Delta t \tag{2.36}$$

2.2.3 Overview of the global PIC algorithm

We have seen in the two previous sections, the numerical implementation of the Maxwell and Vlasov equations in two separated steps. We now show how these two steps are combined to perform a full PIC calculation. It begins with the relation in the spatial domain and then the time ordering of the various equations. To make the notation less cluttered, we use the word "particles" to refer to macro-particles in the rest of the thesis. In this section, we keep the same definition of the spatial domain which is 2D Cartesian coordinates in the (x, z) plane, and the laser propagates along the $z-$axis.

Interpolation between the grid and the particle positions

In the numerical treatment of the Maxwell's equations, the charge and current densities, as well as the electromagnetic fields are evaluated on the numerical grid, whereas for the Vlasov equation, all quantities are calculated at the particle position. There is thus a need to make an interpolation between these two spatial frameworks and this interpolation should be consistent with the shape function $S(\boldsymbol{x} - \boldsymbol{x}_m)$ of the particles. In most PIC codes, this shape function is written as a product of one-dimensional functions. In our case it gives

$$S(\boldsymbol{x} - \boldsymbol{x}_m) = S_x(x - x_m)\, S_z(z - z_m) \tag{2.37}$$

$$\int S_{x,z}(\tau)\, d\tau = 1, \tag{2.38}$$

so that the projection can be performed independently in both directions. Moreover, for symmetry reason, S_x and S_z should be odd functions. Note however that S_x and S_z are not necessarily equal.

Consider the grid positions $\boldsymbol{x}_{j,k} = (j\Delta x, k\Delta z)$ and $P_{j,k}(\boldsymbol{x}_m)$ the projector that will allow calculation of the charge and current densities from the particles through the relations

$$\rho_{j,k} = \frac{1}{V_{cell}} \sum_s q_s \sum_{m=1}^{N_s} w_{s,m} P_{j,k}(\boldsymbol{x}_m) \tag{2.39}$$

$$\boldsymbol{J}_{j,k} = \frac{1}{V_{cell}} \sum_s q_s \sum_{m=1}^{N_s} w_{s,m} \boldsymbol{v}_m P_{j,k}(\boldsymbol{x}_m), \tag{2.40}$$

where $V_{cell} = \Delta x \Delta z$ is the area of the cell of the numerical grid. From Eqs. 2.37-2.38, we can deduce that

$$P_{j,k}(\boldsymbol{x}_m) = P_j(x_m) P_k(z_m), \tag{2.41}$$

and

$$\sum_j P_j(x_m) = \sum_k P_k(z_m) = 1. \tag{2.42}$$

A straightforward solution to determine the projectors is obtained by integrating the shape function around the grid-points on a length given by the cell width :

$$P_j(x_m) = \int_{x_j - \Delta x/2}^{x_j + \Delta x/2} S_x(x - x_m)\, dx \tag{2.43}$$

$$P_k(z_m) = \int_{z_k - \Delta z/2}^{z_k + \Delta z/2} S_z(z - z_m)\, dz, \tag{2.44}$$

these equations satisfy Eq. 2.42.

In a similar way, in order to solve the equation of motion Eq. 2.31, one needs to determine the average fields of Eqs. 2.33-2.34 acting on the particle from their values on the grid.

Following the same procedure as above, we get

$$\bar{\boldsymbol{E}}(\boldsymbol{x}_m) = \sum_{j,k} P_j(x_m) P_k(z_m) \boldsymbol{E}_{j,k} \tag{2.45}$$

$$\bar{\boldsymbol{B}}(\boldsymbol{x}_m) = \sum_{j,k} P_j(x_m) P_k(z_m) \boldsymbol{B}_{j,k}, \tag{2.46}$$

where the functions P_j and P_k are given by Eqs. 2.43-2.44. It is important to note that the projectors used in Eqs. 2.45-2.46 for the projection from the grid to the particles positions are the same as those used in Eqs. 2.39-2.40 for the interpolation from the particle positions to the grid. Otherwise, the asymmetry will introduce nonphysical self-generated fields. In other words, without a symmetrical procedure, a particle can be accelerated by the generated field of its own.

It remains now to specify the optimal size and form of the shape functions. We have seen that this size should be small compared with the characteristic length of the field variation. This is also true in the FDTD approach for the width of the numerical cell because to calculate the derivative, we use the first-order expansion in Eqs. 2.20-2.21. Therefore the size of the shape function should be of the same order as the size of the numerical cell. However there are two additional considerations that have to be taken into account: (i) As

will be discussed in detailed later, the value of the time-step is mainly related to the cell dimension in the direction of laser propagation. As a consequence, in many situations, the constraint in the time-step imposes a much smaller cell size in the propagation direction than in the transverse ones (see Chapter 4). Thus in the propagation direction, the shape function can be significantly larger than the cell size. (ii) The motions of the finite number of particles provoke a statistical fluctuation both in the charge and the current densities, which in turn introduce a fluctuation into electromagnetic fields and then the force acting on the particles. This fluctuation is due to the fact that depending on the form of the shape function, the derivative $\partial^n P_{j,k}(\tau)/\partial\tau^n$ can become infinite at some specific positions. The importance of these fluctuations, also called numerical noise, can be reduced by increasing the number of particles. However a general rule in statistics is that the amplitude of the noise scales only as the inverse of the square root of the number of particles. Hence, a more efficient way to reduce the numerical noise, can be to increase the ratio between the size of the shape function and of the numerical cell, and to choose a form so that the lowest orders derivative of the projector are continuous everywhere.

In a finite-difference solver, the order of the derivative is directly related to the number of invoked points in the grid, that is the ratio between the size of the cell function and the one of the numerical cell. Consequently, one or more grid cells that are of the immediate neighborhood of the particles will contribute to the interpolation. Several canonical expressions for S can be found in [157, 153]. They include the Nearest-Grid-Point (NGP) method, also known as the zero-order weighting; the Cloud-In-Cell (CIC) method, also known as the first-order weighting or area weighting; the Triangular-Shaped density Cloud (TSC). Below we present the expression for the 1D shape function S_x for the three cases.

The simplest shape factor to assign the weight of the fields to the particles is to assign to its nearest-grid-point. For this method, the expression of the assignment function S_x writes:

$$S_x(u) = \begin{cases} 1 & \text{if } \left|\frac{u}{\Delta x}\right| < \frac{1}{2}, \\ 0 & \text{otherwise.} \end{cases} \tag{2.47}$$

The NGP method introduces a discontinuity in field assignment to the particles, it is therefore seldom used.

The CIC method gives a better approximation at the cost of number of arithmetic operations per particle per time-step as compared to the NGP method. The improvement of accuracy is brought about by assigning two grid-points rather than one. The corresponding assignment function S_x writes

$$S_x(u) = \begin{cases} 1 - \left|\frac{u}{\Delta \boldsymbol{x}}\right| & \text{if } \left|\frac{u}{\Delta x}\right| < 1, \\ 0 & \text{otherwise.} \end{cases} \tag{2.48}$$

In the CIC method, the discontinuity in the projection occurs only at the first derivation level.

The TSC method further improves the accuracy of interpolation of field quantities to particles. It involves the contribution of three grid-points, implying that the cost of number of arithmetic operations per particle per time-step is higher than in the CIC method. The expression of its assignment function writes

$$S_x(u) = \begin{cases} \frac{3}{4} - \left|\frac{u}{\Delta x}\right|^2 & \text{if } \left|\frac{u}{\Delta x}\right| \leq \frac{1}{2}, \\ \frac{1}{2}\left(\frac{3}{2} - \left|\frac{u}{\Delta x}\right|\right)^2 & \text{if } \frac{1}{2} < \left|\frac{u}{\Delta x}\right| \leq \frac{3}{2}, \\ 0 & \text{otherwise.} \end{cases} \tag{2.49}$$

Here we see that the discontinuity occurs only at the second-order level. The choice of the interpolation method depends on the average number of particles per numerical cell. In some situations, the single-particle distribution function has locally a very broad energy spectrum, hence a large number of particles are already required to describe the phase space. In that case, a priori one does no need to introduce a high-order interpolation scheme. In other situations, in particular when the cell width is much smaller than the characteristic size of field variations, the number of particles per cell can be limited, which implies using a high-order interpolation procedure for reducing the numerical noise. In our simulations, we have used either the CIC or the TSC methods, depending on the considered cases.

PIC time cycle

We have shown the procedure in PIC calculations that links the particle quantities and quantities on the numerical grid in the spatial domain. Here we address the question of the time ordering of the two systems of equations. We will show that one of the greatest strengths of the PIC method is that it yields to four independent routines, that can be performed sequentially at each time-step, as shown in Fig. 2.4.

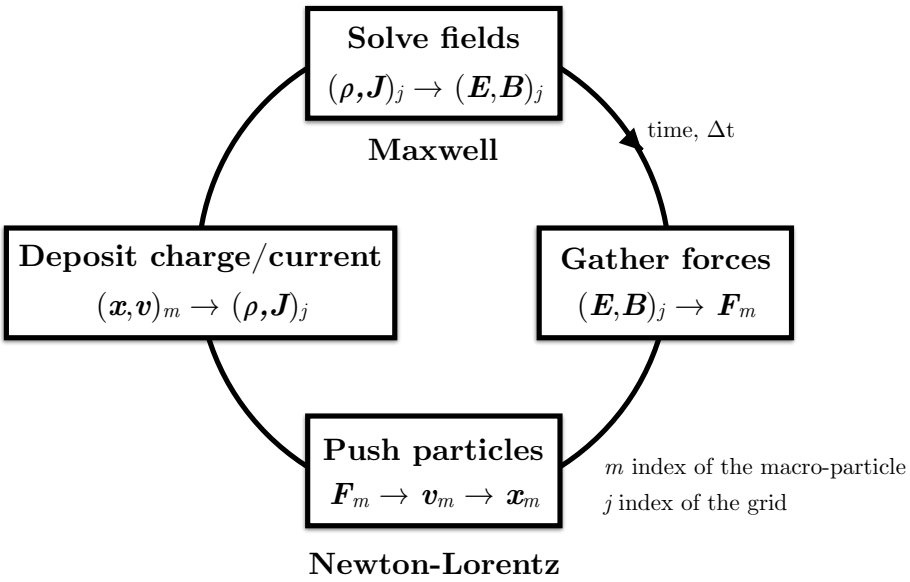

Figure 2.4: The PIC cycle: Illustration of four components that constitute one time-step. The particles are numbered $m = 1, 2 \ldots$; the grid index is j, which becomes vectors in two and three dimensions.

We start at a given time-step n corresponding to the situation indicated by red and blue quantities in Fig. 2.1. The electric fields $\boldsymbol{E}^n$ is known at the time $t^n = n\Delta t$, while the magnetic fields $\boldsymbol{B}^{n-1/2}$ and $\boldsymbol{B}^{n+1/2}$ are known at times $t^{n\pm1/2} = (n \pm 1/2)\Delta t$. For both fields, their values are evaluated on the Yee spatial grid represented in Fig. 2.2. To be consistent with the times related to the charge and the current densities indicated in Fig. 2.1, we assume that the position of the particles $\boldsymbol{x}_m^n$ and $\boldsymbol{x}_m^{n+1}$ are known at t^n and t^{n+1} while their velocities $\boldsymbol{v}_m^{n\pm1/2}$ are known at $t^{n\pm1/2}$.

Based on Fig. 2.4, we will go through each routine one at a time.

- ***Deposit charge/current***. The first step of the calculation is to determine the values of the charge density ρ^n, ρ^{n+1} and the current density $\boldsymbol{J}^{n\pm1/2}$ at specific positions on

the Yee grid from the particle positions and velocities using the projection formulas as given by Eq. 2.39 and Eq. 2.40.

- ***Solve fields***. All the required quantities are now known in order to solve the Maxwell's equations (Eqs. 2.22-2.24), from which we deduce the values of $\boldsymbol{E}^{n+1}$ and of $\boldsymbol{B}^{n+3/2}$.

- ***Gather forces***. We interpolate the values of the fields from the Yee grid to the particle positions, through the projection formulas Eqs. 2.45-2.46. To use the leap-frog scheme for the evolution of the particle velocity from time $t^{n+1/2}$ to time $t^{n+3/2}$, one needs to calculate the force at the time t^{n+1}. For that, we need the values of both $\bar{\boldsymbol{E}}^{n+1}(\boldsymbol{x}_m^{n+1})$ and of $\bar{\boldsymbol{B}}^{n+1}(\boldsymbol{x}_m^{n+1})$. For $\boldsymbol{B}^{n+1}$ we use the time average value $\boldsymbol{B}^{n+1} = (\boldsymbol{B}^{n+1/2} + \boldsymbol{B}^{n+3/2})/2$. To illustrate this procedure we show the corresponding formulas in a 2D Cartesian Yee lattice:

$$\begin{aligned}\bar{\boldsymbol{E}}^{n+1}(\boldsymbol{x}_m^{n+1}) = \sum_{j,k} \Big[& P_{j+\frac{1}{2},k}(\boldsymbol{x}_m^{n+1}) E_{x_{j+\frac{1}{2},k}}^{n+1} \boldsymbol{e_x} + P_{j,k}(\boldsymbol{x}_m^{n+1}) E_{y_{j,k}}^{n+1} \boldsymbol{e_y} \\ & + P_{j,k+\frac{1}{2}}(\boldsymbol{x}_m^{n+1}) E_{z_{j,k+\frac{1}{2}}}^{n+1} \boldsymbol{e_z} \Big], \end{aligned} \tag{2.50}$$

$$\begin{aligned}\bar{\boldsymbol{B}}^{n+1}(\boldsymbol{x}_m^{n+1}) = \sum_{j,k} \frac{1}{2} \Big[& P_{j,k+\frac{1}{2}}(\boldsymbol{x}_m^{n+1}) \left(B_{x_{j,k+\frac{1}{2}}}^{n+\frac{1}{2}} + B_{x_{j,k+\frac{1}{2}}}^{n+\frac{3}{2}} \right) \boldsymbol{e_x} \\ & + P_{j+\frac{1}{2},k+\frac{1}{2}}(\boldsymbol{x}_m^{n+1}) \left(B_{y_{j+\frac{1}{2},k+\frac{1}{2}}}^{n+\frac{1}{2}} + B_{y_{j+\frac{1}{2},k+\frac{1}{2}}}^{n+\frac{3}{2}} \right) \boldsymbol{e_y} \\ & + P_{j+\frac{1}{2},k}(\boldsymbol{x}_m^{n+1}) \left(B_{z_{j+\frac{1}{2},k}}^{n+\frac{1}{2}} + B_{z_{j+\frac{1}{2},k}}^{n+\frac{3}{2}} \right) \boldsymbol{e_z}. \end{aligned} \tag{2.51}$$

- ***Push particles***. Once the fields $\bar{\boldsymbol{E}}^{n+1}(\boldsymbol{x}_m^{n+1})$ and of $\bar{\boldsymbol{B}}^{n+1}(\boldsymbol{x}_m^{n+1})$ are determined at time t^{n+1}, it remains to calculate $\boldsymbol{v}_m^{n+\frac{3}{2}}$ and $\boldsymbol{x}_m^{n+2}$ of the particles using Eqs. 2.35 - 2.36. With the notation $\boldsymbol{u} = \boldsymbol{p}/m_s = \gamma_{s,m}\boldsymbol{v}$, we obtain

$$\frac{\boldsymbol{u}_m^{n+\frac{3}{2}} - \boldsymbol{u}_m^{n+\frac{1}{2}}}{\Delta t} = \frac{q}{m} \left(\bar{\boldsymbol{E}}^{n+1}(\boldsymbol{x}_m^{n+1}) + \frac{\boldsymbol{u}_m^{n+\frac{3}{2}} + \boldsymbol{u}_m^{n+\frac{1}{2}}}{2\gamma_{s,m}^{n+1}} \times \bar{\boldsymbol{B}}^{n+1}(\boldsymbol{x}_m^{n+1}) \right), \tag{2.52}$$

where $(\gamma_{s,m}^{n+1})^2 = 1 + (\boldsymbol{u}^{n+1}/c)^2$, with $\boldsymbol{u}^{n+1} = (\boldsymbol{u}^{n+3/2} + \boldsymbol{u}^{n+1/2})/2$. Notice that Eq. 2.52 is implicit. The name 'implicit' arises because $\boldsymbol{u}^{n+3/2}$ appears on both sides of the equation. Hence, one way of solving Eq. 2.52 is by using an implicit method. However, as pointed out in [152], while calculating the trajectory of particles in the presence of constant $\bar{\boldsymbol{E}}-$ and $\bar{\boldsymbol{B}}-$fields, the orbits generated by this algorithm are not exact, a correction to the $\bar{\boldsymbol{E}} \times \bar{\boldsymbol{B}}$ drift is expected. Boris [152] introduced another method that separates the electric and magnetic forces completely by substituting

$$\boldsymbol{u}^{n+\frac{1}{2}} = \boldsymbol{u}^{-} - \frac{q\bar{\boldsymbol{E}}^{n+1}\Delta t}{2m}, \tag{2.53}$$

$$\boldsymbol{u}^{n+\frac{3}{2}} = \boldsymbol{u}^{+} + \frac{q\bar{\boldsymbol{E}}^{n+1}\Delta t}{2m}. \tag{2.54}$$

Putting these equations into Eq. 2.52, $\boldsymbol{E}^n$ is eliminated completely, leaving

$$\frac{\boldsymbol{u}^{+} - \boldsymbol{u}^{-}}{\Delta t} = \frac{q}{2\gamma_{s,m}^{n} m_s} \left(\boldsymbol{u}^{+} + \boldsymbol{u}^{-} \right) \times \bar{\boldsymbol{B}}^{n+1}, \tag{2.55}$$

This equation is the discretized version of an equation of motion describing the rotation about an axis parallel to $\bar{\boldsymbol{B}}^{n+1}$ with a uniform angular velocity. It can then be solved exactly. The following steps to compute $\boldsymbol{u}^{n+3/2}$ are then:

- add half the $\boldsymbol{E}-$field to $\boldsymbol{u}^{n+1/2}$ using Eq. 2.53 to obtain $\boldsymbol{u}^{-}$,
- rotate $\boldsymbol{u}^{-}$ according to Eq. 2.55 to obtain $\boldsymbol{u}^{+}$,
- add the remaining half of the $\boldsymbol{E}-$field to $\boldsymbol{u}^{+}$ using Eq. 2.54 to obtain $\boldsymbol{u}^{n+1/2}$.

The drawback of this method arises if we apply a constant non-zero $\boldsymbol{E}-$ and $\boldsymbol{B}-$fields in such a way that their mutual contributions cancel, i.e. $\boldsymbol{E} + \boldsymbol{u} \times \boldsymbol{B}/\gamma = 0$. Using the Boris method, it is found that the particle undergoes a spurious force in the case where $\boldsymbol{E} \neq 0$ and $\boldsymbol{B} \neq 0$. In response, Vay has proposed a method to mitigate this effect (refer to [158] for more details).

Regardless of the method used to obtain $\boldsymbol{u}^{n+3/2}$, the position is then updated from the velocity $\boldsymbol{v}^{n+3/2} = \boldsymbol{u}^{n+3/2}/\ \gamma^{n+3/2}$, with $(\gamma^{n+\frac{3}{2}})^2 = 1 + (\boldsymbol{u}^{n+\frac{3}{2}}/c)^2$ by applying Eq. 2.35, giving

$$\boldsymbol{x}^{n+2} = \boldsymbol{x}^{n+1} + \boldsymbol{v}^{n+\frac{3}{2}}\Delta t. \tag{2.56}$$

After having calculated Eq. 2.35, all physical quantities are now determined at time $t + \Delta t$. The calculation can then further continue by repeating the four steps described in this section. This constitutes the PIC time cycle, as shown in Fig. 2.4.

The presented PIC cycle can lead to nonphysical errors because, due to discretization, the continuity equation ($\partial_t \rho + \nabla \cdot \boldsymbol{J} = 0$) is not exactly satisfied. The scheme is therefore not charge conserving, leading to a possible accumulation of errors during the interaction process. To resolve this, Marder has introduced an added term known as the "pseudo-current" [159], $\boldsymbol{F}$ in the Maxwell-Ampere equation to correct the buildup of error. This term is defined as $\boldsymbol{F}(\boldsymbol{x}, t) = \nabla \cdot \boldsymbol{E} - \rho$. For the numerical solution, Maxwell-Ampere equation Eq. 2.2 is thus altered to include the "pseudo-current" as a correction term. Another method to conserve charge in the PIC method is by the Esirkepov algorithm [160], which is the generalization of the method developed by Villasenor and Buneman [161]. This algorithm calculates $\boldsymbol{J}_{j,k}^{n+1/2}$ knowing $\rho_{j,k}^{n+1}$. In Villasernor and Buneman, CIC particle shape factor is assumed whereas in the Esirkepov's method, it is extended to any arbitrary particle shape factor assuming that the particle trajectory over one time-step is linear.

In one-time cycle of the PIC calculation, some recurrence relations are used involving values defined at several previous times. The question then arises on how to initialize the calculation at the initial time $t = 0$. In fact this problem is greatly simplified by starting the calculation in vacuum, at some distances before the entrance into the plasma. However, even in vacuum, the initialization process is not trivial because the analytical formula for the laser amplitude that are usually applied, i.e. of a Gaussian pulse, are not exact solutions of the Maxwell's equations and even less of its discretized form. In Warp, an original method has been implemented to solve this problem. The input field is first transcribed as a source term of current density, and the field generated by this source is directly determined from the Maxwell's equation.

Accuracy and stability of the time integration scheme

By studying how the plane electromagnetic waves are reproduced in the vacuum, i.e. we consider the source terms without the self-consistent dynamics of the charged particles,

therefore $\boldsymbol{J} = 0$ in the Maxwell-Ampere's equation, one could have an insight on the accuracy and stability of the FDTD solver used in the PIC simulation. This type of study is known as the numerical dispersion analysis.

The procedure for the numerical dispersion analysis involves substitution of plane monochromatic traveling-wave trial solution into the discretized Maxwell's equations Eqs. 2.22-2.24. After some algebraic manipulation, an equation will be derived that relates the numerical wave-vector components, k, the wave frequency, ω, and the grid space and time increments, $\Delta\boldsymbol{x}$ and Δt respectively. This equation, also known as the numerical dispersion relation is then numerically solved for several different sets of grid discretization, wave-vector, and wave frequency to illustrate the key nonphysical modeling results associated with numerical dispersion.

Assuming that the fields are of the form $(\boldsymbol{E}, \boldsymbol{B}) = (\boldsymbol{E}_0, \boldsymbol{B}_0)\exp(i\boldsymbol{k}\cdot\boldsymbol{x} - i\omega t)$. For the following demonstration, we take TM mode as an example, same results are obtained in other electromagnetic modes, i.e. TE and TEM modes. In the TM mode, the discretized monochromatic traveling-wave trial solutions yield

$$E_{x}{}^{n}_{j,k} = E_{x_0}\exp\left(i\omega n\Delta t - i(k_x\Delta x + k_z\Delta z)\right), \tag{2.57}$$

$$E_{z}{}^{n}_{j,k} = E_{z_0}\exp\left(i\omega n\Delta t - i(k_x\Delta x + k_z\Delta z)\right), \tag{2.58}$$

$$B_{y}{}^{n}_{j,k} = B_{y_0}\exp\left(i\omega n\Delta t - i(k_x\Delta x + k_z\Delta z)\right), \tag{2.59}$$

where k_x and k_z are, respectively, the $x-$ and $z-$components of the wavenumbers, j and k being, respectively, the indices specifying the sampling points in the $x-$ and $z-$directions. Substituting the traveling-wave expressions into the difference equations Eqs. 2.22-2.24 and considering propagation in vacuum, one gets

$$E_{z_0} = -\frac{c^2\Delta t}{\Delta x}B_{y_0}\frac{\sin(k_x\Delta x/2)}{\sin(\omega\Delta t/2)}, \tag{2.60}$$

$$E_{x_0} = -\frac{c^2\Delta t}{\Delta z}B_{y_0}\frac{\sin(k_z\Delta z/2)}{\sin(\omega\Delta t/2)}, \tag{2.61}$$

$$B_{y_0} = \Delta t\left(E_{x_0}\frac{\sin(k_z\Delta z/2)}{\Delta z} - E_{z_0}\frac{\sin(k_x\Delta x/2)}{\Delta x})\right). \tag{2.62}$$

Upon substituting E_{z_0} of Eq. 2.60 and E_{x_0} of Eq. 2.61 into Eq. 2.62, we obtain

$$\left[\frac{1}{c\Delta t}\sin\left(\frac{\omega\Delta t}{2}\right)\right]^2 = \left[\frac{1}{\Delta x}\sin\left(\frac{k_x\Delta x}{2}\right)\right]^2 + \left[\frac{1}{\Delta z}\sin\left(\frac{k_z\Delta z}{2}\right)\right]^2, \tag{2.63}$$

which is the numerical dispersion relation in the leap-frog scheme, accurate to the second-order, for propagation in vacuum.

From this relation, we first recover the exact vacuum dispersion relation $k_x^2 + k_z^2 = \omega^2/c^2$ in the limiting case where $\omega\Delta t$, $k_x\Delta x$ and $k_z\Delta z$ are all $\ll 1$. However the projection of the particle motions on the grid induces some numerical noise in the source terms of the Maxwell's equations, which can have a broad spectrum both on spatial and time domains. The fields induced by this noise should propagate without amplification, otherwise the time integration scheme becomes instable. If we impose that a real value of ω has to be a solution of Eq. 2.63 for any values of the wavenumber, we obtain the relation

$$1 > (c\Delta t)^2\left[\left(\frac{1}{\Delta x}\right)^2 + \left(\frac{1}{\Delta z}\right)^2\right], \tag{2.64}$$

or $c\Delta t < \Delta z/\sqrt{2}$ for $\Delta x = \Delta z$, which is the well-known *Courant-Friedrichs-Lewy* (CFL) [162] condition. If the CFL condition (Eq. 2.64) is violated, then $\sin(\omega\Delta t/2)$ exceeds unity for $k_x\Delta x$, $k_z\Delta z$ near π. In that case, the complex ω roots give a growth of instability which can be very rapid, resulting in an error in phase or magnitude of the $\boldsymbol{E}-$ and $\boldsymbol{B}-$fields. All these effects are a direct result of the discretization in space and time.

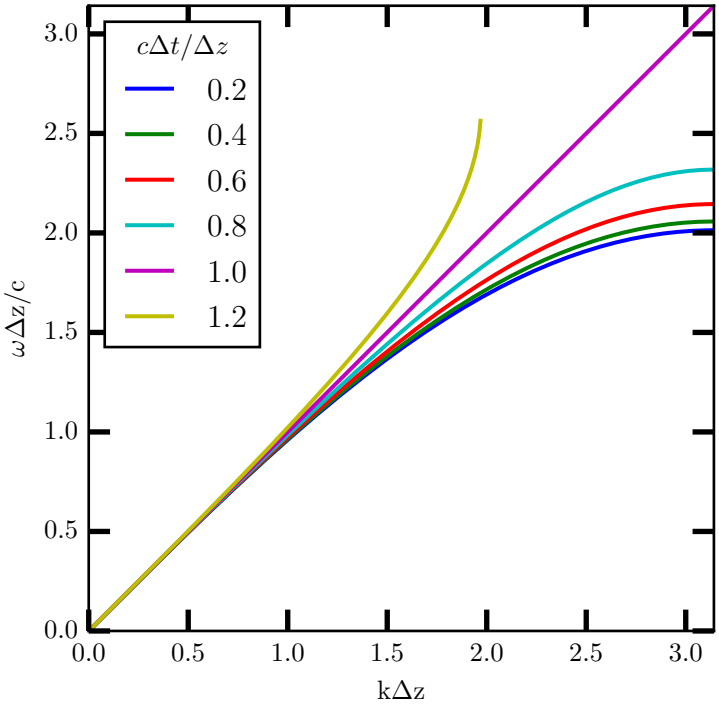

Figure 2.5: One-dimensional vacuum dispersion solution of Maxwell's equations for finite Δz, Δt, from Eq. 2.63. No dispersion error is observed for $c\Delta t/\Delta z = 1.0$, at which one retrieve the correct value of the phase velocity in vacuum.

The CFL condition gives us an upper limit for the time-step in order to get a stable integration scheme. It is also important to analyze whether we gain in accuracy by reducing the time-step. For simplicity, we consider only the 1D case. Figure 2.5 shows a plot of curves $\omega\Delta z/c$ vs. $k\Delta z$ satisfying Eq. 2.63 at different values of $c\Delta t/\Delta z$. We observe that $\omega \leq kc$ when $c\Delta t \leq \Delta z$, meaning that the phase velocity $v_\phi = \omega/k$ is smaller than c. More importantly, we observe that v_ϕ decreases with the time-step, dropping as low as $2c/\pi = 0.637c$ for the smallest value of $\triangle t$, which corresponds to a value for the electron Lorentz factor γ_e as low as 1.3. When $v_\phi < c$, relativistic particles may have $v > v_\phi$ at large wave-vectors (or short wavelengths), generating nonphysical particle-wave growths, or Cerenkov emission [163, 164]. An examination on the collective instabilities involving interaction between relativistic electron beams and these short light waves was performed in Godfrey's work [165, 166, 167]. The reason why Cerenkov effect is a numerical artifact in LWFA becomes clear when we draw a parallel between the numerical and the physical Cerenkov emissions. As explained in [168], the Cerenkov effect can occur when a relativistic charged particle travels through a medium in which the phase velocity of light v_ϕ is lower than c. Hence if the particle travels faster than the phase velocity, i.e $v > v_\phi$, it will emit a characteristic radiation, known as the Cerenkov emission. This effect can happen in dielectric media, such as air or water, but it can never occur neither in vacuum ($v_\phi = c$) nor in plasma ($v_\phi > c$) because a relativistic particle cannot travel at the speed of light, c. Thus the Cerenkov effect is physically impossible in any configurations of laser wakefield-acceleration.

In LWFA, the trapped and accelerated electrons have γ_e larger, and even much larger for the accelerator stage, over a large part of the interaction process. Using $c - v_\phi \simeq 1/(2\gamma_e^2)$, we observe that $c - v_\phi$ has to be very small, that is why the time-step is fixed at its CFL limit in most PIC simulations with FDTD solvers.

In most calculations related to LWFA, the grid dimension along the axis of laser propagation is much smaller in the transverse plane. As a consequence, an important conclusion from the above stability analysis, is that the optimized value of the time-step should satisfy $\Delta t \simeq \Delta z/c$, so that there is a strong correlation between the time-step and the longitudinal dimension of a grid cell. This is a strong restriction, which is a consequence of the FDTD approach.

2.2.4 Conclusions on the FDTD Cartesian PIC method

The FDTD PIC method with a Cartesian grid described above has several advantages in order to optimize the numerical implementation of a LWFA simulation:

- Due to the second-order scheme for spatial derivative, direct correlation between numerical cells is restricted to the neighboring cells. This allows the use of very efficient parallel algorithms based on spatial decomposition, because the overlapping region between domains is small. In fact PIC codes such as Warp have a very good parallel efficiency over thousands of computing nodes.

- The leap-frog scheme has also reduced the length of correlation between the various time-steps. As a consequence, less data have to be kept in memory, simplifying the treatment of large domains.

- Most of the calculations are made through basic operations over large dimensional vectors or tables. This encourages the development of efficient algorithms to optimize vectorization.

The FDTD method on a Cartesian grid also comes with some disadvantages, that can induce severe constraints on LWFA numerical simulation:

- While 2D Cartesian calculations can be used to obtain information on a qualitative level, a 3D approach is mandatory in order to get accurate quantitative results. However, a direct full 3D simulation of the interaction process over several mm requires a huge amount of numerical resources, typically of the order of 10^6 CPU-hours producing more than 10^{12} bytes of binary data. This limits the number of parametric studies that can be done over the large number of physical parameters in LWFA using the 3D Cartesian FDTD solver. To resolve this problem, two numerical techniques have been proposed: (i) a quasi-3D approach in cylindrical geometry [30]. This approach, which will be detailed in Sec. 2.5 has been implemented in Warp. It is a very efficient technique to simulate axisymmetric physical cases and has been used in this thesis for the modeling of the laser-plasma injector; (ii) in cases where there is no identified symmetry, a full 3D PIC simulation remains mandatory but a numerical technique using a relativistic boosted-frame can reduce the computational time. This technique will be presented and analyzed in Chapter 4.

- As shown in the previous subsection, the second-order finite-difference solver induces severe constraints in the numerical resolution to ensure stability and accuracy of a

simulation. For instance, in LWFA, the accelerated electrons can become highly relativistic, possibly leading to spurious numerical Cerenkov effect, which can become the most important limiting factor for the determination of the grid size. In that case, NSFD, high-order FDTD or spectral solvers can become more efficient. This point will be discussed in the next sections.

2.3 Non-Standard Finite-Difference (NSFD) solver

Non-Standard Finite-Difference (NSFD) solvers were introduced to solve discrete ODEs because they bring about higher efficiency and better accuracy as compared to standard FDTD (Yee) solver. In their formulation, the denominators of the derivative terms are modified according to the expected form of the solution. In [169, 170], Cole introduced an implementation of the source-free Maxwell's wave equations for narrow-band applications based on NSFD. Karkkainen et al. adapted it for wideband applications in [171]. The "Cole-Karkkainen" (or CK) [171] solver enlarges the stencil, therefore allowing a larger timestep than with the Yee solver. In addition, at the CFL limit for the time-step and for a given set of parameters, the stencil proposed has no numerical dispersion along the principal axes, provided that the cell size is the same along each dimension, i.e. cubic cells in 3D.

The implementation of the CK solver in a PIC code must introduce the source term into CK source-free formulation in a consistent manner, however it is challenging to modify the NSFD formulation of the Maxwell-Ampere equation to include the source term in a way consistent with the current deposition scheme. In Warp, this problem is mitigated by only applying the enlarged stencil on the Maxwell-Faraday equation, which is source-free while the Maxwell-Ampere equation is discretized in the same way as in the Yee solver. The discretized Maxwell's equations read:

$$D_t \boldsymbol{B} = -\nabla^* \times \boldsymbol{E}, \tag{2.65}$$

$$D_t \boldsymbol{E} = c^2 \nabla \times \boldsymbol{B} - \frac{\boldsymbol{J}}{\epsilon_0}, \tag{2.66}$$

$$\left[\nabla \cdot \boldsymbol{E} = \frac{\rho}{\epsilon_0}\right], \tag{2.67}$$

$$\left[\nabla^* \boldsymbol{B} = 0\right]. \tag{2.68}$$

Eqs. 2.67-2.68 are not solved explicitly if the continuity equation $\partial p/\partial t + \nabla \boldsymbol{J} = 0$ is satisfied. In 2D, assuming the plane (x,z), the differential operators are defined as

$$\nabla = D_x \hat{\boldsymbol{x}} + D_z \hat{\boldsymbol{z}}, \tag{2.69}$$

$$\nabla^* = D_x^* \hat{\boldsymbol{x}} + D_z^* \hat{\boldsymbol{z}}, \tag{2.70}$$

with the finite-difference and sum operators being respectively

$$D_x^* = (\alpha + \beta S_x) D_x, D_z^* = (\alpha + \beta S_z) D_z, \tag{2.71}$$

and

$$(S_x \boldsymbol{F})^n_{j',k'} = \boldsymbol{F}^n_{j'+1/2,k'} + \boldsymbol{F}^n_{j'-1/2,k'}, \tag{2.72}$$

$$(S_z \boldsymbol{F})^n_{j',k'} = \boldsymbol{F}^n_{j',k'+1/2} + \boldsymbol{F}^n_{j',k'-1/2}, \tag{2.73}$$

where j' and k' are related to the position in x and z respectively and can be integers or half-integers. $\boldsymbol{F}$ is a sample vector component, while α and β are constants that verify $\alpha + 2\beta = 1$. The derivation for the 3D case can be found in [172].

Accuracy and stability of the CK solver

The numerical dispersion relation for the CK solver following the analysis in Sec. 2.2.3 is given by

$$\left(\frac{\sin\frac{\omega\Delta t}{2}}{c\Delta t}\right)^2 = C_x\left(\frac{\sin\frac{k_x\Delta x}{2}}{\Delta x}\right)^2 + C_z\left(\frac{\sin\frac{k_z\Delta z}{2}}{\Delta z}\right)^2 \tag{2.74}$$

with

$$C_x = \alpha + 2\beta\cos(k_z\Delta z), \tag{2.75}$$

$$C_z = \alpha + 2\beta\cos(k_x\Delta x). \tag{2.76}$$

The determination of the CFL condition is given by

$$\sin\left(\frac{\omega\Delta t}{2}\right) \leq 1. \tag{2.77}$$

We make the ansatz that the most unstable modes propagate at the Nyquist wavelength along the cell (3D) diagonal, the cell faces (2D) diagonal or the main axes. Considering the 2D case, we obtain $k_x\Delta x = k_z\Delta z$ for the cell faces diagonal, therefore $\sin(k_x\Delta x/2) = \sin(k_z\Delta z/2) = 1$ and $\cos(k_x\Delta x) = \cos(k_z\Delta z) = -1$, leading to $C_x = C_z = \alpha - 2\beta$. With these equalities, we can solve for Eqs. 2.74 and 2.77, the CFL condition in 2D reads

$$c\Delta t \leq 1/\sqrt{(\alpha - 2\beta)\left[(1/\Delta x)^2 + (1/\Delta z)^2\right]}. \tag{2.78}$$

Assuming $\Delta x = \Delta z$ and taking $\alpha = 3/4$ and $\beta = 1/8$, we obtain $c\Delta t = \Delta z$. As a result, there is no dispersion along the principal axes. The 3D formulation of the CFL condition for the CK solver in given in [172].

2.4 High-Order and Pseudo-Spectral Solvers

As shown in the previous section, the numerical Cerenkov emission, which is a well-known artifact in the PIC community [167], can impose a severe limitation on the applicability of the FDTD solver. In particular, it can have dire consequences in flowing plasma simulations, in which the whole plasma is moving at a relativistic speed [173]. Examples of simulations that operate under such condition are simulations of astrophysical shocks [174, 175] and boosted-frame simulations [31, 176, 177]. At first view, the Numerical Cerenkov effect is less dramatic in standard LWFA simulations as only a small part of the plasma, i.e. the trapped electron bunch, travels at an ultra-relativistic speed but these trapped electrons, the most susceptible to be affected by the Cerenkov effect, constitute the part that we are most interested in. That is why its effect, within the LWFA context, has been analyzed in recent works [178, 179]. We have seen that the Cerenkov effect, within the second-order FDTD solver, impose severe constraints in defining the size of the numerical cell and the time-step. The objective of higher-order or spectral methods is to propose a method able to reduce these constraints, in order to increase the numerical efficiency.

For a given numerical cell dimension and time-step, one way to reduce the Numerical Cerenkov radiation in simulations is to extend the FDTD solver by introducing higher order terms in the calculation of the spatial derivatives. It reduces the discretization errors hence more stable with regard to Numerical Cerenkov, at the expanse of a computational cost that rises with the order of accuracy. Beyond a certain order which depends on the details of

implementation and the hardware used for the simulations, it is well known that pseudo-spectral methods become eventually more efficient than finite-difference methods [180]. In fact the pseudo-spectral formulations can be established by taking the limit to infinite order in the high-order solvers. In the following, we will introduce the high-order and the pseudo-spectral solver for the formulation of the Maxwell's equations.

2.4.1 High-Order Finite-Difference solvers

The spatial derivatives defined by Eqs. 2.20-2.21 when extended to a higher order (presumably infinite) have the following formulations:

$$\begin{aligned}(D_x\boldsymbol{F})_{j',k'} &\equiv \frac{1}{\Delta x}\left[C_0(\boldsymbol{F}_{j'+\frac{1}{2},k'}-\boldsymbol{F}_{j'-\frac{1}{2},k'})+C_1(\boldsymbol{F}_{j'+\frac{3}{2},k'}-\boldsymbol{F}_{j'-\frac{3}{2},k'})+\dots\right]\\ &\equiv \frac{1}{\Delta x}\sum_{p=0}^{\infty}\left[C_p(\boldsymbol{F}_{j'+\frac{2p+1}{2},k'}-\boldsymbol{F}_{j'-\frac{2p+1}{2},k'})\right] \qquad (2.79)\\ (D_z\boldsymbol{F})_{j',k'} &\equiv \frac{1}{\Delta z}\left[C_0(\boldsymbol{F}_{j',k'+\frac{1}{2}}-\boldsymbol{F}_{j',k'-\frac{1}{2}})+C_1(F_{j',k'+\frac{3}{2}}-\boldsymbol{F}_{j',k'-\frac{3}{2}})+\dots\right]\\ &\equiv \frac{1}{\Delta z}\sum_{p=0}^{\infty}\left[C_p(\boldsymbol{F}_{j',k'+\frac{2p+1}{2}}-\boldsymbol{F}_{j',k'-\frac{2p+1}{2}})\right], \qquad (2.80)\end{aligned}$$

where j', k' can be integers or half-integers, C_p are the coefficients of discretization given by an algorithm due to Fornberg [181], which are given in Table 2.1 for orders 2 to 20, and at the limit of infinite order, with $\sum_{p=0}^{N}(2p+1)C_p = 1$. These coefficients are applied to equispaced staggered grids [181] only. For example, applying this differentiation operator (extended to order N) to Eq. 2.22 gives us the following expanded expression

$$E_{x_{j+\frac{1}{2},k}}^{n+1/2} = E_{x_{j+\frac{1}{2},k}}^{n-1/2} - c^2\frac{\Delta t}{\Delta z}\sum_{p=0}^{N}C_p\left(B_{y_{j+\frac{1}{2},k+\frac{2p+1}{2}}}^{n} - B_{y_{j+\frac{1}{2},k-\frac{2p+1}{2}}}^{n}\right). \qquad (2.81)$$

More specifically, if we limit the extension to the 6^{th} order, E_x can be expressed as

$$\begin{aligned}E_{x_{j+\frac{1}{2},k}}^{n+1/2} =& E_{x_{j+\frac{1}{2},k}}^{n-1/2} - c^2\frac{\Delta t}{\Delta z}\left[1.1719\left(B_{y_{j+\frac{1}{2},k+\frac{1}{2}}}^{n} - B_{y_{j+\frac{1}{2},k-\frac{1}{2}}}^{n}\right)\right.\\ &\left.-0.0651\left(B_{y_{j+\frac{1}{2},k+\frac{3}{2}}}^{n} - B_{y_{j+\frac{1}{2},k-\frac{3}{2}}}^{n}\right)+0.0047\left(B_{y_{j+\frac{1}{2},k+\frac{5}{2}}}^{n} - B_{y_{j+\frac{1}{2},k-\frac{5}{2}}}^{n}\right)\right]. \qquad (2.82)\end{aligned}$$

From Table 2.1, it is observed that the coefficients of discretization depend on the order of accuracy. For a solver that is accurate to the second-order, only the nodes adjacent to the centered node are included, whereas for higher orders, more distant nodes are included. The more distant the nodes are from the centered node, the smaller the coefficient of discretization, indicating that the weight of the distant grid nodes are weak.

2.4.2 Pseudo-Spectral solvers

In 1973, Haber et al. presented a pseudo-spectral solver that integrates analytically the solution over a finite time-step, under the assumption that the source is constant over that time-step [163]. Haber's pseudo-spectral analytical time-domain (PSATD) algorithm has various advantages over the FDTD as it solves the vacuum Maxwell's equations exactly, has no CFL time-step limit, offers substantial flexibility in plasma and particle beam simulations

Table 2.1: Coefficients of discretization generated from Fornberg's algorithm centered at grid node 0.

Order of accuracy	**Grid nodes** 1/2	3/2	5/2	7/2	9/2	11/2	13/2	15/2	17/2	19/2
2	1.0000									
4	1.1250	-.0417								
6	1.1719	-.0651	.0047							
8	1.1963	-.0798	.0096	-7.0e^{-4}						
10	1.2112	-.0897	.0138	-1.8e^{-3}	1.2e^{-4}					
12	1.2213	-.0969	.0174	-3.0e^{-3}	3.6e^{-4}	-2.2e^{-5}				
14	1.2286	-.1024	.0205	-4.2e^{-3}	6.9e^{-4}	-7.7e^{-5}	4.2e^{-6}			
16	1.2341	-.1066	.0230	-5.3e^{-3}	1.1e^{-4}	-1.6e^{-4}	1.7e^{-5}	-8.5e^{-7}		
18	1.2384	-.1101	.0252	-6.4e^{-3}	1.5e^{-4}	-2.9e^{-4}	4.1e^{-5}	-3.8e^{-6}	1.8e^{-7}	
20	1.2418	-.1129	.0271	-7.4e^{-3}	1.9e^{-4}	-4.3e^{-4}	7.7e^{-5}	-1.0e^{-5}	8.8e^{-7}	-3.7e^{-8}
⋮										
limit $n \longrightarrow \infty$	1.2732	-.1415	.0509	-.0206	.0157	-.0105	.0075	-.0057	.0044	-.0035

and is more stable with regard to Numerical Cerenkov radiation [165, 166, 167]. The other commonly used pseudo-spectral time-domain (PSTD) algorithm offers similar advantages except for a restrictive CFL limit.

Pseudo Spectral Analytical Time Domain (PSATD) algorithm

In the PSATD implementation, the Fourier transformation is used in the calculation of the spatial difference in the $k-$space, while the leap-frog method is retained for the temporal differentiation. Maxwell's equations in the $k-$space are given by

$$\frac{\partial \tilde{\boldsymbol{E}}}{\partial t} = ic\boldsymbol{k} \times \tilde{\boldsymbol{B}} - \tilde{\boldsymbol{J}}, \tag{2.83}$$

$$\frac{\partial \tilde{\boldsymbol{B}}}{\partial t} = -ic\boldsymbol{k} \times \tilde{\boldsymbol{E}}, \tag{2.84}$$

$$\left[i\boldsymbol{k} \cdot \tilde{\boldsymbol{E}} = \tilde{\rho} \right], \tag{2.85}$$

$$\left[i\boldsymbol{k} \cdot \tilde{\boldsymbol{B}} = 0 \right], \tag{2.86}$$

where $\tilde{a}$ is the Fourier Transform of the quantity a. Similarly to the real space formulation, if the continuity equation $\partial\tilde{\rho}/\partial t + i\boldsymbol{k} \cdot \tilde{\boldsymbol{J}} = 0$ is satisfied, then Eq. 2.85 and Eq. 2.86 will automatically be satisfied, thus is is unnecessary to integrate them explicitly.

The PSATD formulation ensues by decomposing the electric field and the current into longitudinal and transverse components, such that $\tilde{\boldsymbol{E}} = \tilde{\boldsymbol{E}}_L + \tilde{\boldsymbol{E}}_T = \hat{\boldsymbol{k}}(\hat{\boldsymbol{k}} \cdot \tilde{\boldsymbol{E}}) - \hat{\boldsymbol{k}} \times (\hat{\boldsymbol{k}} \times \tilde{\boldsymbol{E}})$ and $\tilde{\boldsymbol{J}} = \tilde{\boldsymbol{J}}_L + \tilde{\boldsymbol{J}}_T = \hat{\boldsymbol{k}}(\hat{\boldsymbol{k}} \cdot \tilde{\boldsymbol{J}}) - \hat{\boldsymbol{k}} \times (\hat{\boldsymbol{k}} \times \tilde{\boldsymbol{J}})$, where $\hat{\boldsymbol{k}} = \boldsymbol{k}/k$ and $k^2 = k_x^2 + k_z^2$. With these decomposed quantities, Eq. 2.83 and Eq. 2.84 become

$$\frac{\partial \tilde{\boldsymbol{E}}_T}{\partial t} = ic\boldsymbol{k} \times \tilde{\boldsymbol{B}} - \tilde{\boldsymbol{J}}_T, \tag{2.87}$$

$$\frac{\partial \tilde{\boldsymbol{E}}_L}{\partial t} = -\tilde{\boldsymbol{J}}_L, \tag{2.88}$$

$$\frac{\partial \tilde{\boldsymbol{B}}}{\partial t} = -ic\boldsymbol{k} \times \tilde{\boldsymbol{E}}_T. \tag{2.89}$$

The above system of equations can be solved analytically under the assumption that the sources are constant over a time interval Δt. The original formulation is given in [163] and more detailed derivation is featured in [182]. The discretized analytical solutions are

$$\tilde{\boldsymbol{E}}_T^{n+1} = C\tilde{\boldsymbol{E}}_T^n + iS\hat{\boldsymbol{k}} \times \tilde{\boldsymbol{B}}^n - \frac{S}{ck}\tilde{\boldsymbol{J}}_T^{n+\frac{1}{2}}, \tag{2.90}$$

$$\tilde{\boldsymbol{E}}_L^{n+1} = \tilde{\boldsymbol{E}}_L^n - \Delta t\tilde{\boldsymbol{J}}_L^{n+\frac{1}{2}}, \tag{2.91}$$

$$\tilde{\boldsymbol{B}}^{n+1} = C\tilde{\boldsymbol{B}}^n - iS\hat{\boldsymbol{k}} \times \tilde{\boldsymbol{E}}_T^n + i\frac{1-C}{kc}\hat{\boldsymbol{k}} \times \tilde{\boldsymbol{J}}_T^{n+\frac{1}{2}}, \tag{2.92}$$

with $C = \cos(kc\Delta t)$ and $S = \sin(kc\Delta t)$.

Combining the transverse and longitudinal components, gives

$$\begin{aligned}\tilde{\boldsymbol{E}}^{n+1} =& C\tilde{\boldsymbol{E}}^n + iS\hat{\boldsymbol{k}} \times \tilde{\boldsymbol{B}}^n - \frac{S}{ck}\tilde{\boldsymbol{J}}^{n+\frac{1}{2}} - (1-C)\,\hat{\boldsymbol{k}}\left(\hat{\boldsymbol{k}} \cdot \tilde{\boldsymbol{E}}^n\right) \\ &+ \hat{\boldsymbol{k}}\left(\hat{\boldsymbol{k}} \cdot \tilde{\boldsymbol{J}}^{n+\frac{1}{2}}\right)\left(\frac{S}{kc} - \Delta t\right),\end{aligned} \tag{2.93}$$

$$\tilde{\boldsymbol{B}}^{n+1} = C\tilde{\boldsymbol{B}}^n - iS\hat{\boldsymbol{k}} \times \tilde{\boldsymbol{E}}^n + i\frac{1-C}{kc}\hat{\boldsymbol{k}} \times \tilde{\boldsymbol{J}}^{n+\frac{1}{2}}. \tag{2.94}$$

The above PSATD formulation applies to the field components located at the grid nodes, they can be easily recast on a staggered Yee grid by multiplication by the appropriate phase factors that shift them from the collocated (as in $\boldsymbol{E}-$ and $\boldsymbol{B}-$fields are both taken at the same temporal node) to the staggered times (see Fig. 2.1). In the staggered time configuration, the system of equations writes

$$\tilde{\boldsymbol{E}}^{n+1} = \tilde{\boldsymbol{E}}^n + 2iS_h\hat{\boldsymbol{k}} \times \tilde{\boldsymbol{B}}^{n+\frac{1}{2}} - \frac{2S_h}{ck}\tilde{\boldsymbol{J}}^{n+\frac{1}{2}} + \hat{\boldsymbol{k}}\left(\hat{\boldsymbol{k}} \cdot \tilde{\boldsymbol{J}}^{n+\frac{1}{2}}\right)\left(\frac{2S_h}{kc} - \Delta t\right), \tag{2.95}$$

$$\tilde{\boldsymbol{B}}^{n+\frac{1}{2}} = \tilde{\boldsymbol{B}}^{n-\frac{1}{2}} - 2iS_h\hat{\boldsymbol{k}} \times \tilde{\boldsymbol{E}}^n + i\frac{1-C_h}{kc}\hat{\boldsymbol{k}} \times \left(\tilde{\boldsymbol{J}}^{n+\frac{1}{2}} - \tilde{\boldsymbol{J}}^{n-\frac{1}{2}}\right), \tag{2.96}$$

where $S_h = \sin(kc\Delta t/2)$ and $C_h = \cos(kc\Delta t/2)$.

Pseudo Spectral Time Domain (PSTD) algorithm

The PSTD formulation is a specific case of the PSATD formulation. As demonstrated in [182], by Taylor expanding the coefficients S_h and C_h and keeping only the leading terms, the PSATD formulation reduces to the PSTD formulation [183, 184]:

$$\tilde{\boldsymbol{E}}^{n+1} = \tilde{\boldsymbol{E}}^n + ic\Delta t\boldsymbol{k} \times \tilde{\boldsymbol{B}}^{n+\frac{1}{2}} - \Delta t\tilde{\boldsymbol{J}}^{n+\frac{1}{2}}, \tag{2.97}$$

$$\tilde{\boldsymbol{B}}^{n+\frac{1}{2}} = \tilde{\boldsymbol{B}}^{n-\frac{1}{2}} - ic\Delta t\boldsymbol{k} \times \tilde{\boldsymbol{E}}^{n+1}. \tag{2.98}$$

We can write this system of equations for the TM mode, where only three components are involved, namely E_z, E_x and B_y, therefore giving:

$$\tilde{E_x}^{n+1} = \tilde{E_x}^n - ic\Delta t k_z \tilde{B_y}^{n+\frac{1}{2}} - \Delta t\tilde{J_x}^{n+\frac{1}{2}}, \tag{2.99}$$

$$\tilde{E_z}^{n+1} = \tilde{E_y}^n + ic\Delta t k_x \tilde{B_y}^{n+\frac{1}{2}} - \Delta t\tilde{J_z}^{n+\frac{1}{2}}, \tag{2.100}$$

$$\tilde{B_y}^{n+\frac{1}{2}} = \tilde{B_y}^{n-\frac{1}{2}} - ic\Delta t\left(k_z\tilde{E_x}^n - k_x\tilde{E_z}^n\right). \tag{2.101}$$

Eqs. 2.99-2.101 are convenient for the numerical dispersion analysis that we are performing in the next section.

Accuracy and stability of the time integration

In the following paragraph, we will perform numerical dispersion analysis for the high-order and pseudo-spectral solvers to examine their accuracy and stability.

The procedure for this analysis is similar to the one in Sec. 2.2.3. The numerical dispersion relation given by Eq. 2.63 extended to a higher order, i.e. N order, yields

$$\left[\frac{1}{c\Delta t}\sin\left(\frac{\omega\Delta t}{2}\right)\right]^2 = \left[\frac{1}{\Delta x}\sum_{p=0}^{N} C_p \sin\left(\frac{(2p+1)\,k_x\Delta x}{2}\right)\right]^2 + \left[\frac{1}{\Delta z}\sum_{p=0}^{N} C_p \sin\left(\frac{(2p+1)\,k_z\Delta z}{2}\right)\right]^2, \tag{2.102}$$

where C_p are the coefficients of discretization given by an algorithm due to Fornberg [181], as in Table 2.1.

For the numerical analysis in vacuum on the pseudo-spectral solvers, we neglect $\tilde{\boldsymbol{J}}$ because there is no contribution from the self-consistent dynamics of the charged particles.

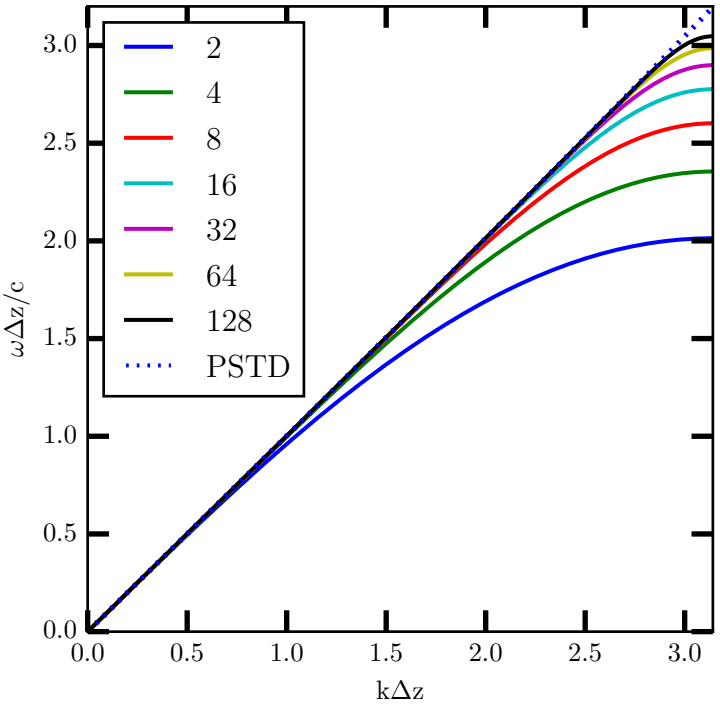

Figure 2.6: One-dimensional vacuum dispersion relation of Maxwell's equations where we have only considered the $z-$axis. All curves shown are plotted for $c\Delta t/\Delta z = 0.2$. Numbers in the legend represent the order of accuracy in the high-order solver.

The PSATD algorithm is free from any numerical dispersion and is not subject to a CFL condition. The solution is exact for any time-step provided that the current source is assumed to be constant over the time-step.

We also perform the numerical dispersion analysis in vacuum on the PSTD algorithm by substituting the traveling wave trial equations Eqs. 2.57-2.59 into Eqs. 2.99-2.101. After some modest amount of algebra, we obtain the following numerical dispersion relation

$$\sin\left(\frac{\omega\Delta t}{2}\right) = \frac{kc\Delta t}{2}. \tag{2.103}$$

Unlike the PSATD algorithm, the PSTD algorithm is subject to numerical dispersion for a finite time-step and to a CFL condition that is given by

$$c\Delta t \leq \frac{2}{\pi}\sqrt{\frac{1}{\Delta x^2}+\frac{1}{\Delta y^2}+\frac{1}{\Delta z^2}}, \tag{2.104}$$

in three dimensions.

Fig. 2.6 shows a plot of $\omega\Delta z/c$ vs. $k\Delta z$ for a fixed $c\Delta t/\Delta z = 0.2$. The numerical dispersion relation of various orders of accuracy spanning from 2 to 128 are evaluated. At the infinite order, we obtain the solution for the PSTD algorithm, constituting the asymptote for the solutions of the high-order solver. At the second-order, we retrieve the result of Fig. 2.5, with a phase velocity $v_\phi = 0.637c < c$ when $k\Delta z \to \pi$, implying that relativistic particles of $v > v_\phi$ might generate nonphysical Cerenkov radiation at large wave-vectors, k. We observe also in Fig. 2.6, that v_ϕ increases with the order of derivation, the highest value being obtained with the PSTD solver. In this regard, other things being equal, the high-order FDTD solver reduces numerical dispersion errors and offers a more stable solution regarding the Numerical Cerenkov emission. With a high-order of accuracy, the numerical dispersion solution in vacuum tends to the ideal solution, given by the asymptote of the numerical dispersion relation from the PSTD algorithm.

2.5 PIC method in the cylindrical coordinates

In the modeling of the injector of the LWFA in the regimes currently explored in experiments, the physics of interest is highly nonlinear and intrinsically three-dimensional. In order to capture all physical phenomena to bring a realistic description of the process, we are often left with the option of carrying out full 3D PIC simulations, which are computationally intensive and often push existing computers to their limits.

Recently, an alternative to full 3D PIC codes that takes advantage of the symmetry of the laser-plasma interaction in underdense plasmas in cylindrical coordinates, (r, z, θ) has been developed [30]. This method applies a Fourier decomposition in θ on the fields and currents in azimuthal harmonics modes $e^{il\theta}$. The complex amplitudes of the fundamental and subsequent harmonics depending on r and z are then used to advance the particles as described in the PIC cycle (see Fig. 2.4). For a linearly polarized laser interacting with a target with cylindrical symmetry, if the laser amplitude also satisfies a cylindrical symmetry, then only three angular modes are required to describe the interaction process. In this case, the use of an angular Fourier decomposition in a PIC model reduces the computational load to roughly three times that of a two-dimensional simulation while capturing the three-dimensional nature of the interaction. It is therefore about two orders of magnitude faster than a full 3D calculation. Moreover, Lifschitz has shown a quantitative agreement between simulations using this model and full 3D calculations [30]. We will also show in Chapter 5 that a good quantitative agreement is obtained while comparing the simulated results with the experimental ones [185].

In this section, we will first introduce the mathematical formulation of the model in cylindrical coordinates, then we will describe its implementation in WARP.

2.5.1 Mathematical formulation of the angular Fourier decomposition algorithm in PIC code

We begin by decomposing the electromagnetic fields, the charge ρ and current densities $\boldsymbol{J}$, expressed in cylindrical coordinates (r, z, θ), into a Fourier series in θ,

$$\begin{aligned}\boldsymbol{F}(r,z,\theta) &= \Re\left(\sum_{l=0}\boldsymbol{F}^l(r,z)e^{il\theta}\right)\\ &= \boldsymbol{F}^0(r,z) + \Re\left(\boldsymbol{F}^1\right)\cos(\theta) - \Im\left(\boldsymbol{F}^1\right)\sin(\theta)\\ &\quad + \Re\left(\boldsymbol{F}^2\right)\cos(2\theta) - \Im\left(\boldsymbol{F}^2\right)\sin(2\theta)\\ &\quad + \dots\end{aligned} \tag{2.105}$$

The amplitudes of each Fourier harmonic (for all fields) $\boldsymbol{F}^l$ are complex, whereas the physical fields they are describing, $\boldsymbol{F}$, are real. The major advantage of this expansion is that it allows modeling of a linearly polarized laser with only the first harmonic (l=1) [30, 186]. For a linearly polarized field, the axis-symmetric laser fields, with amplitude $a(r, z, t)$ and propagating along z are expressed as:

$$\begin{aligned}\boldsymbol{E}(r,z,\theta,t) &= a(r,z,t)\hat{y} = a[\sin(\theta)\hat{e_r} + \cos(\theta)\hat{e_\theta}],\\ \boldsymbol{B}(r,z,\theta,t) &= a(r,z,t)\hat{x} = a[\cos(\theta)\hat{e_r} - \sin(\theta)\hat{e_\theta}].\end{aligned} \tag{2.106}$$

By equating the fields in the set of equations Eqs. 2.106 to the expansion in Eq. 2.105, one obtains:

$$\begin{aligned}E_r^1(r,z,t) &= -ia(r,z,t),\\ E_\theta^1(r,z,t) &= a(r,z,t),\\ B_r^1(r,z,t) &= a(r,z,t),\\ B_\theta^1(r,z,t) &= ia(r,z,t),\end{aligned} \tag{2.107}$$

where only the mode, $l = 1$ contributes. This can be generalized to circularly or elliptically polarized lasers, by combining two linearly polarized lasers.

Once we have the electromagnetic fields, $\boldsymbol{E}$ and $\boldsymbol{B}$ properly defined, we can describe their time evolution using Maxwell-Faraday and Maxwell-Ampere equations Eqs. 2.1-2.2. Substituting the expansions for each field into these equations gives the following set of equations, for each mode l:

$$\frac{\partial B_r^l}{\partial t} = -\frac{il}{r}E_z^l + \frac{\partial E_\theta^l}{\partial z}, \tag{2.108}$$

$$\frac{\partial B_\theta^l}{\partial t} = -\frac{\partial E_r^l}{\partial z} + \frac{\partial E_z^l}{\partial r}, \tag{2.109}$$

$$\frac{\partial B_z^l}{\partial t} = -\frac{1}{r}\frac{\partial}{\partial r}(rE_\theta^l) + \frac{il}{r}E_r^l, \tag{2.110}$$

$$\frac{\partial E_r^l}{\partial t} = \frac{il}{r}B_z^l - \frac{\partial B_\theta^l}{\partial z} - J_r^l, \tag{2.111}$$

$$\frac{\partial E_\theta^l}{\partial t} = \frac{\partial B_r^l}{\partial z} - \frac{\partial B_z^l}{\partial r} - J_\theta^l, \tag{2.112}$$

$$\frac{\partial E_z^l}{\partial t} = \frac{1}{r}\frac{\partial}{\partial r}(rB_\theta^l) - \frac{il}{r}B_r^l - J_z^l, \tag{2.113}$$

where all quantities are complex functions of (r, z).

We can see that the Eqs. 2.108-2.113 are linear, so that the only coupling between the modes has to come through the source term $\boldsymbol{J}$. In particular, each mode propagates independently in vacuum, and in a linear medium. However, modes coupling appears either if the medium is non-uniform in the transverse plane (not considered here) or from nonlinearities in the current.

In the PIC model, the current is given by the sum of the contributions of particles. These particles obey the relativistic equations of motion Eqs. 2.30-2.32.

From these equations of motion, we see that nonlinearities appear from non-local effects, the laser intensities being non uniform, and from relativistic effect through the term $\boldsymbol{v} \times \boldsymbol{B}$. Note that these nonlinearities depend on the field modules, which are independent of the polarization direction and remain mainly axis-symmetric, implying that even with a significant level of nonlinearity, the symmetry of the physical system is still conserved. However this is no longer the case in high density plasma and at ultra-high laser intensities. In all LWFA modeling in this thesis, yet to be shown in Chapter 5, we only consider plasmas with densities much lower than the critical density and laser intensities lower than $10^{19}\,\mathrm{W\,cm^{-2}}$. In such cases, keeping only the $l = 0, 1$ modes is well justified. Codes that are based on this algorithm are said to be "quasi-cylindrical" (or "quasi-3D" by some authors [186]) because they are able to take into account the strong axial symmetry of the physical configuration, in opposition to 2D Cartesian codes; and modes with $l > 0$, in contrast to purely cylindrical codes, which assume that all fields are θ independent, thus only mode $l = 0$ is retained.

2.5.2 Implementation of the quasi-cylindrical model in Warp

In Warp, the numerical implementation of this algorithm consists of solving Eqs. 2.108-2.113. These equations are discretized with a special care for the quantities on axis before introducing them into equations of dynamics (Eqs. 2.35-2.36). It follows the description given in [186].

Discretized Maxwell's equations

The Maxwell's equations written in the cylindrical coordinates Eqs. 2.108-2.113 are discretized on the Yee lattice [151]. The spatial layout of the field quantities are shown in Fig. 2.7.

We define the following numerical operators D_r, D_z (for any fields and source terms $\boldsymbol{F}$):

$$(D_r \boldsymbol{F})^l_{j'+1/2,k'} \equiv \frac{\boldsymbol{F}^l_{j'+1/2,k'} - \boldsymbol{F}^l_{j'-1/2,k'}}{\Delta r}, \tag{2.114}$$

$$(D_z \boldsymbol{F})^l_{j',k'+1/2} \equiv \frac{\boldsymbol{F}^l_{j',k'+1/2} - \boldsymbol{F}^l_{j',k'-1/2}}{\Delta z}, \tag{2.115}$$

where j' and k' can be integers or half-integers.

The discretized equations written in terms of operators D_t (defined earlier by Eqs. 2.18-2.19,

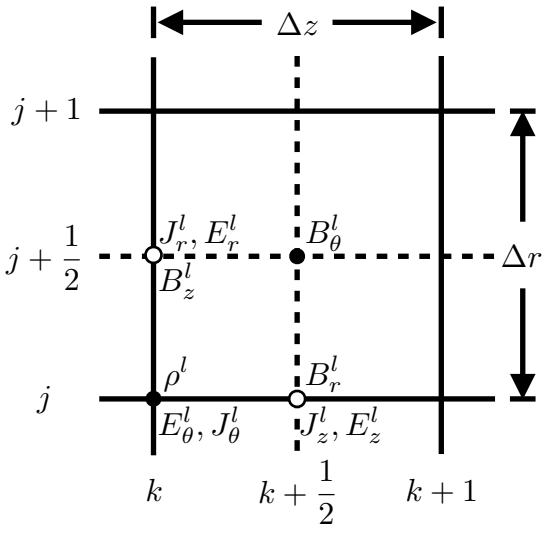

Figure 2.7: Spatial layout of field quantities in the cylindrical coordinates on the Yee lattice. E_r^l, B_z^l, B_θ^l and J_r^l lie on the cylindrical axis of the axial cell.

D_r and D_z read

$$(D_t B_r)^{n,l}_{j,k+\frac{1}{2}} = -\frac{il}{j\Delta r} E_z{}^{n,l}_{j,k+\frac{1}{2}} + (D_z E_\theta)^n_{j,k+\frac{1}{2}}\,, \tag{2.116}$$

$$(D_t B_\theta)^{n,l}_{j+\frac{1}{2},k+\frac{1}{2}} = -(D_z E_r)^{n,l}_{j+\frac{1}{2},k+\frac{1}{2}} + (D_r E_z)^{n,l}_{j+\frac{1}{2},k+\frac{1}{2}}\,, \tag{2.117}$$

$$\begin{aligned}(D_t B_z)^{n,l}_{j+\frac{1}{2},k} =& -\frac{1}{\left(j+\frac{1}{2}\right)\Delta r}\left((j+1)\,E_\theta{}^{n,l}_{j+1,k} - jE_\theta{}^{n,l}_{j,k}\right)\\ &+\frac{il}{\left(j+\frac{1}{2}\right)\Delta r} E_r{}^{n,l}_{j+\frac{1}{2},k}\end{aligned} \tag{2.118}$$

for the magnetic field components, and

$$(D_t E_r)^{n+\frac{1}{2},l}_{j+\frac{1}{2},k} = \frac{il}{\left(j+\frac{1}{2}\right)\Delta r} B_z{}^{n+\frac{1}{2},l}_{j+\frac{1}{2},k} - (D_z B_\theta)^{n+\frac{1}{2},l}_{j+\frac{1}{2},k} - J_r{}^{n+\frac{1}{2},l}_{j+\frac{1}{2},k}, \tag{2.119}$$

$$(D_t E_\theta)^{n+\frac{1}{2},l}_{j,k} = (D_z B_r)^{n+\frac{1}{2},l}_{j,k} - (D_r B_z)^{n+\frac{1}{2},l}_{j,k} - J_\theta{}^{n+\frac{1}{2},l}_{j,k}, \tag{2.120}$$

$$\begin{aligned}(D_t E_z)^{n+\frac{1}{2},l}_{j,k+\frac{1}{2}} =& \frac{1}{j\Delta r}\left(\left(j+\frac{1}{2}\right) B_\theta{}^{n+\frac{1}{2},l}_{j+\frac{1}{2},k+\frac{1}{2}} - \left(j-\frac{1}{2}\right) B_\theta{}^{n+\frac{1}{2},l}_{j-\frac{1}{2},k+\frac{1}{2}}\right)\\ &-\frac{il}{j\Delta r} B_r{}^{n+\frac{1}{2},l}_{j,k+\frac{1}{2}} - J_z{}^{n+\frac{1}{2},l}_{j,k+\frac{1}{2}}\end{aligned} \tag{2.121}$$

for the electric field components. Notice that due to singularities in some of the terms containing the factor $1/r$ on axis ($r = 0$), they are being replaced by specific boundary conditions, which are based on the symmetry properties of the fields. More details are given in [30].

The motion of the particles are still calculated in Cartesian coordinates. The transformation between Cartesian (x, y, z) and cylindrical (r, z, θ) coordinates is simplified by noting that $\exp(i\theta) = x + iy$ so that there is no need to introduce trigonometric functions. The shape function introduced in Eq. 2.26 is now written as

$$S(\boldsymbol{x} - \boldsymbol{x}_m) = S_r\,(r - r_m)\,S_z\,(z - z_m)\,S_\theta\,(\theta - \theta_m)\,, \tag{2.122}$$

where S_r and S_z are given by one of the equations Eqs. 2.47-2.49 depending on the chosen order of projection, whereas to facilitate the projection on the $\exp(il\theta)$ functions, S_θ is taken as the delta function.

The time cycle of the PIC calculation is identical to the one shown in Fig. 2.4 for Cartesian coordinates, with the same four steps: solving Maxwell's equations, projecting the fields to the particle position, pushing the particles and finally interpolating from the particle position to the numerical grid in order to get the charge and current densities. Here again the standard current deposition method is not charge conserving. This problem can be solved by using the Esirkepov algorithm as described in Sec. 2.2.3.

Chapter 3

Ensuring the correctness of the simulation

Computer simulation is crucial in the development of plasma theory, due to the complex nature of the encountered problems. But one might ask how meaningful is the physics produced by simulations? Just how meaningful depends on our understanding on numerical effects. Once a numerical effect has been identified and quantified, a theoretical model is often developed for error prediction in future simulations.

The numerical problem that will be discussed in this chapter is the reflection observed in open boundaries. The technique used for the implementation is Bérenger's Perfectly Matched Layer (PML) [23]. Numerical studies on the FDTD scheme have been done but not systematically extended to high-order FDTD nor PSTD schemes. This chapter first introduces the PML medium, then presents its implementation in the high-order FDTD and PSTD schemes. Finally, an analytical evaluation of the coefficient of reflection is performed and compared with the one evaluated via simulations.

Contents

3.1 PML medium

3.1.1 Overview

When performing simulations with PIC codes in LWFA, open boundaries are crucial to ensure waves and disturbances originating within the model domain (or simulation box) to leave the domain without affecting the interior solution in a way that is not physically realistic. Fig. 3.1 shows an electromagnetic (EM) pulse that propagates from bottom to top in a model domain and arrives at the top boundary. Without any special treatment, the EM pulse is reflected and interferes with the remaining EM pulse that is still in the model domain, leading to its deformation as shown in Fig. 3.1(a). On the contrary, treatment at boundaries with PML enables efficient absorption of the waves at the top boundary, as shown in Fig. 3.1(b).

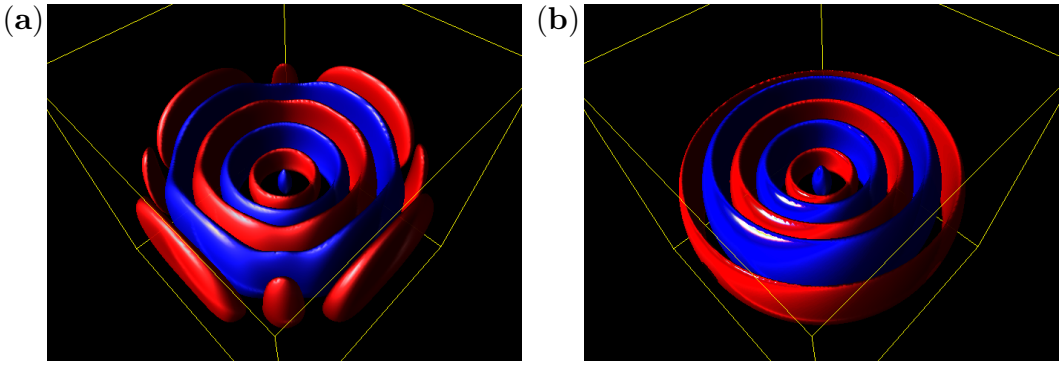

Figure 3.1: Simulation of an electromagnetic (EM) pulse with and without treatment at boundaries. (a) Simulation of an EM pulse exhibits reflections at the boundaries without special treatment, resulting in the deformation of the EM pulse. (b) Application of PML enables efficient absorption of waves at the boundaries.

In some cases, simulation results will be rendered useless if PML is not included. This is the case for LWFA simulations in cylindrical coordinates (see Sec. 2.5). The laser pulse propagating in the plasma will diffract, part of it will hit the radial boundary and be reflected on the axis. Since most of the physical interaction between the laser pulse and the plasma particles takes place on axis, the buildup of numerical errors in this region modifies completely the physical interpretation of the results.

Various techniques to model open boundaries have been used such as the one-way approximation of the wave equation (initially exhibited for acoustic waves) by Engquist and Majda [187], or Bérengers more efficient PML technique which consists in surrounding the computational domain with an absorbing medium whose impedance matches that of free-space. While a PML medium absorbs waves at all wavelength and angle of incidence at the infinitesimal limit, spurious reflections occur due to discretization. The amount of reflection as a function of wavelength and angle of incidence has been evaluated numerically and analytically at low order discretization [188] but not systematically at higher order. While an implementation of the PML in a PSTD solver was given by Ohmura et al. [189], the estimates of the coefficients of reflection with respect to wavelength and angle were not given. The analysis carried out in this article focuses on Bérengers split field original formulation of Maxwells equations of PML medium, as it is the implementation that is currently used in the targeted plasma simulation code.

The exponential convergence of the PML solution to the unbounded domain has been demonstrated in previous work [190] at the infinitesimal limit. This, however, does not guarantee high absorption rates at any angle and frequency with the discretized form of the PML. In particular, since the PML condition is local, it is nonetheless necessary to study carefully its efficiency when used with high-order stencils, when the extent of the stencil can exceed the PML thickness, and especially with pseudo-spectral algorithms that involve global FFT operations. In this study, we extend the theoretical and numerical analysis of the coefficient of reflection of PML to solvers of any order of accuracy, taking the limit of infinite order to obtain the solutions for the pseudo-spectral formulations.

3.1.2 Formulation

We consider, for simplicity and without loss of generality, the transverse electric (TE) mode, which involves in Cartesian coordinates the field components E_x, E_y and B_z. Notice that x- and $y-$axes constitute the transverse directions, and $z-$axis is the longitudinal direction.

A PML medium involves an electric conductivity σ and a magnetic conductivity σ^*, with a split of the Maxwells equations, and writes as follows for the TE mode [23]:

$$\frac{\partial E_x}{\partial t} + \sigma_y E_x = c^2 \frac{\partial B_z}{\partial y}, \tag{3.1}$$

$$\frac{\partial E_y}{\partial t} + \sigma_x E_y = -c^2 \frac{\partial B_z}{\partial x}, \tag{3.2}$$

$$\frac{\partial B_{zx}}{\partial t} + \sigma_x^* B_{zx} = -\frac{\partial E_y}{\partial x}, \tag{3.3}$$

$$\frac{\partial B_{zy}}{\partial t} + \sigma_y^* B_{zy} = \frac{\partial E_x}{\partial y}, \tag{3.4}$$

with $\partial/\partial x$ and $\partial/\partial y$ partial differentials respectively in $x-$ and $y-$directions, and $B_z = B_{zx} + B_{zy}$. This medium absorbs electromagnetic waves at any wavelength and angle of incidence if its impedance matches the one of vacuum, which happens when $\sigma_x/\epsilon_0 = \sigma_x^*/\mu_0$ and $\sigma_y/\epsilon_0 = \sigma_y^*/\mu_0$ (also known as the matching conditions) [23]. If these conditions are satisfied, the impedance of a plane wave in the medium equals its impedance in vacuum. A remark that can be made when looking at the system Eqs. 3.1-3.4 is that if $\sigma_x = \sigma_x = \sigma_y = \sigma_y = 0$, it reduces to the Maxwell's equations of vacuum; if $\sigma_x = \sigma_y = 0$, it reduces to the equations of a conductive medium and finally, if $\sigma_x^* = \sigma_x^* = 0$ and $\sigma_y^* = \sigma_y^* = 0$, it reduces to the equations of the absorbing medium presented in [151].

3.1.3 PML technique

The general frame of the PML technique is pointed out in Fig 3.2. The Maxwell's equations are being solved inside a computational domain in which lies a source of outgoing waves. We have an absorbing layer which is an aggregate of the PML media surrounding the computational domain whose properties will be defined in the following paragraph. The domain is finally ended by perfectly conducting conditions.

On both the left and right sides of the computational domain, the absorbing layers are matched PML$(\sigma_x, \sigma_x^*, 0, 0)$ media, the outgoing waves can propagate without reflection through the interfaces normal to x. Similarly, matched PML$(0, 0, \sigma_y, \sigma_y^*)$ media are used on both upper and lower sides of the computational domain so that the outgoing waves can propagate without reflection through the interfaces normal to y. At the four corners of the

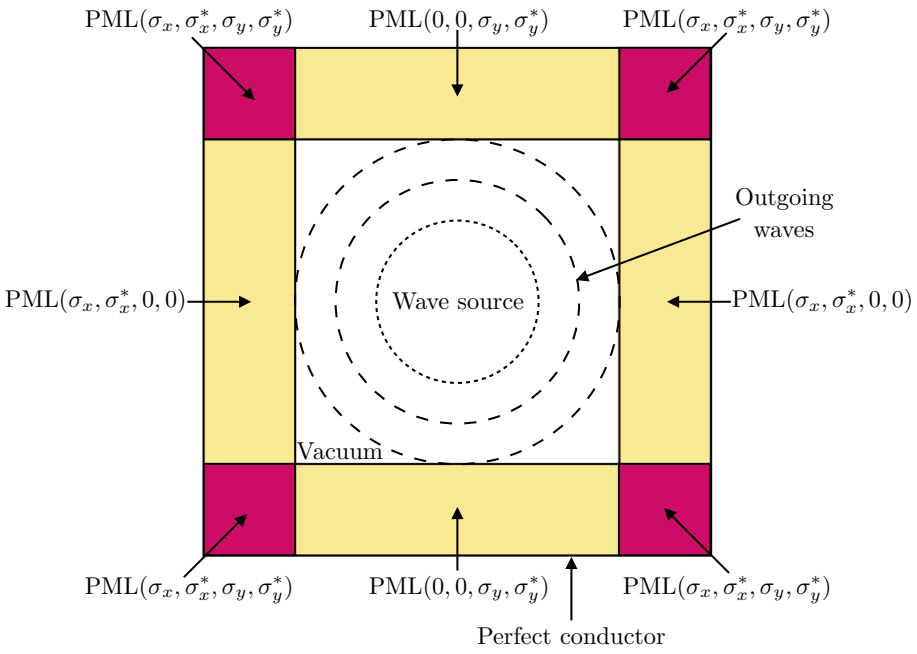

Figure 3.2: General frame of the PML technique. The outgoing waves coming from the wave source hit the PML media with different properties surrounding the computational domain.

domain, the absorbing layers are made of PML($\sigma_x, \sigma_x^*, \sigma_y, \sigma_y^*$) media having conductivities equal to those of the adjacent $(\sigma_x, \sigma_x^*, 0, 0)$ and $(0, 0, \sigma_y, \sigma_y^*)$ media. As a result, there is theoretically no reflection at the interfaces lying between the side layers and the corner layers.

3.1.4 Discretization of the PML

The FDTD discretization of this set of equations Eqs. 3.1-3.4 is given by

$$\frac{E_{x_{j+1/2,k}}^{n+1} - E_{x_{j+1/2,k}}^{n}}{\Delta t} + \sigma_y \frac{E_{x_{j+1/2,k}}^{n+1} + E_{x_{j+1/2,k}}^{n}}{2} = c^2 \frac{B_{z_{j+1/2,k+1/2}}^{n+1/2} - B_{z_{j+1/2,k-1/2}}^{n+1/2}}{\Delta y}, \tag{3.5}$$

$$\frac{E_{y_{j,k+1/2}}^{n+1} - E_{y_{j,k+1/2}}^{n}}{\Delta t} + \sigma_x \frac{E_{y_{j,k+1/2}}^{n+1} + E_{y_{j,k+1/2}}^{n}}{2} = -c^2 \frac{B_{z_{j+1/2,k+1/2}}^{n+1/2} - B_{z_{j-1/2,k+1/2}}^{n+1/2}}{\Delta x}, \tag{3.6}$$

$$\frac{B_{zx_{j+1/2,k+1/2}}^{n+1/2} - B_{zx_{j+1/2,k+1/2}}^{n-1/2}}{\Delta t} - \sigma_x^* \frac{B_{zx_{j+1/2,k+1/2}}^{n+1/2} + B_{zx_{j+1/2,k+1/2}}^{n-1/2}}{2} = \frac{E_{y_{j+1,k+1/2}}^{n} - E_{y_{j,k+1/2}}^{n}}{\Delta x}, \tag{3.7}$$

$$\frac{B_{zy_{j+1/2,k+1/2}}^{n+1/2} - B_{zy_{j+1/2,k+1/2}}^{n-1/2}}{\Delta t} + \sigma_y^* \frac{B_{zy_{j+1/2,k+1/2}}^{n+1/2} + B_{zy_{j+1/2,k+1/2}}^{n-1/2}}{2} = \frac{E_{x_{j+1/2,k+1}}^{n} - E_{x_{j+1/2,k}}^{n}}{\Delta y}. \tag{3.8}$$

After some algebraic manipulation, equations in Eqs. 3.5-3.8 can be written in their explicit linear forms for implementation in a simulation code:

$$E_{x\,j+1/2,k}^{\,n+1} = \alpha_x E_{x\,j+1/2,k}^{\,n} + \beta_x \left(B_{z\,j+1/2,k+1/2}^{\,n+1/2} - B_{z\,j+1/2,k-1/2}^{\,n+1/2} \right), \tag{3.9}$$

$$E_{y\,j,k+1/2}^{\,n+1} = \alpha_y E_{y\,j,k+1/2}^{\,n} + \beta_y \left(B_{z\,\mathrm{j+1/2,k+1/2}}^{\,n+1/2} - B_{z\,j-1/2,k+1/2}^{\,n+1/2} \right), \tag{3.10}$$

$$B_{zx\,j+1/2,k+1/2}^{\,n+1/2} = \alpha_x^* B_{zx\,j+1/2,k+1/2}^{\,n-1/2} + \beta_x^* \left(E_{y\,j+1,k+1/2}^{\,n} - Ey_{j,k+1/2}^{n} \right), \tag{3.11}$$

$$B_{zy\,j+1/2,k+1/2}^{\,n+1/2} = \alpha_y^* B_{zy\,j+1/2,k+1/2}^{\,n-1/2} + \beta_y^* \left(E_{x\,j+1/2,k+1}^{\,n} - E_{x\,j+1/2,k}^{\,n} \right), \tag{3.12}$$

where

$$\begin{cases} \alpha_x &= \frac{2-\sigma_y \Delta t}{2+\sigma_y \Delta t}, \\ \alpha_y &= \frac{2-\sigma_x \Delta t}{2+\sigma_x \Delta t}, \\ \beta_x &= \frac{2c^2}{2+\sigma_y \Delta t} \frac{\Delta t}{\Delta y}, \\ \beta_y &= -\frac{2c^2}{2+\sigma_x \Delta t} \frac{\Delta t}{\Delta x}, \\ \alpha_x^* &= \frac{2-\sigma_x^* \Delta t}{2+\sigma_x^* \Delta t}, \\ \alpha_y^* &= \frac{2-\sigma_y^* \Delta t}{2+\sigma_y^* \Delta t}, \\ \beta_x^* &= -\frac{2}{2+\sigma_x^* \Delta t} \frac{\Delta t}{\Delta x}, \\ \beta_y^* &= \frac{2}{2+\sigma_y^* \Delta t} \frac{\Delta t}{\Delta y}. \end{cases} \tag{3.13}$$

3.1.5 Extension to higher order

Following the general expression for high order spatial derivatives established in Eq. 2.81, the extension to order N of the explicit linear form can be written as the following general expression for discretization following the $x-$direction

$$\begin{aligned} E_{j',k'}^{n+1} &= \alpha_x E_{j',k'}^{n} + \beta_x \left[C_0 \left(B_{j'+1/2,k'}^{n+1/2} - B_{j'-1/2,k'}^{n+1/2} \right) + C_1 \left(B_{j'+3/2,k'}^{n+1/2} - B_{j'-3/2,k'}^{n+1/2} \right) + ... \right] \\ &= \alpha_x E_{j',k'}^{n} + \beta_x \textstyle\sum_{p=0}^{N} C_p \left(B_{j'+(2p+1)/2,k'}^{n+1/2} - B_{j'-(2p+1)/2,k'}^{n+1/2}) \right), \end{aligned} \tag{3.14}$$

where j' and k' can be either integers or half-integers, E and B represent any components of $\boldsymbol{E}-$ and $\boldsymbol{B}-$fields respectively, α_x, β_x are coefficients in Eq. 3.13 and C_p are the coefficients of finite-difference approximation due to Fornberg [181], which are given in Table 2.1 for orders 2 to 20, and at the limit of infinite order, and apply to equispaced staggered-grids. A similar expression applies to $B_{j'+1/2,k'}^{n+1/2}$ discretized following the $x-$direction written as

$$B_{j'+1/2,k'} = \alpha_x^* B_{j'+1/2,k'}^{n-1/2} + \beta_x^* \sum_{p}^{N} C_p \left(E_{j'+p+1,k'}^{n+1/2} - E_{j'+p,k'}^{n+1/2} \right), \tag{3.15}$$

where α_x^* and β_x^* are coefficients in Eq. 3.13. Discretization in the $y-$direction for both $\boldsymbol{E}-$ and $\boldsymbol{B}-$fields is rather straightforward.

3.1.6 Application to staggered-grid PSTD solvers

The PSTD formulation is given in Sec. 2.4.2. In the PSTD implementation, the Fourier transformation is used for the calculation of the spatial differentiation in k-space, while the

Leapfrog method is retained for the temporal differentiation. Following the notations given in [189] the PSTD formulation of the set of equations Eqs. 3.1-3.4 is given by:

$$\frac{\partial E_x}{\partial t} + \sigma_y E_x = c^2 \left[\mathcal{F}^{-1} i k_y \left(\mathcal{F} B_z\right)\right], \tag{3.16}$$

$$\frac{\partial E_y}{\partial t} + \sigma_x E_y = -\, c^2 \left[\mathcal{F}^{-1} i k_x \left(\mathcal{F} B_z\right)\right], \tag{3.17}$$

$$\frac{\partial B_{zx}}{\partial t} + \sigma_x^* B_{zx} = -\left[\mathcal{F}^{-1} i k_x (\mathcal{F} E_y)\right], \tag{3.18}$$

$$\frac{\partial B_{zy}}{\partial t} + \sigma_y^* B_{zy} = \left[\mathcal{F}^{-1} i k_y \left(\mathcal{F} E_x\right)\right], \tag{3.19}$$

where $\mathcal{F}$ and $\mathcal{F}^{-1}$ are respectively the forward and inverse Fourier transformations, and k_x and k_y are the wavenumbers in the $x-$ and $y-$directions respectively.

Assuming the use of a staggered-grid (Yee discretization[151]), the discretized form can be written in its explicit linear form, giving

$$E_{x\,j+1/2,k}^{\,n+1} = \alpha_x E_{x\,j+1/2,k}^{\,n} + \beta_x \left[\mathcal{F}^{-1} i k_y \mathrm{e}^{-ik_y \Delta y/2} \left(\mathcal{F} B_{z\,j+1/2,k}^{\,n+1/2}\right)\right], \tag{3.20}$$

$$E_{y\,j,k+1/2}^{\,n+1} = \alpha_y E_{y\,j,k+1/2}^{\,n} + \beta_y \left[\mathcal{F}^{-1} i k_x \mathrm{e}^{-ik_x \Delta x/2} \left(\mathcal{F} B_{z\,j,k+1/2}^{\,n+1/2}\right)\right], \tag{3.21}$$

$$B_{zx\,j+1/2,k+1/2}^{\,n+1/2} = \alpha_x^* B_{zx\,j+1/2,k+1/2}^{\,n-1/2} + \beta_x^* \left[\mathcal{F}^{-1} i k_x \mathrm{e}^{ik_x \Delta x/2} \left(\mathcal{F} E_{y\,j+1/2,k+1/2}^{\,n}\right)\right], \tag{3.22}$$

$$B_{zy\,j+1/2,k+1/2}^{\,n+1/2} = \alpha_y^* B_{zy\,j+1/2,k+1/2}^{\,n-1/2} + \beta_y^* \left[\mathcal{F}^{-1} i k_y \mathrm{e}^{ik_y \Delta y/2} \left(\mathcal{F} E_{x\,j+1/2,k+1/2}^{\,n}\right)\right]. \tag{3.23}$$

The terms $\mathrm{e}^{ik_x \Delta x/2}$ and $\mathrm{e}^{ik_y \Delta y/2}$ are respectively the shifts in space in $x-$ and $y-$directions on the staggered-grid for E_x and E_y, while the terms $\mathrm{e}^{-ik_x \Delta x/2}$ and $\mathrm{e}^{-ik_y \Delta y/2}$ are respectively the shifts in space in x- and $y-$directions on the staggered-grid for B_z.

The coefficients of $\left(\alpha_x, \beta_x, \alpha_y, \beta_y, \alpha_x^*, \beta_x^*, \alpha_y^*, \beta_y^*\right)$ are the same as shown in the set Eq. 3.13.

3.2 Reflection of a plane wave striking the entire PML

Following [188], the coefficient of reflection of a plane wave propagating in the x-direction perpendicularly to the interface of the PML can be computed with the same analogy to the interferometer of Fabry-Perot by integrating over the multiple transmissions t and reflections r of rays between two rows of the grid (two plates in the interferometer).

Calculating the coefficient of reflection for the entire layer requires knowledge of the coefficients of reflection at each plane of the layer (nodes j, $j + 1/2$, $j + 1$, ...).

3.2.1 Coefficients of reflection at individual planes

We begin by evaluating the coefficient of reflection at a row passing through a node situated at one of the slices in the PML media. The rest of the space is described by centered finite difference of the wave equation in vacuum. We assume that only the plane where the PML scheme applies generates reflections. The basic procedure for the derivation of the coefficient of reflection involves substitution of plane monochromatic traveling wave trial solutions into an expression that consists of only the components of a particular field. For instance, in the derivation of the coefficient of reflection on the full-node, we would like to obtain an expression consisting of only components of the field, E_y, implying that all components

of B_z have to be eliminated. Hence, the method consists of deriving the finite difference expression for the second derivative in time of E_y and then eliminate B_z by substituting the finite difference expression for the first time derivative of B_z in two adjacent nodes. It is instructive to follow the details of the derivation, therefore a walk-through is given in the following paragraphs.

One-dimensional case

Firstly, we express the finite difference expression for the second derivative in time of E_y, given by

$$E_{y_j}^{n+1} = \alpha_y E_{y_j}^{n} + \beta_y \sum_{p=0}^{N} C_p \left(B_{z_{j+(2p+1)/2}}^{n+1/2} - B_{z_{j-(2p+1)/2}}^{n+1/2} \right). \tag{3.24}$$

$$E_{y_j}^{n} = \alpha_y E_{y_j}^{n} + \beta_y \sum_{p=0}^{N} C_p \left(B_{z_{j+(2p+1)/2}}^{n-1/2} - B_{z_{j-(2p+1)/2}}^{n-1/2} \right), \tag{3.25}$$

where $N \in \mathbb{N}$.

Without lack of generality, we consider the second-order for simplicity. Subtracting Eq. 3.25 from Eq 3.24, we obtain

$$E_{y_j}^{n+1} - E_{y_j}^{n} = \alpha \left(E_{y_j}^{n} - E_{y_j}^{n-1} \right) + \beta \left[B_{z_{j+1/2}}^{n+1/2} - B_{z_{j+1/2}}^{n-1/2} - B_{z_{j-1/2}}^{n+1/2} + B_{z_{j-1/2}}^{n-1/2} \right]. \tag{3.26}$$

On the other hand, we also have

$$B_{z_{j+1/2}}^{n+1/2} = B_{z_{j+1/2}}^{n-1/2} + V \left(E_{y_{j+1}}^{n} - E_{y_j}^{n} \right), \tag{3.27}$$

$$B_{z_{j-1/2}}^{n+1/2} = B_{z_{j-1/2}}^{n-1/2} + V \left(E_{y_j}^{n} - E_{y_{j-1}}^{n} \right), \tag{3.28}$$

where $V = c^2 \Delta t / \Delta x$.

The elimination of B_z is obtained by insertions of Eqs. 3.27-3.28 in Eq. 3.26 eliminates, yielding

$$E_{y_j}^{n+1} + (-1 - \alpha + 2\beta V) E_{y_j}^{n} + \alpha E_{y_j}^{n-1} - \beta V E_{y_{j+1}}^{n} - \beta V E_{y_{j-1}}^{n} = 0. \tag{3.29}$$

We now assume a plane monochromatic traveling-wave trial solution of amplitude $\mathrm{e}^{i(\omega \Delta t - k_x \Delta x)}$ striking the PML slice at normal incidence. We also assume that the norm of k_x is conserved by the transmitted and the reflected waves and we define the coefficient of reflection as the complex number r. Under these conditions, the transmitted wave is given by $(1-r)\,\mathrm{e}^{i(\omega \Delta t - k \Delta x)}$, and the signal in front of the slice is the sum of the incident wave and the reflected one, giving $\mathrm{e}^{i(\omega \Delta t - k_x \Delta x)} - r\mathrm{e}^{i(\omega \Delta t + k_x \Delta x)}$. Assuming that the PML is applied at the slice located at j, we have

$$E_{y_{j+N_x}}^{n-N_t} = (1-r)\,\mathrm{e}^{-N_t i \omega \Delta t - N_x i k_x \Delta x}, \tag{3.30}$$

$$E_{y_{j+N_x}}^{n+N_t} = (1-r)\,\mathrm{e}^{N_t i \omega \Delta t - N_x i k_x \Delta x}, \tag{3.31}$$

$$E_{y_{j-(N_x+1)}}^{n-N_t} = \mathrm{e}^{-N_t i \omega \Delta t + (N_x+1) i k_x \Delta x} - r\mathrm{e}^{-N_t i \omega \Delta t - (N_x+1) i k_x \Delta x}, \tag{3.32}$$

$$E_{y_{j-(N_x+1)}}^{n+N_t} = \mathrm{e}^{N_t i \omega \Delta t + (N_x+1) i k_x \Delta x} - r\mathrm{e}^{N_t i \omega \Delta t - (N_x+1) i k_x \Delta x}, \tag{3.33}$$

where $N_t \in \mathbb{N}$ and $N_x \in \mathbb{N}$.

By inserting the plane monochromatic traveling-wave trial solutions, we obtain, to leading order, the coefficient of reflection at a full-node, r_{node}:

$$r_{node} = \frac{a - b\sum_{p=0}^{\infty} C_{coupled_p} \cos\left(pk_x\Delta x\right)}{a - b\sum_{p=0}^{\infty} C_{coupled_p} \mathrm{e}^{-ipk_x\Delta x}}, \tag{3.34}$$

where

$$\begin{cases} a = & \mathrm{e}^{i\omega\Delta t} - 1 - \alpha_y + \alpha_y \mathrm{e}^{-i\omega\Delta t}, \\ b = & 2\beta_y V. \end{cases} \tag{3.35}$$

$C_{coupled_p}$ are the coupled Fornberg's coefficients, defined by

$$C_{coupled_p} = \begin{cases} -\sum_{q=1}^{n_{order}} C_q^2, & \text{if } p = 0, \\ -2\sum_{q=1}^{n_{order}} C_q C_{q-p}, & \text{if } 0 < p < n_{order}, \\ 2\sum_{q=1}^{n_{order}} C_q C_{p-(q-1)}, & \text{if } n_{order} \leq p < 2n_{order} - 1, \\ \sum_{q=1}^{n_{order}} C_q^2, & \text{if } p = 2n_{order} - 1, \end{cases} \tag{3.36}$$

where n_{order} is the order of discretization, and C are the coefficients from Fornberg's algorithm [191] as in Table 2.1.

The derivation of the coefficient of reflection at an inter-node $r_{inter-node}$ (not detailed here) proceeds similarly and gives an expression of the same form as Eq. 3.34, after replacement of α_y by α_y^* and β_y by β_y^* in the definition of a and b.

Two-dimensional case

The derivation of the coefficient of reflection at higher dimension requires more algebraic manipulation. As in the previous section, the derivation of the coefficient of reflection involves the substitution of plane monochromatic traveling-wave trial solutions into an expression that consists of only the components of a particular field.

The equations to be solved at a node are given by

$$E_{y_{j,k+1/2}}^{\ n+1} = \alpha_y E_{y_{j,k+1/2}}^{\ n} - \beta_y \sum_{p=0}^{N} C_p \left(B_{z_{j+(2p+1)/2,k+1/2}}^{\ n+1/2} - B_{z_{j-(2p+1)/2,k+1/2}}^{\ n+1/2} \right), \tag{3.37}$$

$$\begin{aligned} E_{y_{j,k+1/2}}^{\ n} =& E_{y_{j,k+1/2}}^{\ n} + \frac{\Delta x}{\Delta y}\left(E_{x_{j+1/2,k+1}}^{\ n} - E_{x_{j+1/2,k}}^{\ n}\right) \\ & - \frac{\Delta x}{\Delta t}\left(B_{z_{j+1/2,k+1/2}}^{\ n+1/2} - B_{z_{j+1/2,k+1/2}}^{\ n-1/2}\right), \end{aligned} \tag{3.38}$$

$$E_{x_{j+1/2,k+1}}^{\ n} = E_{x_{j+1/2,k+1}}^{\ n-1} + V_x \sum_{p=0}^{N} C_p \left(B_{z_{i+1/2,j+(2p+1)/2}}^{\ n+1/2} - B_{z_{i+1/2,j-(2p+1)/2}}^{\ n+1/2} \right), \tag{3.39}$$

where $V_y = c^2\Delta t/\Delta y$.

A different approach is applied to derive the coefficient of reflection on the inter-node,

for which the following set of equations is solved

$$E_{x}{}^{n+1}_{j+1/2,k} = E_{x}{}^{n}_{j+1/2,k} + V_y \sum_{p=0}^{N} C_p \left(B_{z}{}^{n+1/2}_{j+1/2,k+(2p+1)/2} - B_{z}{}^{n+1/2}_{j+1/2,k-(2p+1)/2} \right), \tag{3.40}$$

$$E_{y}{}^{n+1}_{j,k+1/2} = E_{y}{}^{n}_{j,k+1/2} - V_x \sum_{p=0}^{N} C_p \left(B_{z}{}^{n+1/2}_{j+(2p+1)/2,k+1/2} - B_{z}{}^{n+1/2}_{j-(2p+1)/2,k+1/2} \right), \tag{3.41}$$

$$B_{z}{}^{n+1/2}_{j+1/2,k+1/2} = B_{zx}{}^{n+1/2}_{j+1/2,k+1/2} + B_{zy}{}^{n+1/2}_{j+1/2,k+1/2}, \tag{3.42}$$

$$B_{zx}{}^{n+1/2}_{j+1/2,k+1/2} = \alpha_x^* B_{zx}{}^{n-1/2}_{i+1/2,j+1/2} - \beta_x^* \sum_{p=0}^{N} C_p \left(E_{y}{}^{n}_{j+(p+1),k+1/2} - E_{y}{}^{n}_{j-p,k+1/2} \right), \tag{3.43}$$

$$B_{zy}{}^{n+1/2}_{j+1/2,k+1/2} = B_{zy}{}^{n-1/2}_{j+1/2,k+1/2} + \frac{\Delta t}{\Delta y} \sum_{p=0}^{N} C_p \left(E_{x}{}^{n}_{j+1/2,k+(p+1)} - E_{x}{}^{n}_{j+1/2,k-p} \right), \tag{3.44}$$

where $V_x = c^2 \Delta t / \Delta x$ and $V_x = c^2 \Delta t / \Delta y$.

Solving the systems of equations given above leads to the same form for the expression of the coefficient of reflection at the node and the inter-node, which reads (for a node):

$$r_{node} = \frac{a - b \sum_{p=0}^{\infty} C_{coupled_p} \cos\left(p k_y \Delta y\right) - c \sum_{p=0}^{\infty} C_{coupled_p} \cos\left(k_x \Delta x\right)}{a - b \sum_{p=0}^{\infty} C_{coupled_p} \cos\left(p k_y \Delta y\right) - c \sum_{p=0}^{\infty} C_{coupled_p} \mathrm{e}^{-ipk_x \Delta x}}, \tag{3.45}$$

where

$$\begin{cases} a = & \mathrm{e}^{i\omega\Delta t} - (2 + \alpha_y) + \mathrm{e}^{-i\omega\Delta t} (1 + 2\alpha_y) - \alpha_y \mathrm{e}^{-2i\omega\Delta t}, \\ b = & 2V_y \frac{\Delta t}{\Delta y} \left(1 - \alpha_y \mathrm{e}^{-i\omega\Delta t}\right), \\ c = & 2\beta_y \frac{\Delta t}{\Delta x} \left(1 - \mathrm{e}^{-i\omega\Delta t}\right). \end{cases} \tag{3.46}$$

To determine the coefficient of reflection on an inter-node, $r_{inter-node}$ is obtained by replacing α_y with α_x^* and β_y with β_y^* in the definition of a, b and c.

To guide the reader, the details of the derivation of these equations are given for the second-order case in Appendices A and B, at the node and the inter-node respectively. A table summarizing the coefficients of reflections at grid nodes in various cases is tabulated in Table 3.1 with the corresponding coefficients a, b and c given in Eq. 3.35 for the 1D case, and in Eq. 3.46 for the 2D case. The coefficient of reflection at grid inter-nodes are expressed similarly as expressions at grid nodes, with coefficients $(\alpha_x, \alpha_y, \beta_x, \beta_y)$ replaced by $(\alpha_x^*, \alpha_y^*, \beta_x^*, \beta_y^*)$.

Table 3.1: Key equations of the coefficients of reflection in PML.

Order of accuracy	Plane wave at normal incidence (1D)	Plane wave at oblique incidence (2D)
2	$r_{node} = \frac{a-b(-1+\cos(k_x\Delta x))}{a-b(-1+\mathrm{e}^{-ik_x\Delta x})}$	$r_{node} = \frac{a-b\cos(k_y\Delta y)-c\cos(k_x\Delta x)}{a-\cos(k_y\Delta y)-c\mathrm{e}^{-ik_x\Delta x}}$
>2	$r_{node} = \frac{a-b\sum_{p=0}^{\infty} C_{coupled_p}\cos(pk_x\Delta x)}{a-b\sum_{p=0}^{\infty} C_{coupled_p}\mathrm{e}^{-ipk_x\Delta x}}$	$r_{node} = \frac{a-b\sum_{p=0}^{\infty} C_{coupled_p}\cos(pk_y\Delta y)-c\sum_{p=0}^{\infty} C_{coupled_p}\cos(k_x\Delta x)}{a-b\sum_{p=0}^{\infty} C_{coupled_p}\cos(pk_y\Delta y)-c\sum_{p=0}^{\infty} C_{coupled_p}\mathrm{e}^{-ipk_x\Delta x}}$

3.2.2 Coefficient of the entire PML, R

Following [188], we apply the PML from j_0 to $j_0 + N_L$, where j_0 is the index where the interface of vacuum and the PML media lies and N_L is the depth of the PML (in number of

nodes). The knowledge of the coefficients of reflection and transmission of two consecutive slices, say slices at $j_0+N_L-1/2$ and j_0+N_L, allows us to calculate the coefficient of reflection $R_{j_0+N_L-1/2}$ because of the coupling of these two slices.

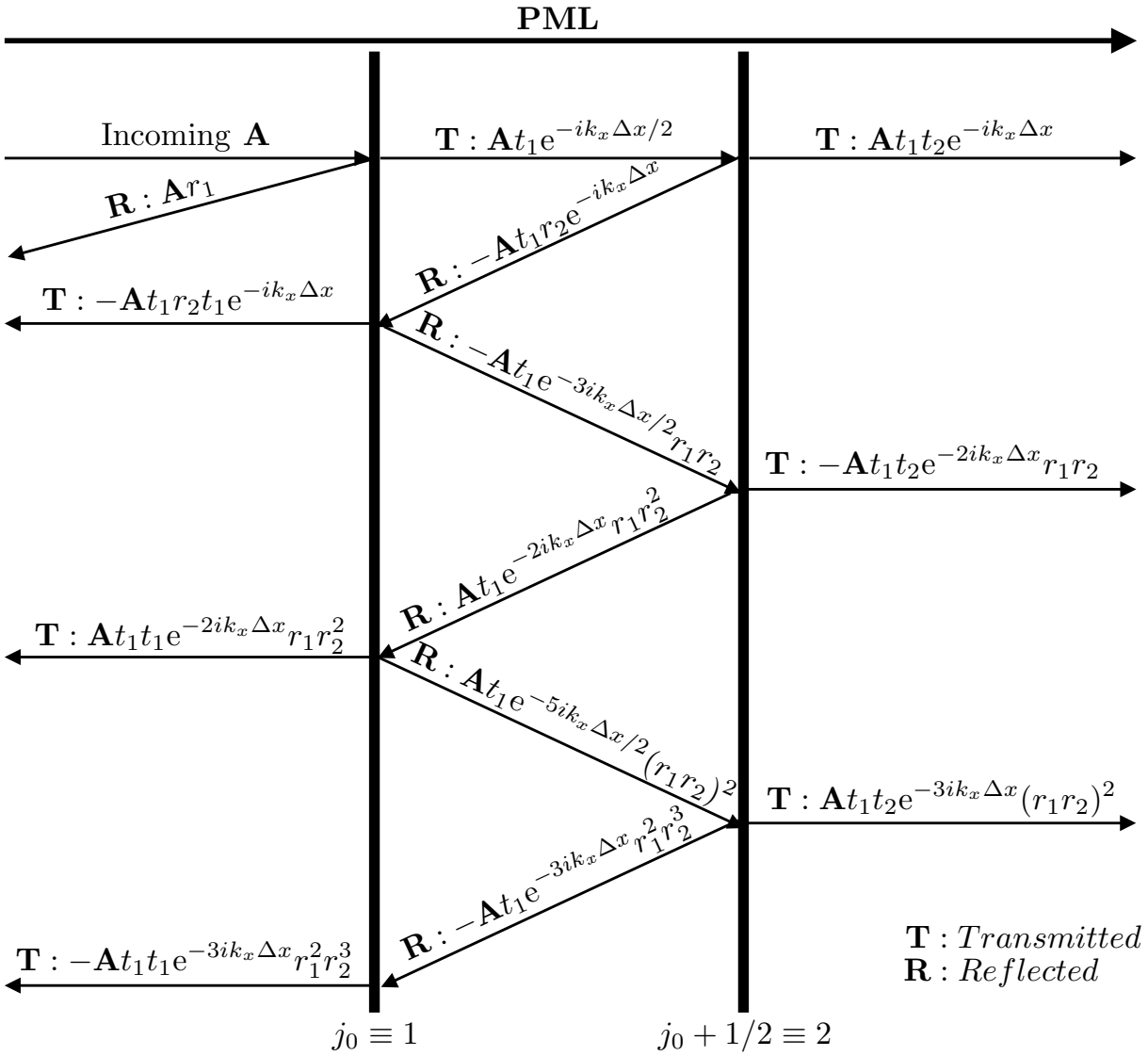

Figure 3.3: A plane wave striking a PML generates multiple reflections inside the layer that must be taken into account to calculate the coefficient of reflection.

Fig. 3.3 illustrates the reflections and transmissions of the wave of the two consecutive slices.

$$\begin{aligned} R_{j_0+N_L-1/2} &= r_1 - t_1r_2t_1\mathrm{e}^{-ik_x\Delta x} + t_1r_2t_1\mathrm{e}^{-ik_x\Delta x}(r_1r_2\mathrm{e}^{-ik_x\Delta x}) \\ &\quad - t_1r_2t_1\mathrm{e}^{-ik_x\Delta x}(r_1r_2\mathrm{e}^{-ik_x\Delta x})^2\ldots \\ &= r_1 - t_1r_2t_1\mathrm{e}^{-ik_x\Delta x}\textstyle\sum_{n=0}^{\infty}(r_1r_2\mathrm{e}^{-ik_x\Delta x})^n \\ &= r_1 - \tfrac{t_1r_2t_1\mathrm{e}^{-ik_x\Delta x}}{1+r_1r_2\mathrm{e}^{-ik_x\Delta x}}. \end{aligned} \tag{3.47}$$

To calculate the coefficient of reflection of the entire layer, R_{j_0}, we iterate backward from $j = j_0 + N_L$ to $j = j_0$ using the recursive formula

$$R_j = r_j - \frac{t_jR_{j+1/2}t_j\mathrm{e}^{-ik_x\Delta x}}{1 + r_jR_{j+1/2}\mathrm{e}^{-ik_x\Delta x}}. \tag{3.48}$$

This formula is valid at all dimensions and, under the assumptions of the model, at all orders.

3.2.3 Coefficient of reflection via numerical simulations

For the evaluation of the coefficient of reflection via numerical experiments, an electromagnetic pulse is injected at $t = 0$ at the left-hand side of the simulation region, in a vacuum region preceding the PML that is situated at the right-hand side. Periodic boundaries are applied to the upper and lower sides. The simpler case of a plane wave at normal incidence to the PML media is studied first, followed by a study of a plane wave traveling at an angle of incidence to the PML.

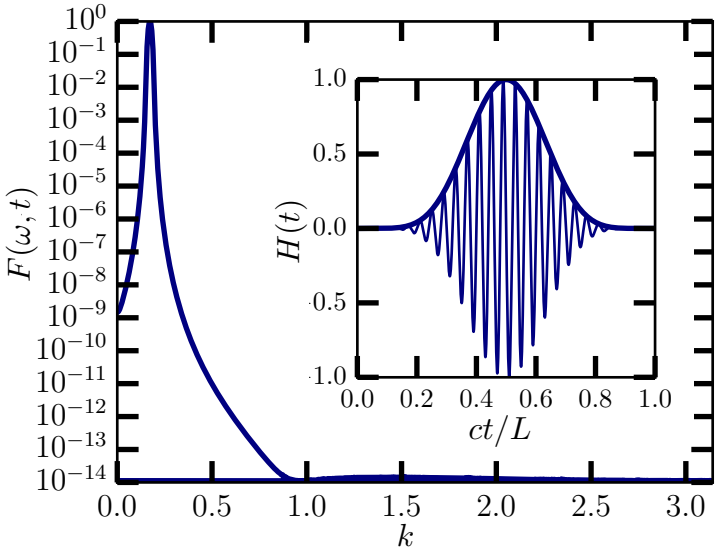

Figure 3.4: Fourier transform of $F(\omega, t, k_y = 0)$ with respect to the wavenumber k shows that the signal is nearly monochromatic. Inset: Harris function $H(t)$ and $F(\omega, t, k_y = 0)$ plotted versus time normalized by L/c.

The injected signal is imposed at the left-hand side $E_{y_0}^0 = F(\omega, t, k_y)$ has the form

$$F(\omega, t, k_y) = \begin{cases} H(t)\sin(\omega t + k_y y), & \text{if } 0 < t < \frac{L}{c}, \\ 0, & \text{otherwise,} \end{cases} \tag{3.49}$$

with $y = k\Delta y$, where k is the index in the transverse $(y-)$ direction, and $H(t)$ the Harris function

$$H(t) = \begin{cases} \frac{1}{32}(10 - 15\cos(\frac{2\pi ct}{L}) + 6\cos(\frac{4\pi ct}{L}) - \cos(\frac{6\pi ct}{L})), & \text{if } 0 < t < \frac{L}{c}, \\ 0, & \text{otherwise,} \end{cases} \tag{3.50}$$

where $L = \Delta x N_x$ represents the position at which the interface between the vacuum and the PML lies and c is the speed of the waves. A plot of this function versus time is reproduced in Fig. 3.4. The product of the $\sin\omega t$ function with the Harris function enables a precise inspection of the coefficient of reflection as a function of frequency.

For convenience, a signal injected with a wavenumber k_0, the transverse wavenumber k_y is set for a grid with N_y cells and periodic boundary condition in the transverse dimension,

such that $k_y = 2\pi N/(N_y \Delta y)$ where $N \in \mathbb{N}$. The longitudinal wavenumber is thus given by $k_x^2 = k_0^2 - k_y^2$ and the angle of incidence θ is defined as $\theta = \arctan(k_x/k_y)$

Once the injected pulse fills the vacuum region preceding the PML, the electric and magnetic field components $E_{x_{inc}}$, $E_{y_{inc}}$ and $B_{z_{inc}}$ are recorded, while the reflected components $E_{x_{ref}}$, $E_{y_{ref}}$ and $B_{z_{ref}}$ are recorded after the incident pulse has been fully reflected by the PML. The coefficient of reflection is then computed as

$$R(\omega, \theta) = \sqrt{\frac{\sum_{j<N_x} \sum_{k<N_y} \left(E_{x_{ref}}^2 + E_{y_{ref}}^2 + c^2 B_{z_{ref}}^2 \right)}{\sum_{j<N_x} \sum_{k<N_y} \left(E_{x_{inc}}^2 + E_{y_{inc}}^2 + c^2 B_{z_{inc}}^2 \right)}}, \tag{3.51}$$

where the subscript "ref" signifies reflected and "inc" signifies incident, j and k are respectively the grid indices in the transverse directions.

3.3 Results

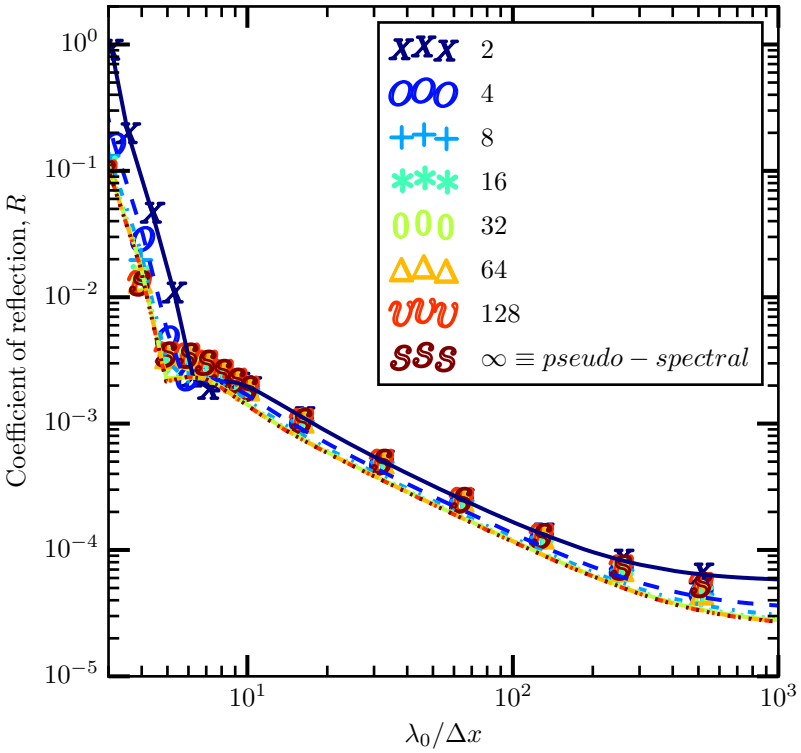

Figure 3.5: Coefficient of reflection, R with respect to the normalized wavelength of a plane wave striking a PML at normal incidence (lines: analytical integration; markers: numerical simulations), for different orders going from 2 to infinity ($\equiv$ pseudo-spectral).

In this section, we compare the coefficient of reflection from a PML for the FDTD solver (of orders 2 to higher orders) and the PSTD solver, as a function of wavelengths and angles, in the case $\Delta x = \Delta y$. To ensure stability at any order, the time-step was chosen to be $c\Delta t/\Delta x = 0.4$, which is slightly below the Courant condition of the PSTD solver when $\Delta x = \Delta y$. Following [23], we define

$$\sigma_j = \sigma_{max} \left(\frac{j \Delta x}{\delta} \right)^n ,$$

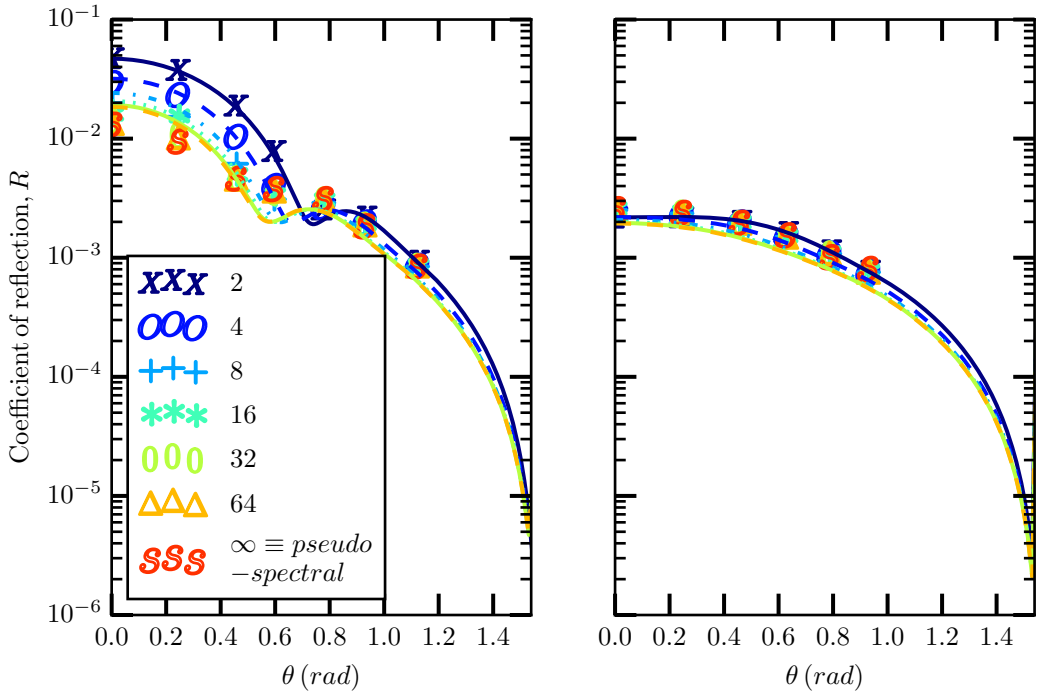

Figure 3.6: Coefficient of reflection, R of a plane wave with respect to its angle of incidence with the PML, for (a) $\lambda_0/\Delta x = 4$ and (b) $\lambda_0/\Delta x = 8$ (lines: analytical integration; markers: numerical simulations).

with $j \in [0; N_L]$ where N_L is the depth of the PML (in number of nodes). The choice of N_L is based on the theoretical coefficient of reflection such that it is large enough, for a given profile of conductivity, that the reflections that occur on this last cell are negligible. Setting $\sigma_{max} = 4/\Delta x$, $\delta = 5\Delta x$ and $n = 2$, together with $N_L = 14$, lead to absorptions of the incident waves by orders of magnitude at any angle, for all wavelength $\lambda_0 > \Delta x/4$. In defining σ^*, one must take into account the half a step in the space grid since $\boldsymbol{E}$ and $\boldsymbol{B}$ are staggered in space, therefore $\sigma^* = \sigma_{j+1/2}$.

Fig. 3.5 presents the coefficient of reflection of a plane wave that is striking a PML at normal incidence, as a function of wavelength. Figs. 3.6(a) and 3.6(b) show the coefficient of reflection of a plane wave with respect to the angle of incidence for a given wavelength, while Figs. 3.7(a) and 3.7(b) show the theoretical estimates for larger wavelengths. The results show that the efficiency of the PML is preserved at any order and even improved at short wavelengths with higher orders. This is also verified by the PSTD solver for which, as expected, the coefficients of reflection are very close to the ones of the FDTD solver at very high order. Tests on other wavelengths and time-steps (not shown here) show the same trend.

There is generally a good agreement between the analytical calculation (represented by solid lines) and the numerical results (represented by markers), but with some discrepancies at higher orders. In fact, at high order, more neighboring grid nodes are taken into account, these nodes are also wave sources themselves, known as "secondary sources". With the current model, these secondary sources are not taken into account, resulting in the mismatch. This is the reason why the discrepancies increase with the order of discretization. Evaluation of improved analytical estimates has been conducted by Vincenti et al. [192].

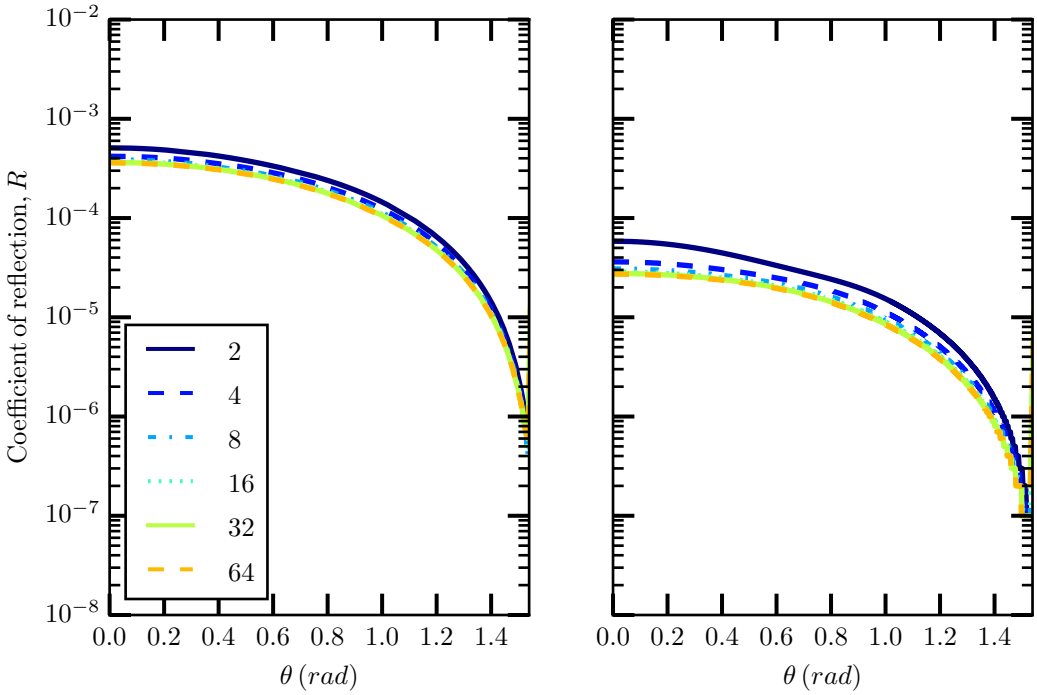

Figure 3.7: Theoretical estimates of the coefficient of reflection, R with respect to angle of incidence with the PML, for (a) $\lambda_0/\Delta x = 32$ and (b) $\lambda_0/\Delta x = 1024$.

3.4 Conclusion

Through this work, we have extended the theoretical and numerical analysis of the coefficient of reflection of PML layers to solvers of any order of accuracy, including at the limit of the infinite order that represents the pseudo-spectral formulations. Results from the analysis, confirmed by numerical simulations, show that the efficiency of PML layers is preserved at high order, and with the PSTD solver.

The analytical expressions that were developed here can be used to predict the coefficients of reflection in various situations with relatively high accuracies. This provides a tool for optimizing the absorption profile in PML layers. The mismatch between the analytical and numerical solutions comes from the fact that only the primary source is considered at high orders [192]. For a fixed LWFA simulation configuration, these analytical expressions can be used to compute an optimal choice of numerical parameters, e.g. the stencil order, space and time-steps so that the solution can be computed in a minimum time and with a guaranteed accuracy.

Chapter 4

Speeding up the simulation

In 2014, Leemans et al. have demonstrated experimentally with supporting numerical modeling the generation of electron beams with an energy of 4.2 GeV using 16 J of laser energy in a 9 cm-long-capillary, a new energy record in LWFA [132]. This is not only challenging experimentally but also in numerical modeling. In this particular case, simulations using the measured laser pulse temporal and spatial profiles propagating in 9 cm-long-capillary were carried out using PIC code INF&RNO [28] in 2D cylindrical coordinates. A typical [2]simulation of such has taken $\sim$ 1 Million Core-Hours (CH) in the case with the highest resolution ($N_z/\lambda_0 = 400$, $N_r/\lambda_0 = 10$), where N_z and N_r refer to the number of grid-points in the longitudinal and transverse directions respectively.

The tremendous increases in laser power and energy, permitting beam energies beyond 10 GeV in the next decade implies that more computational time will be required. To scale up with this, two approaches may be considered: (i) simulations with reduced model, (ii) advances in high performance computing. This chapter focuses a method that curtails computational time by several orders of magnitude: the Lorentz-boosted frame technique [31]. We will first give a brief introduction on the concept, then carry on discussing the accuracy and the speedup for a 100 MeV electron bunch modeling.

Contents

[2]This information is obtained through private communication with the author.

4.1 Overview

Modeling LWFA experiments using PIC algorithm consist of resolving the evolution of a laser driver and an accelerated particle beam into a plasma structure that is of orders of magnitude longer and wider than the accelerated beam. The laser wavelength is usually on the scale of 1 μm while the length of the plasma structure can be on the scale of 1 to 10^3 mm, this disparity in cell size and propagation distance results in very computationally intensive simulations.

Customarily, a moving window that follows the driver, the plasma wave and the accelerated beam is commonly used to save computational time by avoiding meshing the entire plasma that is orders of magnitude longer than other length scales of interest. In a moving window, grid-points in front of the laser are added and grid-points far behind the laser are removed so that the number of grid-points to be resolved is always the same throughout the simulation. However, despite the use of the moving window, a full 3D PIC simulation of a laser plasma accelerator can still be very demanding computationally, as many time-steps are needed to resolve the crossing of the short driver beam with the plasma structure.

The scale gap between the laser pulse and the plasma structure can be reduced by choosing an optimal frame of reference that travels close to the speed of light in the direction of the laser pulse [31], this optimal frame is known as the Lorentz-boosted frame. This change of frame of reference leads to Lorentz contraction and dilation of space and time: the laser pulse wavelength increases and the plasma length shortens, leading to gains both in space and in time, as the crossing time between the laser pulse and the plasma column is reduced. In addition, the plasma column drifts relativistically towards the laser pulse. The choice of the optimal frame is constrained by the resolution required in the Lorentz-boosted frame to capture the relevant plasma structures, and thus depends on the physical problem under consideration.

As previously mentioned in Sec. 2.2.3, the relativistic flowing plasma results in Numerical Cerenkov instability that disrupts the simulation. Several solutions that involve strong smoothing of the currents and fields [193, 172, 194, 178, 195, 196], or arbitrary numerical corrections [197, 198, 199], and the use of Galilean coordinates [200, 201] have been proposed to mitigate this problem.

Another issue that requires equal attention is the accuracy of the simulation results using the Lorentz-boosted frame technique. Simulations with external injection [194] was previously studied and the results on the evolution of the laser and electron beam properties have a 99% agreement between simulations using various reference frames. In [202], the author has studied the convergence of the evolution of the laser between the laboratory (lab) frame in quasi-3D geometry and in the boosted frame, results obtained demonstrated nice agreement in the case without self-injection, however some discrepancies are observed in the case with self-injection of electrons.

In general, the modeling of the self-injection regime poses some challenges due to the strong nonlinear particle dynamics. The choice of the velocity of the boosted frame is normally chosen to be the velocity of the laser group velocity in the linear regime, but in the nonlinear regime, no analytical theory is provided to estimate this quantity, therefore we measure the laser group velocity from existing simulations in the nonlinear regime to determine the optimal velocity of the boosted frame.

The community is also convinced that an accurate result can be obtained with a high number of macro-particles in the injected bunch to allow for significant statistics [176, 202]. These articles only consider the electron bunch charge and energy, while analysis on the

beam emittance, which is sensitive to the numerical resolution [203] is not presented. Here we will show that simulations using the Lorentz-boosted frame technique at high resolution retains the accuracy in the self-injection regime with significant speedup.

4.2 Concept

The Lorentz-boosted frame technique requires one to choose a frame moving near the speed of light in the direction of the laser pulse. This approach exploits the properties of space and time dilation and contraction associated with the Lorentz transformation without alteration to the fundamental equations of particle motion or electrodynamics. The Lorentz transformation results in the expansion of waves emitted by the plasma in the forward direction and the contraction of the ones emitted in the backward direction, indicating that this approach may not resolve all backward propagating waves.

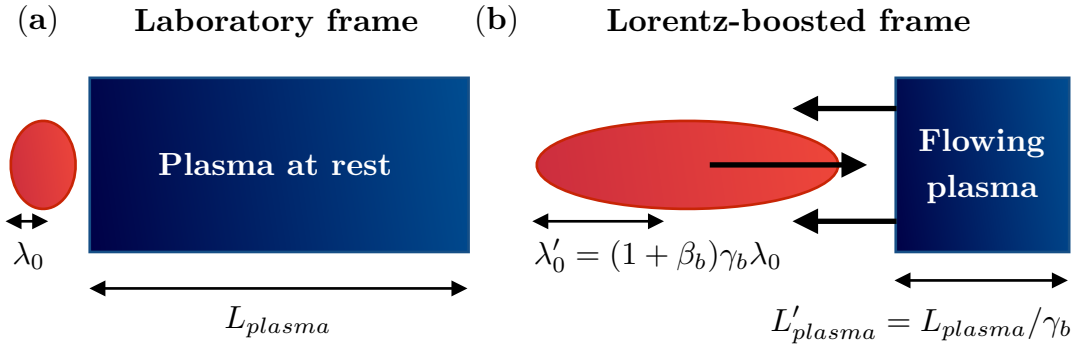

Figure 4.1: Principle of the Lorentz-boosted frame technique. (a) A LWFA simulation which consists of a laser pulse of wavelength λ_0 propagating through a plasma at rest of length L_{plasma} that is of orders of magnitude longer requires a very large number of time-steps. (b) Choosing a frame of reference that is moving close to the speed of light, γ_b in the direction of the laser pulse results in a new longer laser wavelength, λ_0' and a shorter plasma length, L'_{plasma}. The relativistic transformation of space and time reduces the disparity of scales and thereby the number of time-steps to complete the simulation, by orders of magnitude. Adapted from [204].

Fig 4.1 illustrates the concept of the Lorentz-boosted frame technique. Fig 4.1(a) shows that modeling a laser pulse with a wavelength of λ_0 on the order of $\sim 1\,\mu$m traversing the plasma at rest of length L_{plasma} on the order of ~ 1 mm in the lab frame requires at least 10^6 time-steps. Recasting this simulation in a Lorentz-boosted frame at velocity $v_b = \beta_b c$ or in the Lorentz factor γ_b where $\gamma_b = (1-\beta_b)^{-1/2}$ observes a dilation of λ_0 by a factor of $(1+\beta_b)\gamma_b$ and a contraction of L_{plasma} by a factor of γ_b as shown in Fig 4.1(b), thus the number of time-steps that is needed to simulate the laser pulse of λ_0' through a plasma of L'_{plasma} is reduced by a factor of $\gamma_b^2(1+\beta_b)^2$ (see below for the details of the speedup derivation).

The physics of interest in LWFA is the plasma wave driven by the laser pulse, the laser pulse and the accelerated electron beams, the backscatter is weak in the short pulse regime and does not interact strongly with the electron beams as do the forward propagating waves, therefore it can be neglected in the modeling of the plasma accelerator stages. Once the backward-propagating waves arrive at the boundary on the [3]left, it can be efficiently taken care of by the PML (details in Chapter 3). Since all the components of interest

propagate in the forward direction, simulating LWFA experiments in the Lorentz-boosted frame technique is therefore very well adapted.

4.2.1 Theoretical speedup dependency with the Lorentz-boosted frame

The derivation of the speedup reproduced here follows the one given in [205], an extension of [31], which takes into account the group velocity of the laser.

Assuming that the number of plasma periods is fixed in the simulation box, implying the use of the moving window following the laser-driven plasma wave and accelerated electron beam, the speedup is given by the time taken by the laser pulse and the plasma to cross each other, divided by the shortest time scale of interest, that is the laser period. For instance, according to the plasma fluid theory, the plasma wave velocity v_ϕ is set by the laser group velocity in the linear regime, $v_g = c(1 - \omega_p^2/\omega_0^2)^{1/2}$. Therefore the Lorentz factor of the boosted frame γ_b can be chosen to be $\gamma_g = (1 - (v_g/c)^2)^{-1/2}$.

In practice, the stopping condition of a simulation is set in a way such that the last electron beam macro-particle exits the plasma, a measure of the total time of the simulation is then given by

$$T = \frac{L_{plasma} + \eta\lambda_p}{v_g - v_\phi}, \tag{4.1}$$

where λ_p is the plasma wave wavelength, L_{plasma} is the plasma length, v_g and v_ϕ are respectively the group velocity of the laser pulse and the phase velocity of the plasma wave relative to the frame of reference, and η is an adjustable parameter that determines the fraction of the plasma wave to be considered which exits the plasma at the end of the simulation. For instance, an electron beam injected into the n^{th} bucket, η would be set to $n - 1/2$. The numerical cost R_t is thus defined by the ratio of the total time to the shortest time scale of interest:

$$R_t = \frac{Tc}{\lambda_0} = \frac{(L_{plasma} + \eta\lambda_p)}{(\beta_g - \beta_\phi)\,\lambda_0}, \tag{4.2}$$

where $\beta_g = v_g/c$ and $\beta_\phi = v_\phi/c$.

In the lab frame $v_\phi = 0$ because the plasma is at rest, the expression simplifies to

$$R_{lab} = \frac{(L_{plasma} + \eta\lambda_p)}{\beta_g\lambda_0}. \tag{4.3}$$

In a frame moving at $\beta_b c$, the quantities become

$$\begin{cases} \lambda_\phi^* = \lambda_\phi/\gamma_b\,(1 - \beta_g\beta_b) \\ L_{plasma}^* = L_{plasma}/\gamma_b \\ \lambda_0^* = \gamma_b\,(1 + \beta_b)\,\lambda_0 \\ \beta_g^* = (\beta_g - \beta_b)\,/\,(1 - \beta_g\beta_b) \\ v_\phi^* = -\beta_b c \\ T^* = \left(L_{plasma}^* + \eta\lambda_\phi^*\right)/(v_g^* - v_\phi^*) \\ R_t^* = T^* c/\lambda_0^* = \left(L_{plasma}^* + \eta\lambda_p^*\right)\,/\,\left(\beta_g^* + \beta_b\right)\,\lambda_0^* \end{cases} \tag{4.4}$$

[3]By default, the forward propagating waves travel to the right and the backward propagating waves travel to the left in a simulation.

where $\gamma_b = 1/\sqrt{1-\beta_b^2}$.

The estimated speedup from performing the simulation in a boosted frame is given by the ratio of R_{lab} to R_t^*

$$S = \frac{R_{lab}}{R_t^*} = \frac{(1+\beta_b)\left(L_{plasma}+\eta\lambda_p\right)}{L_{plasma}\left(1-\beta_b\beta_g\right)+\eta\lambda_p}. \tag{4.5}$$

If we assume $\beta_g \approx 1$ (which is a valid approximation for most practical cases of interest) and that $\gamma \ll \gamma_g$, the expression Eq. 4.5 tends to the expression derived in [31] for the LWFA case which states that $R_t^* = \alpha R_t/(1+\beta)$ with $\alpha = (1-\beta+l_0/L_{plasma})/(1+l_0/L_{plasma})$, where l_0 is the laser length and is proportional to $\eta\lambda_p$, and $S = R_t/R_t^*$. In general, we aim for higher values of γ_b for maximum speedup.

For accelerator applications, the energy gain is limited by the electron dephasing length [60] that scales as $\sim \lambda_p^3/2\lambda_0^2$ (refer to Sec. 1.5). Acceleration is compromised beyond L_d and in practice, the plasma length is proportional to the dephasing length, i.e. $L_{plasma} = \kappa L_d$, where κ is an adjustable factor. In most cases, $\gamma_g^2 \gg 1$, thus we can approximate $\beta_g \approx 1 - \lambda_0^2/2\lambda_p^2$, and $L_{plasma} = \kappa\lambda_p^3/2\lambda_0^2 \approx \kappa\gamma_g^2\lambda_p/2 \gg \eta\lambda_p$, so that Eq. 4.5 becomes

$$S = (1+\beta_b)^2\gamma_b^2 \frac{\kappa\gamma_g^2}{\kappa\gamma_g^2 + (1+\beta_b)\,\gamma^2\,(\kappa\beta_b/2 + 2\eta)}. \tag{4.6}$$

Eq. 4.6 can be reduced to a more tractable form according to the scenarios as shown in Table 4.1.

Table 4.1: Speedups, S according to values of γ_b

	S (Eq. 4.6)
$\gamma_b \ll \gamma_g$	$(1+\beta_b)^2\gamma_b^2$
$\gamma_b = \gamma_g$	$\frac{2}{1+2\eta/\kappa}\gamma_g^2$
$\gamma_b \to \infty$	$\frac{4}{1+4\eta/\kappa}\gamma_g^2$

Since η and κ are of order unity, and most regimes for accelerator applications in LWFA satisfy $\gamma_g \gg 1$, the speedup that is obtained by using the frame of the plasma wave will be near the maximum obtainable value given by $S_{\gamma_b=\gamma_g\to\infty} = 4\gamma_g^2/(1+4\eta/\kappa)$. However, in the laser-plasma injector, the physics is highly nonlinear, no analytical theories exist, for the moment, that allows a precise determination of γ_g, therefore a lower γ_g than the one predicted using the linear plasma fluid theory is considered, so is the choice for γ_b [206]. To ensure accuracy in results using the Lorentz-boosted frame technique, we choose, in practice, a γ_b that is $\sim 20\%$ of γ_g predicted based on the linear plasma fluid theory. Although the speedup will only scale as $(1+\beta_b)^2\gamma_b^2$, low γ_b reduces the risk of having numerical Cerenkov instability that disrupts the simulation.

Notice that without the use of a moving window, the relativistic effects that are at play in the time domain would also be at play in the spatial domain [31], and the γ^2 scaling would become γ^4. If high γ_b is used, the optimal velocity of the moving window may vanish (i.e no moving window) or even reverse.

4.3 Simulation setups

This section presents the modeling of the dynamics of the self-injected electrons in the blowout regime in 2-1/2D using the Lorentz-boosted frame technique implemented in Warp.

Table 4.2: List of parameters for a LWFA electron injector simulation at 100 MeV

Plasma density on axis	n_0	$10^{19}\,\mathrm{cm}^{-3}$
Plasma longitudinal profile		Flat
Plasma transverse profile		Uniform
Plasma length	L_{plasma}	$500\,\mu$m
Plasma entrance ramp profile		linear
Plasma entrance ramp length		$50\,\mu$m
Laser profile		[4]bi-Gaussian
Laser polarization		linear (in $y-$direction)
Laser focal position	z_f	0 mm
Peak normalized laser field strength	$a_0(z_f)$	5
Laser wavelength	λ_0	$0.8\,\mu$m
Normalized laser spot size	$k_p\sigma$	5.3
Normalized laser length	k_pL	2
Number of grid-points in x		600
Boundary conditions		Open boundaries in $x-$, $z-$directions with PML
Stencil order (for PSATD solver)		32
Cell size in x		$0.083\,\mu$m
Cell size in z		$\lambda_0/128 - \lambda_0/16$
Time-step		At the CFL limit
Particle deposition order		Cubic
Number of plasma particles/cell		4×4 (in $x-$, $z-$directions)

The main physical and numerical parameters of the simulations are given in Table 4.2. They were chosen to be close (though not identical) to a case reported in [207, 193], with the main difference being the value of $a_0 = 5$. In fact, the main aim here is to trigger electron self-injection in the wakefield in order to study its dynamics, thus a high a_0 allows for wavebreaking, a necessary condition for electron self-injection. These simulations are for a fully resolved 100 MeV stage at a density of $10^{19}\,\mathrm{cm}^{-3}$, which can be scaled to describe a 1 GeV stage at a density of $10^{18}\,\mathrm{cm}^{-3}$. The latter is one of the configurations that is being considered as the first stage in the EuPRAXIA project [21]. These simulations are run using both the CK and the PSATD solvers, and with the 4-pass stride-1 filter plus compensation [172]. The CK solver is chosen instead of the standard Yee solver because it improves the dispersion properties while at the same time increasing the stable time-step to $\Delta t = \Delta z/c$. All conducted simulations do not show any sign of numerical instabilities with the settings reported here.

The laser group velocity evaluated for the given parameters using the linear plasma fluid theory is $\gamma_g \approx 13.2$. Warp simulations are performed for γ_b between 1 and 13 and for longitudinal resolutions ranging from $N_z/\lambda_0 = 16$ to $N_z/\lambda_0 = 128$. Note that $\gamma_b = 1$ is the lab frame. The plasma wave simulated in a boosted frame associated with a specific γ_b approaching γ_g in the laboratory is expected to travel at low velocity. The physical features observed in the boosted frame are somewhat different from the ones in the lab frame, in accordance with the properties of the Lorentz transformation [172, 193], rendering direct comparison impossible. Thus to enable comparison between simulations with different γ_b,

we have to make use of the inverse Lorentz transformation to convert boosted frame data back to the lab frame data. The reconstruction of the lab frame data from the boosted frame data is described in the following section.

4.3.1 Correlation between lab and boosted frame data

Conversion of boosted frame quantities back to lab quantities is necessary in order to apply the boosted frame technique to experimental modeling. The relations that make this conversion possible are the inverse Lorentz transformations:

$$\begin{aligned} ct &= \gamma_b \left(ct' + \beta_b z'\right), \\ x &= x', \\ y &= y', \\ z &= \gamma_b \left(z' + \beta_b ct'\right). \end{aligned} \tag{4.7}$$

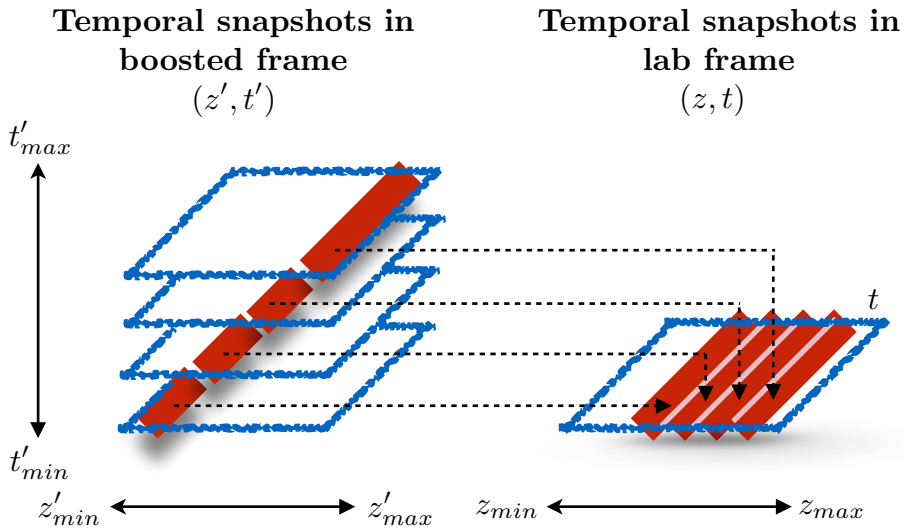

Figure 4.2: Reconstruction of a lab temporal snapshot from a sequence of temporal snapshots in the boosted frame. For instance, a laboratory snapshot at time t requires data from a time range t'_{min} to t'_{max} in the boosted frame. Adapted from [176].

As shown in Fig. 4.2, several boosted frame snapshots of time ranging from t'_{min} to t'_{max} are necessary to reconstruct a temporal snapshot in the lab frame of time t. The boosted frame quantities have to be first inversely Lorentz transformed and then recombined to yield the laboratory snapshot. To achieve this, two approaches can be used: (i) implement this directly in the simulation code such that the laboratory snapshots are built from boosted quantities in runtime, (ii) set up some fixed diagnostic stations in the laboratory planes, then store the histories at these planes. Regardless of the approach, some quantities, e.g. charge or dimensions perpendicular to the boost velocity are Lorentz invariant. Those quantities are therefore readily available from standard diagnostics in the boosted frame calculations. Quantities which do not fall into this category are obtained by simple Lorentz transformation by assuming time invariance. In Warp, the implementation uses Approach (ii) [193]. Since the space-time locations generally do not coincide with the space-time positions of the macro-particles and grid nodes used for the calculation in a boosted frame, some interpolation is

[4]Gaussian in temporal and spatial profiles

performed at runtime during data collection process. This manipulation induces a negligible loss of accuracy. To prevent further loss of information, boosted quantities that have crossed the diagnostic stations are saved in a buffer at each time iteration, and dumped at regular interval for post-processing.

4.4 Results

4.4.1 Cole-Karkkainen solver

Simulations were conducted using the CK solver with the parameters shown in Table 4.2. These parameters are chosen to enable self-injection of electrons. Simulations using Warp are performed for relativistic boost factor $\gamma_b \in [1, 2, 3, 4, 5, 10, 13]$ and for each γ_b, a sweep of the longitudinal resolution, N_z/λ_0 from 16 to 128 is carried out.

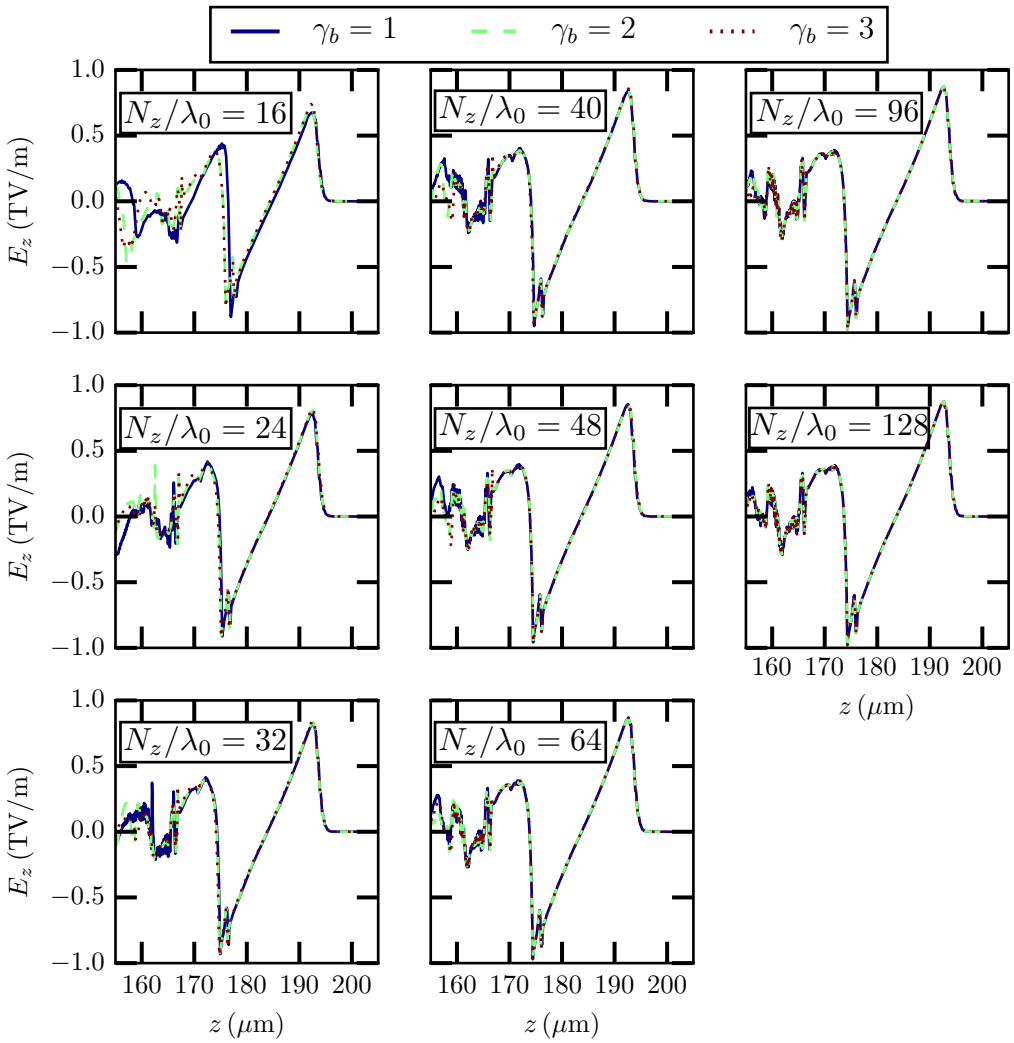

Figure 4.3: A series of plots showing wakefield at $z = 200\,\mu$m. Each panel corresponds to a specific longitudinal resolution given in the box on the upper left corner. In each panel is shown the wakefield of 2-1/2D simulations in the CK solver carried out with $\gamma_b \in [1, 2, 3]$. Note that $\gamma_b = 1$ represents the simulation in the lab frame.

Preliminary results show that the convergence is not attained for $\gamma_b > 3$, therefore those results will not be included here. As mentioned earlier, the high nonlinear effects

in this regime, such as self-compression or self-focusing of the laser pulse put a constraint on the choice of the γ_b. In this regard, γ_b cannot be given directly by the laser group velocity predicted by the linear plasma fluid theory, however using a heuristic approach and measurements from existing simulations, γ_b can be estimated to be $0.2\gamma_g$, with γ_g predicted by the linear plasma fluid theory. Because of this low γ_b, no evidence of numerical Cerenkov instabilities is observed.

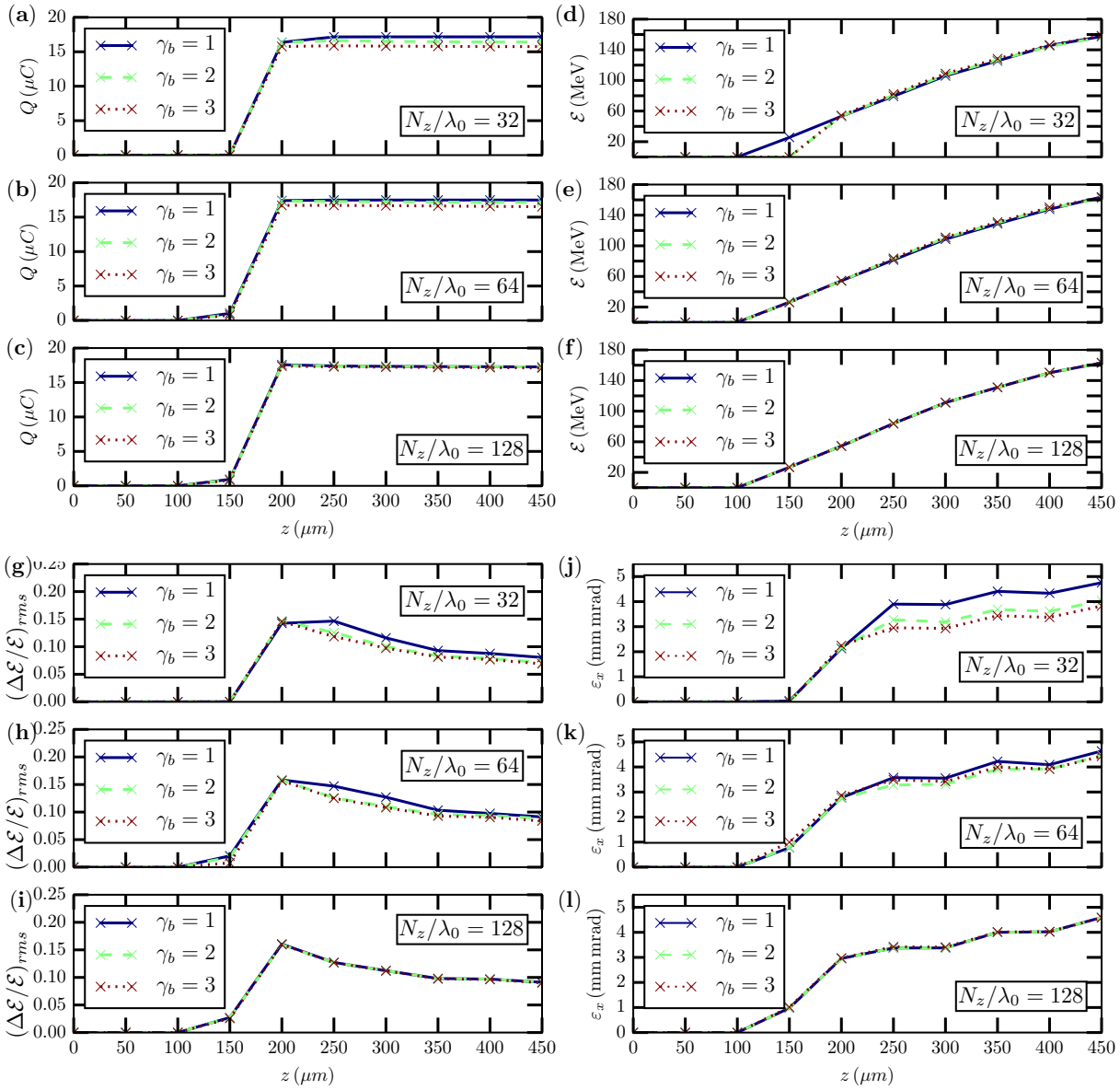

Figure 4.4: Evolution of the injected electron bunch properties with respect to z, the distance of propagation in the plasma. Each plot illustrates simulations using different $\gamma_b \in [1, 2, 3]$ at a specific longitudinal resolution, $N_z/\lambda_0 \in [32, 64, 128]$ as indicated by the legend. Evolution of the electron bunch charge, Q is shown in (a-c); the average energy, $\langle\mathcal{E}\rangle$ in (d-f); the rms energy spread, $(\Delta\mathcal{E}/\mathcal{E})_{rms}$ in (g-i); transverse emittance ε_x in (j-l).

Fig. 4.3 shows a layout of the wakefield, E_z captured at $z = 200\,\mu$m. Each panel corresponds to a specific longitudinal resolution. Wakefield of simulations carried out with $\gamma_b \in [1, 2, 3]$ are compared in each panel. Results show some discrepancies among the wakefield especially at the back of the first blow-out structure at $N_z/\lambda_0 \leq 48$, however for

$N_z/\lambda_0 > 48$, we observe a convergence of all wakefield, and at $N_z/\lambda_0 = 128$, a nice agreement is obtained for all γ_b . The effect of beam loading is also visible for $N_z/\lambda_0 > 24$ at $z = 175\,\mu$m, confirming that the amplitude and the phase of beam loading are correctly recovered. This is further confirmed by the plot of the evolution of the injected bunch properties with respect to the propagation distance, z in the lab frame (see Fig. 4.4).

We now look at the evolution of the injected and accelerated electron bunch. Here we only consider electrons trapped in the first period plasma wave (or first bucket). Fig. 4.4 shows the evolution of the electron bunch properties as it propagates through the plasma for $\gamma_b \in [1, 2, 3]$. For each electron bunch property, only results for longitudinal resolution, $N_z/\lambda_0 \in [32, 64, 128]$ are shown. From Fig. 4.4(a-c), it is observed that the injection happens from $z = 100$ to $200\,\mu m$. For $z > 200\,\mu m$, the electron bunch charge remains constant, implying that self-injection of electrons in the first plasma period has ended. In Fig. 4.4(d-f) is shown the evolution of the average electron bunch energy. Once the electron bunch is injected, it is accelerated throughout the plasma to an average energy of 160 MeV at $z = 450\,\mu m$. The average accelerating field, $\langle E_z \rangle$ is estimated at 5.3 GeV/cm. The evolution of the rms energy spread, $(\Delta\mathcal{E}/\mathcal{E})_{rms}$ of the electron bunch shown in Fig. 4.4(g-i) suggests that it first reaches a maximum value at $z = 200\,\mu$m, then it decreases due to the increase of the average energy of the electron bunch. Finally it plateaus off to a rms energy spread of $\sim$ 10%. Fig. 4.4(j-l) shows the evolution of the transverse emittance, ε_x of the injected electron bunch. A rapid emittance growth is observed during the injection, this is because electrons circulate the spherical cavity before being injected, thus gaining transverse momentum along the trajectory in the self-injection scheme. As a result, the non-zero transverse momentum contributes to the rapid emittance growth. Once the injection phase is over, the emittance growth slows down. This slow growth is explained by the betatron movement of electrons. Since the betatron frequency depends on the energy of the individual electron, they do not all oscillate synchronously, resulting in the slow growth of the emittance. ε_x reaches ≈ 4.5 mm mrad at $z = 450\mu$m.

Fig. 4.4 shows some discrepancies between results given by simulations with $N_z/\lambda_0 \in [32, 64]$ especially for second-order beam properties such as the energy spread and the emittance. In particular, the transverse emittance at $N_z/\lambda_0 = 32$ (Fig. 4.4(b)), we observe a difference of the order of $\sim 10\%$ between $\gamma_b = 1$ and $\gamma_b = 3$, this gives an indication that the longitudinal resolution at $N_z/\lambda_0 = 32$ might not be sufficient to provide accurate modeling of the emittance. On the contrary, a nice agreement is observed for $N_z/\lambda_0 = 128$, suggesting that the higher the longitudinal resolution, the better the agreement between results from simulations with different γ_b. A convergence analysis is provided further in this section to enable quantitative comparison. For this analysis, we consider the average result from all considered relativistic boosted frames at $N_z/\lambda_0 = 128$ as the reference. We choose next to focus on a specific frame (at $z = 200\mu$m) for further and more thorough studies since results in Fig. 4.4 have shown that all electron bunch properties are modeled correctly at all distances of propagation, z for the highest longitudinal resolution $N_z/\lambda_0 = 128$.

Fig. 4.5 shows the injected and accelerated electron bunch (a) charge, (b) average energy, (c) rms energy spread, and (d) transverse emittance at frame $z = 200\mu$m with respect to the longitudinal resolution, N_z/λ_0. Each plot shows results from simulations with $\gamma_b \in [1, 2, 3]$. Notice that $\gamma_b = 1$ corresponds to the lab frame. There is a convergence of results obtained from simulations with different γ_b for all electron bunch properties. Taking the average value of all considered relativistic boosted frames $N_z/\lambda_0 = 128$ as the reference, it is observed that a resolution of $N_z/\lambda_0 = 64$ is required to be within 1% of difference even for the simulation in the lab frame. Results from $\gamma_b = 2$ and 3 converge within 1% of difference at $N_z/\lambda_0 = 48$

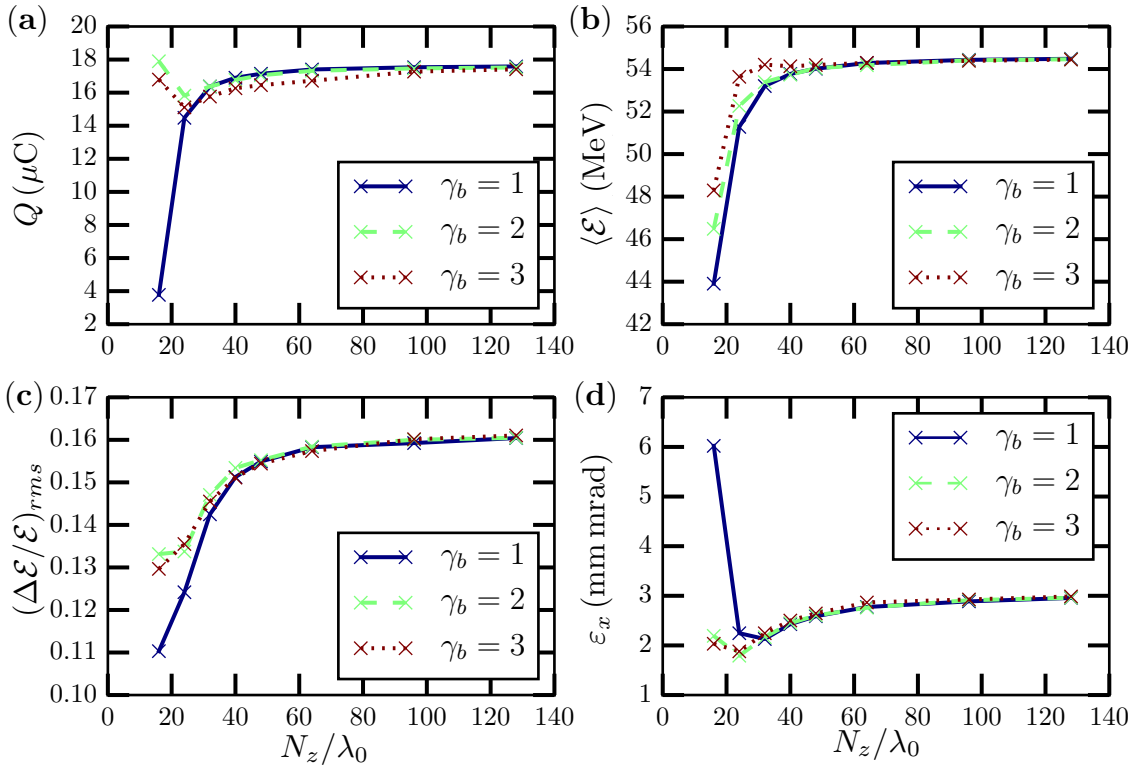

Figure 4.5: Properties of injected and accelerated electron bunch evaluated at $z = 200\,\mu m$ with respect to the longitudinal resolution for $\gamma_b \in [1, 2, 3]$. Simulations were carried out using Warp in 2-1/2D CK solver. Note that $\gamma_b = 1$ corresponds to the simulation in the lab frame. (a) Electron bunch charge, Q, (b) average energy, $\langle \mathcal{E} \rangle$, (c) rms energy spread, $(\Delta \mathcal{E}/\mathcal{E})_{rms}$ and (d) tranverse emittance with respect to longitudinal resolution, N_z/λ_0 are illustrated.

for the electron bunch average energy, the rms energy spread and the transverse emittance as shown in Fig. 4.5(b-d). Convergence for the bunch charge within 1% of difference is obtained at a higher resolution $N_z/\lambda_0 = 128$. The slow convergence in the electron bunch charge is due to a lack of transverse resolution, and we have verified that convergence was improving with increasing transverse resolution (not shown here).

We complete the analysis by presenting the difference in convergence among simulations of all considered γ_b. The convergence analysis takes the average of all considered relativistic factors at $N_z/\lambda_0 = 128$ as the reference case. This choice is made based on the fact that a convergence for all beam properties is attained at this resolution as shown in Fig. 4.5. Fig. 4.6(a-d) show the difference for each electron bunch properties represented in log scale in the y-axis with respect to N_z/λ_0. We observe that the difference in beam quantities decreases with respect to the resolution, implying that high longitudinal resolution helps in attaining convergence. For $\gamma_b = 1$ (lab frame) and $\gamma_b = 2$, the difference is less than 1% when $N_z/\lambda_0 \geq 64$ for all bunch properties except the beam emittance where a higher resolution ($N_z/\lambda_0 = 128$) is required to attain this difference margin. As for $\gamma_b = 3$, the difference drops to less than 1% for $N_z/\lambda_0 \geq 64$ for electron bunch average energy and rms energy spread, however a higher resolution ($N_z/\lambda_0 = 128$) is required to attain this difference margin for electron bunch charge and transverse emittance. We have verified that higher transverse resolution can help in reducing the required longitudinal resolution to attain convergence.

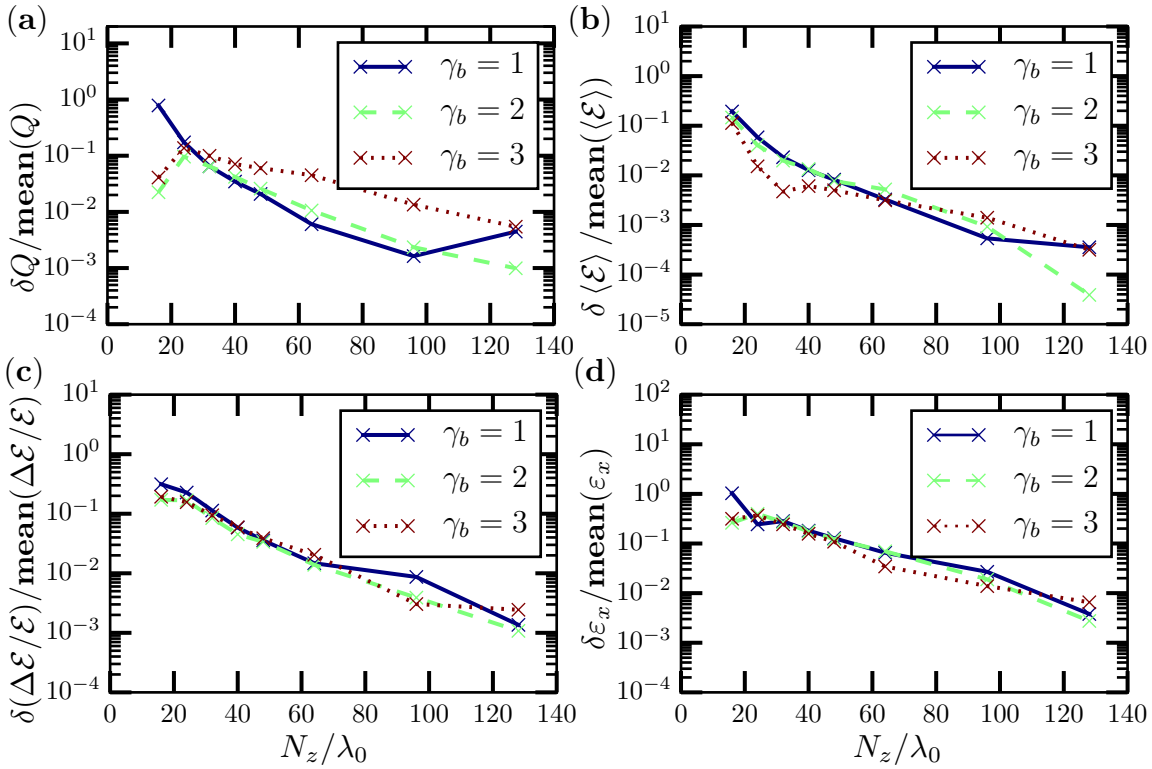

Figure 4.6: Convergence analysis of the results obtained from simulations using the Lorentz-boosted frame technique. The reference case is taken as the average of all considered relativistic factors. Each plot corresponds to different electron bunch properties: (a) the difference in electron bunch charge $\delta Q/\mathbf{mean}(Q)$; (b) in average energy, $\delta\langle\mathcal{E}\rangle/\mathbf{mean}(\langle\mathcal{E}\rangle)$; (c) in rms energy spread, $\delta(\Delta\mathcal{E}/\mathcal{E})/\mathbf{mean}(\Delta\mathcal{E}/\mathcal{E})$; (d) in transverse emittance, $\delta\varepsilon_x/\mathbf{mean}(\varepsilon_x)$.

4.4.2 PSATD solver

Simulations with the laser-plasma parameters as shown in Table 4.2 using the PSATD solver in 2-1/2D are carried out. The stencil order is set to 32. Here we only perform simulations using the Lorentz-boosted frame technique with $\gamma_b \in [2, 3]$, simulations in the lab frame are not performed. The study approach is the same as the previous case. A sweep of longitudinal resolution is done for each relativistic factor of the boosted frame.

We first evaluate the wakefield at $z = 200\,\mu$m obtained from simulations with boosted frames at various longitudinal resolution as shown in Fig. 4.7. In each plot is illustrated the wakefield from simulations with $\gamma_b \in [2, 3]$ for a specific longitudinal resolution. Apart from the case with $N_z/\lambda_0 = 16$, where we observe some discrepancies in the second period of the excited plasma wave, the agreement is excellent for other longitudinal resolutions. For $N_z/\lambda_0 = 32$ onwards, all wakefield structures for boosted frames with $\gamma_b \in [2, 3]$ look identical. The beam loading effects at $z = 175\mu$m are also captured in simulations using the Lorentz-boosted frame technique. The validity of the beam loading effects will be further confirmed by the injected electron bunch properties in the following paragraphs.

Fig. 4.8 shows the evolution of the injected electron bunch properties for high longitudinal resolutions, $N_z/\lambda_0 \in [32, 64, 128]$. These bunch properties are electron bunch charge, average energy, rms energy spread and transverse emittance represented by Fig. 4.8(a-d) respectively. The injected electron bunch has a charge of 17.5 μC, an average energy of 160 MeV, a rms energy spread of $\sim 10\%$ and a transverse emittance of 4.2 mm mrad at $z = 450\,\mu$m. These

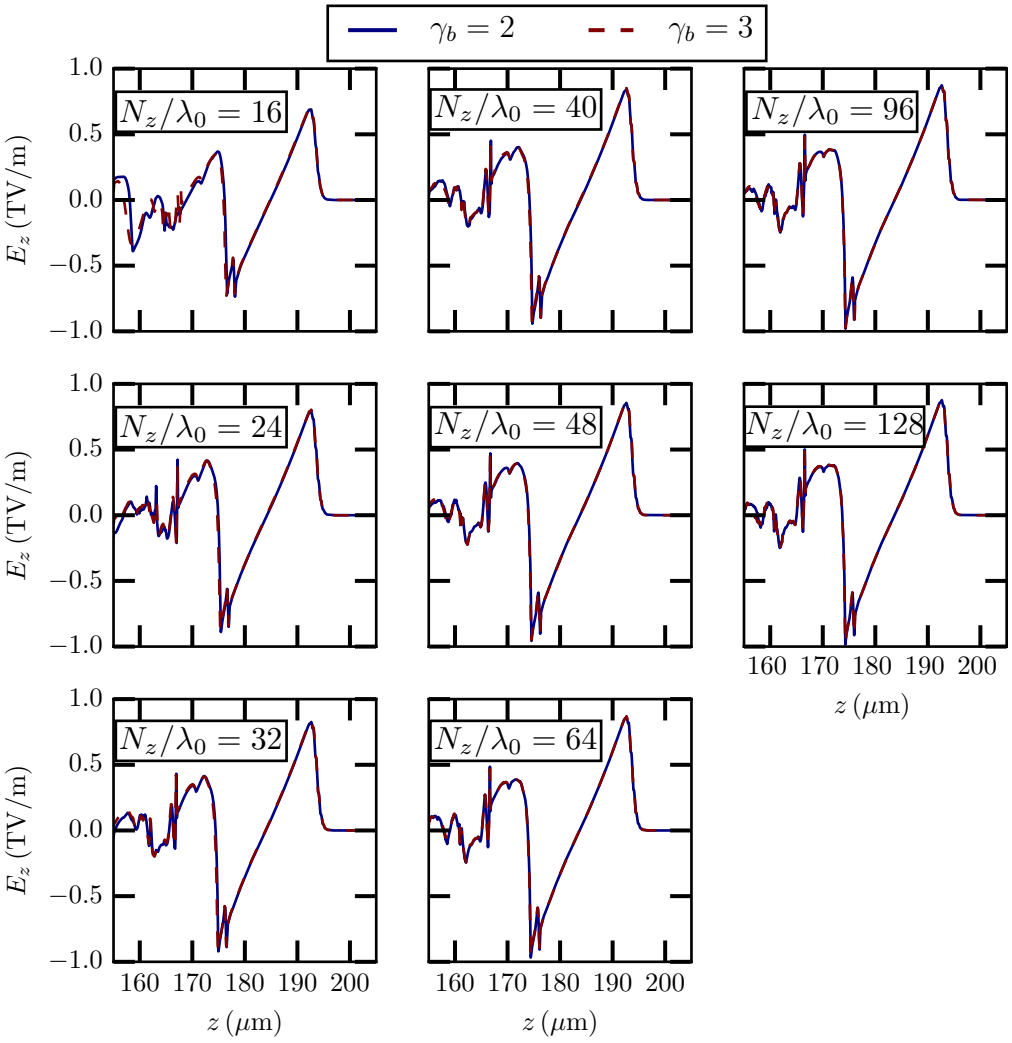

Figure 4.7: A series of plots showing wakefield at $z = 200\,\mu$m. Each panel corresponds to a specific longitudinal resolution given in the box on the upper left. In each panel is shown the wakefield of 2-1/2D simulations using the PSATD solver carried out with $\gamma_b \in [2, 3]$.

results are comparable to the ones obtained using the CK solver, showing a convergence between the CK and the PSATD solvers.

The excellent agreement of the electron bunch properties with respect to distance of propagation, z in Fig. 4.8 for $N_z/\lambda_0 \in [32, 64, 128]$ allows us to further our analysis by choosing a specific frame, $z = 200\,\mu$m. Fig. 4.9 shows the electron bunch properties at $z = 200\,\mu$m with respect to N_z/λ_0 for various γ_b. Results on the electron bunch charge as illustrated by Fig. 4.9(a) show some discrepancies even for $N_z/\lambda_0 = 128$. These discrepancies are within percentage level. For other electron bunch properties as shown in Fig. 4.8(b-d), we observe a convergence of results for both γ_b from $N_z/\lambda_0 = 48$ onwards. As compared to the CK solver (refer to Sec. 4.4.1), the convergence is established at a lower N_z/λ_0 using the PSATD solver.

4.4.3 Runtime analysis

An analysis on the runtime gives an insight on the speedup of the simulations performed using the Lorentz-boosted frame. All simulations are carried out using CPUs of the Cray

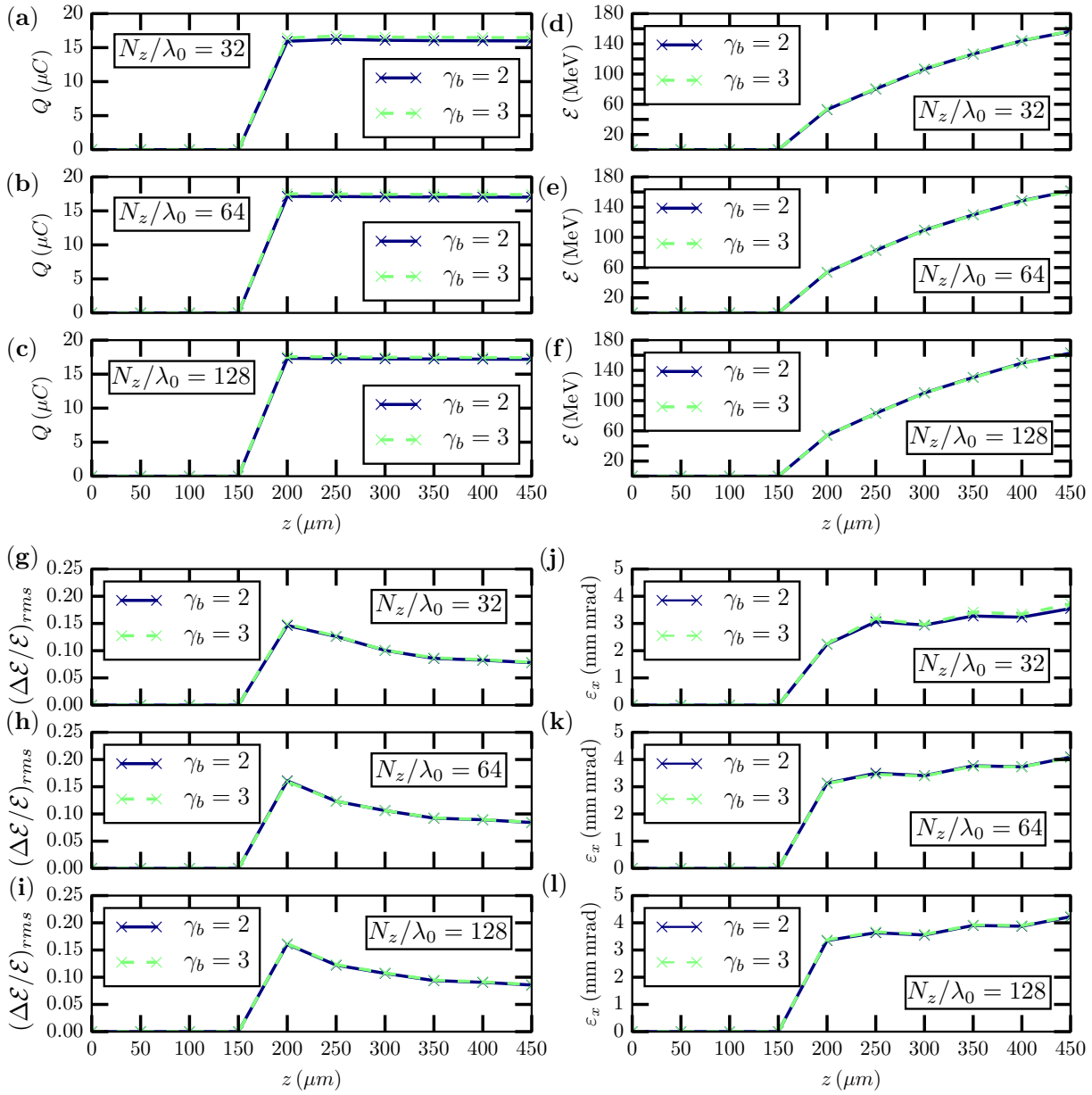

Figure 4.8: Evolution of the injected electron bunch properties with respect to z, the distance of propagation in the plasma. Each plot illustrates simulations with the PSATD solver using different $\gamma_b \in [2, 3]$ at specific longitudinal resolutions, $N_z/\lambda_0 \in [32, 64, 128]$ as indicated by the legend. Evolution of the electron bunch charge, Q is shown in (a-c); the average energy, $\langle\mathcal{E}\rangle$ in (d-f); the rms energy spread, $(\Delta\mathcal{E}/\mathcal{E})_{rms}$ in (g-i); transverse emittance ε_x in (j-l).

XC30 supercomputer at NERSC. In this analysis, the time for the diagnostics is subtracted from the total running time.

Fig. 4.10 shows the runtime expressed in Core-Hours (CH) with respect to the longitudinal resolution N_z/λ_0. We observe that modeling LWFA in a 500 μm plasma with Warp using the CK solver in 2-1/2D lab frame at a decent longitudinal resolution ($N_z/\lambda_0 = 64$) requires 10^4 Core-Hours. Performing the same simulation in a boosted frame with $\gamma_b = 3$, reduces the computational cost by ~ 20 for the CK and the PSATD solvers, while retaining the difference within the percentage level as shown in Fig. 4.6. Note that the PSATD solver implemented in Warp is still a prototype, its implementation is yet to be optimized, this

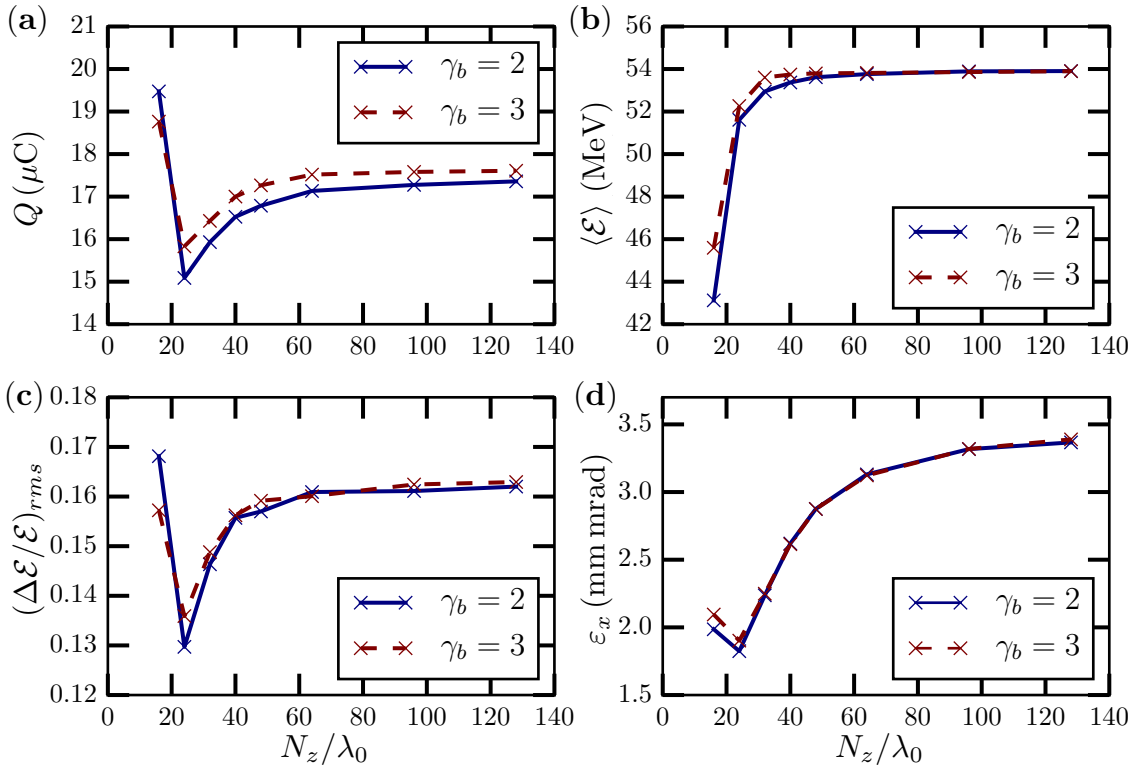

Figure 4.9: Properties of injected and accelerated electron bunch evaluated at $z = 200\,\mu m$ with respect to the longitudinal resolution for $\gamma_b \in [2, 3]$. Simulations were carried out using Warp in 2-1/2D PSATD solver with 32 stencil orders. (a) Electron bunch charge, Q, (b) average energy, $\langle \mathcal{E} \rangle$, (c) rms energy spread, $(\Delta \mathcal{E}/\mathcal{E})_{rms}$, (d) tranverse emittance with respect to longitudinal resolution, N_z/λ_0 are illustrated.

explains why simulations using the PSATD solver are more computationally intensive here as compared to simulations using the CK solver.

We evaluate the analytical speedup for both the CK and the PSATD solvers. The CFL condition for the CK solver is given by

$$c\Delta t \leq \Delta z \sqrt{(\alpha - 2\beta)\left[(1/\Delta x)^2 + (1/\Delta z)^2\right]} \tag{4.8}$$

in 2D, where Δt is the time-step and Δx, Δz are the computational grid cell sizes in x and z, $\alpha = 3/4$, $\beta = 1/8$, are the coefficients for the CK solver. As γ_b varies, the transverse resolution is kept constant, while the longitudinal resolution is kept at a constant fraction of the incident laser wavelength $\Delta z = \zeta \lambda_0$, where $\zeta = 1/(N_z/\lambda_0)$. In a boosted frame, $\Delta z' = \zeta \lambda_0' = \zeta(1 + \beta_b)\gamma_b \lambda_0$. Consequently, the speedup becomes, when using the CK solver

$$S_{CK} = \frac{\Delta z' \sqrt{(\alpha - 2\beta)\left[(1/\Delta x)^2 + (1/\Delta z)^2\right]}}{\Delta z \sqrt{(\alpha - 2\beta)\left[(1/\Delta x)^2 + (1/\Delta z')^2\right]}}, \tag{4.9}$$

where $\alpha = 3/4$ and $\beta = 1/8$. Although there is no CFL condition for the PSATD solver, we have chosen the same CFL condition as the one of the CK solver for all simulations with the PSATD solver so that we can make a direct comparison between the two, thus we obtain $S_{PSATD} = S_{CK}$.

In Fig. 4.11 are plotted the analytical and numerical (with Warp) speedups for the CK solver. The speedup obtained with Warp simulations is in the same order of magnitude

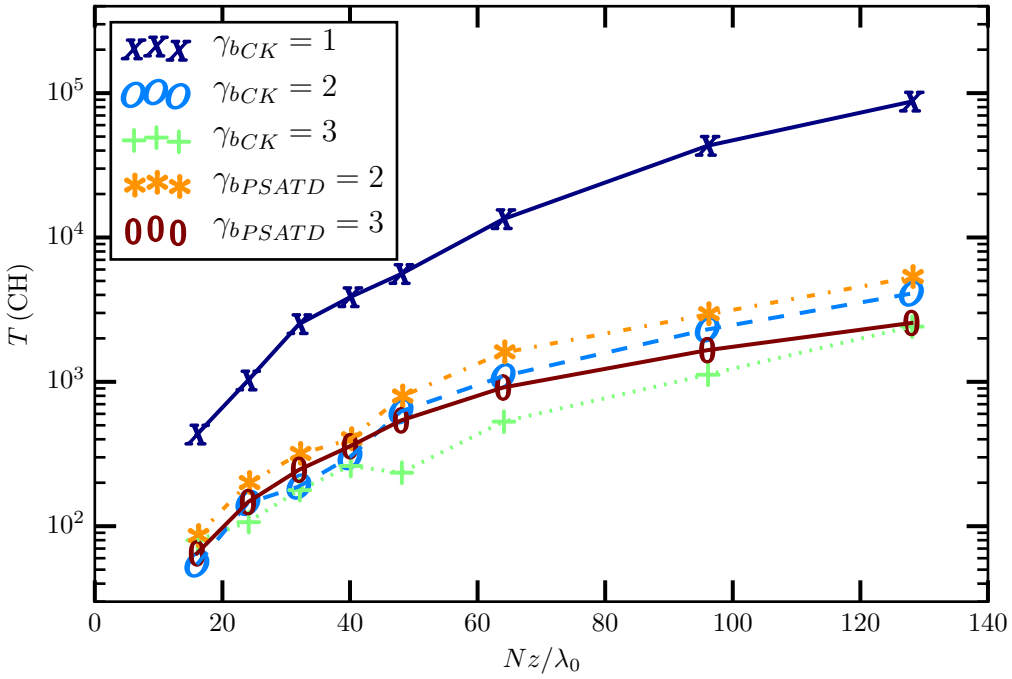

Figure 4.10: Runtime of the simulations expressed in Core-Hours (CH) performed using Warp with respect to the longitudinal resolution, N_z/λ_0. Results from both the CK and the PSATD solvers are plotted. Note that $\gamma_b = 1$ corresponds to the lab frame and that the $y-$axis is plotted in log-scale.

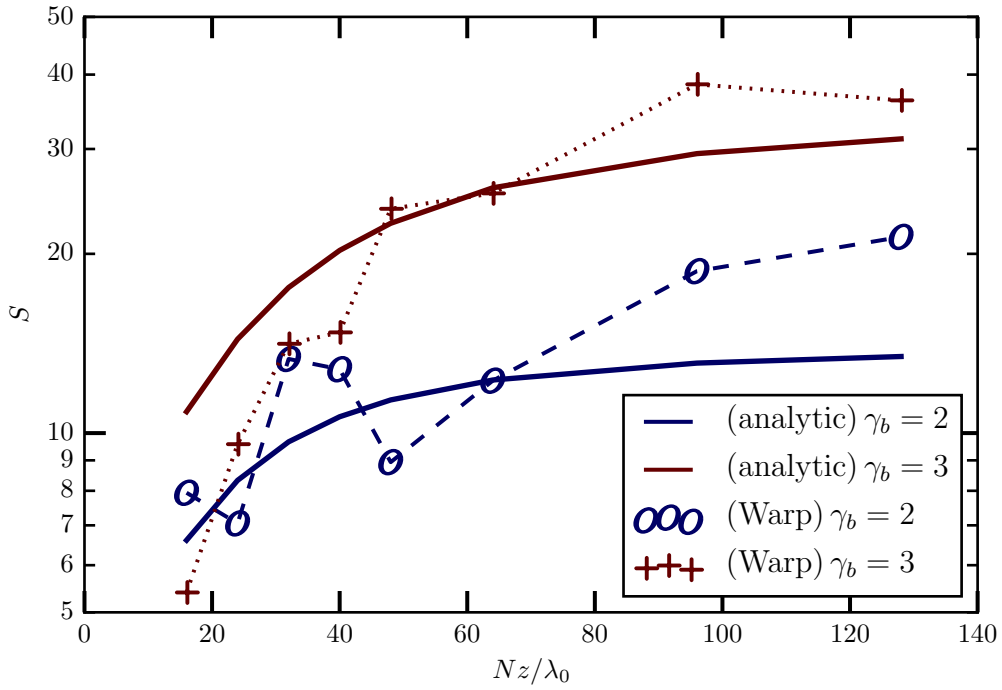

Figure 4.11: Speedup with respect to the longitudinal resolution for $\gamma_b \in [2, 3]$. The analytical speedups are given by Eq. 4.9 and the measured speedups are obtained from Warp simulations using the CK solver.

as the one given by the scaling obtained analytically. The speedup for the PSATD solver cannot be calculated since simulations in the lab frame were not performed, however based

on the analytical speedup, the result should be close to the one given by S_{CK}.

4.5 Conclusion

This chapter gave an overview on the Lorentz-boosted frame technique, which consists of performing simulations in a frame moving near the speed of light in the direction of the laser pulse. The properties of space and time dilation and contraction due to the Lorentz transformation allow large speedup, resulting in the reduction of the computational cost.

Two main issues are identified while using this approach, namely numerical Cerenkov instabilities and accuracy of the modeling in the self-injection scheme. This work addresses the latter. For this study, we modeled a 100 MeV stage at a density of $10^{19}\,\mathrm{cm}^{-3}$, which can be subsequently scaled to describe a 10 GeV stage at a density of $10^{17}\,\mathrm{cm}^{-3}$ [207]. To trigger self-injection of electrons in the wakefield, a_0 is set to 5.

With the theoretical speedup developed in [193], we are able to predict the speedup given the relativistic factor of the boosted frame γ_b and the numerical resolution. The correlation between lab and boosted frame data are also described in this chapter. Although some interpolation is performed at runtime during data collection process, the induced error is minimal. To ensure no further loss of information, field and particle diagnostics are carried out at each time-step, and then dumped at regular interval for post-processing.

Simulations were performed using the CK and the PSATD solvers. Results obtained demonstrated accurate modeling of the evolution of the plasma wakefield, electron bunch properties such as the charge, the average energy, the energy spread and the transverse dynamics with agreement at 99 % percentage level between simulations using various relativistic factor in the Lorentz boosted frame as long as the longitudinal resolution is sufficient, e.g. $N_z/\lambda_0 = 64$. Convergence of results is attained at a lower longitudinal resolution using the PSATD solver as compared to the case using the CK solver. The agreement between results using the CK and the PSATD solvers also agree at 99 % percentage level at the highest longitudinal resolution $N_z/\lambda_0 = 128$. The scaling of the speedup is confirmed, validating our understanding of the Lorentz-boosted frame technique scaling with γ_b and N_z/λ_0. Although simulations in this regime put a constraint on the choice of the relativistic factor of the boosted frame, we still obtain a significant speedup, e.g. $S \approx 36$ with $\gamma_b = 3$ at $N_z/\lambda_0 = 128$ while retaining differences at the percentage level.

Analysis on the accuracy and the speedup for 1 GeV and subsequently 10 GeV stages are left for future work.

Chapter 5

Simulation of the dynamics of electron injection and acceleration

Our group has been developing an experimental program on LWFA experiments to produce electron beams that conform with the specifications established in the CILEX project. Experiments were performed at the Lund Laser Center and at the UHI100 laser facility, CEA Saclay. Simulations were conducted in parallel to analyze experimental results and used as a prediction tool to investigate regimes not yet being explored in experiments. Since the currently explored regimes in experiments are strongly nonlinear and intrinsically three dimensional, a realistic description of the process requires the use of a three-dimensional, kinetic approach. 3D PIC simulations provide detailed information about the laser-plasma interaction, but demand extreme computer resources. An alternative that is based on the azimuthal Fourier decomposition algorithm [30] is instead used, as it provides a quasi-3D description with a computational load reduced to the one similar to bi-dimensional calculations (refer to Sec. 2.5).

The first part of this chapter demonstrates the capability of Warp in producing reliable results. The second part is devoted to the optimization of the injector. In the final part some results on the extension to higher energy electron bunch will be presented.

Contents

5.1 Simulations using Fourier decomposition algorithm

We have performed Warp simulations with the Fourier decomposition algorithm taking as input data values of experimental parameters close to the ones described in [104]. The experimental diagnostics have only provided global parameters such as energy, duration, waist and maximum intensity at the focal position in vacuum and the energy distribution of the accelerated electron bunch as the output. In the calculation, since we had to specify the temporal and spatial forms of the laser amplitude, therefore in all presented results, the laser intensity was assumed to be axisymmetric and Gaussian in time and in the radial direction. In this configuration only two angular Fourier modes were required, leading to a much lower computational load than a full 3D calculation.

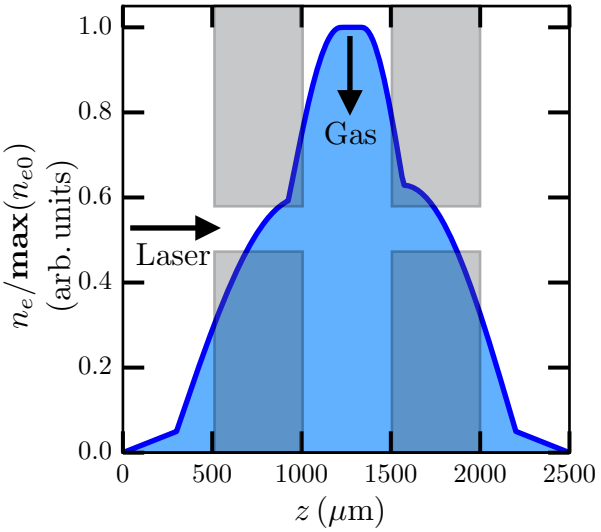

Figure 5.1: Normalized ELISA longitudinal density profile for an inner cell length of $L_{cell} = 500\mu$m. Gray areas indicate the locations of the entrance and exit plates in which holes are drilled. The gas inlet is located on the top and the laser propagates from left to right.

As for the longitudinal density profile, we used the so-called ELISA [32] profile, the density profile achieved in a gas cell developed as an injector medium for multi-stage experiments planned in the frame of the CILEX project [20]. Fig. 5.1 shows the ELISA profile computed by 3D FLUID simulations performed using openFOAM [208], and characterized experimentally [32]. The 500 μm gray areas represent the locations of the entrance and exit plates of the gas cell in which holes are drilled. The gas inlet is located on the top. It is considered as the reference profile for the numerical studies presented here. As will be seen below, the density profile has a strong influence on the electron trapping and acceleration processes.

For experiments described in [104], the plasma is a mixture of gases ($H_2 + N_2$). To model this, a field ionization module based on the ADK model [80] was introduced in Warp to model ionization dynamics. A summary of the parameters used in our calculations is given in Table 5.1. In this table $a_0(z_f)$ is the peak normalized laser amplitude reached in vacuum at z_f. The value of 1.1 is attained in the focal plane $z = z_f$, in vacuum.

Maximum electron number density on axis	$\max(n_0)$	$7.8 \times 10^{18}\,\mathrm{cm}^{-3}$
Longitudinal density profile		ELISA profile
Plasma length	L_{plasma}	2.5 mm
Gas composition		$99\%H_2 + 1\%N_2$
Laser profile		$\mathrm{bi-Gaussian}^a$
Peak normalized laser amplitude	$a_0(z_f)$	1.1
Laser wavelength	λ_0	$0.8\,\mu$m
Laser radius at $1/e^2$	r_L	$17\,\mu$m
Laser duration (FWHM)	τ	40 fs
Laser focal position	z_f	0.9 mm
Laser polarization		linear (in $y-$direction)
Number of Fourier modes		2
Number of particles/cell		36 macro
Cell size in r	Δr	$\lambda_0/2$
Cell size in z	Δz	$\lambda_0/50$

[a] Gaussian in temporal and spatial profiles

Table 5.1: List of parameters.

5.1.1 Electron beam characteristics

Electron beam energy spectrum

We first compare, in Fig. 5.2, the experimental electron beam energy spectrum with the simulated one, determined at the exit of the gas cell, $z = L_{plasma} = 2.5\,\mathrm{mm}$.

We observe in this figure that the electron beam has a rather large energy distribution suggesting continuous injection of electrons, with the highest energy extending to $\approx 150\,\mathrm{MeV}$. The simulated spectrum has a maximum energy within the experimental error bars, it also reproduces well, above 56 MeV, the experimental shape of the curve. This shows a good agreement between the experimental and the simulated results. Moreover, the simulation exhibits a peak at 17 MeV with a FWHM energy spread, $\Delta\mathcal{E}/\mathcal{E} \approx 69\%$, a piece of information that cannot be obtained with the experimental setup used.

In Fig. 5.3, is plotted the contribution of the different origin of electrons in the total spectrum at $z = L_{plasma}$. In the simulation, all electrons are tagged and can be sorted according to their origin: the blue dashed line represents the charge density of electrons ionized from $N^{5+} \rightarrow N^{6+}$ and the red dashed-dotted line represents the charge density of electrons ionized from $N^{6+} \rightarrow N^{7+}$. We observe that only the two electrons, initially in the K-shell of nitrogen, are accelerated to high energies. The other electrons coming either from outer shells of nitrogen or from hydrogen are not trapped but contribute in building the plasma wake. This is in agreement with the 3D OSIRIS particle-in-cell code results [77]. Note also that the 6^{th} electrons yield the main contribution to the highest part of the spectrum, while the 7^{th} electrons contribute mainly to the low energy peak.

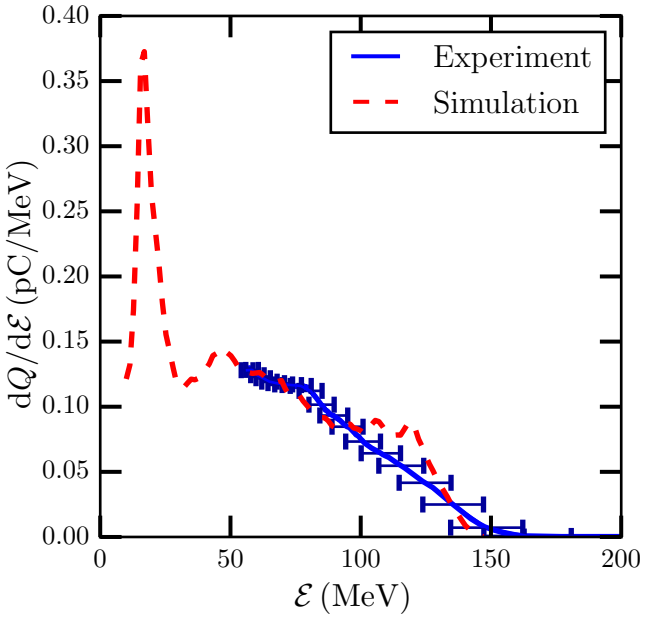

Figure 5.2: Comparison between simulated and experimental electron beam energy spectrum. The experimental result has an energy cutoff at 56 MeV, thus the simulated energy spectrum is normalized by the experimental energy spectrum value at 56 MeV. Blue horizontal lines are the experimental error bars.

Beam emittance

As mentioned in Chapter 1, the divergence and emittance are two important characteristics of the emitted electron beam. We have plotted in Fig. 5.4, electron distributions in phase space in (x, p_x) and (y, p_y) at the exit of the gas cell, the electron momentum being normalized by $m_e c$. From these data are measured a rms divergence of 4.6 mrad in $x-$direction and 24 mrad in $y-$direction, whereas the emittance, are respectively of $\varepsilon_x = 0.6$ mm mrad and $\varepsilon_y = 17.1$ mm mrad. The higher values in the $y-$direction are related to the polarization of the laser field: after tunnel ionization the electron acquires a quiver velocity in the direction of the polarization.

5.1.2 Beam dynamics

Correlation between the injection and acceleration processes

In order to analyze the results presented in Sec. 5.1.1, we have looked at the correlation between the injection process and the acceleration one. Here we back-tracked 20000 randomly sampled trapped electrons (10000 for $N^{5+} \rightarrow N^{6+}$ and 10000 for $N^{6+} \rightarrow N^{7+}$) beginning from z_{exit} back to their ionization position, also corresponding to the position of their first appearance in the simulation.

In Fig. 5.5, we have plotted the final energy of the electrons as a function of their trapping position for (a) the 6^{th} and (b) the 7^{th} electrons. As the trapping position increases, electrons are trapped further away from the gas cell entrance, the length of acceleration decreases; only electrons trapped at the early stage are accelerated to the highest energy because their acceleration length is longer than those trapped at the later stage. In particular the 7^{th} electrons have lower energies, in accordance with Fig. 5.3, because they are trapped later. We observe also in Fig. 5.5 that the position-energy correlation is not linear, in particular,

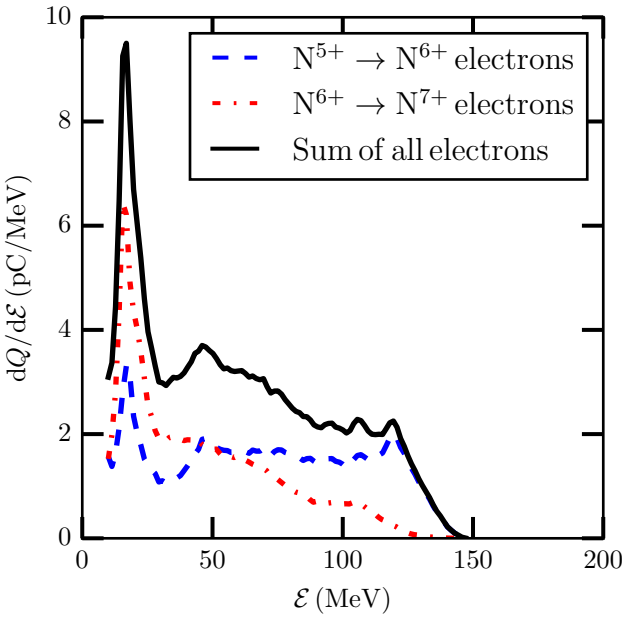

Figure 5.3: Energy spectrum for different electron population depending on their origin: the 6^{th} electrons (dashed line), the 7^{th} electrons (dashed-dotted line) and the sum of all electrons (solid line) at $z = L_{plasma}$.

for the high energy part, e.g. electrons with $\mathcal{E} = 120\,\text{MeV}$ at $z = L_{plasma}$. For these electrons, the trapping positions spread over more than $100\,\mu$m in the trapping positions, yet they still obtain the same final energy.

Laser amplitude and plasma wave

In order to explain the data of Figs. 5.3 and 5.5, we now look at the evolution of the laser amplitude and of the plasma wave, which are responsible for both the trapping and for the acceleration processes. In Fig. 5.6, we have plotted the evolution of $a_0(z)$ in vacuum (green dotted line) and during the laser propagation in the plasma with ELISA density profile (gray dashed line). The focal plane of the laser z_f in vacuum, is located at $900\,\mu$m. The entrance of the gas cell, where the density starts increasing rapidly is positioned at z_f. Relativistic self-focusing dominates over diffraction when $P_L/P_C(z) \gtrsim 1$ (see Chapter 1), P_L being the maximum value of the laser power and $P_C(z)$ the value at z, of the critical power for relativistic self-focusing. Close to the gas cell entrance, P_L remains constant while $P_C(z)$, being inversely proportional to the density, strongly decreases with z. Therefore $P_L/P_C(z)$ increases rapidly and becomes higher than 1. The value of $P_L/P_C(z)$ however remains relatively modest, therefore the self-focusing is rather smooth, the maximum of intensity being reached close to the gas cell exit. In Fig. 5.6 vertical lines mark 3 positions, corresponding to (1) the start of the trapping process, (2) the maximum value of $a_0(z)$ and (3) the end of the trapping process. We can observe that the trapping region corresponds also to the domain of high plasma density. Therefore, in our conditions, the density profile appears as the dominant parameter controlling the trapping process.

In Figs. 5.7 are plotted the laser fields and the plasma wave amplitudes on axis at the three positions labeled in Fig. 5.6. At position (1) the interaction occurs in a quasi-linear regime, where the laser envelope is still Gaussian and the plasma wave quasi-periodic. At the maximum of the laser intensity, in position (2), nonlinearities become apparent, both on the

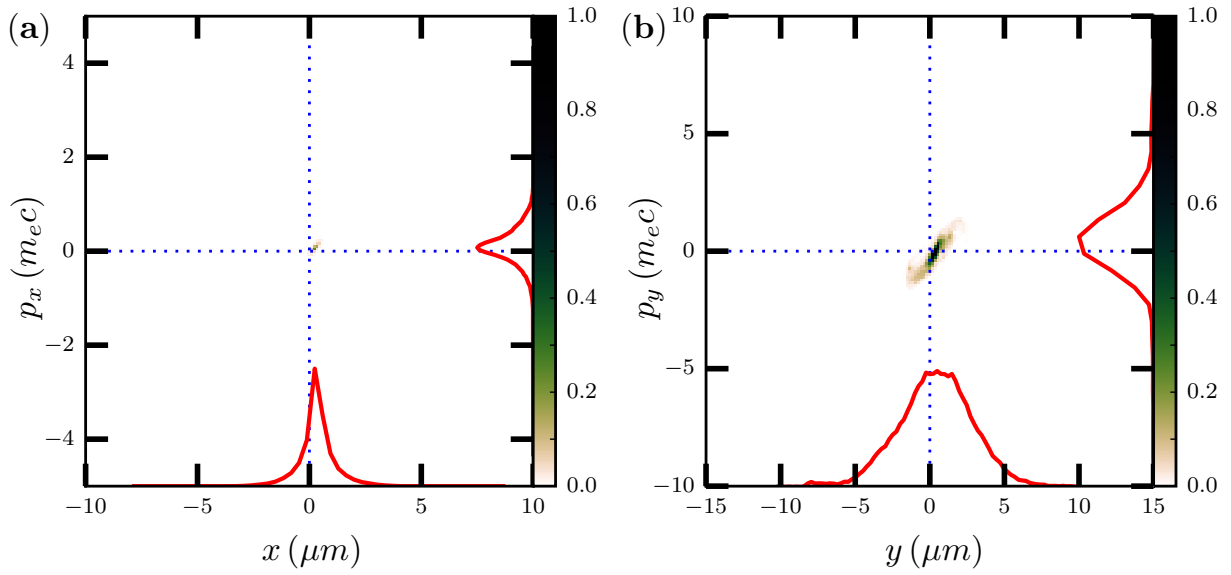

Figure 5.4: A set of points representative of an electron beam in the a) $(x, p_x)-$, b) $(y, p_y)-$phase space. The color bar represents the relative density of the electrons.

plasma wave and also on the deformation of the laser pulse. The accelerating field amplitude has increased, taking into account the additional normalization factor which depends on the density, and a peak at $z = 1402\,\mu$m corresponding to the back of the first oscillation behind the laser is visible. This peak is due to the field generated by trapped electrons. Beam loading effects are therefore significant in this case. Position (3) is similar to the second one. However, due to the decrease in density, and also in $a_0(z)$, the amplitude of the wakefield has decreased, while the relative contribution of the beam loading effect has increased because the accumulated trapped charges have generated their own field that distorted the wakefield significantly. Information on the transverse properties of the laser and plasma wave structure at the three positions is given in Fig. 5.8.

Fig. 5.8 shows the electronic density map with the laser amplitude at the three positions mentioned earlier. Fig. 5.8(1) confirms that a quasi-linear regime is at the beginning of the injection, in particular the transverse size of the plasma wave is similar to the laser pulse one. At this position, the laser ponderomotive force is not strong enough to expel all plasma electrons from the vicinity of the axis. On the contrary, at position (2), the transverse size of the laser pulse is minimum leading to the highest field amplitude $a_0 \approx 3$. A full matched blown-out structure can then be formed, yielding the highest accelerating field. At position (3) the transverse size of the laser pulse has increased, diffraction becoming dominant over self-focusing, leading to a decrease of the laser intensity.

Concerning the trapping of the 7^{th} electrons, the simulation shows that, due to their strong binding energy, these ions are ionized only for the highest values of $a_0(z)$. The principal trapping condition for these electrons become simply that they first have to be generated, but once created they are even more easily trapped than the 6^{th} electrons.

The fact that electrons with quite different trapping position obtain the same final energy can be explained by the following: the first trapped electrons when accelerated, move toward the front of the cavity, whereas newly generated electrons are trapped at the back of the cavity where the accelerating field reached a higher value, therefore the electrons trapped at the later stage can reach the same energy as the electrons trapped at the earlier stage.

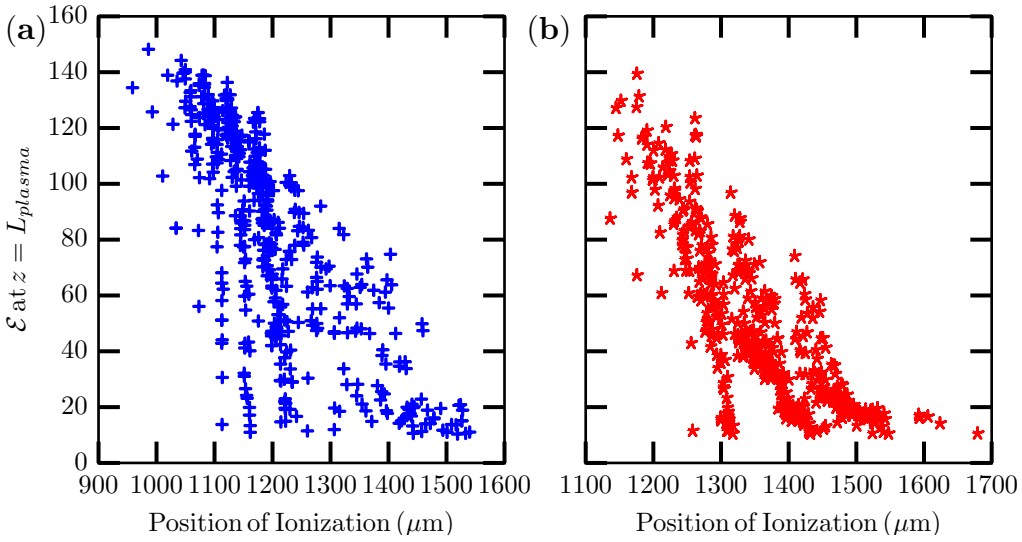

Figure 5.5: Trapped electrons final energy is plotted against injection position for (a) the 6^{th} and (b) the 7^{th} electrons. Electrons are chosen with an energy, $E \geq 10\,\mathrm{MeV}$ at the exit of the plasma, $z = 2.5\,\mathrm{mm}$.

Conclusion

In this section, we have presented the modeling of a laser-driven plasma acceleration experiment with Warp using the azimuthal Fourier decomposition algorithm. The use of the realistic density profile has allowed to perform direct comparisons with experimental results, which show good agreement. This is also the case for the other experimental data (not shown here), using the same set-up and presented in [104]. In [104], the author has performed an experiment on the influence of the laser focal positions on the generated electron bunch in a gas cell using the ionization-induced injection scheme, the supporting simulations using Warp with the azimuthal Fourier decomposition algorithm have produced precisely the experimental energy distribution of the electron bunch. Therefore the validity of the code is confirmed, and in particular the fact that, in the considered conditions, accurate results can be obtained with only two Fourier harmonics. A detailed analysis of the simulation results has allowed to get more insights of electron trapping and acceleration process when the ionization-induced injection and density gradient effects are combined. The high efficiency of the quasi-3D model has allowed to perform a direct parametric investigation for optimizing electron beam properties.

5.2 Optimization of the injector by tailoring density profiles

We have shown in the previous section that Warp simulations using azimuthal Fourier decomposition algorithm produce reliable results. We have then performed numerical studies using the same code framework to determine optimized conditions for controlled ionization injection using a moderate power laser pulse, propagating in a gas cell. Previous simulations have also given indications on the choice of parameters for optimization. In Fig 5.6 the shaded area corresponds to the injection length of $726\,\mu\mathrm{m}$; in this case, the corresponding spectra exhibit a large energy spread, indicating that the length is too long. In order to

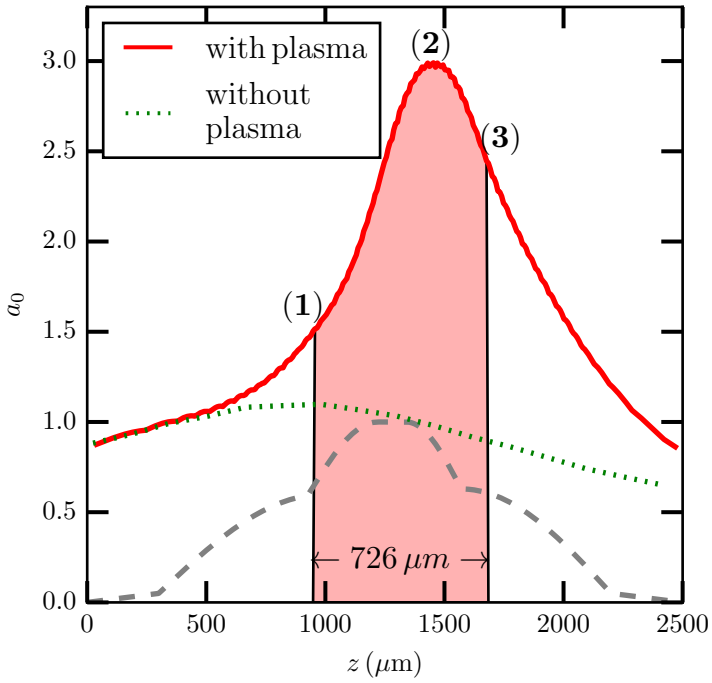

Figure 5.6: Evolution of a_0, we define three positions: (1) the beginning of injection, (2) the a_0 is maximum, (3) the end of injection. The blue shaded region represents the injection range, and the range is of 726 μm. The green dotted line represents the evolution of a_0 in vacuum, the maximum value of a_0 is at $z_f = 900\,\mu$m. The black line shows the longitudinal density profile of the gas cell.

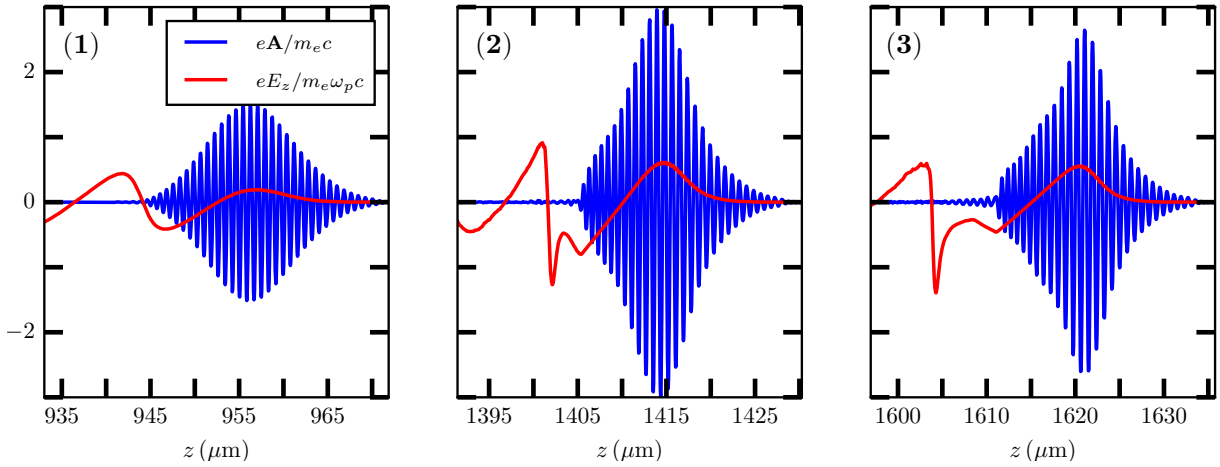

Figure 5.7: Vector potential of the laser, A normalized to m_ec/e and the wakefield, E_z normalized to m_ecw_p/e at positions (1), (2) and (3) as shown in Fig. 5.6.

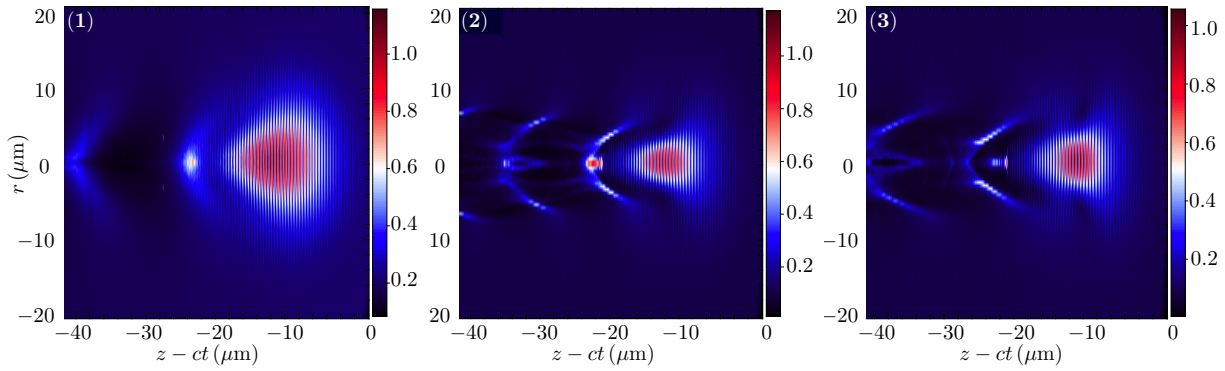

Figure 5.8: Normalized electronic density map together with the normalized laser field at the three positions reported in Fig. 5.6. All quantities are normalized to their maximum.

control the energy spread, a shorter injection length is necessary. Several methods can be considered to control this injection length, either by shortening the plasma length or by focusing the laser pulse near the exit of the gas cell, leading to a slow growth of a_0, hence delaying the ionization injection process.

By analyzing the dynamics of electron injection and acceleration in this moderately nonlinear regime, we identify the mechanisms controlling the beginning and the end of injection, and propose a way of tuning finely the electron beam energy while preserving its energy spread, by tailoring the longitudinal density profile of the last acceleration zone. This method produces electron beams with a FWHM energy spread, $\Delta\mathcal{E}$ of $\sim 9\,\mathrm{MeV}$ for a peak energy of 82.6 MeV.

5.2.1 Choice of parameters

Laser and plasma parameters are chosen in order to achieve electron acceleration to energies in the range of $50 - 200\,\mathrm{MeV}$, well suited for an injector. The lower limit at 50 MeV ensures that space charge effects will not be dominant at the exit of the plasma, and that the influence of the energy spread can be minimized as it scales as $1/\gamma^2$. The upper limit is fixed at 200 MeV to allow for a compact transport line for electron beam manipulation before coupling to the first accelerating structure as is planned in the CILEX project. In addition, the electron beam is required to have a small normalized transverse emittance of $\varepsilon_n \sim 1\,\mathrm{mm\,mrad}$, a small energy spread (typically less than 10%) and a large enough charge (≥ 10 pC).

The parameters used in our calculations are very similar to the ones in Table 5.1, with L_{plasma} reduced to 2.4 mm and z_f extended to 1.9 mm. These modifications allow us to control the evolution of a_0 which in turn controls the injection of electrons in the wakefield. More details will be given further in this section. The plasma electron density, n_0, is chosen to be in the range of $(10^{18} - 10^{19})\,\mathrm{cm}^{-3}$. In this range, the density is high enough for self-focusing of the laser pulse to be achieved, while low enough for the dephasing length L_d, $L_d \propto (\lambda_p^3/\lambda_0^2)a_0 \propto n_{e0}^{-3/2}$ (where a constant of order unity has been neglected), to be in the mm-range and allow for electron acceleration to energies in the required range.

Fig. 5.9 shows the evolution of a_0, the maximum amplitude of the normalized vector potential of the laser pulse (red solid line), and the plasma electron density normalized to its maximum (gray dashed line, ELISA profile), with respect to the propagation axis z.

The shaded region of length $\sim 630\,\mu\mathrm{m}$ represents the window of electron injection in the laser wakefield structure. Four positions are marked: z_0 representing the beginning of

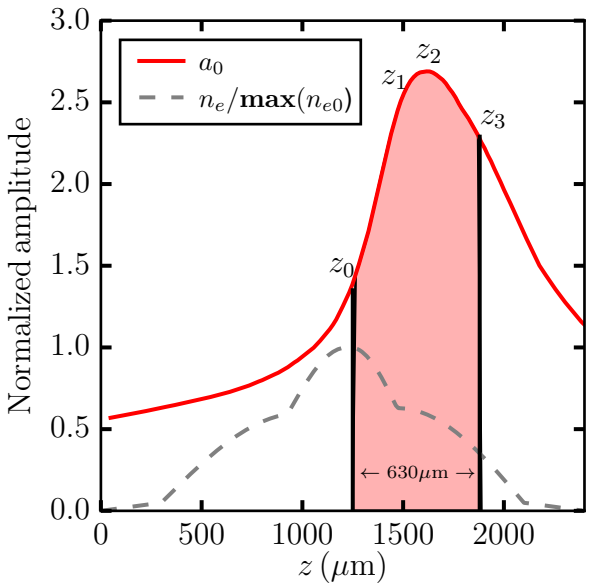

Figure 5.9: Evolution of a_0 with respect to the propagation axis z. The gray dashed line shows the longitudinal density profile of the gas cell, or ELISA profile. The shaded area represents the injection range of length $\sim 630\,\mu$m. We define four markers in the injection zone: z_0, the position where injection begins; z_1, a position between z_0 and z_2; z_2 the position where a_0 is maximum; z_3, the position where injection stops.

electron injection, z_1 a position in the region between the beginning of electron injection and the position where a_0 reaches its maximum value z_2, and z_3 the end of electron injection. The laser pulse with moderate power, and normalized vector potential, a_0, is incident with a focus position in vacuum at 1.9 mm, a position located in the down-ramp of ELISA profile. The reasons for using a moderate laser power are two-fold: as can be seen in Fig. 5.9, it leads to a slow growth of a_0 due to self-focusing of the laser pulse in the smooth up-ramp of density before reaching a maximum, thus delaying the trigger of the ionization-induced injection mechanism, and controlling the start of the injection to limit the energy spread; it prevents a_0 from reaching a value high enough for self-injection of electrons. The values of $a_0 \in [1.5, 2.7]$ during the trapping of electrons are in agreement with previous observations of ionization-induced injection and are below the self-injection threshold [77]. The combination of laser focal position and density tailoring controls the evolution of a_0.

5.2.2 Electron beam properties

In this section we discuss the properties of the resulting electron beam obtained with the parameters shown in Sec. 5.2.1.

Electron beam energy distribution

The electron beam energy distribution is analyzed at the exit of the gas cell at the $z-$axis, z_{exit}, equal to the total plasma length: $z_{exit} = L_{plasma} = 2.4\,$mm. In Fig. 5.10 the charge density of the accelerated electron beam (black solid line) is plotted as a function of electron energy.

The energy distribution is shown for $\mathcal{E} \geq 10\,$MeV, corresponding to the minimum energy of trapped electrons. This energy is linked to the structure of the generated wakefield,

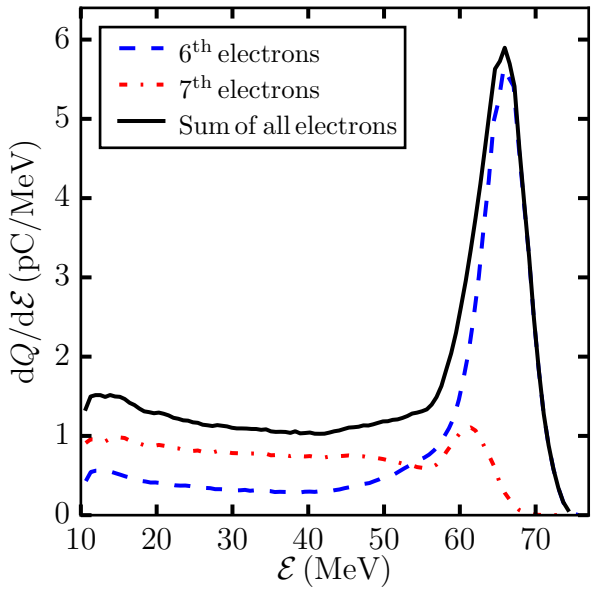

Figure 5.10: The blue dashed line shows the energy spectrum of the 6^{th} electrons, whereas the red, dashed-dotted line shows the energy spectrum of the 7^{th} electrons. The black solid line represents the sum of the two spectra. Only K-shell electrons contribute to the electron beam energy spectrum at z_{exit}. Other electrons are not trapped but contribute to building the plasma wake. An energy cutoff at 10 MeV is applied.

depending strongly on the interaction between the laser and the longitudinal density profile shown in Fig. 5.9. For an electron to be trapped in the wakefield, its Lorentz factor γ is required to fulfill the condition [77]

$$\Delta\Psi + 1 = \frac{\gamma}{\gamma_\phi^2}, \tag{5.1}$$

where $\Delta\Psi = e(\Psi_f - \Psi_i)/(m_e c^2)$, $\gamma_\phi = (1 - {v_\phi}^2/c^2)^{-1/2}$, and v_ϕ is the wake phase velocity. Ψ is the wake potential and the subscripts i and f denote the ionization and trapped positions, respectively. Consider the end of the injection phase $z = z_3$, we take the value of γ_ϕ at this position. Assuming that all trapped electrons are ionized at the maximum of the laser envelope, and trapped at the back of the first period of the plasma wave, Ψ_i and Ψ_f are then taken at the corresponding positions. Using Eq. 5.1, we evaluate the value of γ at $z = z_3$ and infer that the trapped electrons have at least $\gamma \sim 20$ at the end of the injection phase. For this reason, the following analysis will focus on electrons with $\gamma \geq 20$.

As shown in Fig. 5.10, the electron spectrum is peaked at 65.7 MeV with a FWHM energy spread, $\Delta\mathcal{E}/\mathcal{E} = 13.1\%$. The highest energy extends to ~ 74 MeV. Only electrons initially in the K-shell of nitrogen are accelerated to higher energies as shown by the dashed blue line and red dashed-dotted line. Other electrons coming either from nitrogen or from hydrogen are not trapped but contribute to building the plasma wake. Similar to the simulation presented in Sec. 5.1, the 6^{th} electrons yield a higher charge and are the dominant contributors to the higher energy range of the energy spectrum, while the 7^{th} electrons yield a lower charge and are dominant contributors to the lower energy range.

Dynamics of electron injection

Following the same analysis technique as in Sec. 5.1.2, we study the correlation between the energy of electrons at z_{exit} and their position of ionization, as shown in Fig. 5.11.

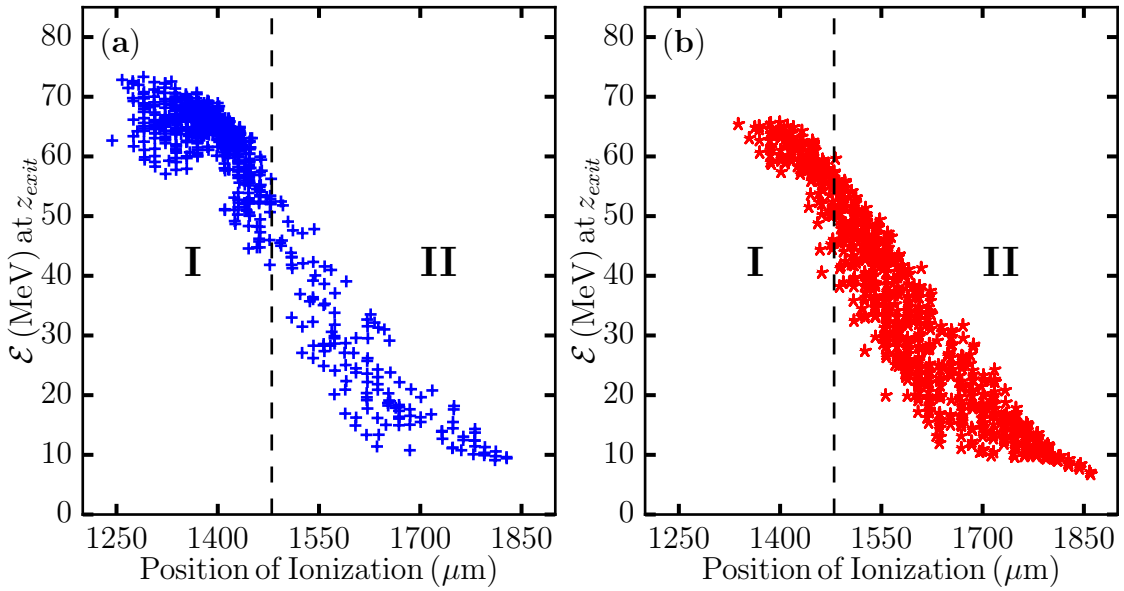

Figure 5.11: Trapped K-shell electrons energy at z_{exit} as a function of their ionization position; a) blue crosses: electrons from $N^{5+} \rightarrow N^{6+}$, b) red asterisks: electrons from $N^{6+} \rightarrow N^{7+}$. Two regions are marked in the distributions: distribution **I** has energy larger than 55 MeV and a position of ionization smaller than $z = 1480\,\mu$m; distribution **II** exhibits a decrease of energy for increased position of ionization.

In Fig. 5.11 is shown the energy of trapped electrons at z_{exit} from (a) $N^{5+} \rightarrow N^{6+}$ and (b) $N^{6+} \rightarrow N^{7+}$. The trapped K-shell electrons are ionized in the range from 1250 μm to 1880 μm. Two kinds of electron distributions can be identified: Distribution **I** corresponds to electrons that have an energy higher than ~ 55 MeV and a position of ionization smaller that $z = 1480\,\mu$m, while Distribution **II** corresponds to electrons with energy at z_{exit} decreasing with respect to their position of ionization. The 6^{th} electrons are ionized earlier in the propagation than the 7^{th} electrons, due to a lower ionization potential, 552 and 667 eV, respectively. The total charge is evaluated by taking into account both the 6^{th} and the 7^{th} electrons. In Distribution **I**, the total charge is 42.6 pC, and 41.6 pC in Distribution **II**, indicating that Distribution **I** represents 50.6% of the total number of trapped electrons.

Distribution **I** has a position of ionization between 1250 μm and 1480 μm, an energy at z_{exit} in the range of $55 - 74$ MeV, and the spectrum is peaked at 65.7 MeV as shown in Fig. 5.10. The line dividing the two distributions is located at $z = 1480\,\mu$m, and corresponds to the position of the change of slope in the density down-ramp of the ELISA profile (see Fig. 5.9), indicating that the shape of the density profile has a major influence at the distribution of injected electrons.

For distribution **I**, the 6^{th} electrons contribute a charge of 35.6 pC while only 7.0 pC is provided by the 7^{th} electrons. No obvious correlation between the ionization position and the electron energy at z_{exit} is discerned for distribution **I**, i.e. electrons that are ionized later in this interval can have the same energy as earlier ionized electrons, inferring that the injection and the acceleration processes are independent.

Distribution **II** starts at $z = 1480\,\mu$m and ends at $z = 1880\,\mu$m. A clear correlation between the electron ionization position and electron energy at the exit of the plasma is observed, i.e. higher energy electrons are ionized first, implying continuous injection and acceleration of electrons. In this distribution, the 7^{th} electrons, as shown in Fig. 5.11(b), provide a charge of 27.8 pC while the 6^{th} electrons provide a charge of 13.8 pC, as shown in Fig. 5.11(a).

Dynamics of beam loading

We further investigate the correlation between injection and acceleration processes by looking into the amplitude of accelerating wave structures.

In Fig. 5.12 are plotted the normalized laser field (blue), the normalized longitudinal wakefield (red) and the energy of electrons divided by 40 MeV (represented by a set of points with color scale for charge density) as a function of space around three positions in the density profile $z_1 = 1435\,\mu$m, z_2, and z_3 as marked in Fig. 5.9. The laser propagates from

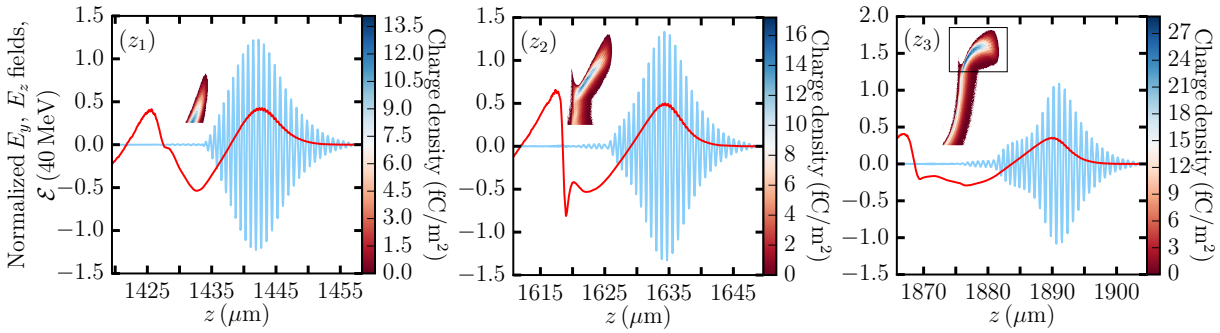

Figure 5.12: Evolution of the normalized laser field, $eE_y/2mc\omega_0$ (in light blue), the normalized wakefield, $eE_z/mc\mathbf{max}(\omega_\mathbf{p})$ (in red) and the energy, $\mathcal{E}$ of electrons (represented by a set of points) for the three positions of interest z_{1-3} as marked in Fig. 5.9. The color bar represents charge density. The black rectangle at z_3 represents electrons in the high charge density region, with energy above 50 MeV.

left to right. Electrons that satisfy the trapping condition, given by Eq. 5.1 are trapped in the first bucket, defined by the region of negative E_z bounded by zero crossing.

At z_1, the laser envelope is already deformed due to self-focusing, and the nonlinear accelerating wakefield is distorted due to the wakefield of injected electrons. Ionized electrons that satisfy the trapping condition are trapped and accelerated at the back of the bucket. However the widening of accelerating structures causes later trapped electrons to lag behind earlier injected ones; the latter are accelerated to a higher energy as compared to the former, an evidence of continuous injection of electrons in the bucket.

At the position of maximum laser intensity, z_2, we observe an increase in the charge density as compared to the previous position z_1, suggesting that more electrons are trapped in the bucket, and the wake is severely modified due to beam loading effects. Electrons at the back of the bucket experience a strong accelerating field, therefore their energy quickly catches up with previously injected electrons, consequently forming two high energy distributions. At the end of the ionization region, at z_3, the accelerating plasma wave structure is heavily beam loaded, resulting in the inhibition of further injection. The flattened normalized wakefield, $E_{Nlnorm} = 0.22$, giving $E_{Nl} = 59.1$ GV/m, accelerates a rather energetic, homogenized electron beam with a central energy of 62.6 MeV in the highest charge density region, corresponding to the peak observed in the spectrum of Fig. 5.10.

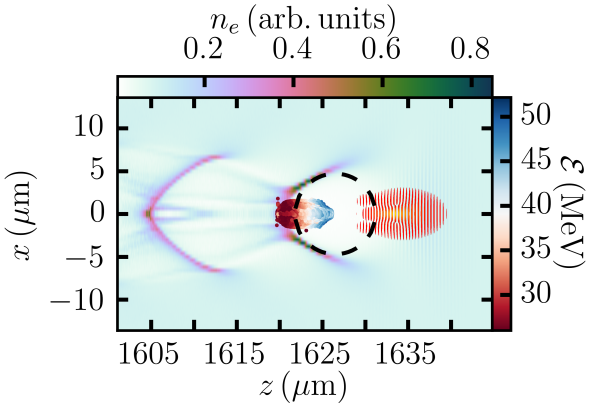

Figure 5.13: Electron density in the (z, x) plane at z_2, with superimposed laser amplitude and injected electron beam. The horizontal color bar represents the normalized electron density in arbitrary unit and the vertical color bar depicts the energy of trapped electrons. A black dashed circle of 4.7 μm radius is superimposed on the map to show the shape of the blown-out region.

Fig. 5.13 shows a 2D map in the $x - z$ plane of the electron density at position z_2. The laser amplitude is located between $z = 1628\,\mu m$ and $z = 1638\,\mu m$. A black dashed-line circle is superimposed to delimit the blown-out region. Trapped electrons are located in a region extending from the sheath of high density at the back of the cavity to the center of the blown-out region. The charge of the injected electron beam in this structure is $Q = 37.2\,\mathrm{pC}$. This value can be compared to the analytical prediction for the amount of charge that can be loaded in the nonlinear wakes given by Eq. 1.94. At z_2, the simulation gives $k_p R_b = 1.74$ and $E_{Nlnorm} = 0.55$, giving $E_{Nl} = 147.7\,\mathrm{GV/m}$. Inserting these values in Eq. 1.94, we obtain $Q_{Nl} = 28.5\,\mathrm{pC}$. This analytical prediction is of the same order of magnitude as the amount of charge calculated in the simulation, thus confirming that the operating regime is a beam-loaded blown-out regime.

At the end of the injection region, z_3, the high-energy electron beam has a peak energy of 62.6 MeV and a FWHM energy spread, $\Delta\mathcal{E}/\mathcal{E} = 14.2\%$. Considering only high energy electrons in the energy range above 50 MeV, their charge $Q_{\mathrm{high}} = 43.6\,\mathrm{pC}$ and they are distributed over a length, $\ell_{\mathrm{beam}} = 6\,\mu\mathrm{m}$. The charge of electrons with an energy of $\geq 10\,\mathrm{MeV}$ at z_{exit} is $Q_{\geq 10\mathrm{MeV}} = 84.1\,\mathrm{pC}$. The ratio of $Q_{\mathrm{high}}/Q_{\geq 10\mathrm{MeV}} \sim 0.52$, indicating that a significant amount of charge is found in the peak at z_3. Fig. 5.14 shows the evolution of the charge density with respect to the electron energy for three positions during the injection process. At z_1, the injection process has just begun, the spectrum exhibits a decrease of charge density with respect to electron energy, a characteristic of the continuous injection process. At z_2, a peak with a central energy of 32 MeV is formed. At z_3, an increase of the population of electrons in the peak energy region is observed. Electrons injected earlier are now situated at the center of the bucket and form the bulk of the peak; they experience smaller accelerating wakefield compared to later injected electrons, some of which caught up with the initially injected ones and ended up populating the peak region.

At the exit of the gas cell, z_{exit} the same electron beam has increased its peak energy to $\mathcal{E}_{peak} = 65.7\,\mathrm{MeV}$, and its FWHM energy spread is reduced to $\Delta\mathcal{E}/\mathcal{E} = 13.1\%$. On one hand, the accelerating wakefield remains relatively flat throughout the length of the electron beam up to the exit of the plasma gas cell, therefore the energy spread is preserved. On the other hand, due to the decrease in density along the propagation axis, the accelerating

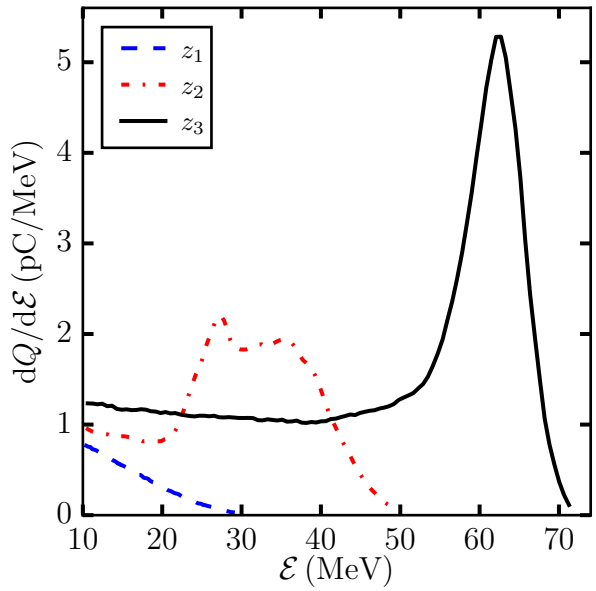

Figure 5.14: Evolution of the charge density with respect to the energy with an energy cutoff at 10 MeV at three different positions: z_{1-3} corresponding to the cases of Fig. 5.12.

wakefield becomes weaker, so that the energy gained by the electron beam between z_3 and z_{exit} is small, ≈ 3.1 MeV.

The accelerating field, E_z can be deduced directly with the equation $\Delta\mathcal{E} = eL_{acc}E_z$. The length over which most of acceleration occurs, L_{acc} is the distance between the beginning and end of position of ionization of the trapped electrons, respectively 1250 μm and 1880 μm (see Fig. 5.11). For $\Delta\mathcal{E} = 65.7$ MeV with $L_{acc} = 630\,\mu$m, $E_z = 104.3$ GV/m, which corresponds to the average field in the injection zone.

The presented results can be explained by the same mechanism as described previously in Sec. 5.1. The fact that electrons with quite different trapping positions reach the same final energy is due to the strong increase and the deformation of the accelerating fields during the trapping of electrons due to nonlinear effects, this leads to the homogenization of energy of the initially trapped and later trapped electrons.

Beam emittance

Here we evaluate the normalized beam emittance following Eq. 1.99 along each axis. The emittance in $x-$ and in $y-$ directions are plotted as functions of electron energy in Fig. 5.15(a) and (b) respectively; the insets of Fig. 5.15(a) and (b) show the distribution of electrons in $(x, p_x)-$ and in $(y, p_y)-$ phase space at the exit of the plasma, z_{exit}.

Considering all electrons with $\mathcal{E} \geq 10$ MeV in the first bucket, $\varepsilon_{x,rms} = 0.33$ mm mrad and $\varepsilon_{y,rms} = 2.09$ mm mrad. $\varepsilon_{y,rms}$ is larger than $\varepsilon_{x,rms}$ because of the oscillation of electrons in the laser polarization $y-$direction. Defining the rms divergence as $\theta_\perp = \Delta p_{\perp,rms}/p_\parallel$, gives $\theta_x = 6.9$ mrad and $\theta_y = 18.5$ mrad at position z_{exit}.

Figs. 5.15(a) and (b) show that the emittance along the $x-$ and $y-$ axis are roughly constant with respect to electron energy, indicating that only the ionization process contributes to electron position $x_{i,rms}$ and momentum $p_{i,rms}$.

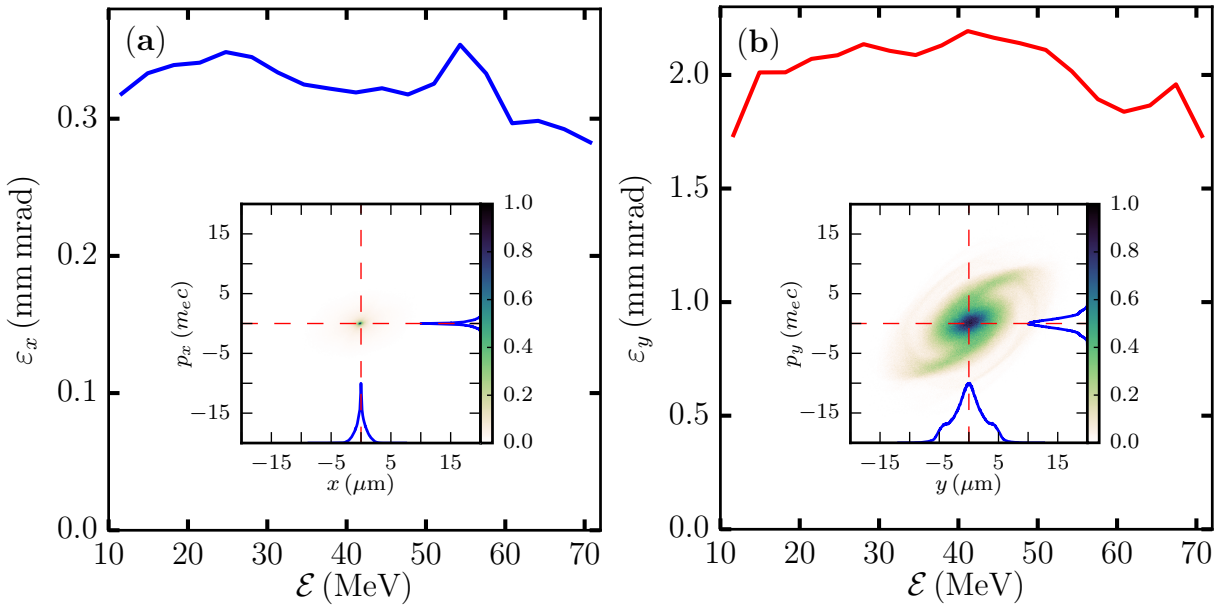

Figure 5.15: Emittance of the electron beam at the exit of the plasma, z_{exit} as a function of electron energy in (a) $x-$ and in (b) $y-$ directions. The energy bin interval is 6.4 MeV. Insets of (a) and (b) represent the distribution of electrons with $\mathcal{E} \geq 10$ MeV in $(x, p_x)-$ and in $(y, p_y)-$ phase space. The color bars represent the electron density normalized to its maximum.

5.2.3 Tuning electron beam energy while preserving energy spread

Experimental results [105] in two overlapping gas jets show that tailoring the density profile leads to the separation of the processes of electron injection and acceleration and permits independent control of both. The results in the previous section give indications on the ways to control injection and acceleration processes independently in a single gas target. In this section we explore the energy tunability of the electron beam with preservation of its energy spread.

Starting from the results obtained at z_3, the position where the injection stops for the ELISA profile, we tailor the density profile along the z-axis for $z > z_3$ in order to tune electron energy. The high energy part of the spectrum with $\mathcal{E} \geq 50$ MeV and the largest electron charge are selected at the end of the injection process ($z = 1900\,\mu$m), as indicated by the black rectangle in Fig. 5.12(z_3). As pointed out in Sec. 5.2.2, this electron beam represents a significant portion (52%) of the total trapped electrons.

The strategy to maximize the energy gain of this electron beam while preserving its energy spread is to achieve the largest possible, flat accelerating wakefield while maintaining the electron beam in the acceleration phase. Numerical experiments were performed to further investigate this idea by tailoring the longitudinal density profile in the acceleration phase.

Flat density

A first example is illustrated in Figs. 5.16-5.17. The longitudinal density profile of interest is shown in Fig. 5.16. This density profile is chosen as an attempt to maximize the accelerating field after the injection process without alteration of the plasma wave wavelength.

In Fig. 5.17(a) are plotted the electron beam distribution together with the laser field and the wakefield at z_4, and at z_{exit} in Fig. 5.17(b). Although electrons have gained ~ 20 MeV

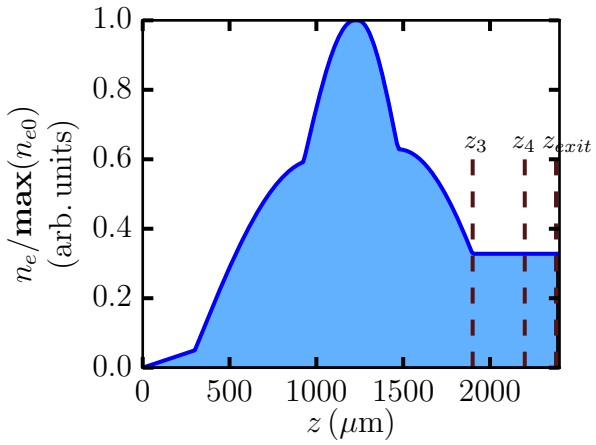

Figure 5.16: Tailored longitudinal density profile with a constant density extended from the end of the injection process. Three positions are marked, z_3, the end of the injection process; z_4, intermediate position between the end of the injection and the exit of the gas cell, z_{exit}.

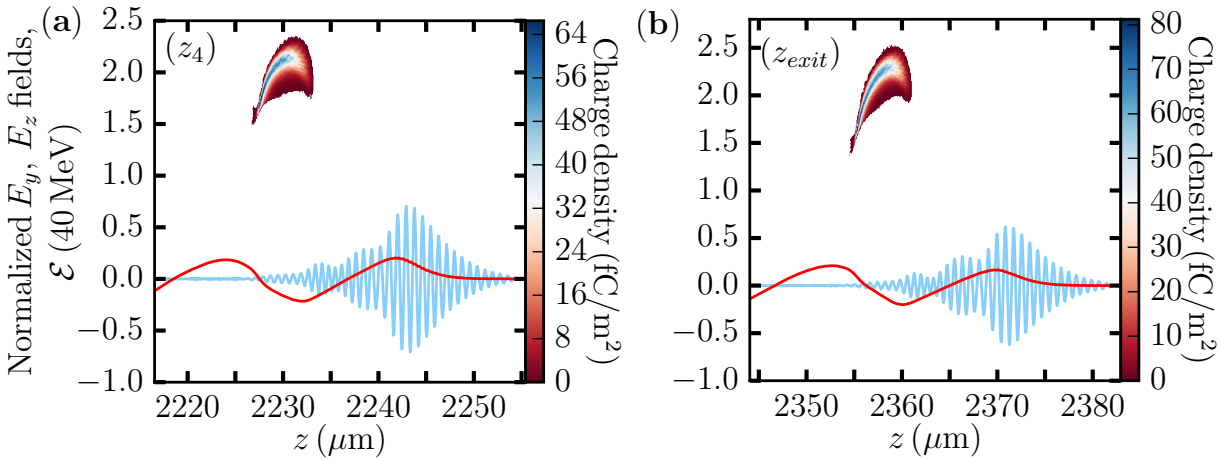

Figure 5.17: Two distinct instants z_4 and z_{exit} of the normalized laser fields, $eE_y/2m_ec\omega_0$ (in light blue), the normalized wakefield, $eE_z/m_ec\mathbf{max}(\omega_\mathbf{p})$ (in red) and the energy, $\mathcal{E}$ of traced electrons ($\mathcal{E} \geq 50\,\mathrm{MeV}$ at z_3) represented by a set of points, are shown in (a) and (b).

between z_3 and z_4, the accelerating wakefield is no longer flat, and electrons at the head and the tail of the beam experience weaker accelerating wakefield as compared to the center part, resulting in the growth of energy spread in both these areas. As a_0 becomes ~ 1, the plasma wave is gradually becoming a regular sinusoidal oscillation with frequency $\omega_p(z)$. From Fig. 5.12, the longitudinal accelerating wakefield at z_3 is bounded between 1868 μm and 1885 μm, having a length of 18 μm. However this length is reduced significantly at z_4 or z_{exit}. At z_4, the accelerating wakefield is bounded between 2227 μm and 2236 μm and at z_{exit}, the accelerating wakefield is bounded between 2356 μm and 2365 μm, giving a length of 9 μm in both cases. This results in the tail of the electron beam slipping into the decelerating wakefield; as a consequence, the tail of the beam is being decelerated while the head is still being accelerated, resulting in an asymmetrical growth of the energy spread.

Fig. 5.18 shows the spectra of accelerated electrons with energy $\mathcal{E} \geq 30\,\mathrm{MeV}$ at different positions z_3, z_4 and z_{exit}. These spectra show that the electron beam energy is increased, as well as the charge at the peak energy between z_3 and z_4, thus improving the FWHM $\Delta\mathcal{E}/\mathcal{E}$ to 11.5%; however a decrease of 14.4% of the charge at the peak energy and an increase in

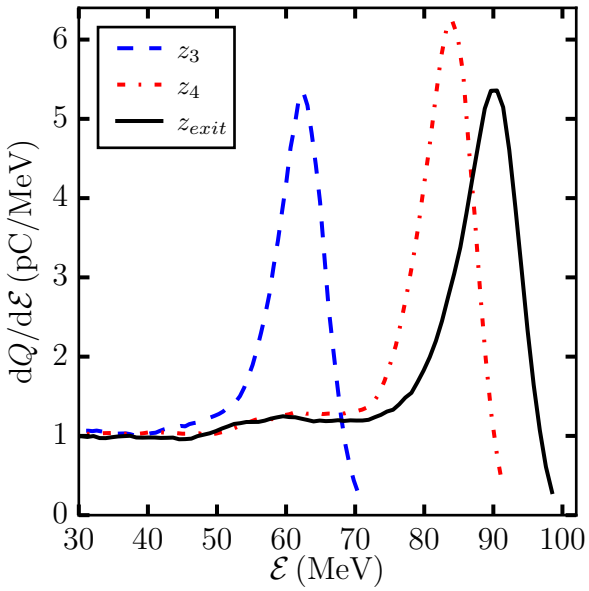

Figure 5.18: Charge density of accelerated electrons having $\mathcal{E} \geq 30\,\mathrm{MeV}$ with respect to electron energy obtained from the simulation using the longitudinal density profile featured in Fig. 5.16 at different positions z_3, z_4 and z_{exit}.

the FWHM $\Delta\mathcal{E}/\mathcal{E}$ to 12% for the spectrum at z_{exit} results from the fact that some electrons are decelerated. This observation is explained by the shrinkage of the accelerating fields structure, leading to the subsequent slippage of electrons into the decelerating wakefield, as shown in Fig. 5.17(c).

The evolution of the laser vector potential, a_0 for this case is similar to the one represented in Fig. 5.9, inferring that the variation in the density profile between z_3 and z_{exit} has no great influence on the laser propagation.

The energy gain starting from the end of the injection process z_3 up to the exit of the gas cell z_{exit} is $\Delta\mathcal{E} = 28.2\,\mathrm{MeV}$, corresponding to an average accelerating field in the acceleration phase of $E_z = 56.4\,\mathrm{GV/m}$.

In Fig. 5.19 are plotted the emittance along $x-$ and $y-$ directions with respect to electron energy, corresponding to the profile of Fig. 5.16. $\varepsilon_{x_{rms}}$ and $\varepsilon_{y_{rms}}$ are preserved, their values are comparable to those shown in Fig. 5.15. This result also confirms that there is no significant influence on the emittance caused by the interaction occurring between the tail of the laser pulse and the head of the electron beam, as observed in Fig. 5.17.

Linear density down-ramp

The slippage of the tail of the electron beam into the decelerating wakefield as shown in Fig. 5.17(b) leads to the growth of energy spread. Phase slippage in increasing density taper has been proposed [130, 209, 210, 211, 212] for controlling electron energy. Conversely, the decrease of longitudinal plasma density is used here to minimize the growth of energy spread. In order to maintain the electron beam in the plasma wave focusing and accelerating phase up to z_{exit}, the plasma wave extension has to be larger than the beam extension i.e. $\lambda_p(z)/4 \gtrsim \ell_{beam}$. For $\ell_{\mathrm{beam}} \sim 6\mu\mathrm{m}$, with $\lambda_p[\mu\mathrm{m}] \sim 3.3 \times 10^{10}\sqrt{n_e[\mathrm{cm}^{-3}]}$, it gives $n_e \leq 1.94 \times 10^{18}\,\mathrm{cm}^{-3}$. From Fig. 5.17(a) it can be observed that the plasma wave is approaching the linear regime and that the electron beam begins to slip into the decelerating wakefield. We can therefore

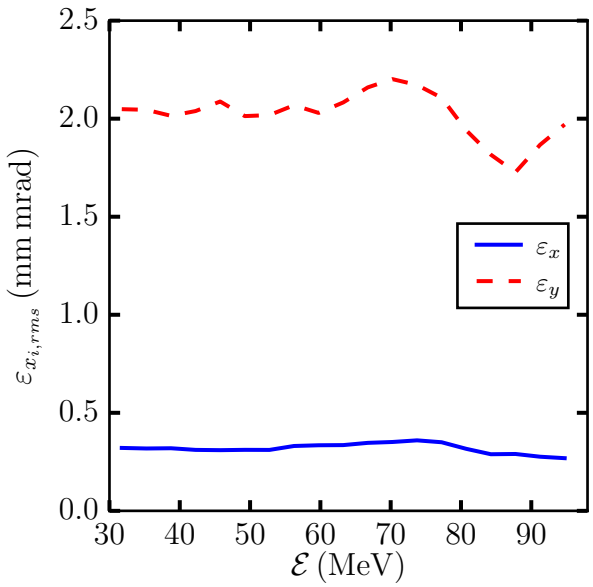

Figure 5.19: Normalized beam emittances, $\varepsilon_{x_{rms}}$ (blue solid line) and $\varepsilon_{y_{rms}}$ (dashed red line) simulated with the longitudinal density profile in Fig. 5.16 with respect to energy. The energy bin interval is 6.8 MeV.

impose $n_e(z_4) = 1.94 \times 10^{18}\,\mathrm{cm}^{-3}$ and use a linear density gradient from z_3 as shown in Fig. 5.20.

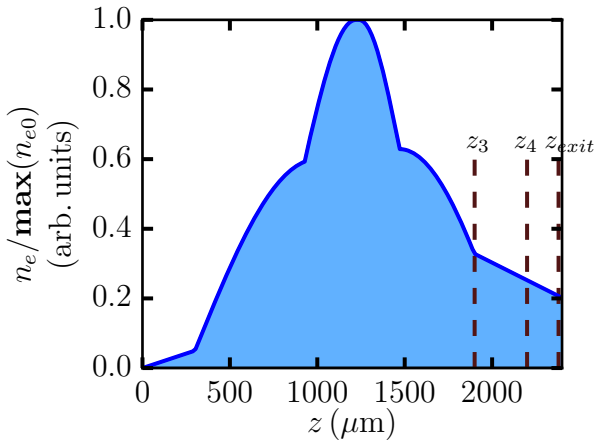

Figure 5.20: Tailored longitudinal density profile with a linear density down-ramp extended from the end of the injection process to the plasma exit. Three positions are marked, z_3, the end of the injection process; z_4, intermediate position between the end of the injection and the exit of the gas cell, z_{exit}.

In Fig. 5.21(a) and (b) are plotted the evolution of the electron beam distribution, together with the laser field and wakefield at two distinct positions z_4 and z_{exit}. The gradual decrease of density increases λ_p and helps the electron beam to stay in the accelerating phase of the wakefield; the symmetry of this electron beam is preserved over a longer distance compared to the case with a flat density shown in Fig. 5.17. Also, due to the weaker accelerating wakefield as the density is decreased, the energy gain of the electron beam is reduced, $\Delta\mathcal{E} = 17\,\mathrm{MeV}$, with an average accelerating field in the acceleration phase of $E_z = 34\,\mathrm{GV/m}$.

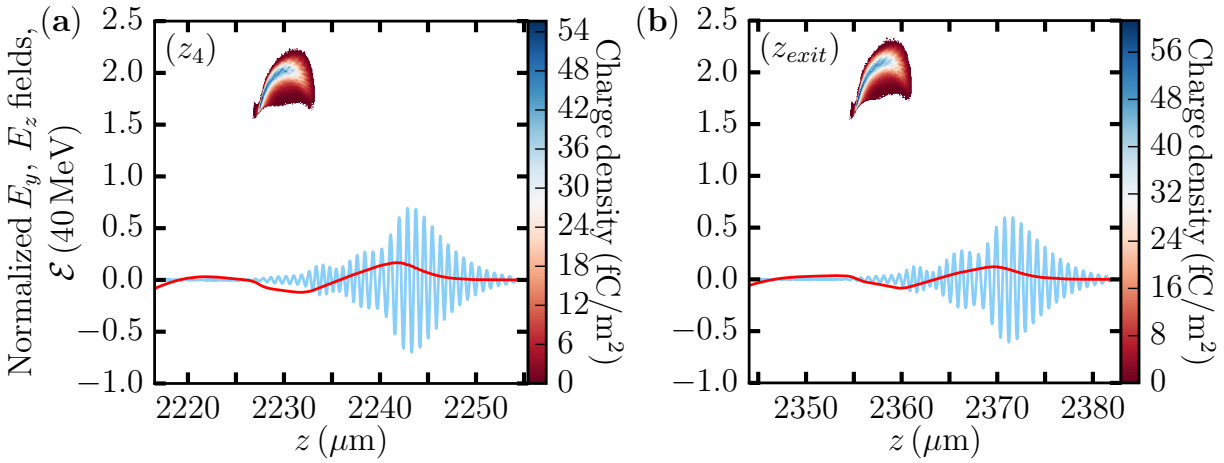

Figure 5.21: Two distinct instants z_4 and z_{exit} of the normalized laser fields, $eE_y/2mc\omega_0$ (in light blue), the normalized wakefield, $eE_z/mc\mathbf{max}(\omega_\mathbf{p})$ (in red) and the energy, $\mathcal{E}$ of traced electrons ($\mathcal{E} \geq 50\,\mathrm{MeV}$ at z_3) represented by a set of points, are shown in (a) and (b).

Fig. 5.22 depicts the evolution of the spectrum of the electron beam at z_3, z_4 and z_{exit}. Between z_3, z_4, the energy of the electron beam and the charge at the peak both increase, while the FWHM $\Delta\mathcal{E}$ is preserved. The comparison of spectra at z_4 and z_{exit} shows that the peak energy is increased by 20 MeV, therefore FWHM $\Delta\mathcal{E}/\mathcal{E}$ is reduced from 14.2% (at z_3) to 11.0% (at z_{exit}).

5.2.4 Discussion

The normalized beam emittances with respect to energy shown in Fig. 5.23 are very similar to those in Fig. 5.19. Using profiles in Fig. 5.16 and 5.20, $\varepsilon_{x_{rms}}$ and $\varepsilon_{y_{rms}}$ in both cases are preserved.

Fig. 5.24 summarizes the energy distribution of the electron beams in the peak for each of the three longitudinal density profiles. The final charge remains at $Q = 43.6\,\mathrm{pC}$ for all three simulations, implying that no electron loss during the acceleration process.

In this simulation, the evolution of the laser vector potential, a_0 remains similar to the one represented in Fig. 5.9. This suggests that the tailored density profile in this region has no great influence on the laser propagation.

Table 5.2 summarizes the values of peak energy and energy spread for the three cases. For the simulation with profile (a), $\mathcal{E}_{peak}$ at z_{exit} is lower due to the decreasing accelerating

Table 5.2: Comparison of the peak energy, $\mathcal{E}$ and FWHM $\Delta\mathcal{E}/\mathcal{E}$ of the accelerated electron beams in different longitudinal density profile.

	Longitudinal density profile	**Peak energy, $\mathcal{E}_{peak}$(MeV)**	**FWHM $\Delta\mathcal{E}/\mathcal{E}$(%)**
(a)	ELISA profile	65.7	13.1
(b)	Descending gradient	82.6	11.0
(c)	Plateau	90.8	12.0

wakefield in the descending phase of the density. The simulation with profile (c) gives the highest $\mathcal{E}_{peak}$ and the FWHM $\Delta\mathcal{E}/\mathcal{E}$ at z_{exit} is decreased to 12%. The result that offers the

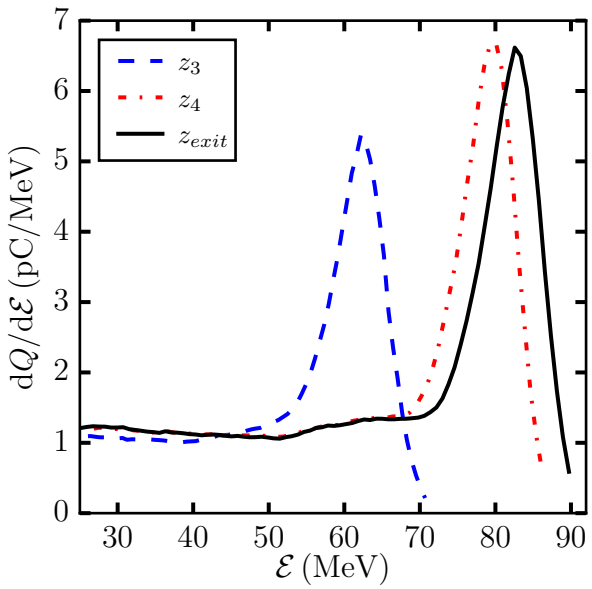

Figure 5.22: Charge density of the accelerated electrons with respect to the electron energy simulated using the longitudinal density profile featured in Fig. 5.20 at different positions z_3, z_4 and z_{exit} .

best compromise with the considered parameters is from the simulation with profile (b), the FWHM $\Delta\mathcal{E}/\mathcal{E}$ is decreased to 11% and the $\mathcal{E}_{peak}$ is increased by $\sim 16.9\,\mathrm{MeV}$ as compared to the result from the initial longitudinal density profile, depicted by profile (a).

From the presented results, the growth in FWHM $\Delta\mathcal{E}/\mathcal{E}$ observed in Fig. 5.17(c) is mainly caused by the evolution from nonlinear, beam-loaded accelerating wakefield to sinusoidal oscillations when a_0 declines. This effect is mitigated using a descending gradient with the appropriate density predicted using the linear theory. Simulations with this longitudinal density profile show a decrease in the FWHM energy spread.

Conclusion

We have presented a detailed analysis of electron dynamics in the injection and acceleration processes. With the chosen laser plasma parameters, simulation results produce an electron beam with $\mathcal{E}_{peak}$ of 65.7 MeV, a FWHM energy spread $\Delta\mathcal{E}/\mathcal{E}$ of 13.1% and a charge of 43.6 pC, where the FWHM energy spread is yet to be improved. The moderate power laser pulse restricts the injection to only ionization-induced injection and a focal position in the descending gradient of the longitudinal density profile allows a slow growth of the vector potential, a_0, delaying the ionization processes, resulting in the shortening of the injection range as compared to the plasma length. In this parameter range, beam loading effects are responsible for two distinct phenomena: the inhibition of the injection process and the homogenization of the energy distribution of the trapped electron beam.

By separating injection and acceleration processes, an additional degree of control is gained in the acceleration process. We tailored the longitudinal density profile starting from the position of the end of the injection process up to the end of the plasma, in order to accelerate the electron beam to a higher energy while preserving its energy spread.

The presented method demonstrates a way to optimize the energy and the energy spread of electron beams needed for injection into a multi-stage plasma-based accelerator. Other

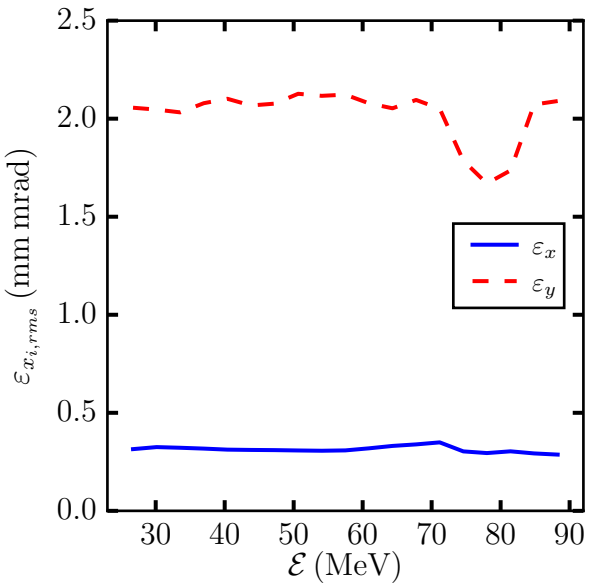

Figure 5.23: Normalized beam emittances, $\varepsilon_{x,rms}$ (blue solid line) and $\varepsilon_{y,rms}$ (dashed red line) simulated with the longitudinal density profile in Fig. 5.20 with respect to energy. Only electrons of $\mathcal{E} \geq 25\,\text{MeV}$ are depicted. The energy bin interval is 6.7 MeV.

beam parameters should also be optimized before they could be used in high energy applications, such as the beam charge, to be increased by at least a factor of 2, and the beam emittance, to be reduced to 1mm mrad or less. Optimization of these two parameters while maintaining the energy spread is foreseen through tailoring of the driving laser beam distribution and is the goal of future work.

Results from Warp simulations using three Fourier modes in the azimuthal Fourier decomposition algorithm show no significant modification in the beam properties, confirming the accuracy of simulations using two Fourier modes, as presented here. The best possible result with the considered parameters is obtained using the descending gradient in the longitudinal density profile. This approach takes into consideration the maximization of the accelerating wakefield and the rephasing of the electron beam to minimize the FWHM energy spread. It is shown that both the charge and the emittance in $x-$ and $y-$ directions of the electron beam are preserved and the FWHM $\Delta\mathcal{E}/\mathcal{E}$ is reduced.

5.3 Extension to higher energy electron beam

In the previous section, we have optimized the longitudinal density profile. In the best case which involves using a linear density down-ramp in the acceleration phase, simulations gave us an electron beam of peak energy 82.6 MeV, a FWHM energy spread $\Delta\mathcal{E}/\mathcal{E}$ of 11% and a charge of 43.6 pC. In this section, we determine the laser-plasma parameters that allow electron beam energy to extend to the 200 MeV energy range while maintaining or improving the other parameters. This study aims to prepare future experiments at the Apollon-10P facility in the CILEX project [20]. Preliminary experiments are carried out at the UHI100 laser facility (CEA-Saclay) to test and possibly determine an optimized configuration for the control of electron injection using the ionization-induced injection mechanism, that would subsequently be implemented on Apollon-10P facility as an injector for multistage experiments. At the UHI100 laser facility, a Ti:Sa laser system delivers 100 TW pulses with 25 fs

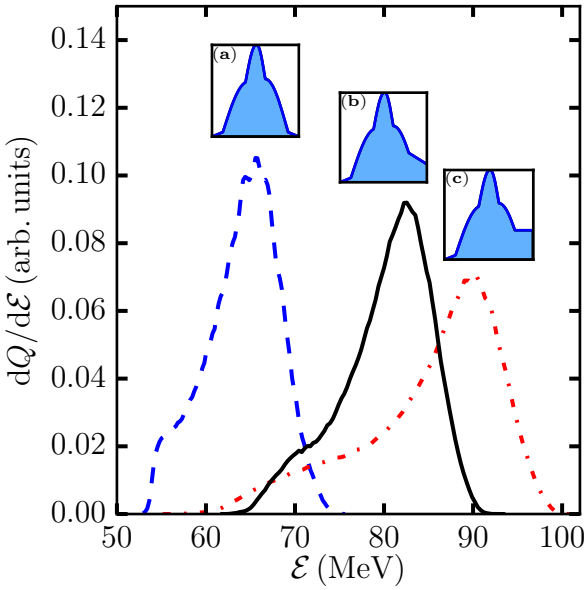

Figure 5.24: Energy distribution of the traced electron beam ($\mathcal{E} \geq 50\,\mathrm{MeV}$ at z_3) at the exit of the gas cell, z_{exit}, the onsets above each spectrum show the corresponding tailored longitudinal density profile: (a) with ELISA profile, (b) with a descending gradient, (c) with a plateau.

pulse duration, at 10 Hz repetition rate. The laser-plasma parameters chosen for the study presented in this section are close to the ones of this facility for comparison with future experiments.

5.3.1 Choice of parameters

Considering that the energy gain is $\Delta\mathcal{E} = eE_z L_{acc}$. In order to increase the beam energy to $\sim$ 200 MeV, the approach is either to increase the laser strength a_0 which in turn increases E_z, or to extend the acceleration length L_{acc}, which is approximately the dephasing length L_d. Since the chosen injection mechanism is the ionization injection, a fine control on the evolution of a_0 is necessary to avoid continuous injection of electrons in the wakefield, in order to prevent any degradation of the energy spread of the electron beam. As observed in Fig. 1.10(b), the ionization process $N^{5+} \rightarrow N^{6+}$ is triggered when $a_0 \sim 1.2$ whereas $N^{6+} \rightarrow N^{7+}$ is triggered when $a_0 \sim 1.5$. As a result, the value of a_0 has to be kept moderate throughout the plasma length, indicating that the initial a_0 and the maximum electron number density on axis have to be set relatively low to avoid strong self-focusing of the laser, which would lead to a strong increase of a_0. This will also prevent the injection of electrons via self-injection mechanism. Another parameter that allows for the control of a_0 evolution is the laser focal position. By having the focal position in the down-ramp of the density profile, we are able to delay the triggering of the ionization-induced injection, hence controlling the start of injection to limit the energy spread.

The proposed longitudinal plasma profile for this study considers a realistic geometry of a gas cell as shown by the gray dashed line in Fig. 5.25. The entrance of the gas cell is located at $z = 1500\,\mu$m and the exit is located at $z = 3000\,\mu$m. A smooth up-ramp and down-ramp of the plasma density are included to model the gas leakage when the gas cell is filled. The presence of the gradual increase of the plasma density in the gas cell can be translated as a gradual decrease of the plasma wave wavelength. Consequently, injected

electrons will always be kept at the back of the bucket so that they always experience the highest accelerating gradient in the nonlinear plasma wave. This longitudinal density profile can be manufactured by making the diameter of the entrance larger than the one of the exit.

We have seen in Sec. 5.2 that beam loading effect has a strong influence in the trapping and acceleration processes. One advantage of the injection through ionization is that we can get some control on the dynamic of beam loading through a specific parameter, which is the concentration of N_2. In order to analyze more closely the influence of this parameter on electron beam properties, calculations were performed by varying the concentration of N_2 between 0.5% and 3%, while having other parameters kept constant.

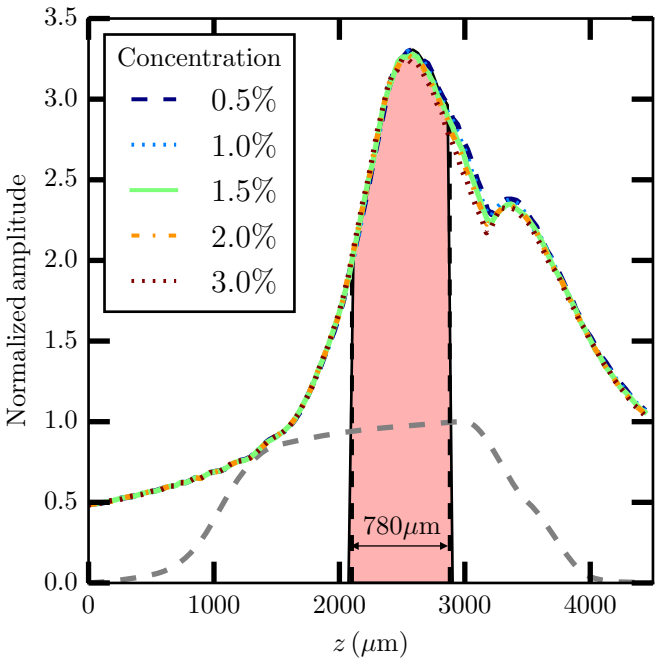

Figure 5.25: Evolution of a_0 for different C_{N_2} with respect to the propagation axis z. The gray dashed line shows a predicted longitudinal density profile. The shaded area represents the injection range of length $\sim 780\,\mu$m.

In Fig. 5.25 is shown the evolution of a_0 for 5 different C_{N_2} and the same longitudinal density profile, the maximum value of the free electron density being $n_e = 4.48 \times 10^{18}\,\mathrm{cm}^{-3}$. Note that this value of density corresponds to the sum of electrons coming both from hydrogen and from the L-shell of nitrogen. Here again, we observe that the evolution of a_0 depends strongly on the longitudinal density profile. a_0 first increases slowly at the up-ramp where the density is low and when the laser enters the higher density region ($z > 1500\,\mu$m), laser self-focusing takes place and the a_0 increases to 3.25 at $z = 2500\,\mu$m, then the laser starts to diffract. However the density is still high at $z = 3000\,\mu$m, leading to another turn of self-focusing, thus we observe an increase of a_0 to 2.37 at $z = 3200\,\mu$m before decreasing till $z = L_{plasma} = 4.5\,$mm. Regardless of C_{N_2}, the evolution of a_0 is very similar, implying that a_0 is weakly correlated to C_{N_2}.

In Fig. 5.25, we have indicated by a shaded area the electron injection range of $780\,\mu$m wide, starting from $z = 2100\,\mu$m. No further injection in the first bucket is detected after $2880\,\mu$m due to beam loading effects. Evidence will be given in the following paragraphs to demonstrate that the inhibition of electron injection in the wakefield is due to beam loading effects. These electrons are then accelerated in the remaining plasma length to attain 200 MeV.

Table 5.3.1 shows a summary of the parameters used in our calculations. Note that for this preliminary study, we are interested in the energy and trapped charge of the injected and accelerated electron beam, the numerical resolution in both directions are fixed at relatively low values so that results can be obtained in a shorter time.

Table 5.3: List of parameters.

Plasma length	L_{plasma}	4.5 mm
Laser profile		bi − Gaussian[a]
Peak normalized laser amplitude	$a_0(z_f)$	1.5
Laser wavelength	λ_0	0.8 μm
Laser spot radius at $1/e^2$	r_L	16.1 μm
Laser duration (FWHM)	τ	23.78 fs
Laser focal position	z_f	3 mm
Laser polarization		linear (in $y-$direction)
Number of Fourier modes		2
Number of particles/cell		64 macro
Cell size in r	Δr	$\lambda_0/2$
Cell size in z	Δz	$\lambda_0/20$

[a]Gaussian in temporal and spatial profiles

Table 5.4 shows $C_{\mathrm{N_2}}$ and the corresponding atomic density of the gas mixture. This atomic density is determined such that the total electron number of the background plasma remains the same after ionization processes for the different gas compositions studied. For example, we set the atomic density $(n_{at})_{(3\%\,\mathrm{N_2})}$ (the subscript $3\%\,\mathrm{N_2}$ refers to the gas composition $97.0\%\,\mathrm{H_2} + 3.0\%\,\mathrm{N_2}$) to $4 \times 10^{18}\,\mathrm{cm^{-3}}$. When all L-shell electrons of the nitrogen atom are ionized, the background plasma has an electron density of $(1 \times 0.97 + 5 \times 0.03)(n_{at}) = 4.48 \times 10^{18}\,\mathrm{cm^{-3}}$. We can now deduce the required initial $(n_{at})_{(2\%\,\mathrm{N_2})}$ such that the background plasma has the same electron density of $4.48 \times 10^{18}\,\mathrm{cm^{-3}}$:

$$(1 \times 0.98 + 5 \times 0.02)(n_{at})_{(2\%\,\mathrm{N_2})} = 4.48 \times 10^{18}\,\mathrm{cm^{-3}}$$
$$(n_{at})_{(2\%\,\mathrm{N_2})} = 4.148 \times 10^{18}\,\mathrm{cm^{-3}}.$$

Table 5.4: Atomic density on axis for each gas composition

Gas composition	Atomic density (n_{at}) $[\times 10^{18}\,\mathrm{cm^{-3}}]$
$99.5\%\,\mathrm{H_2} + 0.5\%\,\mathrm{N_2}$	4.391
$99.0\%\,\mathrm{H_2} + 1.0\%\,\mathrm{N_2}$	4.307
$98.5\%\,\mathrm{H_2} + 1.5\%\,\mathrm{N_2}$	4.226
$98.0\%\,\mathrm{H_2} + 2.0\%\,\mathrm{N_2}$	4.148
$97.0\%\,\mathrm{H_2} + 3.0\%\,\mathrm{N_2}$	4.0

5.3.2 Electron beam properties

Simulations corresponding to different C_{N_2} as shown in Table 5.4 were carried out. In this section, we present the properties of the resulting electron beam.

Electron beam charge

We evaluate the injected and accelerated electron beam charge. Fig. 5.26 shows the relation between the beam charge and the plasma length for all C_{N_2}. The injected beam charge is evaluated for electrons that satisfy the trapping condition, $H < H_s$ and are contained in the FWHM of the electron beam energy distribution.

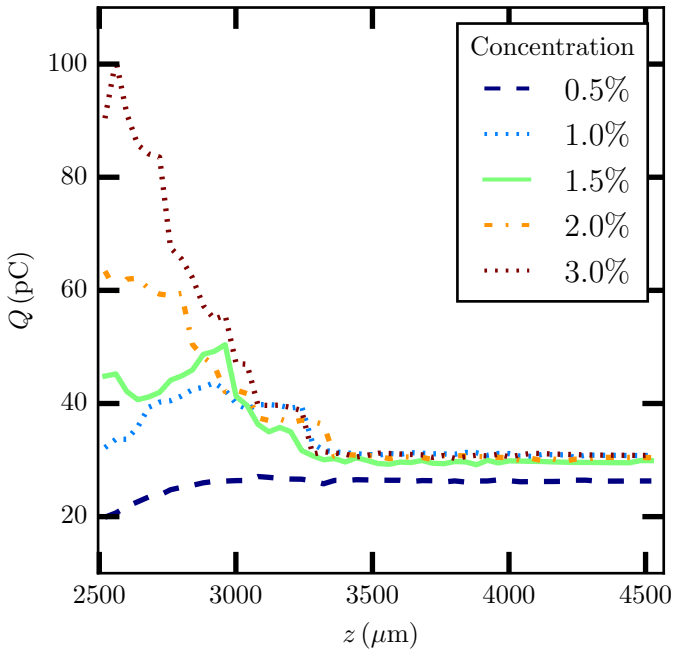

Figure 5.26: Evolution of the trapped beam charge with respect to the plasma length z for different C_{N_2}. The beam charge is evaluated for electrons that satisfy the trapping condition, $H < H_s$ and are contained in the FWHM of the electron beam energy distribution.

Fig. 5.26 shows that, at the early stage of the interaction, the charge exhibits a peak for position $z < 3000\,\mu$m for cases with $C_{N_2} > 0.5\,\%$, we also observe that the higher the N_2 concentration, the higher the accelerated electron beam charge. This peak charge is followed by a decrease of the trapped electron beam charge versus z, due to beam loading effects. In fact the space charge of the trapped electron beam cancels the laser-driven wakefield, inhibiting further injection of electrons. In addition to saturating the amount of trapped charge, the initially injected electrons are lost as z increases. This can be explained by studying the injection volume in phase space. During the injection process, the injection volume in phase space is large, electrons that satisfy the trapping condition are trapped and accelerated in one of the trapping orbits depending on the phase of their ionization. Beam loading effects shrink the injection volume, causing electrons previously trapped near the separatrix to be removed from the trapping orbits. These findings are in agreement with the findings in [82]. In a second phase of the acceleration process, the charge remains constant starting from $z = 3300\,\mu$m till the exit of the plasma at $z = L_{plasma}$. At $z = 4.5\,$mm, the charge evaluated for $C_{N_2} > 0.5\,\%$ is $Q = 31\,$pC whereas for $C_{N_2} = 0.5\,\%$, the beam charge is $Q = 26.3\,$pC. As a consequence of a lower charge, beam loading effects are less significant.

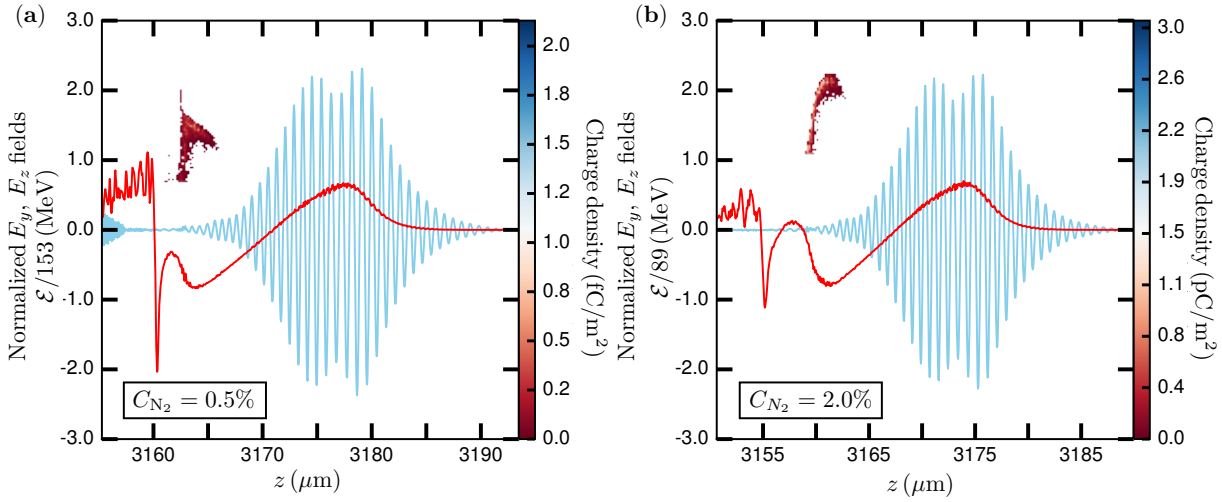

Figure 5.27: Normalized E_y, E_z fields and $\mathcal{E}$ for two nitrogen concentration to show evidence of beam loading effects for different C_{N_2}: (a) $C_{N_2} = 0.5\%$, (b) $C_{N_2} = 2\%$. The beam loading effects are more important in (b) than in (a) as the generated space charge field by trapped electrons has distorted the plasma wave field to the point it changes its sign.

Fig. 5.27 shows the normalized E_y, E_z fields and $\mathcal{E}$ for two C_{N_2}: (a) $C_{N_2} = 0.5\%$, (b) $C_{N_2} = 2\%$. In both cases, the longitudinal length of the relativistic electron bunch length is comparable to the characteristic length of the field variation, implying that the electron bunch is sensitive to any variation in the accelerating field. We observe a bump in the accelerating wakefield, E_z (in red) at $z = 3162\,\mu$m in Fig. 5.27(a) and $z = 3158\,\mu$m in Fig. 5.27(b) due to beam loading effects. In fact, a significant amount of electrons is trapped in the wakefield, and they in turn generate a space charge field that is larger than the plasma wave electrostatic field. In Fig. 5.27(b), this space charge field is so large that it alters the sign of E_z. Electrons that are located in this positive E_z will now be removed from the accelerating structure and their energy diminishes.

Electron beam energy distribution

The electron beam energy distribution is analyzed at $z = L_{plasma}$. Fig. 5.28 shows the charge density of the accelerated electron beam as a function of electron energy for each C_{N_2}. The electron energy spans from 100 to 300 MeV. The energy cutoff at 100 MeV is determined following the same analysis as discussed in Sec. 5.2.2.

Fig. 5.28 shows that, for $C_{N_2} > 0.5\,\%$, the electron spectra peak around 229.1−244.5 MeV, whereas for $C_{N_2} = 0.5\,\%$, the electron spectrum peaks around 261.3 MeV. Spectra for the cases with strong beam loading effects ($C_{N_2} > 0.5\,\%$) are very similar whereas the case with weak beam loading effects ($C_{N_2} = 0.5\,\%$) exhibits a higher electron beam peak energy. This again is tied to the distortion of the laser-driven wakefield due to beam loading effects. This distortion causes a diminution in the accelerating field experienced by the injected electrons, resulting in lower electron beam peak energy in the case with strong beam loading effects. The exact value of the electron beam peak energy and the energy spread evaluated at $z = L_{plasma}$ corresponding to the different gas composition is given in Table 5.5.

In Fig. 5.29(a) is plotted the evolution of the injected electron beam peak energy with respect to the position z according to the plasma longitudinal density profile for different N_2 concentrations. A linear increase of the $\mathcal{E}_{peak}$ is observed for all C_{N_2} between $z = 2500\mu$m and

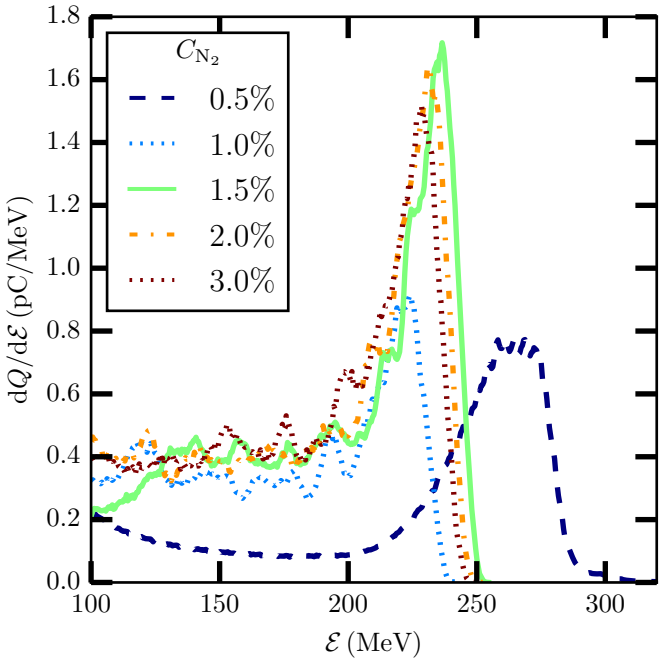

Figure 5.28: Each line shows the energy spectrum of electrons evaluated at $z = L_{plasma}$ for different N_2 concentrations comprised in $[0.5\,\%, 1.0\,\%, 1.5\,\%, 2.0\,\%, 2.5\,\%]$. An energy cutoff at 100MeV is applied.

Table 5.5: Peak energy, $\mathcal{E}_{peak}$ and FWHM $\Delta\mathcal{E}/\mathcal{E}$ evaluated at $z = L_{plasma}$.

Gas composition	Peak energy, $\mathcal{E}_{peak}$ (MeV)	FWHM $\Delta\mathcal{E}/\mathcal{E}$ (%)
$99.5\%\,H_2 + 0.5\%\,N_2$	261.3	15.9
$99.0\%\,H_2 + 1.0\%\,N_2$	244.5	10.3
$98.5\%\,H_2 + 1.5\%\,N_2$	236.1	9.5
$98.0\%\,H_2 + 2.0\%\,N_2$	232.3	10.3
$97.0\%\,H_2 + 3.0\%\,N_2$	229.1	12.0

$z = 3160\,\mu$m, the accelerating field E_z, for $C_{N_2} = 0.5\,\%$ is 228 GV/m, and for $C_{N_2} > 0.5\,\%$ of the order of 215 GV/m. $\mathcal{E}_{peak}$ remains constant for $z > 3600\,\mu$m because the laser-driven accelerating wakefield is becoming weak due to the density down-ramp. The linear increase of $\mathcal{E}_{peak}$ with respect to z can be used as a scaling law to tune the electron bunch peak energy. For instance, in the EuPRAXIA project, the required energy range of the electron bunch for the injector is 150 MeV. To achieve this using the scaling law, we have to reduce the acceleration length to $3000\,\mu$m, however the energy spread might be larger, e.g $\Delta\mathcal{E}/\mathcal{E} = 13\,\%$ for $C_{N_2} = 1.5\,\%$ at $z = 3000\,\mu$m. In practice, we can tailor the density of the acceleration phase $z > 2880\,\mu$m of the density profile (Fig. 5.25) by removing the region between $z = 3000\,\mu$m and $z = 3500\,\mu$m, resulting in a steeper down-ramp and a shorter plasma length.

Fig. 5.29(b) shows the evolution of the injected electron beam FWHM energy spread with respect to the plasma length z for different N_2 concentrations. FWHM $\Delta\mathcal{E}/\mathcal{E}$ decrease in all cases between $z = 2500\,\mu$m and $z = 3240\,\mu$m, then plateau-off for $z > 3300\,\mu$m. The diminution of the energy spread can be explained by the following causes:

- the distortion of the laser-driven wakefield due to beam loading effects remove electrons

that are trapped near the separatrix. Therefore, by getting rid of these low energy electrons, the energy spread is improved.

- the injection of electrons in the wakefield is inhibited when beam loading becomes significant as observed in Fig. 5.26, this will eliminate the growth of FWHM $\Delta\mathcal{E}$ due to injection. Moreover, due to beam loading, the variation with z of the longitudinal field is smaller, yielding an additional reduction in the growth of FWHM $\Delta\mathcal{E}$. Simultaneously, electrons are accelerated once they get injected in the wakefield, leading to the increase of $\mathcal{E}_{peak}$, resulting in an improved ratio $\Delta\mathcal{E}/\mathcal{E}_{peak}$.

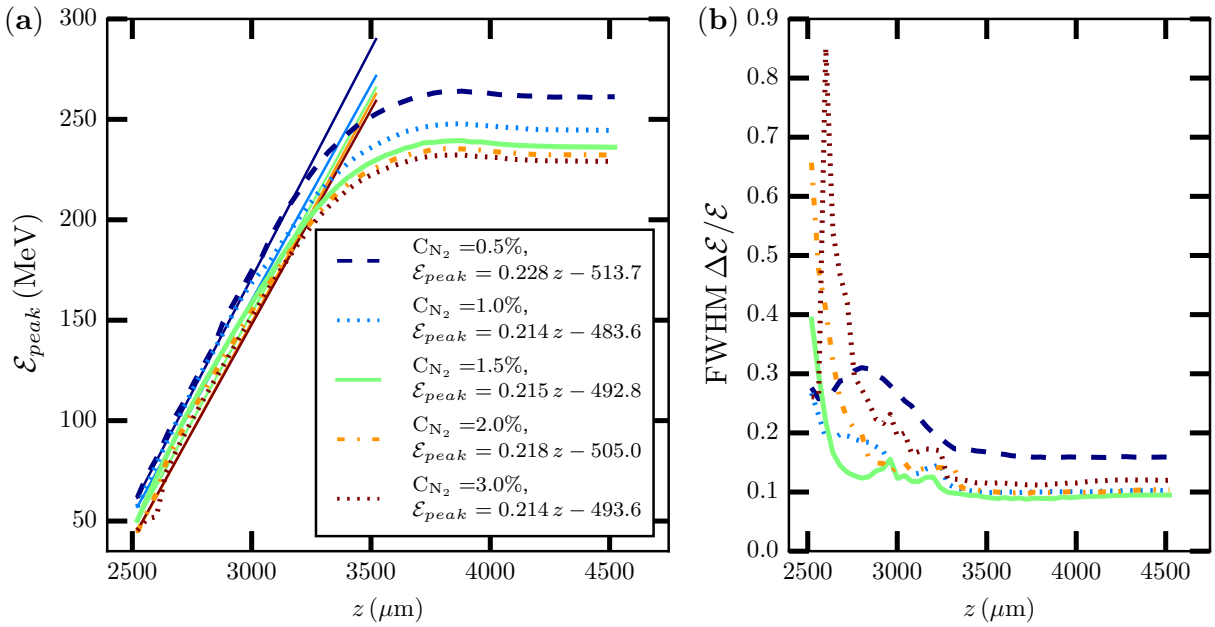

Figure 5.29: Evolution of the injected (a) electron beam peak energy, $\mathcal{E}_{peak}$, (b) electron beam FWHM energy spread, $\Delta\mathcal{E}/\mathcal{E}$ with respect to the plasma length z for different N_2 concentration comprised in $[0.5\,\%, 1.0\,\%, 1.5\,\%, 2.0\,\%, 2.5\,\%]$.

The FWHM $\Delta\mathcal{E}/\mathcal{E}$ remains quasi-constant for $z > 3300\,\mu$m because electrons experience a weaker laser-driven accelerating field due to the density down-ramp. As shown in Fig. 5.29(a), electrons are not gaining much energy beyond this plasma length.

Among all C_{N_2}, the case with $C_{N_2} = 0.5\,\%$ delivers an accelerated electron beam with the lowest charge and the highest energy spread, therefore it is not the most optimal concentration. With higher C_{N_2}, we are able to increase the beam charge and reduce the energy spread due to beam loading effects. Since the accelerated electron beam in these cases have very similar charge and peak energy, we therefore consider the case that offers the smallest energy spread. From Table 5.5, we see that $C_{N_2} = 1 - 2\,\%$ corresponds to our optimum configuration. The following is a more detailed study devoted to this case.

5.3.3 Detailed study with $C_{N_2} = 1.5\,\%$

For this study with $C_{N_2} = 1.5\,\%$, in order to get accurate results for all the characteristics of the accelerated electrons we performed a new calculation with a high accuracy. In particular the grid sizes in both directions have been reduced: $N_z/\lambda_0 = 50$ and $N_r/\lambda_0 = 6$. This is necessary to ensure the convergence of the results, as emphasized in Chapter 4.

Electron beam energy distribution

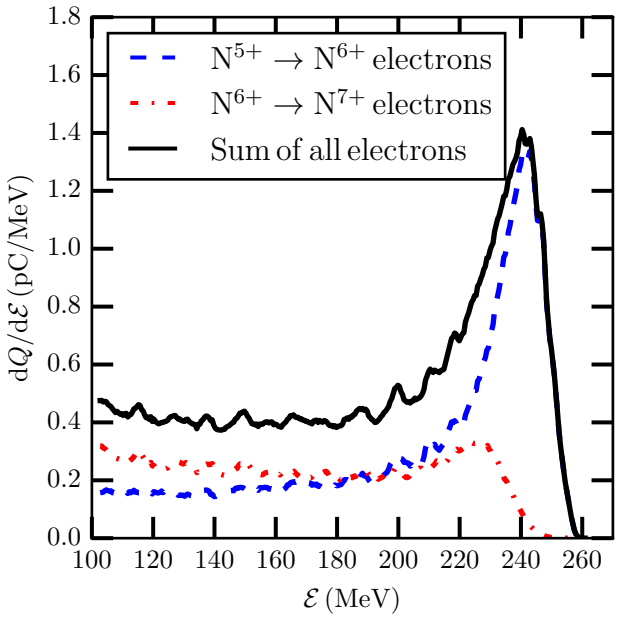

Figure 5.30: The blue dashed line shows the energy spectrum of electrons from $N^{5+} \rightarrow N^{6+}$, whereas the red, dashed-dotted line shows the energy spectrum of electrons from the ionization of $N^{6+} \rightarrow N^{7+}$. The black solid line represents the sum of the two spectra. Only K-shell electrons contribute to the electron beam energy spectrum at z_{exit}. Other electrons are not trapped but contribute to building the plasma wake. An energy cutoff at 100 MeV is applied.

Fig. 5.30 shows the electron beam energy distribution given at $z = L_{plasma} = 4.5\,\text{mm}$. The charge density of the accelerated electron beam is plotted as a function of electron energy. Electrons are tagged in the simulation, therefore we are able to trace the origin of these injected electrons. In blue is the contribution of the 6^{th} electrons, in red is the contribution of the 7^{th} electrons and in black is the sum of both contributions. Only K-shell electrons are injected into the wakefield. Note that the high energy electrons that populate the peak are the 6^{th} electrons.

As compared to Fig. 5.28, $\mathcal{E}_{peak}$ is now 240.9 MeV and its corresponding $dQ/d\mathcal{E}$ has decreased by a factor of 20 %. The FWHM energy spread has increased to 12 %; the total charge, however, remains at $\sim 30\,\text{pC}$ considering electrons contained in the FWHM of the energy distribution.

Beam emittance

Here we evaluate the beam emittance of the electron beam at $z = L_{plasma}$. Considering all electrons contained in the FWHM energy spread, $\mathcal{E} \in [221.2, 248.6]\,\text{MeV}$, $\varepsilon_{x,rms} = 4.2\,\text{mm mrad}$, $\varepsilon_{y,rms} = 4.4\,\text{mm mrad}$. We deduce also the transverse rms divergence, $\theta_{x,rms} = 5.3\,\text{mrad}$, $\theta_{y,rms} = 5.5\,\text{mrad}$. Contrary to the previous case in Sec. 5.2, the emittance and divergence are of the same order of magnitude in both directions. This can be explained by the space charge effect (see Fig 5.32).

Figs. 5.31(a) and 5.31(b) shows the emittance with respect to electron energy evaluated at $z = L_{plasma}$. The emittance along the $x-$ and $y-$axes are roughly constant with respect

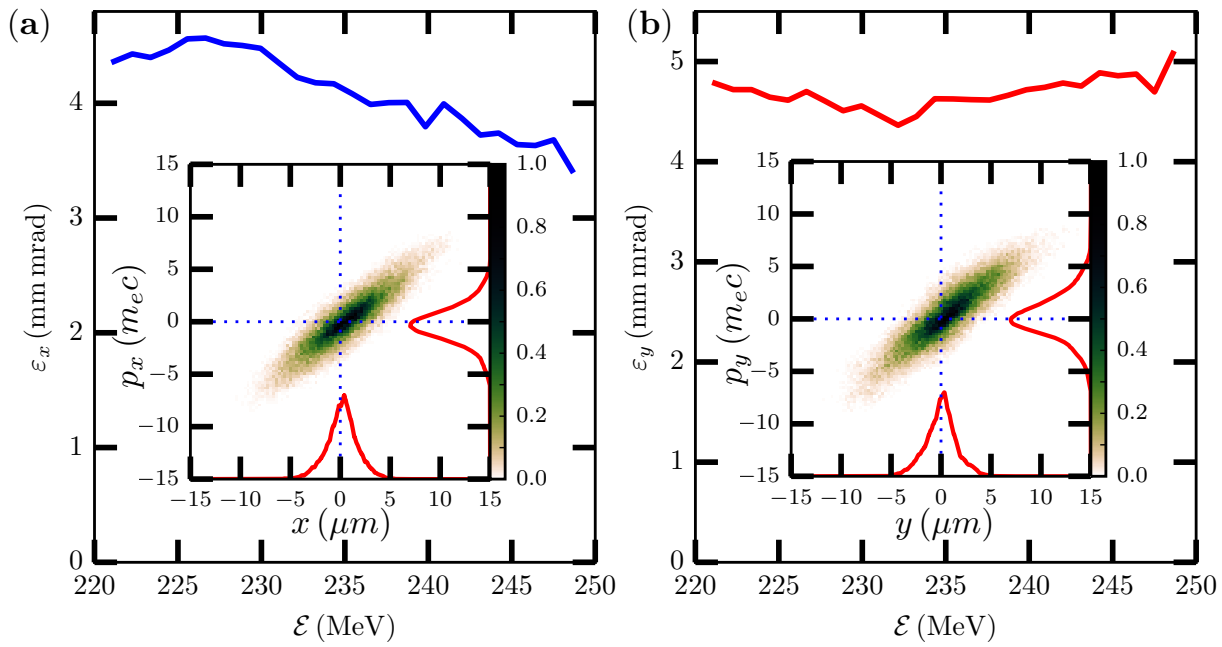

Figure 5.31: Emittance of the electron bunch at the exit of the plasma, $z = L_{plasma}$, as a function of electron energy in (a) $x-$ and in (b) $y-$directions. Insets of (a) and (b) represent the distribution of electrons contained in the FWHM energy spread in (x, p_x) and in (y, p_y) phase space. The color bars represent the electron density normalized to its maximum.

to electron energy and the distribution of electrons in the phase space in both directions are also very similar.

Fig. 5.32 shows the evolution of the emittance with respect to z for electrons that are contained in the FWHM energy spread. We observe that $z < 3000\,\mu$m, the values of the emittance are close to the ones found in Sec. 5.2, that is $< 1\,$mm mrad in the $x-$direction and $\sim 2\,$mm mrad in the $y-$direction. However, for $z > 3000\,\mu$m, we observe an increase of the emittance in both directions. This increase can be due to several effects: (i) the space charge field, (ii) the non-adiabatic evolution of the plasma-wave due to the density gradient, (iii) the interaction with the tail of the laser field; (iv) the numerical noise. Concerning the space charge, -the volume of the bunch is of the order of $8 \times (\sigma_x \times \sigma_y \times \sigma_z)_{rms} = 8 \times 0.48 \times 0.77 \times 0.6\,\mu\text{m}^3$ while its charge is of 42.7 pC, leading to an electron density of about $1.5 \times 10^{20}\,\text{cm}^{-3}$, which is much larger than the plasma density, therefore the space charge effect is important during the acceleration phase. Even at $z = L_{plasma}$, where the volume has increased up to $8 \times (\sigma_x \times \sigma_y \times \sigma_z)_{rms} = 8 \times 3.7 \times 3.9 \times 0.53\,\mu\text{m}^3$ the average density of the bunch is still $4.4 \times 10^{18}\,\text{cm}^{-3}$.

The duration of the laser pulse, was determined from the experimental specification of the UHI100 facility. For this duration, as can be seen in Fig. 5.27(a-b), there is some overlapping between the electron bunch and the tail of the laser pulse, which can have a non-negligible effect on the emittance growth. For both the space charge and the interaction with the laser, their influence on the electron bunch should be strongly reduced by the relativistic effect. However, a more detailed analysis is required when considering a combination of the two. The reduction through relativistic effect is due to a cancellation of the electric field contribution by the magnetic field one. In the FDTD scheme used to solve the Maxwell's equations, the numerical implementation can lead to a loss in accuracy in estimating this cancellation. This point can only be tested, looking at the convergence of the results, as

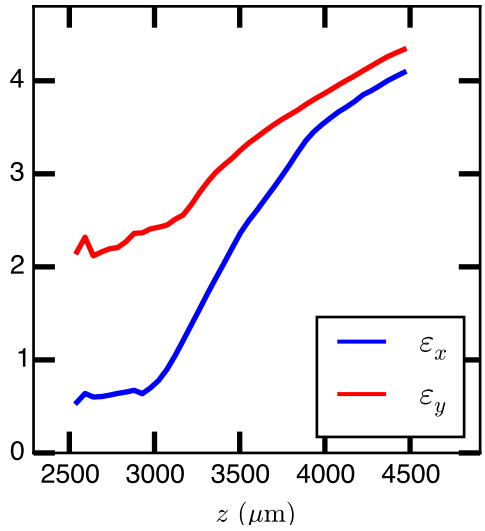

Figure 5.32: Evolution of the emittance of the electron with respect to z. In blue shows $\varepsilon_{x,rms}$ and in red shows $\varepsilon_{y,rms}$.

presented in Chapter 4. That is why a complete convergence study for our considered case remains to be done. However, the present calculation was performed at high resolution, the increase of the emittance by a factor of two between $z = 2500\,\mu$m and $z = 4500\,\mu$m as shown in Fig. 5.32 is unlikely to be only due the numerical implementation.

Conclusion

In this section, we have studied the effect of the concentration of N_2 on the electron beam properties. From this study, the optimal case, which is the case with $C_{N_2} = 1.5\%$ has been determined. This concentration gives the highest charge together with the lowest energy spread. We then provided a more detailed analysis of this case performed with a high numerical resolution of ($N_z/\lambda_0 = 50$, $N_r/\lambda_0 = 6$).

The principal finding is that beam loading effects can be beneficial in helping to inhibit the injection process, therefore limiting the energy spread. The obtained results for the charge and for the distribution in energy of the relativistic electrons are in accordance with the specifications as stated in CiLEX and EuPRAXIA projects. The flip side of the coin is that space charge effects in high N_2 concentration also become more significant, resulting in emittance and divergence growths in the down-ramp of the longitudinal plasma density profile. The optimum values we get for the emittance and divergence at the exit of the plasma, $z = L_{plasma}$ are respectively $\varepsilon_{x,rms} = 4.2\,$mm mrad, $\varepsilon_{y,rms} = 4.4\,$mm mrad, $\theta_{x,rms} = 5.3\,$mrad and $\theta_{y,rms} = 5.5\,$mrad. These values do not yet conform with the specifications as stated in CiLEX and EuPRAXIA projects, therefore mitigation of the emittance and the divergence growths will be the focus of future work.

5.4 Conclusion

In this chapter, we have shown that Warp with the azimuthal Fourier decomposition is capable of producing reliable results for ionization-induced injection. The benchmark that we have done with the experimental result of the group shows a very good agreement.

We proceeded by using the same technique to optimize our electron injector by tailoring density profiles. In this study, beam loading effects played two roles: the inhibition of the injection process and the homogenization of the energy distribution of the trapped electron beam. This resulted in the separation of injection and acceleration processes. We then tailored the density in this acceleration zone to tune the peak energy of the electron beam while preserving all other beam properties. The optimal case is to have a descending gradient in the acceleration zone, in which we succeeded in producing an electron beam of $Q = 43.6\,\mathrm{pC}$, $\mathcal{E}_{peak} = 82.6\,\mathrm{MeV}$, FWHM $\Delta\mathcal{E}/\mathcal{E} = 11\%$, $\varepsilon_{x,rms} = 0.33\,\mathrm{mm\,mrad}$, $\varepsilon_{y,rms} = 2.09\,\mathrm{mm\,mrad}$. $\varepsilon_{y,rms}$ is larger due to the oscillation of electrons in the laser polarization ($y-$direction).

Finally, we studied the influence of the N_2 concentration on the beam properties. In this study, we aimed to produce a higher energy electron beam, extended to $> 200\,\mathrm{MeV}$. A realistic longitudinal density profile was used in the simulation. Results show that strong beam loading effects have led to electrons that were trapped near the separatrix to be removed and decelerated, improving the energy spread around the peak energy distribution. The optimal C_{N_2} from this study is $1.5\,\%$. We then analyzed in detail this case with higher numerical resolutions. As beam loading effects inhibited the injection process, the trapped electrons produced a space charge force that was larger than the transverse Lorentz force in the plasma wave, resulting in emittance growth. The emittances in both transverse directions at $z = L_{plasma}$ are similar, $\varepsilon_{x,rms} \approx \varepsilon_{y,rms} \sim 4.3\,\mathrm{mm\,mrad}$.

The electron beams generated in Secs. 5.2 and 5.3 satisfy the charge and the energy requirements specified in CILEX and EuPRAXIA projects. However the emittance is larger than the specified one. As for future work, optimization will be carried out to discover a configuration to lower the emittance to $\sim 1\mathrm{mm\,mrad}$.

Conclusion

This body of research work focuses on the modeling of the injector using the PIC code Warp and on the numerical methods such as the Lorentz-boosted frame to speedup calculations and the Perfectly Matched Layer (PML) to ensure the precision in numerical calculations.

The outcome of this thesis has demonstrated the efficiency of the PML in the high-order FDTD and the pseudo-spectral solvers. Besides, it has also demonstrated the convergence of the results performed in simulations using the Lorentz-boosted frame technique. This technique speeds up simulations by a large factor (~ 36) while preserving their accuracy. The modeling work in this thesis has allowed analysis and understanding of experimental results, as well as prediction of results for future experiments. Ways to optimize the laser-plasma injector to deliver an electron bunch that conforms with the specifications of future accelerators were also presented.

Main findings

In this section we summarize the main findings of this thesis.

Convergence of simulated results for a $100\,\mathrm{MeV}$ stage in the nonlinear regime using the Lorentz-boosted frame technique

Simulations with the Lorentz-boosted frame technique consist of choosing the optimal frame of reference that travels close to the speed of light in the direction of the laser pulse. The direct consequence of this change of frame is the Lorentz contraction and dilation of space and time. With the laser pulse wavelength being extended and the plasma length being shortened, the crossing time between both the components is also reduced, leading to a large speedup. Simulations of external injection into the wakefield with Warp in 3D Cartesian coordinates or without self-injection with OSIRIS using azimuthal Fourier decomposition algorithm were previously studied and the results obtained were very similar to the ones obtained using a full 3D PIC code in the lab frame. However, the modeling of the self-injection regime poses some challenges due to strong nonlinear particle dynamics. In this thesis, we modeled the dynamics of self-injected electrons in the blowout regime at a plasma density of $10^{19}\,\mathrm{cm}^{-3}$ at various relativistic factors in the Lorentz-boosted frame. The obtained results demonstrate accurate modeling of the evolution of the plasma wakefield, and of electron bunch properties such as the charge, the average energy, the energy spread and the transverse dynamics with agreement at $> 99\,\%$ level between simulations using various relativistic factor in both the Cole-Karkkainen (CK) and the Pseudo Spectral Analytical Time Domain (PSATD) solvers.

Efficiency of the PML in the high-order FDTD and the PSTD solvers is preserved

Bérenger's Perfectly Matched Layer is the state-of-the-art for solving unbounded electromagnetic problems with the FDTD method. It ensures waves and disturbances originating with the model domain to leave the domain without affecting the interior solution in a way that is not physically realistic. Through this work, we have extended the theoretical and numerical analysis of the coefficient of reflection of the PML to solvers of any order of accuracy, including at the limit of the infinite order that represents the pseudo-spectral formulations. The theoretical and numerical analysis conducted demonstrated the preservation of the efficiency of the PML for the high-order FDTD and the PSTD solvers. Using the PML with a suitable numerical resolution and depth of the PML, the induced error is of the order of $< 10^{-3}$.

Validation of simulated results with Warp using azimuthal Fourier decomposition algorithm

The azimuthal Fourier decomposition algorithm takes advantage of the symmetry of the laser-plasma interaction in underdense plasmas in cylindrical coordinates (r, z, θ). This method applies a Fourier decomposition in θ on the fields and currents in azimuthal harmonics modes $e^{il\theta}$. It offers a quasi-3D description of the LWFA with a computational load that is similar to bi-dimensional calculations, enabling parametric studies to be carried out. We have modeled a laser-plasma injector working in the ionization-induced injection scheme with a realistic density profile and experimental laser-plasma parameters using this algorithm in Warp. Results from the comparison between simulated and experimental results have shown very good agreement. A detailed analysis of simulation results has also given more insights of electron trapping and acceleration processes when ionization-induced injection and density gradient schemes are combined.

Optimization of the laser-plasma injector by tailoring density profiles

Using Warp with azimuthal Fourier decomposition algorithm, we have performed simulations to optimize a laser-plasma injector. Laser-plasma parameters are chosen in order to achieve electron acceleration in the range of $50 - 200\,\mathrm{MeV}$, an energy spread $< 10\,\%$, a normalized emittance of $\sim 1\,\mathrm{mm\,mrad}$ and a charge of $\geq 10\,\mathrm{pC}$. Using first the laser-plasma parameters of experiments performed at the Lund Laser Center, the model was shown to reproduce experimental results. Then L_{plasma} was reduced and the laser was focused at the down-ramp of the ELISA profile to delay the triggering of the ionization-induced injection, a reduction of the global injection volume was achieved. As a result, we obtained an electron beam with a FWHM energy spread of 13.1 %, peak energy of 65.7 MeV, a charge of 43.6 pC and normalized emittances of $\varepsilon_{x,rms} = 0.33\,\mathrm{mm\,mrad}$, $\varepsilon_{y,rms} = 2.09\,\mathrm{mm\,mrad}$. The difference in $\varepsilon_{x,rms}$ and $\varepsilon_{y,rms}$ is due to the fact that electrons gain momentum under the laser polarization effect in the $y-$direction. We then separated the injection and acceleration processes to gain an additional degree of control on the electron beam properties. By tailoring the longitudinal density profile starting from the position of the end of the injection process up to the exit of the plasma, we were able to tune the electron beam peak energy while preserving its energy spread. The best possible result with the considered parameters was obtained using the descending gradient in the longitudinal density profile, the electron beam has a peak energy of 82.6 MeV and a FWHM energy spread of 11 %, the other properties are preserved.

Optimization of the laser-plasma injector by studying the influence of the N_2 concentration in the plasma

To better prepare for future experiments at Apollon-10P facility in the frame of the CILEX project, experiments are carried out at the UHI100 laser facility at CEA Saclay to explore laser-plasma configurations able to achieve a 200 MeV peak energy electron beam. Simulations were conducted in parallel with experiments. Parameters are chosen to be close to the ones of this facility. From the study of the role of the longitudinal density profile, the laser focal position and the plasma length, we gained a better understanding of the dynamics of ionization-induced injected electrons in a realistic longitudinal density profile. We have further studied the influence of the concentration of nitrogen (C_{N_2}), another key parameter for the electron beam properties. We showed that a high C_{N_2} induces strong beam loading effects that can limit the energy spread around the peak energy, however it also causes the space charge effect to be more significant in the accelerated electron beam, resulting partly in the emittance growth in the down-ramp of the longitudinal density profile where the plasma density is decreasing. For the optimal case, which is with $C_{\mathrm{N}_2} = 1.5\,\%$, the obtained electron beam at the exit of the plasma, $z = L_{plasma}$, has a charge of 30.7 pC, a peak energy of 240.9 MeV, a FWHM energy spread of 12 % and a normalized emittance of ~ 4.3 mm mrad in both transverse directions.

Future prospects

The research work presented in this thesis has opened up several prospects in the modeling of the laser-plasma injector both in the numerical and physical aspects.

Numerical aspect

Extension of the PML efficiency study to the PSATD solver

In this thesis, we have provided an approximative theoretical model for the evaluation of the PML efficiency in the high-order FDTD and the PSTD solvers. Following this work, Henri et al. [192] have presented a more accurate model for these two solvers. This proposed model takes into account secondary sources. The theoretical and numerical analysis of the PML is now extended on the PSATD solver, the study is currently underway.

Implementation of the PML in cylindrical coordinates

In this thesis, we have shown that PIC simulations with azimuthal Fourier decomposition algorithm are very reliable to model LWFA. A typical simulation requires ~ 20000 CPU-hours with reasonable numerical resolutions. In the explored configuration, we took a transverse box size that is of $6.25 \times r_L$ to avoid any reflection onto the axis when the diffracted laser field reaches the radial box boundary. As a result, this increases significantly the number of grids to be computed in the radial direction. Implementing the PML in cylindrical coordinates based on the formulation described in [213] will allow us to reduce the number of grids in the radial direction, and subsequently computational time.

Convergence of simulated results for a 1 GeV stage in the nonlinear regime using the Lorentz-boosted frame technique

Convergence studies for the 100 MeV stage at $10^{19}\,\mathrm{cm}^{-3}$ in the nonlinear regime have shown promising results in 2-1/2D simulations with Warp using the Lorentz-boosted frame technique. Since the regime currently explored for injectors is at few times $10^{18}\,\mathrm{cm}^{-3}$, which allows for a 1 GeV stage modeling, performing a convergence study both in the CK and the PSATD solvers at this condition will interest the LWFA community. This will encourage more parametric studies with the Lorentz-boosted frame technique as the computational cost is substantially reduced. Furthermore, this future work will provide optimal numerical parameters to produce accurate results in simulations using the Lorentz-boosted frame technique in the nonlinear regime. We will therefore be one-step closer to performing a full 3D PIC simulation for 10 GeV-stage and beyond for our future collider application.

More accurate modeling of the laser-electron beam interaction in LWFA simulations with ionization-induced injection scheme

LWFA simulations with ionization-induced injection scheme come with their own challenges. As can be seen in Fig. 5.27, there is an overlap between the electron bunch and the back of the laser pulse, which can induce a non-negligible emittance growth to the accelerated electron bunch. In our study, two contributors to this emittance growth have been identified: the space charge effect and the interaction of the laser pulse, however the presence of the relativistic effect should reduce the contribution of these factors with the cancellation of the electric field by the magnetic field. In fact this cancellation might not be exact due to the numerical implementation in the standard FDTD solver. Therefore a convergence study as presented in Chapter 4 should be performed to test out the optimal numerical resolution. Another envisaged solution is to perform simulations using a third-order accurate interpolation method to improve the interpolation of the $\boldsymbol{B}-$field as proposed in [67, 203], instead of the standard second-order accurate method in time.

Physical aspect

Mitigation of the emittance growth at the end of the injection process in a laser-plasma injector

While modeling the currently explored regime for a 200 MeV electron bunch, we have encountered an emittance growth which is partly due to the interaction between the laser pulse and the accelerated electron bunch. To avoid this interaction, one solution is to reduce the laser duration and readjust the plasma density to satisfy the resonant condition ($c\tau_L \sim \lambda_p$). Simulations with a shorter pulse are currently ongoing and they have already shown some promising results. The best emittance values obtained in the optimization work in this thesis are $\varepsilon_x = 0.33\,\mathrm{mm\,mrad}$ and $\varepsilon_y = 2.09\,\mathrm{mm\,mrad}$, which are still larger than $\sim 1\,\mathrm{mm\,mrad}$ as required for accelerator applications. Thus a novel configuration to reduce the emittance to $\sim 1\,\mathrm{mm\,mrad}$ constitutes one of the future work.

More realistic simulations with measured laser spatiotemporal profile

A recent article on the space-time characterization of ultra-intense femtosecond laser beams [214] has demonstrated experimentally a spatiotemporal reconstruction of the laser field $\boldsymbol{E}_L(r,t)$. These new measurements allow an in-depth characterization and optimization of

ultra-intense lasers and ultimately to the advanced control of relativistic motion of electrons in LWFA. Inserting these measurements in PIC simulations enables a more realistic description of the interaction between laser and plasma, and provides a better understanding of the experiments.

Modeling of the coupling between the injector, the transport system and the accelerator

One of the key objectives in the design of a laser-plasma based particle accelerator is to conduct a start-to-end simulation of the multi-stage accelerator. In this thesis, an extensive study on the injector has been conducted, the next step consists of extracting the accelerated electron bunch and injecting it in the transport system. Two methods can be considered for the modeling of the transport system: the electrostatic solver in Warp or some particle tracking codes. For the modeling of the accelerator stage, which consists of a long plasma medium ($\sim 1\,\mathrm{m}$), operating in a quasi-linear regime (no self-injection should be expected), some of the suitable tools for its modeling are the Lorentz-boosted frame technique [31], or quasi-static methods such as WAKE [25].

Appendix A

Derivation of the coefficient of reflection at the grid nodes

The explicit derivation of the coefficient of reflection at the grid nodes is given in this appendix for the second order case, where we consider

$$C_p = \begin{cases} 1 & \text{if } p = 1, \\ 0 & \text{otherwise.} \end{cases} \tag{A.1}$$

The set of equations Eqs. 3.37-3.39 is solved by first differencing Eq. 3.38 in time, giving

$$\begin{aligned} E_{y_{j+1,k+1/2}}^{\ n} - E_{y_{j+1,k+1/2}}^{\ n-1} = \ & E_{y_{j,k+1/2}}^{\ n} - E_{y_{j,k+1/2}}^{\ n-1} \\ & + \tfrac{\Delta x}{\Delta y}\left(E_{x_{j+1/2,k+1}}^{\ n} - E_{x_{j+1/2,k}}^{\ n} - E_{x_{j+1/2,k+1}}^{\ n-1} + E_{x_{j+1/2,k}}^{\ n-1}\right) \\ & - \tfrac{\Delta x}{\Delta t}\left(B_{z_{j+1/2,k+1/2}}^{\ n+1/2} - 2B_{z_{j+1/2,k+1/2}}^{\ n-1/2} + B_{z_{j+1/2,k+1/2}}^{\ n-3/2}\right), \end{aligned} \tag{A.2}$$

followed by differencing Eq. 3.39 according to the transverse $y-$direction

$$\begin{aligned} E_{x_{j+1/2,k+1}}^{\ n} - E_{x_{j+1/2,k}}^{\ n} \ & = E_{x_{j+1/2,k+1}}^{\ n-1} - E_{x_{j+1/2,k}}^{\ n-1} \\ & + V_y\left(B_{z_{j+1/2,k+3/2}}^{\ n-1/2} - 2B_{z_{j+1/2,k+1/2}}^{\ n-1/2} + B_{z_{j+1/2,k-1/2}}^{\ n-1/2}\right), \end{aligned} \tag{A.3}$$

where $V_y = c^2\Delta t/\Delta y$.

Eliminating E_x in Eq. A.2 by using Eq. A.3, yields

$$\begin{aligned} E_{y_{j+1,k+1/2}}^{\ n} - E_{y_{j+1,k+1/2}}^{\ n-1} \ & = E_{y_{j,k+1/2}}^{\ n} - E_{y_{j,k+1/2}}^{\ n-1} \\ & + \tfrac{\Delta x}{\Delta y} V_y\left(B_{z_{j+1/2,k+3/2}}^{\ n-1/2} - 2B_{z_{j+1/2,k+1/2}}^{\ n-1/2} + B_{z_{j+1/2,k-1/2}}^{\ n-1/2}\right) \\ & - \tfrac{\Delta x}{\Delta t}\left(B_{z_{j+1/2,k+1/2}}^{\ n+1/2} - 2B_{z_{j+1/2,k+1/2}}^{\ n-1/2} + B_{z_{j+1/2,k+1/2}}^{\ n-3/2}\right), \end{aligned} \tag{A.4}$$

Differencing then Eq. A.4 in the $x-$direction, gives

$$\begin{aligned} E_{y_{j+1,k+1/2}}^{\ n} - E_{y_{j+1,k+1/2}}^{\ n-1} \ & - E_{y_{j,k+1/2}}^{\ n} + E_{y_{j,k+1/2}}^{\ n-1} \\ & = E_{y_{j,k+1/2}}^{\ n} - E_{y_{j,k+1/2}}^{\ n-1} - E_{y_{j-1,k+1/2}}^{\ n} + E_{y_{j-1,k+1/2}}^{\ n-1} \\ & + \tfrac{\Delta x}{\Delta y} V_y\left(B_{z_{j+1/2,k+3/2}}^{\ n-1/2} - 2B_{z_{j+1/2,k+1/2}}^{\ n-1/2} + B_{z_{j+1/2,k-1/2}}^{\ n-1/2}\right) \\ & - \tfrac{\Delta x}{\Delta y} V_y\left(B_{z_{j-1/2,k+3/2}}^{\ n-1/2} - 2B_{z_{j-1/2,k+1/2}}^{\ n-1/2} + B_{z_{j-1/2,k-1/2}}^{\ n-1/2}\right) \\ & - \tfrac{\Delta x}{\Delta t}\left(B_{z_{j+1/2,k+1/2}}^{\ n+1/2} - 2B_{z_{j+1/2,k+1/2}}^{\ n-1/2} + B_{z_{j+1/2,k+1/2}}^{\ n-3/2}\right) \\ & + \tfrac{\Delta x}{\Delta t}\left(B_{z_{j-1/2,k+1/2}}^{\ n+1/2} - 2B_{z_{j-1/2,k+1/2}}^{\ n-1/2} + B_{z_{j-1/2,k+1/2}}^{\ n-3/2}\right), \end{aligned} \tag{A.5}$$

where $V_y = c^2\Delta t/\Delta y$.

Finally, Eq. 3.38 is used to eliminate B_z from A.5, giving

$$\begin{aligned} E_{y_{j,k+1/2}}^{n+1} - E_{y_{j,k+1/2}}^{n} &= E_{y_{j,k+1/2}}^{n} - E_{y_{j,k+1/2}}^{n-1} + \alpha_y \left(E_{y_{j,k+1/2}}^{n-1} + E_{y_{j,k+1/2}}^{n-2} \right) \\ &- \alpha_y \tfrac{\Delta t}{\Delta y} V_y \left(E_{y_{j,k+3/2}}^{n-1} - 2E_{y_{j,j+1/2}}^{n-1} + E_{y_{j,k-1/2}}^{n-1} \right) \\ &+ \tfrac{\Delta t}{\Delta y} V_y \left(E_{y_{j,k+3/2}}^{n} - 2E_{y_{j,k+1/2}}^{n} + Ey_{j,k-1/2}^{n} \right) \\ &+ \beta_y \tfrac{\Delta t}{\Delta x} \left(E_{y_{j+1,k+1/2}}^{n} - 2E_{y_{j,k+1/2}}^{n} + \mathrm{E}_{\mathrm{y}_{j-1,k+1/2}}^{n} \right) \\ &- \beta_y \tfrac{\Delta t}{\Delta x} \left(E_{y_{j+1,k+1/2}}^{n-1} - 2E_{y_{j,k+1/2}}^{n-1} + E_{y_{j-1,k+1/2}}^{n-1} \right), \end{aligned} \tag{A.6}$$

where (α_y, β_y) are given in Eq. 3.13, $V_y = c^2\Delta t/\Delta y$.

Expression A.6 now consists only of E_y, enabling the substitution of a plane monochromatic traveling wave trial-solutions for the evaluation of the coefficient of reflection, r_{node}. Assuming a trial solution of the form $\mathrm{e}^{i\omega\Delta t - i(k_x\Delta x + k_y\Delta y)}$, and that the norms k_x and k_y are conserved by the transmitted and the reflected waves, so the transmitted wave is given by $(1-r)\mathrm{e}^{i\omega\Delta t - i(k_x\Delta x + k_y\Delta y)}$, and the signal in front of the slice in $x-$direction is defined as a sum of the incident wave and the reflected one, giving $\mathrm{e}^{i\omega\Delta t - i(k_x\Delta x + k_y\Delta y)} - r\mathrm{e}^{i\omega\Delta t + i(k_x\Delta x + k_y\Delta y)}$ (where r represents the coefficient of reflection).

Considering that the slice is at j, we have

$$\begin{aligned} Ey_{j,k+1/2}^{n+1} &= (1-r)\mathrm{e}^{i\omega\Delta t - i(k_y\Delta y/2)}, \\ Ey_{j,k+1/2}^{n} &= (1-r)\mathrm{e}^{-i(k_y\Delta y/2)}, \\ Ey_{j,k+1/2}^{n-1} &= (1-r)\mathrm{e}^{-i\omega\Delta t - i(k_y\Delta y/2)}, \\ Ey_{j,k+1/2}^{n} &= (1-r)\mathrm{e}^{-i(k_y\Delta y/2)}, \\ Ey_{j,k+1/2}^{n-1} &= (1-r)\mathrm{e}^{-i\omega\Delta t - i(k_y\Delta y/2)}, \\ Ey_{j,k+1/2}^{n-2} &= (1-r)\mathrm{e}^{-2i\omega\Delta t - i(k_y\Delta y/2)}, \\ Ey_{j,k+3/2}^{n-1} &= (1-r)\mathrm{e}^{-i\omega\Delta t - i(3k_y\Delta y/2)}, \\ Ey_{j,k-1/2}^{n-1} &= (1-r)\mathrm{e}^{-i\omega\Delta t - i(-k_y\Delta y/2)}, \\ Ey_{j,k+3/2}^{n} &= (1-r)\mathrm{e}^{-i(3k_y\Delta y)/2}, \\ Ey_{j+1,k+1/2}^{n} &= (1-r)\mathrm{e}^{-i(-k_x\Delta x - k_y\Delta y)/2}, \\ Ey_{j+1,k+1/2}^{n-1} &= (1-r)\mathrm{e}^{-i\omega\Delta t - i(-k_x\Delta x - k_y\Delta y)/2}, \\ Ey_{j-1,k+1/2}^{n} &= \mathrm{e}^{-i(-k_x\Delta x + k_y\Delta y/2)} - r\mathrm{e}^{-i(k_x\Delta x + k_y\Delta y/2)}, \\ Ey_{j-1,k+1/2}^{n-1} &= \mathrm{e}^{-i\omega\Delta t - i(-k_x\Delta x + k_y\Delta y/2)} - r\mathrm{e}^{-i\omega\Delta t - i(k_x\Delta x + k_y\Delta y/2)}. \end{aligned} \tag{A.7}$$

Inserting the plane monochromatic traveling-wave trial solutions of A.7 in Eq. A.6, and solving yields the coefficient of reflection at the grid nodes, r_{node}.

$$r_{node} = \frac{a - b\cos(k_y\Delta y) - c\cos(k_x\Delta x)}{a - \cos(k_y\Delta y) - c\mathrm{e}^{-ik_x\Delta x}}, \tag{A.8}$$

where

$$\begin{cases} a = \mathrm{e}^{i\omega\Delta t} - (2+\alpha_y) + \mathrm{e}^{-i\omega\Delta t}(1+2\alpha_y) + \alpha_y\mathrm{e}^{-2i\omega\Delta t}, \\ b = 2V_y\frac{\Delta t}{\Delta y}\left(1 - \alpha_y\mathrm{e}^{-i\omega\Delta t}\right), \\ c = 2\beta_y\frac{\Delta t}{\Delta x}\left(1 - \mathrm{e}^{-i\omega\Delta t}\right). \end{cases}$$

Appendix B

Derivation of the coefficient of the reflection at the grid inter-node

The explicit derivation of the coefficient of reflection at the grid nodes is given in this appendix for the second order case, where we consider

$$C_p = \begin{cases} 1 & \text{if } p = 1, \\ 0 & \text{otherwise.} \end{cases} \tag{B.1}$$

The set of equations Eqs. 3.40-3.44 is solved by first differencing Eq.3.43.

$$\begin{aligned} B_{zx}{}^{n+1/2}_{i+1/2,j+1/2} - B_{zx}{}^{n-1/2}_{i+1/2,j+1/2} = \; & \alpha_x^* \left(B_{zx}{}^{n-1/2}_{i+1/2,j+1/2} - B_{zx}{}^{n-3/2}_{i+1/2,j+1/2} \right) \\ & -\beta_x^* \left(E_{y}{}^{n}_{i+1,j+1/2} - E_{y}{}^{n}_{i,j+1/2} - E_{y}{}^{n-1}_{i+1,j+1/2} + E_{y}{}^{n-1}_{i,j+1/2} \right), \end{aligned} \tag{B.2}$$

where (α_x^*, β_x^*) are coefficients in Eq. 3.13.

Then, by using $B_{zx}{}^{n+1/2}_{j+1/2,k+1/2} = B_{z}{}^{n+1/2}_{j+1/2,k+1/2} - B_{zy}{}^{n+1/2}_{j+1/2,k+1/2}$ in B.3, we get

$$\begin{aligned} B_{z}{}^{n+1/2}_{j+1/2,k+1/2} - B_{z}{}^{n-1/2}_{j+1/2,k+1/2} = \; & \alpha_x^* \left(B_{z}{}^{n-1/2}_{j+1/2,k+1/2} - B_{z}{}^{n-3/2}_{j+1/2,k+1/2} \right) \\ & -\alpha_x^* \left(B_z y{}^{n+1/2}_{j+1/2,k+1/2} - B_{zy}{}^{n-1/2}_{j+1/2,k+1/2} \right) \\ & +B_{zy}{}^{n-1/2}_{j+1/2,k+1/2} - B_{zy}{}^{n-3/2}_{i+1/2,k+1/2} \\ & -\beta_x^* \left(E_{y}{}^{n}_{j+1,k+1/2} - E_{y}{}^{n}_{j,k+1/2} - E_{y}{}^{n-1}_{j+1,k+1/2} + E_{y}{}^{n-1}_{j,k+1/2} \right). \end{aligned} \tag{B.3}$$

Using equation 3.44, we obtain

$$\begin{aligned} B_{z}{}^{n+1/2}_{j+1/2,k+1/2} - B_{z}{}^{n-1/2}_{j+1/2,k+1/2} = \; & \alpha_x^* \left(B_{z}{}^{n-1/2}_{j+1/2,k+1/2} - B_{z}{}^{n-3/2}_{j+1/2,k+1/2} \right) \\ & -\alpha_x^* \tfrac{\Delta t}{\Delta y} \left(E_{x}{}^{n-1}_{j+1/2,k+1} - E_{x}{}^{n-1}_{j+1/2,k} \right) \\ & +\tfrac{\Delta t}{\Delta y} \left(E_{x}{}^{n}_{j+1/2,k+1} - E_{x}{}^{n}_{j+1/2,k} \right) \\ & -\beta_x^* \left(E_{y}{}^{n}_{j+1,j+1/2} - E_{y}{}^{n}_{j,k+1/2} - E_{y}{}^{n-1}_{j+1,k+1/2} + E_{y}{}^{n-1}_{j,k+1/2} \right). \end{aligned} \tag{B.4}$$

In order to express equation B.4 only by B_z, we eliminate E_y and E_x by differencing in time and by substituting E_y of Eq. 3.41 and E_x of Eq. 3.40,which gives

$$\begin{aligned} B_{z_{j+1/2,k+1/2}}^{n+1/2} - B_{z_{j+1/2,k+1/2}}^{n-1/2} = \quad & B_{z_{j+1/2,k+1/2}}^{n-1/2} - B_{z_{j+1/2,k+1/2}}^{n-3/2} \\ & + \alpha_x^* \left(B_{z_{j+1/2,k+1/2}}^{n-1/2} - 2B_{z_{j+1/2,k+1/2}}^{n-3/2} + B_{z_{j+1/2,k+1/2}}^{n-5/2} \right) \\ & - \alpha_x^* V_y \tfrac{\Delta t}{\Delta y} \left(B_{z_{j+1/2,k+3/2}}^{n-3/2} - 2B_{z_{j+1/2,k+1/2}}^{n-3/2} + B_{z_{j+1/2,j-1/2}}^{n-3/2} \right) \\ & + V_y \tfrac{\Delta t}{\Delta y} \left(B_{z_{j+1/2,k+3/2}}^{n-1/2} - 2B_{z_{j+1/2,k+1/2}}^{n-1/2} + B_{z_{j+1/2,k-1/2}}^{n-1/2} \right) \\ & + \beta_x^* V_x \left(B_{z_{j+3/2,k+1/2}}^{n-1/2} - 2B_{z_{j+1/2,k+1/2}}^{n-1/2} + B_{z_{j-1/2,k+1/2}}^{n-1/2} \right) \\ & - \beta_x^* V_x \left(B_{z_{j+3/2,k+1/2}}^{n-3/2} - 2B_{z_{j+1/2,k+1/2}}^{n-3/2} + B_{z_{j-1/2,k+1/2}}^{n-3/2} \right), \end{aligned} \tag{B.5}$$

Assuming a plane monochromatic traveling-wave trial solution as of the form $\mathrm{e}^{i\omega\Delta t - i(k_x\Delta x + k_y\Delta y)}$, one has

$$\begin{aligned} B_{z_{j+1/2,k+1/2}}^{n+1/2} &= (1-r)\mathrm{e}^{i\omega\Delta t/2 - i(k_x\Delta x + k_y\Delta y)/2}, \\ B_{z_{j+1/2,k+1/2}}^{n-1/2} &= (1-r)\mathrm{e}^{-i\omega\Delta t/2 - i(k_x\Delta x + k_y\Delta y)/2}, \\ B_{z_{j+1/2,k+1/2}}^{n-3/2} &= (1-r)\mathrm{e}^{-3i\omega\Delta t/2 - i(k_x\Delta x + k_y\Delta y)/2}, \\ B_{z_{j+1/2,k+1/2}}^{n-5/2} &= (1-r)\mathrm{e}^{-5i\omega\Delta t/2 - i(k_x\Delta x + k_y\Delta y)/2}, \\ B_{z_{j+1/2,k+3/2}}^{n-3/2} &= (1-r)\mathrm{e}^{-3i\omega\Delta t/2 - i(k_x\Delta x + 3k_y\Delta y)/2}, \\ B_{z_{j+1/2,k-1/2}}^{n-3/2} &= (1-r)\mathrm{e}^{-3i\omega\Delta t/2 - i(k_x\Delta x - k_y\Delta y)/2}, \\ B_{z_{j+1/2,k+3/2}}^{n-1/2} &= (1-r)\mathrm{e}^{-i\omega\Delta t/2 - i(k_x\Delta x + 3k_y\Delta y)/2}, \\ B_{z_{j+1/2,k-1/2}}^{n-1/2} &= (1-r)\mathrm{e}^{-i\omega\Delta t/2 - i(k_x\Delta x - k_y\Delta y)/2}, \\ B_{z_{j+3/2,k+1/2}}^{n-1/2} &= (1-r)\mathrm{e}^{-i\omega\Delta t/2 - i(3k_x\Delta x + k_y\Delta y)/2}, \\ B_{z_{j+3/2,k+1/2}}^{n-3/2} &= (1-r)\mathrm{e}^{-3i\omega\Delta t/2 - i(3k_x\Delta x + k_y\Delta y)/2}, \\ B_{z_{j-1/2,k+1/2}}^{n-1/2} &= \mathrm{e}^{-i\omega\Delta t/2 - i(-k_x\Delta x + k_y\Delta y/2)} - r\mathrm{e}^{-i\omega\Delta t/2 - i(k_x\Delta x + k_y\Delta y/2)}, \\ B_{z_{j-1/2,k+1/2}}^{n-3/2} &= \mathrm{e}^{-3i\omega\Delta t/2 - i(-k_x\Delta x + k_y\Delta y/2)} - r\mathrm{e}^{-3i\omega\Delta t/2 - i(k_x\Delta x + k_y\Delta y/2)}, \end{aligned} \tag{B.6}$$

By inserting the plane monochromatic traveling-wave trial solutions of B.6 in equation B.5, we deduce the coefficient of reflection on the inter-node, $r_{inter-node}$.

$$r_{inter-node} = \frac{a - b\cos(k_y\Delta y) - c\cos(k_x\Delta x)}{a - \cos(k_y\Delta y) - c\mathrm{e}^{-ik_x\Delta x}}, \tag{B.7}$$

where

$$\begin{cases} a = \mathrm{e}^{i\omega\Delta t} - \left(2 + \alpha_y^*\right) + \mathrm{e}^{-i\omega\Delta t}(1 + 2\alpha_y^*) + \alpha_y^*\mathrm{e}^{-2i\omega\Delta t}, \\ b = 2V_y \tfrac{\Delta t}{\Delta y} \left(1 - \alpha_y^*\mathrm{e}^{-i\omega\Delta t}\right), \\ c = 2\beta_y^* \tfrac{\Delta t}{\Delta x} \left(1 - \mathrm{e}^{-i\omega\Delta t}\right). \end{cases}$$

Appendix C

Author's publications and presentations

Publications

1. P. Lee, G. Maynard, T.L. Audet, B. Cros, R. Lehe, and J.-L. Vay. Dynamics of electron injection and acceleration driven by laser wakefield in tailored density profiles. Physical Review Accelerator and Beams, 19(11):112802, November 2016.

2. P. Lee, T. L. Audet, R. Lehe, J.-L. Vay, G. Maynard, and B. Cros. Modeling laser-driven electron acceleration using WARP with Fourier decomposition. Nuclear Instruments and Methods in Physics Research Section A: Accelerators, Spectrometers, Detectors and Associated Equipment, December 2015.

3. P. Lee, J.-L. Vay. Efficiency of the Perfectly Matched Layer with high-order finite-difference and pseudo-spectral Maxwell solvers. Computer Physics Communications, 194:1-9, September 2015.

4. T. L. Audet, M. Hansson, P. Lee, F. G. Desforges, G. Maynard, S. Dobosz Dufrenoy, R. Lehe, J.-L. Vay, B. Aurand, A. Persson, I. Gallardo Gonzalez, A. Maitrallain, P. Monot, C.-G. Wahlstrom, O. Lundh, and B. Cros. Investigation of ionization-induced electron injection in a wakefield driven by laser inside a gas cell. Physics of Plasmas, 23(2):023110, February 2016.

5. T. L. Audet, F. G. Desforges A. Maitrallain, S. Dobosz Dufrenoy, M. Bougeard, G. Maynard, P. Lee, M.Hansson, B. Aurand, A. Persson, I. Gallardo Gonzalez, P. Monot, C. G. Wahlstrom, O. Lundh, and B. Cros. Electron injector for compact staged high energy accelerator. Nuclear Instruments an Methods in Physics Research Section A: Accelerators, Spectrometers, Detectors and Associated Equipment, 829:304308, September 2016.

6. J.-L. Vay, R. Lehe, H. Vincenti, B.B. Godfrey, I. haber, P. Lee. Recent advances in high-performance modeling of plasma-based acceleration using the full PIC method. Nuclear Instruments an Methods in Physics Research Section A: Accelerators, Spectrometers, Detectors and Associated Equipment, 829:353-357, September 2016.

Proceedings

1. P. Lee, J.-L. Vay. Efficiency of the Perfectly Matched Layer with high-order finite-difference and pseudo-spectral Maxwell solvers. AIP Conference Proceedings, 1777(1):050002,

October 2016.

2. F. G. Desforges, B. S. Paradkar, M. Hansson, T. L. Audet, J. Ju, I. Gallardo- Gonzlez, B. Aurand, P. Lee, L. Senje, A. Persson, S. Dobosz Dufrnoy, O. Lundh, G. Maynard, P. Monot, J. L. Vay, C.-G. Wahlström, and B. Cros. Analysis of electron injection in laser wakefield acceleration using betatron emission in capillary tubes. Proceedings SPIE, 9514, 2015.

Oral Presentations

1. Laser Wakefield Electron Acceleration (LWFA) with WARP PIC code using Lorentz Boosted Frame technique (Invited talk). Workshop on Hybrid and PIC Simulations/PHARE Kick-off Meeting on Nov. 9, 2016 at Jussieu Campus, UPMC, Paris, France.

2. Etude et conception de laccelerateur delectrons dans le cadre du projet CILEX. Journees daccelerateur Societe Francaise de la Physique (SFP) du 4 au 7 oct., 2015 à Roscoff, Bretagne, France.

Posters

1. Dynamics of electron injection and acceleration driven by laser wakefield in tailored density profiles. Advanced Accelerator Concepts Workshop from July 31 to Aug. 5, 2016 at Gaylord National Resort and Convention Center, National Harbor, National Harbor, USA.

2. Modeling laser-driven electron acceleration using WARP with azimuthal Fourier decomposition algorithm. European Advanced Accelerated Concepts from Sept. 13 to 19 2015 at La Biodola, Isola d'Elba, Italy.

3. Study of the Perfectly Matched Layer (PML) in high-order FDTD and pseudo-spectral Maxwell solvers. Advanced Accelerated Concepts from July 13 to 18 2014 at Dolce Hayes Mansion, San Jose, California, USA.

4. Etude et conception de l'accélérateur d'electrons par sillage laser dans le cadre du projet CILEX avec le code WARP. Forum de la Fédération Lasers et Plasmas du 14 au 19 juin 2015 à l'Ile de Porquerolles, France.

Appendix D

Résumé

L'accélérateur à base de plasma: une alternative à l'accélérateur conventionnel

L'accélération par sillage laser (ASL) repose sur l'interaction entre un faisceau laser de haute intensité et un plasma sous-dense. Au travers de cette interaction, le mouvement des électrons crée une région de basse densité électronique dans le plasma après le passage du laser. Les ions, étant plus lourds que les électrons, sont peu déplacés dans l'échelle du mouvement d'électrons. Le champ électrique induit par cette perturbation de densité électronique fait osciller la densité à l'arrière du faisceau laser, créant ainsi une onde de plasma qui se propage avec le faisceau laser.

L'idée d'utiliser un plasma comme milieu d'accélération des électrons a suscité un grand intérêt parce qu'il peut supporter un grand champ accélérateur, $E_0(\mathrm{V/m}) = cm_e\omega_p/e \approx 96\sqrt{n_0(\mathrm{cm}^{-3})}$, avec ω_p la longueur d'onde de l'onde plasma, c la vitesse de la lumière, m_e la masse d'électron, e la charge électronique et n_0 la densité de plasma. Ce champ accélérateur est appelé le champ électrique limite de déferlement non-relativiste des plasmas froids [48]. Si l'on considère $n_0 = 10^{18}\,\mathrm{cm}^{-3}$, $E_0 \approx 96\,\mathrm{GV/m}$, qui est de trois ordres de grandeur plus élevé que celui d'un accélérateur radio-fréquence linéaire conventionnel, rendant envisageable la réalisation de futurs accélérateurs plus compacts.

En plus de ce champ accélérateur élevé, l'onde de plasma a pour une longueur d'onde de $\lambda_p(\mu\mathrm{m}) \approx 3.3 \times 10^{10}/\sqrt{n_0(cm^{-3})}$, e.g. $\lambda_p \approx 33\,\mu m$ pour $n_0 = 10^{18}\,\mathrm{cm}^{-3}$. Quant à la longueur du faisceau d'électrons généré, elle sera la moitié de celle dernière. Cette longueur est de deux ordres de grandeur plus courte que celle du faisceau d'électrons générée par les photo-injecteurs. Cela ouvre de nouvelles applications dans les domaines qui nécessitent des faisceaux d'électrons de courte durée, e.g. en science des matériaux, où la courte durée du faisceau permet la mesure des mouvements d'électrons en échelle atomique.

Il y a eu des progrès dans ces deux dernières décennies sur l'ASL. Les électrons ont pu atteindre une énergie d'1 GeV dans les canaux à plasma préformés à partir de la décharge dans un capillaire. Cela a été démontré avec un faisceau laser de 40 TW puissance crête [12]. D'autres expériences ont également démontré une accélération de faisceau d'électrons $> 1\,\mathrm{GeV}$ dans un plasma non-préformé avec un laser de 200 TW [13]. En utilisant les lasers de classe Petawatt, les faisceaux d'électrons peuvent atteindre 2 GeV dans une cellule de gaz de 7 cm [14]. Le faisceau avec une queue de 3 GeV dans sa distribution a été observé dans un système de double jets de gaz de 1.4 cm [15]. Le dernier record est détenu par [132] avec une production de faisceau d'électrons de 4.2 GeV avec un laser de 16 J dans un canal de plasma guidé préformé par une décharge dans un capillaire de 9 cm.

Pour la conception d'un collisionneur des particules, il est impératif d'avoir un faisceau de haute énergie et de bonne qualité. Dans cette optique, beaucoup d'efforts on été versé pour la production des faisceaux d'électrons quasi-monoénergetique [16, 17, 18]. Notre groupe est impliqué dans l'optimisation des faisceaux d'électrons expérimentalement et via les simulations. Un des objectifs est de déterminer un jeu de paramètres laser-plasma pour générer un faisceau d'électrons de petite dispersion en énergie, convenant à l'injection à un étage accélérateur laser-plasma, avec grande charge et basse émittance. La spécification de ces propriétés dépend des applications, mais la plupart des applications nécessitent une dispersion en énergie de $< 10\%$, une charge de $> 10\,\mathrm{pC}$ et une émittance transverse de $0.1\,\mathrm{mm\,mrad}$.

L'accélérateur laser-plasma dans un schéma multi-étages

L'accélération d'un faisceau d'électrons dans un étage accélérateur laser-plasma est limitée à une longueur imposée par la diffraction, l'épuisement du faisceau laser, et le déphasage des électrons. Pour un plasma préformé de 1 m à $n_0 = 10^{17}\,\mathrm{cm}^{-3}$, avec un guide d'onde, un faisceau d'électron de 10 GeV devrait être généré en principe. Toutefois, cette énergie est encore insuffisante pour le collisionneur des particules. Pour arriver à l'énergie suffisante pour un collisionneur qui est de l'ordre de quelque TeV, la solution consiste à accélérer ce faisceau d'électrons dans un schéma multi-étages. Un schéma multi-étages est composé d'un injecteur où les électrons sont injectés dans le sillage laser, d'une ligne de transport où le faisceau d'électrons de l'injecteur et mis en forme et transporté à l'étage suivant et d'un accélérateur où le faisceau d'électrons est accéléré davantage à une plus grande énergie. Récemment, Steinke et al. ont réussi à coupler deux étages indépendants d'ASL, ceci représente une étape importante dans le développement de l'accélérateur de particules à base de plasma et pour les autres applications nécessitant des électrons d'énergie au-delà de l'énergie que peut produire par un seul étage.

En Europe, plusieurs projets qui portent sur la démonstration d'un accélérateur multi-étages fiable sont en cours. Le projet CILEX (Centre Interdisciplinaire Lumière Extrême) qui a pour l'objectif de mettre en place, sur le site de l'Orme des Merisiers, un centre de recherche interdisciplinaire, au meilleur niveau international, autour d'un laser multi-faisceaux multi-PW APOLLON. Ce centre sera dédié aux lasers ultra-brefs de forte puissance (1PW et 10PW, $\geq$ 15fs) à l'étude de l'ASL multi-étages parmi d'autres études. Dans ce projet, un premier laser crée une onde plasma non linéaire dans une cellule de gaz pour générer un faisceau d'électrons. Ce faisceau d'électrons est ensuite mis en forme et transportée via une ligne de transport au second étage, où un deuxième laser crée une onde de plasma quasi-linéaire pour éviter la génération de faisceaux d'électrons secondaires dans un capillaire diélectrique. Le capillaire diélectrique sert de guide d'onde laser. Le second étage accélère le faisceau d'électrons du premier étage à une énergie plus élevée.

Le projet européen EuPRAXIA [21] en est un autre dédié à l'étude de l'ASL. Ce projet dure 4 ans, débuté au 1$^{\mathrm{er}}$ novembre 2015. L'objectif de ce projet est de livrer un rapport d'études conceptuelles pour un accélérateur à base de plasma capable de générer un faisceau d'électrons de 5 GeV de qualité industrielle. Il agit comme une étape intermédiaire entre les expériences destinées pour la preuve de principe et des accélérateurs ultra-compacts pour la science, l'industrie ou la médecine.

Notre groupe est un des partenaires dans ces deux projets. Nous sommes impliqués dans les travaux expérimentaux et numériques sur l'accélération d'électrons dans l'ASL. Les expériences sont réalisés à l'installation laser d'UHI100 située au CEA Saclay, en France, et

au centre de laser de Lund (LLC) en Suède.

Simulations Particle-in-Cell (PIC), un outil pour l'analyse et la prédiction

Trois catégories de modèles plasmiques peuvent être utilisées pour décrire les interactions laser-plasma dans le cas d'un laser de haute intensité (de l'ordre de $\geq 10^{18}\mathrm{W/cm}^2$, et de courte durée ($\leq$ 1ps). Ces modèles sont les modèles statique, fluide et cinétique. Pour décrire l'ASL, l'approche cinétique est souvent utilisée. L'approche cinétique détermine la distribution des particules de façon auto-cohérente. Elle est souvent utilisée dans les simulations pour décrire la propagation de laser, l'onde de plasma fortement non linéaire où l'amplitude des ondes est grande, avec la présence des interactions entre les ondes et les particules, e.g. les phénomènes de piégeage et du déferlement. La méthode PIC est la méthode la plus utilisée parmi toutes les méthodes dans cette approche. Il suit l'évolution du faisceau laser sur une courte durée, associée à la période de laser et simule le mouvement des particules chargées, ou du plasma en conséquence.

Dans l'ASL, la physique qui nous intéresse concerne l'onde de plasma générée par le faisceau de laser, son transport dans le plasma et la dynamique des électrons relativistes qui sont piégés et/ou accélérés par l'onde de plasma. L'interaction entre le faisceau d'électrons et le sillage manifeste des effets non linéaires qui ne peuvent être pris en compte que par le modèle cinétique. Celle-ci constitue la raison pour laquelle la communauté travaillant dans la conception et l'optimisation des expériences de l'ASL a opté pour cette approche.

Toutes les simulations dans ces travaux de thèse sont effectuées avec le code PIC Warp [22]. Warp est un code open-source, co-développé par le groupe mené par Dr. Jean-Luc Vay au Laboratoire National de Lawrence Berkeley (LBNL). C'est un code tri-dimensionnel, dépendant du temps, et capable de décrire plusieurs espèces, avec une description du réseau d'accélérateur. Depuis ces dernières années, l'ajout des nouveaux modules dans Warp a permis une modélisation efficace des expériences de l'ASL.

Plusieurs défis se présentent dans le travail de la modélisation. Il est surtout important d'utiliser un schéma numérique qui assure la précision des calculs car la présence des erreurs qui sont à priori petites s'accumulent dès les premiers pas de calcul et cela pourrait avoir un effet non négligeable sur les propriétés finales du faisceau d'électrons. Dans cette optique, beaucoup d'efforts ont été consacrés pour dériver des nouveaux schémas numériques ces dernières années afin d'améliorer encore la précision des calculs. La plupart de ces schémas optimisé sont implémentés dans Warp et ils sont utilisées dans nos calculs. Pour un schéma numérique donné, en géométrie cylindrique, il y a trois paramètres principaux, qui jouent le rôle de réglage de précision dans un calcul: la largeur de la cellule numérique Δz, Δr dans la direction longitudinale et transverse, et le nombre de macro-particules par cellule. Le pas de temps étant fixé par Δz, le temps de calcul pour un calcul complet est donc proportionnel à $1/(\Delta z^2 \times \Delta r)$. Un calcul typique pour l'injecteur effectué dans cette thèse a nécessité $\sim$ 20000 d'heures CPU. La plupart des calculs sont effectués avec une résolution de $\Delta z = \lambda_0/30$ et $\Delta r = \lambda_0/4$, avec λ_0 la longueur d'onde laser. D'après cette loi d'échelle, il est évident que les études paramétriques ne sont plus faisables avec des pas Δz et Δr plus petits. Bien que nous puissions obtenir quelques indications à partir de l'expertise accumulée dans la communauté, la forte non linéarité de notre problématique nous empêche à obtenir les estimations quantitatives de la précision d'un calcul. Cette précision ne peut être mise en évidence que par l'étude de convergence sur un exemple d'une classe de configuration donnée. Cette étude de convergence fait l'objet d'étude de cette thèse. En générale, nous

pouvons affirmer que les résolutions choisies dans nos calculs sont suffisantes pour évaluer avec une grande précision les propriétés du premier ordre d'un faisceau d'électrons telles que l'énergie moyenne et la dispersion en énergie, par contre dans l'évaluation des propriétés du second ordre telles que l'émittance, quelques incertitudes persistent. Certains calculs pour des configurations spécifiques ont été effectués en haute résolution pour déterminer précisément les propriétés du second ordre.

Couche absorbante parfaite de Bérenger (PML)

La résolution numérique choisie a déjà imposé l'utilisation d'un grand nombre d'heures CPU pour une simulation PIC. Afin de réduire ce nombre, la taille de la boîte de simulation devrait être réduite au minimum. Pour ce faire, la condition à frontières ouvertes est importante pour assurer l'absorption de toutes les ondes sortant d'un domaine de calcul sans les renvoyer dans ce domaine. Par exemple, dans la simulation de la propagation d'un faisceau laser de puissance moyenne dans un plasma plus long que la longueur de Rayleigh, nous verrons le faisceau laser qui diffracte, une partie de cette onde va atteindre les interfaces transverses du domaine de calcul. S'il n'y a pas de traitement spécial aux interfaces, les ondes de laser se réfléchiront et affecteront les composants qui sont encore dans le domaine de calcul. Une des implémentations la plus efficace pour résoudre les problèmes à frontières ouvertes est la couche absorbante parfaite de Bérenger (PML) [23]. La propriété essentielle d'une PML qui la distingue d'un matériau absorbant ordinaire est le fait qu'elle est conçue de telle sorte que les ondes incidentes l'atteignant depuis un matériau non PML ne se réfléchissent pas à l'interface. Les études de l'efficacité de la PML dans un schéma standard de Yee [151] ont été réalisées mais non pas systématiquement aux ordres élevés. Une partie de cette thèse est donc dédiée à l'étude de l'efficacité de la PML implémentée dans la méthode FDTD aux ordres élevés et dans la méthode spectrale.

Pour cette étude de l'efficacité, nous avons mesuré à partir des simulations numériques, les coefficients de réflexion d'une onde qui atteint la PML dans deux cas de figure: (i) l'onde atteint l'interface de la PML perpendiculairement, (ii) l'onde atteint l'interface avec un angle incident. Nous avons également développé un modèle théorique pour estimer ces coefficients de réflexion en nous basant sur l'interféromètre de Fabry-Perrot. Les résultats obtenus montrent qu'il y a un excellent accord entre les résultats numériques et théoriques. De plus, ils montrent aussi que l'efficacité de la PML est conservée dans la méthode FDTD aux ordres élevés et dans la méthode spectrale. Le modèle développé ici permet donc de prédire avec une bonne précision les coefficients de réflexion, qui pourra ensuite être utilisé pour optimiser les paramètres numériques d'une simulation d'ASL, e.g. le pas de grille et de temps, ainsi que l'ordre de stencil afin d'effectuer un calcul PIC en un temps le plus court possible tout en garantissant la précision.

Technique de Lorentz-boosted frame

Les paragraphes précédents nous apprennent que la plus petite échelle dans les simulations d'ASL est la longueur d'onde de laser, alors que la longueur d'onde de plasma est de 2 à 3 fois plus grande. Une telle différence dans les échelles pose un grand défi dans les simulations PIC. En effet, une simulation PIC en 3D pour un étage de 10 GeV, consistant en la propagation d'un laser de longueur d'onde $\lambda_0 = 0.8\,\mu$m dans un plasma de 30 cm à une densité de plasma de $10^{17}\,\mathrm{cm}^{-3}$ nécessite au moins 1 million pas de calculs. Avec la puissance d'ordinateur dont nous disposons aujourd'hui, nous ne sommes pas encore en mesure de le réaliser; des

optimisations numériques s'avèrent donc nécessaires.

Une technique pour réduire le temps de calcul d'une simulation PIC est la technique de Lorentz-boosted frame (LBF). Cette approche tire parti des propriétés de la dilatation et la contraction d'espace-temps associées à la transformation de Lorentz, sans modification des équations fondamentales de mouvement des particules ou de l'électrodynamique. Cette approche se base sur la non variance de la transformation de Lorentz appliquée aux deux ou plus de composants de différent ratio en espace et en temps qui se croisent à une vitesse relativiste, le nombre de pas de calcul est donc proportionnel au ratio de la plus grande échelle de temps d'intérêt sur la plus petite échelle. Dans les simulations d'ASL, en choisissant une fenêtre qui se déplace à la vitesse du groupe de laser, la longueur d'onde de laser sera dilaté et la longueur de plasma sera contracté, par conséquent le temps de croisement entre ces deux composants sera raccourci, ainsi que le temps de calcul. Un des objectifs de ma thèse est d'assurer que cette technique donne des résultats précis, les études de convergence sont donc effectuées. Cette étude consiste en la comparaison des résultats présentés avec des figures de mérite pour les simulations effectuées avec et sans la technique de Lorentz-boosted frame en fonction de la résolution numérique. L'étude de convergence dans le régime linéaire et non linéaire avec l'injection externe des électrons a été réalisée [205], et a montré une convergence remarquable. Dans [202], a été réalisée la simulation de l'ASL dans le régime non linéaire avec l'auto-injection des électrons, les résultats obtenus montrent qu'il y a quelques incertitudes avec la technique de Lorentz-boosted frame. Dans le cadre de ma thèse, je me suis focalisé à l'étude de convergence dans le régime non linéaire avec l'auto-injection en utilisant la méthode FDTD et la méthode spectrale. Avec cette étude, nous répondons aux trois problématiques:

- Est-ce que les simulations avec la technique de Lorentz-boosted frame donnent des résultats précis dans le régime non linéaire avec auto-injection?
- Est-ce que les simulations avec la méthode FDTD et la méthode spectrale convergent?
- Quelle est l'accélération que nous pourrions obtenir?

A partir des résultats obtenus, nous avons démontré que la technique de Lorentz-boosted frame permet de modéliser précisément l'évolution du champs de sillage, les propriétés du faisceau d'électrons telles que l'énergie moyenne, la dispersion en énergie et la dynamique transverse avec 99 % de concordance pour les résolutions numériques suffisantes, e.g. $N_z/\lambda_0 = 64$ sont obtenues. La convergence est atteinte avec une résolution plus faible pour la méthode spectrale comparée à la méthode FDTD. Il y a aussi une concordance à 99 % entre les résultats obtenus pour ces différentes méthodes de calcul à la plus haute résolution longitudinale $N_z/\lambda_0 = 128$. La loi d'échelle de l'accélération de calcul est aussi confirmée, cela a validé notre compréhension de la technique de Lorentz-boosted frame en fonction des facteurs relativistes de la fenêtre γ_b et N_z/λ_0. Bien que les simulations dans ce régime aient imposé des contraintes sur le choix de γ_b, nous obtenons quand-même une accélération significative, e.g. $S \approx 36$ avec $\gamma_b = 3$ et $N_z/\lambda_0 = 128$ tout en gardant un faible écart de moins de 1 %.

Simulation de la dynamique d'injection et d'accélération d'électrons

L'activité principale de notre équipe est centrée sur le développement des programmes expérimentaux pour l'ASL afin de produire des faisceaux d'électrons qui conforment aux spécifications établies dans le cadre du projet CILEX. Des expériences ont été effectuées a Lund

Laser Center en Suède et à l'installation d'UHI100 au CEA Saclay. Les simulations sont réalisées en parallèle avec les expériences pour analyser les résultats expérimentaux et pour prédire les régimes qui n'ont pas encore été explorés dans les expériences. Les régimes qui sont actuellement explorés dans les expériences sont fortement non linéaires et intrinsèquement tridimensionnels. Pour avoir une description réaliste de cette interaction fait appel à l'approche cinétique en 3D. Les simulations PIC en 3D fournissent les informations détaillées de l'interaction laser plasma, mais elles demandent des ressources de calculs exorbitantes. Une alternative consiste donc à utiliser les modèles réduits.

Plusieurs modèles réduits avec approximations des éléments physiques ont été proposés pour décrire l'interaction laser-plasma dans le cadre d'une simulation d'ASL en un temps de calcul accessible. Parmi ces méthodes sont la méthode de la fenêtre glissante [24], les méthodes quasi-statiques [25, 26, 27], la méthode pondéromotive centre guidé (PCG) [28, 29] pour la modélisation de la propagation du faisceau laser. Dans certains cas, ces méthodes se combinent, i.e. les équations du champ quasi-statique sont intégrées dans l'approximation PCG dans QuickPIC [26, 27]. Chacune de ces méthodes permet une accélération par rapport à la simulation PIC complète en 3D grâce aux approximations dans la description physique du système. Ces approximations pourraient manquer des éléments importants en physique, e.g. les méthodes quasi-statiques ne modélisent pas correctement l'auto-injection, l'approximation PCG ne permet pas de modéliser la longueur d'épuisement pour les faisceaux laser de haute intensité, l'utilisation de ces approximations dépendra donc à la problématique étudiée. Un autre modèle réduit tirant parti de la symétrie de l'interaction laser-plasma dans un plasma sous-dense en coordonnées cylindriques (r, z) [30] a été proposé, appelé le modèle quasi-3D. Cette méthode est bien adaptée pour les simulations d'ASL avec supposition que le faisceau laser est quasi-symétrique par rapport l'axe. Cet algorithme fait une décomposition Fourier en direction azimutale sur les champs et les courants lors de la résolution des équations de Maxwell. Le plus grand avantage de cette approche est qu'elle permet une description tri-dimensionnelle de l'interaction laser-plasma à un temps de calcul comparable à celui de la simulation PIC en 2D. Vu les avantages de ce nouvel algorithme, il est utilisé dans toutes les simulations pour les travaux d'analyse et d'optimisation.

Dans un premier temps, une simulation avec le code Warp en utilisant le modèle quasi-3D, et comme paramètres d'entrées les paramètres proches de ceux utilisés dans l'expérience effectuée lors de la campagne d'expériences à LLC a été réalisée. Ces expériences portaient sur l'étage d'injecteur où les électrons sont piégés dans le sillage en utilisant le schéma d'injection par ionisation. L'expérience consiste en tirant un faisceau de laser dans une cellule de gaz de longueur variable, appelée ELISA [32] remplie de H_2 et quelque pourcentage de N_2. Son profil de densité est bien caractérisé expérimentalement et avec les simulations de type fluide (openFOAM).

La confrontation numérique-expérience montre que les résultats issus de la simulation et de l'expérience sont assez semblables. En examinant la distribution des électrons en fonction d'énergie du faisceau d'électrons accélérés, la simulation a réussi à reproduire la tendance globale de cette distribution. Nous avons aussi comparé le résultat d'une série de simulations correspondant à différents cas de figure réalisés en expérience, il y a eu un très bon accord entre la simulation et l'expérience, cela montre que le code Warp avec le modèle quasi-3D est un outil fiable pour la modélisation de l'ASL. Une analyse détaillée de la simulation a également donné un aperçu sur la dynamique de piégeage et daccélération d'électrons dans le sillage dans le cas de couplage de deux schémas d'injection: l'injection par ionisation et l'injection par gradient descendant, que nous exploiterons par la suite pour le travail d'optimisation de faisceau d'électrons.

Optimisation de l'injecteur laser-plasma

Il existe de nombreux paramètres pouvant être optimisés dans l'ASL, nous en avons choisi deux qui sont: l'influence de gradient descendant et le pourcentage d'azote. Les paramètres laser-plasma sont choisis de façon à obtenir un faisceau d'électron d'une énergie entre $50 - 200\,\mathrm{MeV}$, une dispersion en énergie $< 10\,\%$ et une émittance normalisée de $\sim 1\,\mathrm{mm\,mrad}$ et une charge de $\geq 10\,\mathrm{pC}$. Les paramètres laser-plasma sont proches de ceux de l'expérience à LLC mais pour limiter la dispersion en énergie, la longueur de plasma L_{plasma} est réduite et le laser est focalisé au gradient descendant du profil d'ELISA. Ces deux ajustements ont pour objectif retarder le déclenchement de l'injection par ionisation, par conséquent nous réduisons le volume d'injection, ainsi que la dispersion en énergie. La simulation avec ce jeu de paramètres a généré un faisceau d'électron d'une dispersion en énergie évaluée en largeur à mi hauteur (FWHM) de $13.1\,\%$, une énergie de pointe à $65,7\,\mathrm{MeV}$, une charge de $43.6\,\mathrm{pC}$, et des émittances normalisées $\varepsilon_{x,rms} = 0.33\,\mathrm{mm\,mrad}$ et $\varepsilon_{y,rms} = 2.09\,\mathrm{mm\,mrad}$. La différence entre $\varepsilon_{x,rms}$ et $\varepsilon_{y,rms}$ est due à l'effet de polarisation de laser selon la direction y, cet effet a mené à un gain de moment des électrons dans cette direction. Nous avons ensuite séparé la partie d'injection et d'accélération, cela nous donne un degré de liberté de plus sur le contrôle des propriétés de faisceau d'électrons. En modifiant le profil de densité longitudinal à partir de la position qui marque la fin de l'injection jusqu'à la sortie de la cellule de gaz, nous avons pu régler l'énergie de pointe du faisceau d'électrons accéléré tout en conservant sa dispersion en énergie. Le meilleur résultat obtenu parmi tous les paramètres considérés est celui avec un gradient descendant dans la partie d'accélération du profil de densité. Le faisceau d'électrons a une énergie de pointe de $82.6\,\mathrm{MeV}$ et une dispersion en énergie de $11\,\%$, les autres paramètres sont conservés.

Afin de mieux préparer les futures expériences à l'installation Apollon-10P dans le cadre du projet CILEX, les expériences sont réalisées à l'installation UHI100 au CEA Saclay pour explorer les configurations laser-plasma capables de générer un faisceau d'électrons avec une énergie de pointe de $200\,\mathrm{MeV}$. Les simulations sont effectuées en parallèle avec les expériences. Dans les simulations, les paramètres sont choisis de telle sorte qu'ils soient proches de ceux de l'installation UHI100. Les études précédentes sur le rôle du profil longitudinal de densité, le point focal du laser et la longueur de plasma ont amélioré notre compréhension sur la dynamique des électrons injectés par ionisation dans un profil longitudinal de densité réaliste. Ensuite, nous avons étudié l'influence de la concentration d'azote (C_{N_2}), un autre paramètre clé pour contrôler les propriétés d'électron. A partir de cette étude, nous avons montré que quand C_{N_2} est élevée, cela induit un fort effet charge d'espace qui dégrade la dispersion en énergie autour de l'énergie de pointe. Toutefois, il existe une concentration optimale, dans notre cas, $C_{\mathrm{N}_2} = 1.5\,\%$. Le faisceau d'électrons obtenu à la sortie de la cellule, $z = L_{plasma}$ a une charge de $30.7\,\mathrm{pC}$, une énergie de pointe de $240.9\,\mathrm{MeV}$, une dispersion en énergie évaluée à FWHM de $12\,\%$, et une émittance normalisée de $\sim 4.3\,\mathrm{mm\,mrad}$ dans les deux directions transverses.

Perspectives

Ces travaux de recherche ont ouvert des perspectives dans la physique et la modélisation numérique de l'injecteur laser-plasma.

En ce qui concerne l'aspect numérique, nous pourrons réduire le temps de calcul des simulations d'ASL en appliquant la technique de Lorentz-boosted frame et en implémentant la PML en coordonnées cylindriques. Afin de décrire les structures fines dues à l'interaction laser-plasma, nous pourrions opter pour une implémentation du raffinement de maillage.

En terme de physique, il est essentiel d'améliorer la compréhension de l'émittance dans un injecteur laser-plasma pour pouvoir la réduire davantage. Dans les futures simulations, nous mettrons directement le profil spatio-temporel du laser pour étudier l'influence des défauts de laser sur les propriétés du faisceau d'électrons généré. Par la suite, nous simulerons le couplage entre l'injecteur, la ligne de transport et l'accélérateur dans le schéma d'accélérateur multi-étages.

Nomenclature

α	the ratio of laser power and critical power, P_L/P_{C}
α_f	fine structure constant
$\boldsymbol{\sigma}$	standard deviation
$\boldsymbol{A}$	vector potential
$\boldsymbol{a}$	normalized vector potential
$\boldsymbol{B}$	magnetic field
$\boldsymbol{B}_{inc}$	incident $B-$field
$\boldsymbol{B}_{ref}$	reflected $E-$field
$\boldsymbol{E}$	electric field
$\boldsymbol{E}_{inc}$	incident $E-$field
$\boldsymbol{E}_{ref}$	reflected $E-$field
$\boldsymbol{p^f}$	fast component momentum
$\boldsymbol{p^s}$	slow component momentum
$\boldsymbol{p}$	momentum
$\Delta\mathcal{E}_{\mathrm{FWHM}}$	energy spread at full-width at half-maximum
$\Delta\mathcal{E}_{\mathrm{rms}}$	root-mean-square energy spread
δn	normalized perturbed density
Δt	time-step
Δv	velocity differential
Δx	computational grid cell size in y
Δy	computational grid cell size in y
Δz	computational grid cell size in z
ϵ_0	permittivity constant
η	adjustable parameter that determines the fraction of the plasma wave to be considered which exits the plasma at the end of the simulation
γ	Lorentz factor
γ_{K}	Keldysh parameter
γ_b	Loretnz factor of the Lorentz-boosted frame
γ_g	Lorentz factor of the laser group velocity
κ	factor of the dephasing length
λ_0	laser wavelength
λ_0'	laser wavelength in the boosted frame
λ_{C}	Compton wavelength
λ_D	Debye length
λ_p	plasma wavelength
$\langle\mathcal{E}\rangle$	mean energy
$\mathcal{E}$	energy
$\mathcal{E}_{peak}$	peak energy
ℓ_{beam}	length of the electron beam
CFL	Courant-Friedrichs-Lewy
CIC	Cloud-In-Cell
CK	Cole-Karkkainen
DC	direct current
FDTD	Finite-Difference Time-Dependent
LHS	left-hand-side
LWFA	Laser Wakefield Acceleration

NGP Nearest-Grid-Point

NSFD Non-Standard Finite-Difference

ODE Ordinary Differential Equation

P_{ioniz} ionization probability

PDE Partial Differential Equation

PIC particle-in-cell

PML Perfectly Matched Layer

PSATD Pseudo-Spectral Analytical Time Domain

PSTD Pseudo-Spectral Time-Domain

RHS right-hand-side

SVEA Slowly Varying Envelope Approximation

TSC Triangular-Shaped density Cloud

μ_0 permeability constant

∇ nabla operator

∇^2 Laplacian

ν_c mean electron-ion collision frequency

ω_0 laser frequency

ω_p plasma frequency

ϕ scalar potential

Ψ wake potential

Ψ_f wake potential at trapped position

Ψ_i wake potential at ionization position

τ_L laser duration

$\tilde{\boldsymbol{p}}$ normalized momentum

$\varepsilon_{n,rms}$ normalized emittance

φ wave phase

a_0 maximum amplitude of the normalized vector potential

B_L laser magnetic field

c speed of light

C_{N_2} concentration of N_2

C_p Fornberg coefficients

e elementary charge

E_L laser electric field

$E_{z,max}$ maximum electric field amplitude of the plasma wave

H Harris function

i imaginary number

I_a electron binding strength

K focusing constant

k_0 laser wavenumber

k_B Boltzmann constant

k_p plasma wavenumber

l azimuthal harmonic mode

L'_{plasma} length of the plasma structure in the boosted frame

l_0 laser length

L_d electron dephasing length

L_s density scale length

L_{acc} acceleration length

L_{cell} gas cell length

L_{pd} pump depletion length

L_{plasma} length of the plasma structure

L_z interaction length

m_e electron mass

n_0 plasma density or ambient electron number density

n_c critical density

N_D	Debye number
n_e	electron density
n_i	ion density
N_L	depth of the PML
N_r	number of grid-points in the radial direction
N_z	number of grid-points in the longitudinal direction
P	projector function
P_{C}	critical power
P_L	laser power
Q	charge
Q_l	charge in the linear regime
Q_{Nl}	charge in the nonlinear regime
r_0	minimum laser spot radius
r_b	blowout radius
r_L	laser spot radius
r_m	maximum blowout radius
$r_{inter-node}$	coefficient of reflection at the grid inter-node
r_{node}	coefficient of reflection at the grid node
S	speedup
T	total time of the simulation
T_e	electron temperature
T_L	laser period
T_p	plasma period
U_H	ionization potential of hydrogen
U_I	ionization potential
U_p	laser ponderomotive potential
v_b	velocity of the Lorentz-boosted frame
v_g	group velocity
v_ϕ	phase velocity
v_{th}	thermal velocity
w_0	laser waist
Z	atomic number
Z_R	Rayleigh length

Bibliography

[1] CMS Collaboration. Observation of a new boson at a mass of 125 GeV with the CMS experiment at the LHC. *Physics Letters B*, 716(1):30–61, September 2012.

[2] Michael Benedikt and Frank Zimmermann. The Future Circular Collider study. *CERN Courier*, March 2014.

[3] Stanford University. What is FACET?

[4] E. Esarey, C. B. Schroeder, and W. P. Leemans. Physics of laser-driven plasma-based electron accelerators. *Reviews of Modern Physics*, 81(3):1229–1285, August 2009.

[5] T. Tajima and J. M. Dawson. Laser Electron Accelerator. *Physical Review Letters*, 43(4):267–270, July 1979.

[6] F. Amiranoff, J. Ardonceau, M. Bercher, D. Bernard, B. Cros, A. Debraine, J. M. Dieulot, J. Fusellier, F. Jacquet, J. M. Joly, M. Juillard, G. Matthieussent, P. Matricon, P. Miné, B. Montès, P. Mora, R. Morano, J. Morillo, F. Moulin, P. Poilleux, A. E. Specka, and C. Stenz. The plasma beat-wave acceleration experiment at Ecole Polytechnique. *Nuclear Instruments and Methods in Physics Research Section A: Accelerators, Spectrometers, Detectors and Associated Equipment*, 363(3):497–510, September 1995.

[7] F. Amiranoff, D. Bernard, B. Cros, F. Jacquet, G. Matthieussent, P. Miné, P. Mora, J. Morillo, F. Moulin, A. E. Specka, and C. Stenz. Electron acceleration in Nd-laser plasma beat-wave experiments. *Physical Review Letters*, 74(26):5220–5223, June 1995.

[8] C. E. Clayton, K. A. Marsh, M. Everett, A. Lal, and C. Joshi. Demonstration of plasma beat wave acceleration of electrons from 2 MeV to 20 MeV. In *Proceedings of International Conference on Particle Accelerators*, pages 2551–2555 vol.4, May 1993.

[9] Pisin Chen, J. M. Dawson, Robert W. Huff, and T. Katsouleas. Acceleration of Electrons by the Interaction of a Bunched Electron Beam with a Plasma. *Physical Review Letters*, 54(7):693–696, February 1985.

[10] John M. Dawson. Nonlinear Electron Oscillations in a Cold Plasma. *Physical Review*, 113(2):383–387, January 1959.

[11] Victor Malka, Jérôme Faure, Yann A. Gauduel, Erik Lefebvre, Antoine Rousse, and Kim Ta Phuoc. Principles and applications of compact laserplasma accelerators. *Nature Physics*, 4(6):447–453, June 2008.

[12] W. P. Leemans, B. Nagler, A. J. Gonsalves, Cs Tóth, K. Nakamura, C. G. R. Geddes, E. Esarey, C. B. Schroeder, and S. M. Hooker. GeV electron beams from a centimetre-scale accelerator. *Nature Physics*, 2(10):696–699, October 2006.

[13] C. E. Clayton, J. E. Ralph, F. Albert, R. A. Fonseca, S. H. Glenzer, C. Joshi, W. Lu, K. A. Marsh, S. F. Martins, W. B. Mori, A. Pak, F. S. Tsung, B. B. Pollock, J. S. Ross, L. O. Silva, and D. H. Froula. Self-Guided Laser Wakefield Acceleration beyond 1 GeV Using Ionization-Induced Injection. *Phys. Rev. Lett.*, 105(10), September 2010.

[14] Wentao Wang, Wentao Li, Jiansheng Liu, Cheng Wang, Qiang Chen, Zhijun Zhang, Rong Qi, Yuxin Leng, Xiaoyan Liang, Yanqi Liu, Xiaoming Lu, Cheng Wang, Ruxin Li, and Zhizhan Xu. Control of seeding phase for a cascaded laser wakefield accelerator with gradient injection. *Appl. Phys. Lett.*, 103(24):243501, 2013.

[15] Hyung Taek Kim, Ki Hong Pae, Hyuk Jin Cha, I. Jong Kim, Tae Jun Yu, Jae Hee Sung, Seong Ku Lee, Tae Moon Jeong, and Jongmin Lee. Enhancement of Electron Energy to the Multi-GeV Regime by a Dual-Stage Laser-Wakefield Accelerator Pumped by Petawatt Laser Pulses. *Phys. Rev. Lett.*, 111(16), October 2013.

[16] S. P. D. Mangles, C. D. Murphy, Z. Najmudin, A. G. R. Thomas, J. L. Collier, A. E. Dangor, E. J. Divall, P. S. Foster, J. G. Gallacher, C. J. Hooker, D. A. Jaroszynski, A. J. Langley, W. B. Mori, P. A. Norreys, F. S. Tsung, R. Viskup, B. R. Walton, and K. Krushelnick. Monoenergetic beams of relativistic electrons from intense laserplasma interactions. *Nature*, 431(7008):535–538, September 2004.

[17] C. G. R. Geddes, Cs Toth, J. van Tilborg, E. Esarey, C. B. Schroeder, D. Bruhwiler, C. Nieter, J. Cary, and W. P. Leemans. High-quality electron beams from a laser wakefield accelerator using plasma-channel guiding. *Nature*, 431(7008):538–541, September 2004.

[18] J. Faure, Y. Glinec, A. Pukhov, S. Kiselev, S. Gordienko, E. Lefebvre, J.-P. Rousseau, F. Burgy, and V. Malka. A laserplasma accelerator producing monoenergetic electron beams. *Nature*, 431(7008):541–544, September 2004.

[19] S. Steinke, J. van Tilborg, C. Benedetti, C. G. R. Geddes, C. B. Schroeder, J. Daniels, K. K. Swanson, A. J. Gonsalves, K. Nakamura, N. H. Matlis, B. H. Shaw, E. Esarey, and W. P. Leemans. Multistage coupling of independent laser-plasma accelerators. *Nature*, 530(7589):190–193, February 2016.

[20] B. Cros, B. S. Paradkar, X. Davoine, A. Chancé, F. G. Desforges, S. Dobosz-Dufrénoy, N. Delerue, J. Ju, T. L. Audet, G. Maynard, M. Lobet, L. Gremillet, P. Mora, J. Schwindling, O. Delferrière, C. Bruni, C. Rimbault, T. Vinatier, A. Di Piazza, M. Grech, C. Riconda, J. R. Marquès, A. Beck, A. Specka, Ph. Martin, P. Monot, D. Normand, F. Mathieu, P. Audebert, and F. Amiranoff. Laser plasma acceleration of electrons with multi-PW laser beams in the frame of CILEX. *Nuclear Instruments and Methods in Physics Research Section A: Accelerators, Spectrometers, Detectors and Associated Equipment*, 740:27–33, March 2014.

[21] EuPRAXIA. Compact European plasma accelerator with superior beam quality.

[22] J.-L. Vay, D. P. Grote, R. H. Cohen, and A. Friedman. Novel methods in the Particle-In-Cell accelerator Code-Framework Warp. *Comput. Sci. Disc.*, 5(1):014019, December 2012.

[23] Jean-Pierre Bérenger. A perfectly matched layer for the absorption of electromagnetic waves. *Journal of Computational Physics*, 114(2):185–200, October 1994.

[24] C. D. Decker, W. B. Mori, and T. Katsouleas. Particle-in-cell simulations of Raman forward scattering from short-pulse high-intensity lasers. *Physical Review E*, 50(5):R3338–R3341, November 1994.

[25] Patrick Mora and Jr. Thomas M. Antonsen. Kinetic modeling of intense, short laser pulses propagating in tenuous plasmas. *Physics of Plasmas*, 4(1):217, 1997.

[26] C. Huang, V. K. Decyk, C. Ren, M. Zhou, W. Lu, W. B. Mori, J. H. Cooley, T. M. Antonsen, and T. Katsouleas. QUICKPIC: A highly efficient particle-in-cell code for modeling wakefield acceleration in plasmas. *Journal of Computational Physics*, 217(2):658–679, September 2006.

[27] Weiming An, Viktor K. Decyk, Warren B. Mori, and Thomas M. Antonsen, Jr. An Improved Iteration Loop for the Three Dimensional Quasi-static Particle-in-cell Algorithm: QuickPIC. *J. Comput. Phys.*, 250:165–177, October 2013.

[28] C. Benedetti, C.B. Schroeder, E. Esarey, and W.P. Leemans. Efficient modeling of laser-plasma accelerators using the ponderomotive-based code Inf&rno. Rostock-Warnemünde, Germany, 2012.

[29] Benjamin M. Cowan, David L. Bruhwiler, Estelle Cormier-Michel, Eric Esarey, Cameron G. R. Geddes, Peter Messmer, and Kevin M. Paul. Characteristics of an envelope model for laserplasma accelerator simulation. *Journal of Computational Physics*, 230(1):61–86, January 2011.

[30] A. F. Lifschitz, X. Davoine, E. Lefebvre, J. Faure, C. Rechatin, and V. Malka. Particle-in-Cell modelling of laserplasma interaction using Fourier decomposition. *Journal of Computational Physics*, 228(5):1803–1814, March 2009.

[31] J.-L. Vay. Noninvariance of Space- and Time-Scale Ranges under a Lorentz Transformation and the Implications for the Study of Relativistic Interactions. *Physical Review Letters*, 98(13):130405, March 2007.

[32] T. L. Audet, F. G. Desforges, A. Maitrallain, S. Dobosz Dufrénoy, M. Bougeard, G. Maynard, P. Lee, M. Hansson, B. Aurand, A. Persson, I. Gallardo González, P. Monot, C. G. Wahlström, O. Lundh, and B. Cros. Electron injector for compact staged high energy accelerator. *Nuclear Instruments and Methods in Physics Research Section A: Accelerators, Spectrometers, Detectors and Associated Equipment*, 829:304–308, September 2016.

[33] J. D. Lawson. Lasers and Accelerators. *IEEE Transactions on Nuclear Science*, 26:4217, June 1979.

[34] P. M. Woodward. A method of calculating the field over a plane aperture required to produce a given polar diagram. *Journal of the Institution of Electrical Engineers - Part IIIA: Radiolocation*, 93(10):1554–1558, 1946.

[35] Robert B Palmer. A laser-driven grating linac. *Particle Accelerators*, 11(2):81–90, 1980.

[36] Dwight R. Nicholson. *Introduction to Plasma Theory*. Wiley, New York, 1 edition edition, March 1983.

[37] Francis F. Chen. *Introduction to plasma physics and controlled fusion. Volume 1, Plasma physics*. Springer, 2nd edition, 2010.

[38] William L. Kruer. *The Physics of Laser Plasma Interactions*. Avalon Publishing, January 2003. Google-Books-ID: uAF_HWb8FAQC.

[39] E. Esarey, P. Sprangle, J. Krall, and A. Ting. Overview of plasma-based accelerator concepts. *IEEE Transactions on Plasma Science*, 24(2):252–288, April 1996.

[40] P. Sprangle, E. Esarey, A. Ting, and G. Joyve. Laser wakefield acceleration and relativistic optical guiding. *Applied Physics Letters*, 53(22):2146–2148, November 1988.

[41] E. Esarey, A. Ting, P. Sprangle, and G. Joyce. The laser wakefield accelerator. *Comments on Plasma Physics and Controlled Fusion*, 12(4):191–204, 1989.

[42] E. A. Startsev and C. J. McKinstrie. Multiple scale derivation of the relativistic ponderomotive force. *Physical Review E*, 55(6):7527–7535, June 1997.

[43] D. Bauer, P. Mulser, and W. Steeb. Relativistic ponderomotive force, Uphill acceleration, and transition to chaos. *Physical Review Letters*, 75(25):4622–4625, December 1995.

[44] L.M. Gorbunov and V. I. Kirsanov. Excitation of plasma waves by an electromagnetic wave packet. *Sov. Phys. JETP*, 66(2):290–294, 1987.

[45] R.V. Polovin A.I. Akhiezer. Theory of Wave Motion of an Electron Plasma. *JETP*, 3(5):696, November 1956.

[46] Alain Decoster. Nonlinear travelling waves in a homogeneous cold collisionless plasma. *Physics Reports*, 47(5):285–422, November 1978.

[47] Robert J. Noble. Plasma-wave generation in the beat-wave accelerator. *Physical Review A*, 32(1):460–471, July 1985.

[48] J. Dawson. OneDimensional Plasma Model. *The Physics of Fluids*, 5(4):445–459, April 1962.

[49] J. Dawson and C. Oberman. HighFrequency Conductivity and the Emission and Absorption Coefficients of a Fully Ionized Plasma. *The Physics of Fluids*, 5(5):517–524, May 1962.

[50] P. Sprangle, E. Esarey, and A. Ting. Nonlinear theory of intense laser-plasma interactions. *Physical Review Letters*, 64(17):2011–2014, April 1990.

[51] S. V. Bulanov, V. I. Kirsanov, and A. S. Sakharov. Excitation of ultra-relativistic Langmuir waves by electromagnetic pulses. *Physica Scripta*, 1990(T30):208, 1990.

[52] V. I. Berezhiani and I. G. Murusidze. Relativistic wake-field generation by an intense laser pulse in a plasma. *Physics Letters A*, 148(6-7):338–340, August 1990.

[53] V. N. Tsytovich, U. De Angelis, and R. Bingham. Beat-wave-wake acceleration by short high intensity laser pulses. *Comments on Plasma Physics and Controlled Fusion*, 12(5):249–256, 1989.

[54] E. Esarey, R. F. Hubbard, W. P. Leemans, A. Ting, and P. Sprangle. Electron Injection into Plasma Wakefields by Colliding Laser Pulses. *Phys. Rev. Lett.*, 79(14):2682–2685, October 1997.

[55] W. B. Mori, C. D. Decker, and W. P. Leemans. Relativistic harmonic content of non-linear electromagnetic waves in underdense plasmas. *IEEE Transactions on Plasma Science*, 21(1):110–119, February 1993.

[56] R. J. Kingham and A. R. Bell. Enhanced Wakefields for the 1d Laser Wakefield Accelerator. *Physical Review Letters*, 79(24):4810–4813, December 1997.

[57] S. Dalla and M. Lontano. On the maximum longitudinal electric field of a large amplitude electron plasma wave excited by a short electromagnetic radiation pulse. *Physics Letters A*, 173:456–461, February 1993.

[58] E. Esarey, P. Sprangle, J. Krall, and A. Ting. Self-focusing and guiding of short laser pulses in ionizing gases and plasmas. *IEEE Journal of Quantum Electronics*, 33(11):1879–1914, November 1997.

[59] S. V. Bulanov, F. Pegoraro, and A. M. Pukhov. Two-Dimensional Regimes of Self-Focusing, Wake Field Generation, and Induced Focusing of a Short Intense Laser Pulse in an Underdense Plasma. *Physical Review Letters*, 74(5):710–713, January 1995.

[60] C. B. Schroeder, E. Esarey, C. G. R. Geddes, C. Benedetti, and W. P. Leemans. Physics considerations for laser-plasma linear colliders. *Physical Review Special Topics - Accelerators and Beams*, 13(10):101301, October 2010.

[61] A. Ting, K. Krushelnick, C. I. Moore, H. R. Burris, E. Esarey, J. Krall, and P. Sprangle. Temporal Evolution of Self-Modulated Laser Wakefields Measured by Coherent Thomson Scattering. *Physical Review Letters*, 77(27):5377–5380, December 1996.

[62] E. Esarey, B. Hafizi, R. Hubbard, and A. Ting. Trapping and Acceleration in Self-Modulated Laser Wakefields. *Physical Review Letters*, 80(25):5552–5555, June 1998.

[63] J. Faure, C. Rechatin, A. Norlin, A. Lifschitz, Y. Glinec, and V. Malka. Controlled injection and acceleration of electrons in plasma wakefields by colliding laser pulses. *Nature*, 444(7120):737–739, December 2006.

[64] A. Pukhov and J. Meyer-ter Vehn. Laser wake field acceleration: the highly non-linear broken-wave regime. *Applied Physics B*, 74(4-5):355–361, April 2002.

[65] Patrick Mora and Thomas M. Antonsen. Electron cavitation and acceleration in the wake of an ultraintense, self-focused laser pulse. *Physical Review E*, 53(3):R2068–R2071, March 1996.

[66] W. Lu, C. Huang, M. Zhou, M. Tzoufras, F. S. Tsung, W. B. Mori, and T. Katsouleas. A nonlinear theory for multidimensional relativistic plasma wave wakefields. *Physics of Plasmas*, 13(5):056709, 2006.

[67] Rémi Lehe. *Improvement of the quality of laser-wakefield accelerators: towards a compact free-electron laser*. PhD thesis, Ecole Polytechnique, France, 2014.

[68] A. Pukhov, S. Gordienko, S. Kiselev, and I. Kostyukov. The bubble regime of laserplasma acceleration: monoenergetic electrons and the scalability. *Plasma Physics and Controlled Fusion*, 46(12B):B179, 2004.

[69] I. Kostyukov, A. Pukhov, and S. Kiselev. Phenomenological theory of laser-plasma interaction in bubble regime. *Physics of Plasmas*, 11(11):5256–5264, October 2004.

[70] W. Lu, M. Tzoufras, C. Joshi, F. S. Tsung, W. B. Mori, J. Vieira, R. A. Fonseca, and L. O. Silva. Generating multi-GeV electron bunches using single stage laser wakefield acceleration in a 3d nonlinear regime. *Phys. Rev. ST Accel. Beams*, 10(6), June 2007.

[71] Eric Esarey and Mark Pilloff. Trapping and acceleration in nonlinear plasma waves. *Physics of Plasmas*, 2(5):1432, 1995.

[72] S. Y. Kalmykov, A. Beck, S. A. Yi, V. N. Khudik, M. C. Downer, E. Lefebvre, B. A. Shadwick, and D. P. Umstadter. Electron self-injection into an evolving plasma bubble: Quasi-monoenergetic laser-plasma acceleration in the blowout regime. *Physics of Plasmas*, 18(5):056704, 2011.

[73] I. Kostyukov, E. Nerush, A. Pukhov, and V. Seredov. Electron Self-Injection in Multidimensional Relativistic-Plasma Wake Fields. *Physical Review Letters*, 103(17):175003, October 2009.

[74] F. S. Tsung, Wei Lu, M. Tzoufras, W. B. Mori, and C. Joshi. Simulation of monoenergetic electron generation via laser wakefield accelerators for 525tw lasers. *Physics of Plasmas*, 13(5):056708, May 2006.

[75] S. Corde, C. Thaury, A. Lifschitz, G. Lambert, K. Ta Phuoc, X. Davoine, R. Lehe, D. Douillet, A. Rousse, and V. Malka. Observation of longitudinal and transverse self-injections in laser-plasma accelerators. *Nature Communications*, 4:1501, February 2013.

[76] Hai-Cheng Wu, Bai-Song Xie, Ming-Ping Liu, Xue-Ren Hong, Shan Zhang, and M. Y. Yu. Electron trajectories and betatron oscillation in the wake bubble in laser-plasma interaction. *Physics of Plasmas*, 16(7):073108, July 2009.

[77] A. Pak, K. A. Marsh, S. F. Martins, W. Lu, W. B. Mori, and C. Joshi. Injection and Trapping of Tunnel-Ionized Electrons into Laser-Produced Wakes. *Phys. Rev. Lett.*, 104(2), January 2010.

[78] C. McGuffey, A. G. R. Thomas, W. Schumaker, T. Matsuoka, V. Chvykov, F. J. Dollar, G. Kalintchenko, V. Yanovsky, A. Maksimchuk, K. Krushelnick, V. Yu Bychenkov, I. V. Glazyrin, and A. V. Karpeev. Ionization Induced Trapping in a Laser Wakefield Accelerator. *Phys. Rev. Lett.*, 104(2), January 2010.

[79] Hans A. Bethe and E.E. Salpeter. *Quantum Mechanics of One- and Two-Electron Atoms / Hans A. Bethe / Springer*. Springer US, 1977.

[80] M.V Ammosov, N.B Delone, and V. Krainov. Tunnel ionization of complex atoms and of atomic ions in an alternating electric field. *Sov. Phys. JETP*, 64:1191, 1986.

[81] M. Chen, E. Cormier-Michel, C. G. R. Geddes, D. L. Bruhwiler, L. L. Yu, E. Esarey, C. B. Schroeder, and W. P. Leemans. Numerical modeling of laser tunneling ionization in explicit particle-in-cell codes. *Journal of Computational Physics*, 236:220–228, March 2013.

[82] M. Chen, E. Esarey, C. B. Schroeder, C. G. R. Geddes, and W. P. Leemans. Theory of ionization-induced trapping in laser-plasma accelerators. *Physics of Plasmas*, 19(3):033101, 2012.

[83] J. S. Liu, C. Q. Xia, W. T. Wang, H. Y. Lu, Ch Wang, A. H. Deng, W. T. Li, H. Zhang, X. Y. Liang, Y. X. Leng, X. M. Lu, C. Wang, J. Z. Wang, K. Nakajima, R. X. Li, and Z. Z. Xu. All-Optical Cascaded Laser Wakefield Accelerator Using Ionization-Induced Injection. *Phys. Rev. Lett.*, 107(3), July 2011.

[84] B. B. Pollock, C. E. Clayton, J. E. Ralph, F. Albert, A. Davidson, L. Divol, C. Filip, S. H. Glenzer, K. Herpoldt, W. Lu, K. A. Marsh, J. Meinecke, W. B. Mori, A. Pak, T. C. Rensink, J. S. Ross, J. Shaw, G. R. Tynan, C. Joshi, and D. H. Froula. Demonstration of a Narrow Energy Spread, $\sim$ 0.5 GeV Electron Beam from a Two-Stage Laser Wakefield Accelerator. *Phys. Rev. Lett.*, 107(4), July 2011.

[85] A. J. Gonsalves, K. Nakamura, C. Lin, D. Panasenko, S. Shiraishi, T. Sokollik, C. Benedetti, C. B. Schroeder, C. G. R. Geddes, J. van Tilborg, J. Osterhoff, E. Esarey, C. Toth, and W. P. Leemans. Tunable laser plasma accelerator based on longitudinal density tailoring. *Nat Phys*, 7(11):862–866, August 2011.

[86] Ming Zeng, Nasr A. M. Hafz, Kazuhisa Nakajima, Li-Ming Chen, Wei Lu, Warren B. Mori, Zheng-Ming Sheng, and Jie Zhang. Controlled ionization-induced injection by tailoring the gas-density profile in laser wakefield acceleration. *J. Plasma Phys.*, 78(04):363–371, February 2012.

[87] C. Thaury, E. Guillaume, A. Lifschitz, K. Ta Phuoc, M. Hansson, G. Grittani, J. Gautier, J.-P. Goddet, A. Tafzi, O. Lundh, and V. Malka. Shock assisted ionization injection in laser-plasma accelerators. *Sci. Rep.*, 5:16310, November 2015.

[88] C. Kamperidis, V. Dimitriou, S. P. D. Mangles, A. E. Dangor, and Z. Najmudin. Low energy spread electron beams from ionization injection in a weakly relativistic laser wakefield accelerator. *Plasma Phys. Control. Fusion*, 56(8):084007, July 2014.

[89] S. Bulanov, N. Naumova, F. Pegoraro, and J. Sakai. Particle injection into the wave acceleration phase due to nonlinear wake wave breaking. *Physical Review E*, 58:R5257–R5260, November 1998.

[90] H. Suk, N. Barov, J. B. Rosenzweig, and E. Esarey. Plasma Electron Trapping and Acceleration in a Plasma Wake Field Using a Density Transition. *Physical Review Letters*, 86(6):1011–1014, February 2001.

[91] C. G. R. Geddes, K. Nakamura, G. R. Plateau, Cs. Toth, E. Cormier-Michel, E. Esarey, C. B. Schroeder, J. R. Cary, and W. P. Leemans. Plasma-Density-Gradient Injection of Low Absolute-Momentum-Spread Electron Bunches. *Physical Review Letters*, 100(21):215004, May 2008.

[92] J. Faure, C. Rechatin, O. Lundh, L. Ammoura, and V. Malka. Injection and acceleration of quasimonoenergetic relativistic electron beams using density gradients at the edges of a plasma channel. *Physics of Plasmas*, 17(8):083107, August 2010.

[93] Z. H. He, B. Hou, J. A. Nees, J. H. Easter, J. Faure, K. Krushelnick, and A. G. R. Thomas. High repetition-rate wakefield electron source generated by few-millijoule, 30 fs laser pulses on a density downramp. *New Journal of Physics*, 15(5):053016, 2013.

[94] M. Hansson, B. Aurand, X. Davoine, H. Ekerfelt, K. Svensson, A. Persson, C.-G. Wahlström, and O. Lundh. Down-ramp injection and independently controlled acceleration of electrons in a tailored laser wakefield accelerator. *Phys. Rev. ST Accel. Beams*, 18(7), July 2015.

[95] A. Buck, J. Wenz, J. Xu, K. Khrennikov, K. Schmid, M. Heigoldt, J. M. Mikhailova, M. Geissler, B. Shen, F. Krausz, S. Karsch, and L. Veisz. Shock-Front Injector for High-Quality Laser-Plasma Acceleration. *Physical Review Letters*, 110(18), May 2013.

[96] K. Schmid, A. Buck, C. M. S. Sears, J. M. Mikhailova, R. Tautz, D. Herrmann, M. Geissler, F. Krausz, and L. Veisz. Density-transition based electron injector for laser driven wakefield accelerators. *Phys. Rev. ST Accel. Beams*, 13(9), September 2010.

[97] P. Brijesh, C. Thaury, K. T. Phuoc, S. Corde, G. Lambert, V. Malka, S. P. D. Mangles, M. Bloom, and S. Kneip. Tuning the electron energy by controlling the density perturbation position in laser plasma accelerators. *Physics of Plasmas*, 19(6):063104, 2012.

[98] D. Umstadter, J. K. Kim, and E. Dodd. Laser Injection of Ultrashort Electron Pulses into Wakefield Plasma Waves. *Physical Review Letters*, 76(12):2073–2076, March 1996.

[99] G. Fubiani, E. Esarey, C. B. Schroeder, and W. P. Leemans. Beat wave injection of electrons into plasma waves using two interfering laser pulses. *Physical Review E*, 70(1):016402, July 2004.

[100] H. Kotaki, S. Masuda, M. Kando, J. K. Koga, and K. Nakajima. Head-on injection of a high quality electron beam by the interaction of two laser pulses. *Physics of Plasmas*, 11(6):3296–3302, May 2004.

[101] X. Davoine, E. Lefebvre, J. Faure, C. Rechatin, A. Lifschitz, and V. Malka. Simulation of quasimonoenergetic electron beams produced by colliding pulse wakefield acceleration. *Physics of Plasmas*, 15(11):113102, November 2008.

[102] X. Davoine, E. Lefebvre, C. Rechatin, J. Faure, and V. Malka. Cold Optical Injection Producing Monoenergetic, Multi-GeV Electron Bunches. *Physical Review Letters*, 102(6):065001, February 2009.

[103] R. Lehe, A. F. Lifschitz, X. Davoine, C. Thaury, and V. Malka. Optical Transverse Injection in Laser-Plasma Acceleration. *Physical Review Letters*, 111(8):085005, August 2013.

[104] T. L. Audet, M. Hansson, P. Lee, F. G. Desforges, G. Maynard, S. Dobosz Dufrénoy, R. Lehe, J.-L. Vay, B. Aurand, A. Persson, I. Gallardo González, A. Maitrallain, P. Monot, C.-G. Wahlström, O. Lundh, and B. Cros. Investigation of ionization-induced electron injection in a wakefield driven by laser inside a gas cell. *Physics of Plasmas*, 23(2):023110, February 2016.

[105] G. Golovin, S. Chen, N. Powers, C. Liu, S. Banerjee, J. Zhang, M. Zeng, Z. Sheng, and D. Umstadter. Tunable monoenergetic electron beams from independently controllable laser-wakefield acceleration and injection. *Phys. Rev. ST Accel. Beams*, 18(1), January 2015.

[106] M. Vargas, W. Schumaker, Z.-H. He, Z. Zhao, K. Behm, V. Chvykov, B. Hou, K. Krushelnick, A. Maksimchuk, V. Yanovsky, and A. G. R. Thomas. Improvements to laser wakefield accelerated electron beam stability, divergence, and energy spread using three-dimensional printed two-stage gas cell targets. *Appl. Phys. Lett.*, 104(17):174103, April 2014.

[107] P. Lee, G. Maynard, T.L. Audet, B. Cros, R. Lehe, and J.-L. Vay. Dynamics of electron injection and acceleration driven by laser wakefield in tailored density profiles. *Physical Review Accelerators and Beams*, 19(11):112802, November 2016.

[108] A. G. R. Thomas, Z. Najmudin, S. P. D. Mangles, C. D. Murphy, A. E. Dangor, C. Kamperidis, K. L. Lancaster, W. B. Mori, W. Rozmus, and K. Krushelnick. Effect of Laser-Focusing Conditions on Propagation and Monoenergetic Electron Production in Laser-Wakefield Accelerators. *Phys. Rev. Lett.*, 98(095004), 2007.

[109] P. Sprangle and E. H. Esarey. Interaction of ultrahigh laser fields with beams and plasmas. *Physics of Fluids B: Plasma Physics*, 4(7):2241–2248, March 1992.

[110] C. G. Durfee, J. Lynch, and H. M. Milchberg. Development of a plasma waveguide for high-intensity laser pulses. *Physical Review E*, 51(3):2368–2389, March 1995.

[111] C. G. Durfee and H. M. Milchberg. Light pipe for high intensity laser pulses. *Physical Review Letters*, 71(15):2409–2412, October 1993.

[112] E. W. Gaul, S. P. Le Blanc, A. R. Rundquist, N. H. Matlis, H. Langhoff, and M. C. Downer. Production and characterization of a fully-ionized He plasma channel. *AIP Conference Proceedings*, 569(1):105–111, May 2001.

[113] S. Karsch, J. Osterhoff, A. Popp, T. P. Rowlands-Rees, Zs Major, M. Fuchs, B. Marx, R. Hörlein, K. Schmid, L. Veisz, S Becker, U. Schramm, B. Hidding, G. Pretzler, D. Habs, F. Grüner, F. Krausz, and S. M. Hooker. GeV-scale electron acceleration in a gas-filled capillary discharge waveguide. *New Journal of Physics*, 9(11):415, 2007.

[114] P. A. Walker, N. Bourgeois, W. Rittershofer, J. Cowley, N. Kajumba, A. R. Maier, J. Wenz, C. M. Werle, S. Karsch, F Grüner, D. R. Symes, P. P. Rajeev, S. J. Hawkes, O. Chekhlov, C. J. Hooker, B. Parry, Y. Tang, and S. M. Hooker. Investigation of GeV-scale electron acceleration in a gas-filled capillary discharge waveguide. *New Journal of Physics*, 15(4):045024, 2013.

[115] P. Sprangle, E. Esarey, J. Krall, and G. Joyce. Propagation and guiding of intense laser pulses in plasmas. *Physical Review Letters*, 69(15):2200–2203, October 1992.

[116] B. Cros, C. Courtois, G. Matthieussent, A. Di Bernardo, D. Batani, N. Andreev, and S. Kuznetsov. Eigenmodes for capillary tubes with dielectric walls and ultraintense laser pulse guiding. *Physical Review E*, 65(2):026405, January 2002.

[117] N. E. Andreev, B. Cros, L. M. Gorbunov, G. Matthieussent, P. Mora, and R. R. Ramazashvili. Laser wakefield structure in a plasma column created in capillary tubes. *Physics of Plasmas*, 9(9):3999–4009, August 2002.

[118] F. G. Desforges, M. Hansson, J. Ju, L. Senje, T. L. Audet, S. Dobosz-Dufrénoy, A. Persson, O. Lundh, C.-G. Wahlström, and B. Cros. Reproducibility of electron beams from laser wakefield acceleration in capillary tubes. *Nuclear Instruments and Methods in Physics Research Section A: Accelerators, Spectrometers, Detectors and Associated Equipment*, 740:54–59, March 2014.

[119] M. Hansson, L. Senje, A. Persson, O. Lundh, C.-G. Wahlström, F.G. Desforges, J. Ju, T.L. Audet, B. Cros, S. Dobosz Dufrénoy, and P. Monot. Enhanced stability of laser wakefield acceleration using dielectric capillary tubes. *Physical Review Special Topics - Accelerators and Beams*, 17(3):031303, March 2014.

[120] Paul Gibbon. *Short Pulse Laser Interactions With Matter: An Introduction*. Imperial College Press, London, September 2005.

[121] A. E. Siegman. *Lasers*. University Science Books, 1986.

[122] Guo-Zheng Sun, Edward Ott, Y. C. Lee, and Parvez Guzdar. Self-focusing of short intense pulses in plasmas. *Physics of Fluids*, 30:526–532, February 1987.

[123] Claire Ellen Max, Jonathan Arons, and A. Bruce Langdon. Self-Modulation and Self-Focusing of Electromagnetic Waves in Plasmas. *Physical Review Letters*, 33(4):209–212, July 1974.

[124] A. G. Litvak. Finite-amplitude Wave Beams in a Magnetoactive Plasma. *Soviet Journal of Experimental and Theoretical Physics*, 30:344, 1969.

[125] Sv Bulanov, In Inovenkov, Vi Kirsanov, Nm Naumova, and As Sakharov. Nonlinear Depletion of Ultrashort and Relativistically Strong Laser-Pulses in an Underdense Plasma. *Physics of Fluids B-Plasma Physics*, 4(7):1935–1942, July 1992. WOS:A1992JB51100024.

[126] W. Horton and T. Tajima. Pump depletion in the plasma-beat-wave accelerator. *Physical Review A*, 34(5):4110–4119, November 1986.

[127] E. Esarey, B. A. Shadwick, C. B. Schroeder, and W. P. Leemans. Nonlinear Pump Depletion and Electron Dephasing in Laser Wakefield Accelerators. volume 737, pages 578–584, December 2004.

[128] Denis Teychenné, Guy Bonnaud, and Jean-Louis Bobin. Wave-breaking limit to the wake-field effect in an underdense plasma. *Physical Review E*, 48(5):R3248–R3251, November 1993.

[129] Patrick Mora. Particle acceleration in a relativistic wave in the adiabatic regime. *Physics of Fluids B: Plasma Physics*, 4(6):1630–1634, June 1992.

[130] T. Katsouleas. Physical mechanisms in the plasma wake-field accelerator. *Phys. Rev. A*, 33(3):2056–2064, March 1986.

[131] W. P. Leemans, C. W. Siders, E. Esarey, N. E. Andreev, G. Shvets, and W. B. Mori. Plasma guiding and wakefield generation for second-generation experiments. *IEEE Transactions on Plasma Science*, 24(2):331–342, April 1996.

[132] W.P. Leemans, A.J. Gonsalves, H.-S. Mao, K. Nakamura, C. Benedetti, C.B. Schroeder, Cs. Tóth, J. Daniels, D.E. Mittelberger, S.S. Bulanov, J.-L. Vay, C.G.R. Geddes, and E. Esarey. Multi-GeV Electron Beams from Capillary-Discharge-Guided Subpetawatt Laser Pulses in the Self-Trapping Regime. *Physical Review Letters*, 113(24):245002, December 2014.

[133] Xiaoming Wang, Rafal Zgadzaj, Neil Fazel, Zhengyan Li, S. A. Yi, Xi Zhang, Watson Henderson, Y.-Y. Chang, R. Korzekwa, H.-E. Tsai, C.-H. Pai, H. Quevedo, G. Dyer, E. Gaul, M. Martinez, A. C. Bernstein, T. Borger, M. Spinks, M. Donovan, V. Khudik, G. Shvets, T. Ditmire, and M. C. Downer. Quasi-monoenergetic laser-plasma acceleration of electrons to 2 GeV. *Nature Communications*, 4:1988, June 2013.

[134] F. S. Tsung, Ritesh Narang, W. B. Mori, C. Joshi, R. A. Fonseca, and L. O. Silva. Near-GeV-Energy Laser-Wakefield Acceleration of Self-Injected Electrons in a Centimeter-Scale Plasma Channel. *Phys. Rev. Lett.*, 93(18), October 2004.

[135] M. Tzoufras, W. Lu, F. S. Tsung, C. Huang, W. B. Mori, T. Katsouleas, J. Vieira, R. A. Fonseca, and L. O. Silva. Beam Loading in the Nonlinear Regime of Plasma-Based Acceleration. *Phys. Rev. Lett.*, 101(14), September 2008.

[136] Wim Leemans and Eric Esarey. Laser-driven plasma-wave electron accelerators. *Phys. Today*, 62(3):44–49, March 2009.

[137] Stanley Humphries Humphries. *Charged Particle Beams*. Dover Publications, Mineola, New York, reprint edition edition, April 2013.

[138] C. DesRosiers, V. Moskvin, A. F. Bielajew, and L. Papiez. 150-250 MeV electron beams in radiation therapy. *Physics in Medicine and Biology*, 45(7):1781, 2000.

[139] C. Yeboah, G. A. Sandison, and V. Moskvin. Optimization of intensity-modulated very high energy (50250 MeV) electron therapy. *Physics in Medicine and Biology*, 47(8):1285, 2002.

[140] Anders Brahme. *Biologically Optimized Radiation Therapy*. WSPC, March 2014.

[141] Kazuhisa Nakajima. Compact X-ray sources: Towards a table-top free-electron laser. *Nature Physics*, 4(2):92–93, February 2008.

[142] E. Brunetti, R. P. Shanks, G. G. Manahan, M. R. Islam, B. Ersfeld, M. P. Anania, S. Cipiccia, R. C. Issac, G. Raj, G. Vieux, G. H. Welsh, S. M. Wiggins, and D. A. Jaroszynski. Low Emittance, High Brilliance Relativistic Electron Beams from a Laser-Plasma Accelerator. *Physical Review Letters*, 105(21):215007, November 2010.

[143] Kazuhisa Nakajima, Aihua Deng, Xiaomei Zhang, Baifei Shen, Jiansheng Liu, Ruxin Li, Zhizhan Xu, Tobias Ostermayr, Stefan Petrovics, Constantin Klier, Khalid Iqbal, Hartmut Ruhl, and Toshiki Tajima. Operating plasma density issues on large-scale laser-plasma accelerators toward high-energy frontier. *Physical Review Special Topics - Accelerators and Beams*, 14(9):091301, September 2011.

[144] Martin Reiser. *Theory and Design of Charged Particle Beams*. Wiley-VCH, Weinheim, 2 edition edition, May 2008.

[145] Klaus Floettmann. Some basic features of the beam emittance. *Physical Review Special Topics - Accelerators and Beams*, 6(3):034202, March 2003.

[146] M. Migliorati, A. Bacci, C. Benedetti, E. Chiadroni, M. Ferrario, A. Mostacci, L. Palumbo, A. R. Rossi, L. Serafini, and P. Antici. Intrinsic normalized emittance growth in laser-driven electron accelerators. *Physical Review Special Topics - Accelerators and Beams*, 16(1):011302, January 2013.

[147] C.B. Schroeder, J.-L. Vay, E. Esarey, S.S. Bulanov, C. Benedetti, L.-L. Yu, M. Chen, C.G.R. Geddes, and W.P. Leemans. Thermal emittance from ionization-induced trapping in plasma accelerators. *Physical Review Special Topics - Accelerators and Beams*, 17(10):101301, October 2014.

[148] P. Michel, C. B. Schroeder, B. A. Shadwick, E. Esarey, and W. P. Leemans. Radiative damping and electron beam dynamics in plasma-based accelerators. *Physical Review E*, 74(2):026501, August 2006.

[149] J.L. Shaw, N. Lemos, L.D. Amorim, N. Vafaei-Najafabadi, K.A. Marsh, F.S. Tsung, W.B. Mori, and C. Joshi. Role of Direct Laser Acceleration of Electrons in a Laser Wakefield Accelerator with Ionization Injection. *Physical Review Letters*, 118(6):064801, February 2017.

[150] A. Pukhov, Z.-M. Sheng, and Meyer ter Vehn. Particle acceleration in relativistic laser channels. *Physics of Plasmas*, 6(7):2847–2854, June 1999.

[151] Kane Yee. Numerical solution of inital boundary value problems involving maxwell's equations in isotropic media. *IEEE Transactions on Antennas and Propagation*, 14:302–307, May 1966.

[152] J. Boris. Relativistic plasma simulation-optimization of a hybrid code. 1970.

[153] R.W Hockney and J.W Eastwood. Computer Simulation Using Particles, January 1988.

[154] R.L. Morse and C.W. Nielson. Numerical Simulation of the Weibel Instability in One and Two Dimensions. *The Physics of Fluids*, 14(4):830–840, April 1971.

[155] H. Ruhl and P. Mulser. Relativistic Vlasov simulation of intense fs laser pulse-matter interaction. *Physics Letters A*, 205(5):388–392, September 1995.

[156] E. Sonnendrücker, F. Filbet, A. Friedman, E. Oudet, and J. L. Vay. Vlasov simulations of beams with a moving grid. *Computer Physics Communications*, 164(13):390–395, December 2004.

[157] C.K. Birdsall and Langdon. Plasma Physics via Computer Simulation, October 2004.

[158] J.-L. Vay. Simulation of beams or plasmas crossing at relativistic velocity. *Physics of Plasmas*, 15(5):056701, February 2008.

[159] B. Marder. Eliminating boundary-induced errors in the pseudo-current method. *Journal of Computational Physics*, 104(1):273, 1993.

[160] T. Zh. Esirkepov. Exact charge conservation scheme for Particle-in-Cell simulation with an arbitrary form-factor. *Computer Physics Communications*, 135(2):144–153, April 2001.

[161] John Villasenor and Oscar Buneman. Rigorous charge conservation for local electromagnetic field solvers. *Computer Physics Communications*, 69:306–316, March 1992.

[162] R. Courant, K. Friedrichs, and H. Lewy. On the Partial Difference Equations of Mathematical Physics. *IBM Journal of Research and Development*, 11(2):215–234, March 1967.

[163] I. Haber, R. Lee, H. H. Klein, and Boris Boris, J. P. Advances in electromagnetic plasma simulation techniques. 1973.

[164] Jay P. Boris and Roswell Lee. Nonphysical Self Forces in Some Electromagnetic Plasma-Simulation Algorithms. *Journal of Computational Physics*, 12:131–136, May 1973.

[165] Brendan B. Godfrey and A. Bruce Langdon. Stability of the Langdon-Dawson advective algorithm. *Journal of Computational Physics*, 20(2):251–255, 1976.

[166] Brendan B. Godfrey. Canonical momenta and numerical instabilities in particle codes. *Journal of Computational Physics*, 19(1):58–76, 1975.

[167] Brendan B. Godfrey. Numerical Cherenkov instabilities in electromagnetic particle codes. *Journal of Computational Physics*, 15(4):504–521, 1974.

[168] John David Jackson. *Classical Electrodynamics, third edition.* John Wiley & Sons, Inc., New York, 3rd edition edition, 1998.

[169] J. B. Cole. A high-accuracy realization of the Yee algorithm using non-standard finite differences. *IEEE Transactions on Microwave Theory and Techniques*, 45(6):991–996, June 1997.

[170] J. B. Cole. High-accuracy Yee algorithm based on nonstandard finite differences: new developments and verifications. *IEEE Transactions on Antennas and Propagation*, 50(9):1185–1191, September 2002.

[171] Mikko Kärkkäinen, Erion Gjonaj, Thomas Lau, and Thomas Weiland. Low-Dispersion Wake Field Calculation Tools. *Proceedings of ICAP*, pages 35–40, 2006.

[172] J. L. Vay, C. G. R. Geddes, E. Cormier-Michel, and D. P. Grote. Numerical methods for instability mitigation in the modeling of laser wakefield accelerators in a Lorentz-boosted frame. *Journal of Computational Physics*, 230(15):5908–5929, July 2011.

[173] Xinlu Xu, Peicheng Yu, Samual F. Martins, Frank S. Tsung, Viktor K. Decyk, Jorge Vieira, Ricardo A. Fonseca, Wei Lu, Luis O. Silva, and Warren B. Mori. Numerical instability due to relativistic plasma drift in EM-PIC simulations. *Computer Physics Communications*, 184(11):2503–2514, November 2013.

[174] Anatoly Spitkovsky. Particle Acceleration in Relativistic Collisionless Shocks: Fermi Process at Last? *The Astrophysical Journal Letters*, 682(1):L5, July 2008.

[175] Uri Keshet, Boaz Katz, Anatoly Spitkovsky, and Eli Waxman. Magnetic Field Evolution in Relativistic Unmagnetized Collisionless Shocks. *The Astrophysical Journal Letters*, 693(2):L127, 2009.

[176] Samuel F. Martins, Ricardo A. Fonseca, Luís O. Silva, Wei Lu, and Warren B. Mori. Numerical simulations of laser wakefield accelerators in optimal Lorentz frames. *Computer Physics Communications*, 181(5):869–875, May 2010.

[177] Lorenzo Sironi, Anatoly Spitkovsky, and Jonathan Arons. The Maximum Energy of Accelerated Particles in Relativistic Collisionless Shocks. *The Astrophysical Journal*, 771(1):54, 2013.

[178] Brendan B. Godfrey and Jean-Luc Vay. Suppressing the numerical Cherenkov instability in FDTD PIC codes. *Journal of Computational Physics*, 267:1–6, June 2014.

[179] R. Lehe, A. Lifschitz, C. Thaury, V. Malka, and X. Davoine. Numerical growth of emittance in simulations of laser-wakefield acceleration. *Physical Review Special Topics - Accelerators and Beams*, 16(2):021301, February 2013.

[180] Gustafsson Bertil, Kreiss Heinz-Otto, and Oliger Joseph. *Time-Dependent Problems and Difference Methods*. Wiley, New York, 1995.

[181] Bengt Fornberg. Generation of finite difference formulas on arbitrarily spaced grids. *Mathematics of Computation*, 51(184):699–706, 1988.

[182] Jean-Luc Vay, Irving Haber, and Brendan B. Godfrey. A domain decomposition method for pseudo-spectral electromagnetic simulations of plasmas. *Journal of Computational Physics*, 243:260–268, June 2013.

[183] Q. H. Liu. The PSTD algorithm: A time-domain method requiring only two cells per wavelength. *Microwave and Optical Technology Letters*, 15(3):158–165, June 1997.

[184] John M. Dawson. Particle simulation of plasmas. *Reviews of Modern Physics*, 55(2):403–447, April 1983.

[185] P. Lee, T. L. Audet, R. Lehe, J.-L. Vay, G. Maynard, and B. Cros. Modeling laser-driven electron acceleration using WARP with Fourier decomposition. *Nuclear Instruments and Methods in Physics Research Section A: Accelerators, Spectrometers, Detectors and Associated Equipment*, December 2015.

[186] A. Davidson, A. Tableman, W. An, F. S. Tsung, W. Lu, J. Vieira, R. A. Fonseca, L. O. Silva, and W. B. Mori. Implementation of a hybrid particle code with a PIC description in r-z and a gridless description in phi into OSIRIS. *Journal of Computational Physics*, 281:1063–1077, January 2015.

[187] Bjorn Engquist and Andrew Majda. Absorbing boundary conditions for the numerical simulation of waves. *Mathematics of Computation*, 31(139):629–651, 1977.

[188] Jean-Luc Vay. Asymmetric Perfectly Matched Layer for the Absorption of Waves. *Journal of Computational Physics*, 183(2):367–399, December 2002.

[189] Y. Ohmura and Y. Okamura. Staggered Grid Pseudo-spectral Time-domain Method for Light Scattering Analysis. *Piers 2010 Cambridge: Progress in Electromagnetics Research Symposium Proceedings, Vols 1 and 2*, pages 121–124, 2010. WOS:000305490800023.

[190] Matti Lassas and Erkki Somersalo. On the existence and convergence of the solution of PML equations. *Computing*, 60(3):229–241, September 1998.

[191] B. Fornberg. High-Order Finite Differences and the Pseudospectral Method on Staggered Grids. *SIAM Journal on Numerical Analysis*, 27(4):904–918, August 1990.

[192] H. Vincenti and J. L. Vay. Detailed analysis of the effects of stencil spatial variations with arbitrary high-order finite-difference Maxwell solver. *Computer Physics Communications*, 200:147–167, March 2016.

[193] J.-L. Vay, C. G. R. Geddes, C. Benedetti, D. L. Bruhwiler, E. Cormier-Michel, B. M. Cowan, J. R. Cary, and D. P. Grote. Modeling Laser Wakefield Accelerators in a Lorentz Boosted Frame. *AIP Conference Proceedings*, 1299(1):244–249, November 2010.

[194] J.-L. Vay, C. G. R Geddes, E. Cormier-Michel, and D. P. Grote. Effects of hyperbolic rotation in Minkowski space on the modeling of plasma accelerators in a Lorentz boosted frame. *Physics of Plasmas*, 18(3):030701, March 2011.

[195] Brendan B. Godfrey and Jean-Luc Vay. Improved numerical Cherenkov instability suppression in the generalized PSTD PIC algorithm. *Computer Physics Communications*, 196:221–225, November 2015.

[196] B. B. Godfrey, J. L. Vay, and I. Haber. Numerical Stability Improvements for the Pseudospectral EM PIC Algorithm. *IEEE Transactions on Plasma Science*, 42(5):1339–1344, May 2014.

[197] Peicheng Yu, Xinlu Xu, Adam Tableman, Viktor K. Decyk, Frank S. Tsung, Frederico Fiuza, Asher Davidson, Jorge Vieira, Ricardo A. Fonseca, Wei Lu, Luis O. Silva, and Warren B. Mori. Mitigation of numerical Cerenkov radiation and instability using a hybrid finite difference-FFT Maxwell solver and a local charge conserving current deposit. *Computer Physics Communications*, 197:144–152, December 2015.

[198] Peicheng Yu, Xinlu Xu, Viktor K. Decyk, Frederico Fiuza, Jorge Vieira, Frank S. Tsung, Ricardo A. Fonseca, Wei Lu, Luis O. Silva, and Warren B. Mori. Elimination of the numerical Cerenkov instability for spectral EM-PIC codes. *Computer Physics Communications*, 192:32–47, July 2015.

[199] Fei Li, Peicheng Yu, Xinlu Xu, Frederico Fiuza, Viktor K. Decyk, Thamine Dalichaouch, Asher Davidson, Adam Tableman, Weiming An, Frank S. Tsung, Ricardo A. Fonseca, Wei Lu, and Warren B. Mori. Controlling the numerical Cerenkov

instability in PIC simulations using a customized finite difference Maxwell solver and a local FFT based current correction. *Computer Physics Communications*, 214:6–17, May 2017.

[200] M. Kirchen, R. Lehe, B. B. Godfrey, I. Dornmair, S. Jalas, K. Peters, J.-L. Vay, and Maier. Stable discrete representation of relativistically drifting plasmas. *Physics of Plasmas*, 23(10):100704, October 2016.

[201] Remi Lehe, Manuel Kirchen, Brendan B. Godfrey, Andreas R. Maier, and Jean-Luc Vay. Elimination of numerical Cherenkov instability in flowing-plasma particle-in-cell simulations by using Galilean coordinates. *Physical Review E*, 94(5):053305, November 2016.

[202] Peicheng Yu, Xinlu Xu, Asher Davidson, Adam Tableman, Thamine Dalichaouch, Fei Li, Michael D. Meyers, Weiming An, Frank S. Tsung, Viktor K. Decyk, Frederico Fiuza, Jorge Vieira, Ricardo A. Fonseca, Wei Lu, Luis O. Silva, and Warren B. Mori. Enabling Lorentz boosted frame particle-in-cell simulations of laser wakefield acceleration in quasi-3d geometry. *Journal of Computational Physics*, 316:747–759, July 2016.

[203] R. Lehe. Laser-plasma lens for laser-wakefield accelerators. *Phys. Rev. ST Accel. Beams*, 17(12), December 2014.

[204] Jean-Luc Vay and Rémi Lehe. Simulations for Plasma and Laser Acceleration. *Reviews of Accelerator Science and Technology*, 09:165–186, January 2016.

[205] J.-L. Vay, C. G. R. Geddes, E. Esarey, C. B. Schroeder, W. P. Leemans, E. Cormier-Michel, and D. P. Grote. Modeling of 10 GeV-1 TeV laser-plasma accelerators using Lorentz boosted simulations. *Physics of Plasmas*, 18(12):123103, December 2011.

[206] S. F. Martins, R. A. Fonseca, W. Lu, W. B. Mori, and L. O. Silva. Exploring laser-wakefield-accelerator regimes for near-term lasers using particle-in-cell simulation in Lorentz-boosted frames. *Nature Physics*, 6(4):311–316, March 2010.

[207] E. Cormier-Michel, C. G. R. Geddes, E. Esarey, C. B. Schroeder, D. L. Bruhwiler, K. Paul, B. Cowan, and Leemans. Scaled simulations of a 10 GeV accelerator. *AIP Conference Proceedings*, 1086(1):297–302, January 2009.

[208] H. G. Weller, G. Tabor, H. Jasak, and C. Fureby. A tensorial approach to computational continuum mechanics using object-oriented techniques. *Computers in Physics*, 12(6):620, 1998.

[209] P. Sprangle, B. Hafizi, J. R. Peñano, R. F. Hubbard, A. Ting, C. I. Moore, D. F. Gordon, A. Zigler, D. Kaganovich, and T. M. Jr Antonsen. Wakefield generation and GeV acceleration in tapered plasma channels. *Physical Review E*, 63(5), April 2001.

[210] SV Bulanov, VA Vshivkov, and GI Dudnikova. Laser acceleration of charged particles in inhomogeneous plasma. 1. *Fizika Plazmy*, 23(4):284–295, 1997.

[211] A. Pukhov and I. Kostyukov. Control of laser-wakefield acceleration by the plasma-density profile. *Physical Review E*, 77(2), February 2008.

[212] W. Rittershofer, C. B. Schroeder, E. Esarey, F. J. Gr\Íuner, and W. P. Leemans. Tapered plasma channels to phase-lock accelerating and focusing forces in laser-plasma accelerators. *Physics of Plasmas*, 17(6):063104, June 2010.

[213] F. L. Teixeira and W. C. Chew. Perfectly matched layer in cylindrical coordinates. In *IEEE Antennas and Propagation Society International Symposium 1997. Digest*, volume 3, pages 1908–1911 vol.3, July 1997.

[214] G. Pariente, V. Gallet, A. Borot, O. Gobert, and F. Quéré. Spacetime characterization of ultra-intense femtosecond laser beams. *Nature Photonics*, 10(8):547–553, August 2016.

université PARIS-SACLAY

ÉCOLE DOCTORALE
Ondes et Matière (EDOM)

Titre : Modélisation d'un injecteur laser-plasma pour l'accélération multi-étages

Mots clefs : accélération par sillage laser, code PIC, Warp, technique de Lorentz-boosted frame, couche absorbante parfaite de Bérenger (PML)

Résumé : L'accélération par sillage laser (ASL) repose sur l'interaction entre un faisceau laser intense et un plasma sous-dense. Au travers de cette interaction, une onde de plasma est générée avec un fort champ accélérateur, de trois ordres de grandeur plus élevé que celui d'un accélérateur conventionnel, rendant envisageable la réalisation d'accélérateurs futurs plus compacts. Pour la conception d'un futur accélérateur, un faisceau d'électrons de forte charge, faible dispersion en énergie et faible émittance doit être accéléré à des grandes énergies. Pour ce faire, la solution consiste à accélérer ces électrons dans un schema multi-étages, qui est composé de trois étages: un injecteur, une ligne de transport et un accélérateur.
Ce travail de thèse porte sur la modélisation de l'injecteur avec le code PIC Warp et sur les méthodes numériques telles que la technique de Lorentz-boosted frame pour diminuer le temps de calcul et la couche absorbante parfaite de Bérenger (PML) pour assurer la précision des calculs numériques. Ce travail de thèse a démontré l'efficacité de la PML dans les schemas FDTD à des ordres élevés et pseudo-spectral. Il a aussi démontré la convergence des résultats des simulations réalisées avec la technique de Lorentz-boosted frame dans un régime fortement non-linéaire de l'injecteur, permettant d'accélérer les calculs d'un facteur important (~ 36) tout en assurant leur précision. La modélisation effectuée dans cette thèse a permis d'analyser et de comprendre les résultats expérimentaux, ainsi que de prédire les résultats des futures expériences. Plusieurs méthodes d'optimisation de l'injecteur ont également été proposées pour la génération d'un faisceau d'électrons conforme aux spécifications d'un futur accélérateur.

Title : Modeling of a laser-plasma injector for the multi-stage accelerator

Keywords : laser wakefield acceleration, PIC code, Warp, Lorentz-boosted frame technique, Perfectly Matched Layer (PML)

Abstract : Laser Wakefield Acceleration (LWFA) relies on the interaction between an intense laser pulse and an under-dense plasma. This interaction generates a plasma wave with a strong accelerating field, which is three orders of magnitude higher than the one of the conventional accelerator; more compact accelerator is therefore theoretically possible. In the design of a future accelerator, a high quality electron bunch with a high charge, low energy spread and low emittance has to be accelerated to high energies. A solution for this is a multi-stage accelerator, which consists of an injector, a transport line and accelerator stages.
This research work focuses on the modeling of the injector using the PIC code Warp and on the numerical methods such as the Lorentz-boosted frame to speedup calculations and the Perfectly Matched Layer (PML) to ensure the precision in numerical calculations. The outcome of this thesis has demonstrated the efficiency of the PML in the high-order FDTD and the pseudo-spectral solvers. Besides, it has also demonstrated the convergence of the results performed in simulations using the Lorentz-boosted frame technique. This technique speeds up simulations by a large factor (~ 36) while preserving their accuracy. The modeling work in this thesis has allowed analysis and understanding of experimental results, as well as prediction of results for future experiments. This thesis has also shown ways to optimize the injector to deliver an electron bunch that conforms with the specifications of future accelerators.

Université Paris-Saclay
Espace Technologique / Immeuble Discovery
Route de l'Orme aux Merisiers RD 128 / 91190 Saint-Aubin, France